# JOURNAL OF THE AERONAUTICAL SCIENCES

VOLUME 24 MAY, 1957 NUMBER 5


ST. LOUIS
MAY 8 1957
PUBLIC LIBRARY

## CONTENTS


Recent Developments in the Method of the Rheoelectric Analogy Applied to Aerodynamics ..... LUCIEN C. MALAVARD 321

The Plastic Bending of an Eccentrically Loaded Column ..... WILLIAM E. BOYCE 332

Theory of the Finite-Span Blowing Wing ..... H. B. HELMBOLD 339

Dissociation Effects in Hypersonic Viscous Flows ..... Y. H. KUO 345

Buckling of Thin-Walled Circular Cylinders Under Axial Compression and Internal Pressure ..... Y. C. FUNG AND E. E. SECHLER 351

The Aerodynamic Variable Nozzle ..... A. I. MARTIN 357

The Balance Method Applied to Swept-Wing Stress Analysis ..... LUIGI BROGLIO 363

Correlation of Cone-Cylinder Normal Force and Pitching Moment Data by the Hypersonic Similarity Rule ..... WILLIAM H. DORRANCE AND ROBERT G. NORELL 371

Readers' Forum ..... 378


*Published by*
INSTITUTE OF THE AERONAUTICAL SCIENCES, INC.

# JOURNAL OF THE AERONAUTICAL SCIENCES

*Editor:* W. R. SEARS
*Director, Graduate School of Aeronautical Engineering, Cornell University*

*Associate Editor:* ROBERT R. DEXTER *Managing Editor:* RITA J. TURINO
*Editorial Assistant:* CAROLINE TAYLOR

## Editorial Committee

**Aerodynamics and Fluid Mechanics**
Holt Ashley
H. Julian Allen
Dean R. Chapman
Francis H. Clauser
Hugh L. Dryden
John C. Evvard
Antonio Ferri
Alexander Flax
Wallace D. Hayes
R. T. Jones
Carl Kaplan
H. W. Liepmann
C. C. Lin
H. F. Ludloff
Harold Luskin
Clark B. Millikan
C. D. Perkins
H. J. E. Reid
George S. Schairer
G. B. Schubauer
John Stack
Theodore Theodorsen
Arthur N. Tifford
Th. von Kármán

**Flight Testing**
R. R. Gilruth
Melvin N. Gough
W. L. Howland
W. F. Milliken, Jr.

**Rotating Wing Aircraft**
F. B. Gustafson
K. H. Hohenemser
Bartram Kelley
R. B. Maloy
Ralph McClarren
R. H. Miller
R. H. Prewitt
Igor I. Sikorsky

**Structures**
John E. Duberg
N. J. Hoff
Samuel Levy
J. F. McBrearty
W. Ramberg
E. E. Sechler
F. R. Shanley
C. R. Strang
S. Timoshenko

**Meteorology**
C. F. Brooks
D. M. Little
F. W. Reichelderfer
K. C. Spengler

**Vibration and Flutter**
Lee Arnold
M. A. Biot
R. L. Bisplinghoff
Harold A. Cheilek
I. E. Garrick
Martin Goland

**Aircraft Design**
W. E. Beall
E. H. Heinemann
Hall L. Hibbard
Richard Hutton
C. L. Johnson
A. A. Kartveli
E. G. Stout
F. K. Teichmann

**Electronics**
Welcome W. Bender
K. C. Black
M. V. Kiebert, Jr.
David S. Little
S. B. Rogers
Paul Rosenberg
L. M. Sherer

**Physiologic Problems**
H. G. Armstrong
Louis H. Bauer
Robert J. Benford
W. Randolph Lovelace, II
Ross A. MacFarland

**Flight Propulsion**
William Bollay
George W. Brady
R. P. Kroon
Frank E. Marble
Abe Silverstein
Martin Summerfield
E. S. Taylor

**Instruments**
Alan G. Binnie
Charles H. Colvin
Frank R. Cook
C. S. Draper
S. G. Eskin
C. F. Savage
R. C. Sylvander

## SUBSCRIPTION RATES

JOURNAL OF THE AERONAUTICAL SCIENCES, Published Monthly. United States and Possessions: 1 Year, $15.00; Single Copies, $1.50. Foreign Countries Including Canada (American Currency Rates): 1 Year, $16.00; Single Copies, $1.50.

AERONAUTICAL ENGINEERING REVIEW, Published Monthly. United States and Possessions: 1 Year, $3.00; Single Copies, $0.50. Foreign Countries Including Canada (American Currency Rates): 1 Year, $3.50; Single Copies, $0.50.

Notices of change of address should be sent to the Institute at least 30 days prior to actual change of address.

Manuscripts for publication, proofs, and all correspondence should be addressed to the Editorial Office of the JOURNAL.

Publication Office, 20th and Northampton Sts., Easton, Pa. Correspondence regarding subscriptions may be addressed to the Editorial Office of the JOURNAL OF THE AERONAUTICAL SCIENCES, 2 East 64th Street, New York 21, N.Y.

*© Copyright, 1957, by the Institute of the Aeronautical Sciences, Inc.*

Entered as Second-Class Matter at the Post Office, Easton, Pa., May 1, 1937. Acceptance for mailing at a special rate of Postage provided for in the Act of August 24, 1912. Authorized April 29, 1937.

JOURNAL OF THE AERONAUTICAL SCIENCES

VOLUME 24 MAY, 1957 NUMBER 5

# Recent Developments in the Method of the Rheoelectric Analogy Applied to Aerodynamics

LUCIEN C. MALAVARD*

*University of Paris*

SUMMARY

Rheoelectric analogies (using the electrolytic tank or conducting paper) can be employed either as a means for the graphical representation of a theoretical flow field or as a procedure for calculating aerodynamic characteristics. The following recent applications, corresponding to these two aspects, are discussed:

(1) A simple method for the direct plotting of isogradient and isoargument lines of a plane harmonic field (application to the plotting of the isobars around airfoil sections, to the determination of jet lines, to the tracing out of lines of constant modulus, and to conformal mapping).

(2) Interpretation by electrical analogy of a linearized theory of a wing jet flap, and results obtained on an airfoil section; a method for studying jet flap action on a lifting surface.

(3) Calculation by electrical analogy of the aerodynamic characteristics of the annular wing; analog representations of various parameters (camber, thickness, conicity); and the analog model of the annular wing considered as a lifting surface.

## INTRODUCTION

THE EARLIEST APPLICATIONS of the rheoelectric analogy method to aerodynamics problems go back more than thirty years. This method is now considered classical, and the use of the electric tank and of graphite conducting paper for tracing the streamlines or equipotential lines of a theoretical flow is well known. At the International Congress of Applied Mechanics in 1938, J. Pérès[1] presented a general overall view of the method, citing several typical applications and, in particular the results of work undertaken under his direction and carried out in a special laboratory which he had created as early as 1932.

Since that time, and always under the direction of J. Pérès, the analogy method has been the subject of continually increasing efforts in France. At the present time two laboratories are in continuous operation, one at the National Scientific Research Center (CNRS), the other at the National Office of Aeronautical Study and Research (ONERA), the latter specializing in questions relating to aeronautics.

The various applications of the method to the classical problems of airfoil theory, lifting line and lifting surface theory, propellers, compressible fluids, etc., have been presented in detail in a recent AGARDograph,[2] where necessary information was given concerning analog setups, model preparation, experimental procedure, and the conversion of test data into useful form.

As currently employed, electrical analogies present two quite different aspects. (a) The engineer may be satisfied with determining a simple graphical representation of a given flow, tracing out, for example, the streamlines about an object, these being identified in the analogy with the equipotential lines defined in an electric tank. There is thus obtained an "image" of the flow the interest of which is comparable from a theoretical standpoint to that of viewing a real flow in the wind tunnel. (b) The rheoelectrical analogy method can also be used as a "calculating machine" intended to obtain the practical solution of certain types of mathematical problems. In this case, the experimental setups constitute an analogue calculator wherein the given data and the results are translated into electrical quantities. In this case it is rarely necessary to carry out a plot of the flow field.

The aim of the present paper is to present some results of recent studies carried out in the CNRS and ONERA laboratories. These studies have been carried out since the editing of the AGARDograph mentioned above. They were selected to illustrate the two aspects of the analogy method mentioned under (a) and (b) above. The following topics are discussed: (1) the direct plot-

Presented at the Aerodynamics—I Session, Twenty-Fifth Annual Meeting, IAS, New York, January 28–31, 1957.

* Professeur à la Sorbonne, Chaire d'Aviation, Paris.

ting of the constant velocity lines of plane flow fields, (2) the analog calculation of the aerodynamic characteristics of a wing subjected to blowing at the trailing edge (jet flap), and (3) the analog calculation of the annular wing.

The utility of the method may be judged on the basis of these examples. This utility might appear questionable today when large high-speed electronic computing machines are available; however, aside from the simplicity and the economy of the experimental means employed, it will be seen that the rheoelectric analogy method can, on the one hand, furnish useful aid to the engineer by providing him with a concrete basis for theoretical reasoning and, on the other hand, can enable the calculator to avoid complete mathematical formulation of a given problem when the general data have been prescribed.

As is well known, the rheoelectrical analogy method consists in identifying any function $\varphi(x, y, z)$ governed by the Laplace equation with the distribution of electrical potential $V(x, y, z)$ in a homogenous conduction medium that is suitably fed electrically, the contours of the medium being made to reproduce the form of the field under study.

To represent the plane flow of an incompressible perfect fluid a conducting sheet (Teledeltos conducting paper, for example) or a plane electric tank containing a conducting liquid of shallow depth (usually tap water can be used). The study of three-dimensional flows is carried out in large, deep tanks. For rotationally symmetric flows, slightly inclined tanks are used wherein the wedge of liquid formed by the bottom and the free surface corresponds to a slice of the flow contained between two neighboring meridian planes.

Special attention must be paid to correct representation of the boundary conditions, these usually defining the type of electrical feed to be used on the analog model. In order to represent the usual classical boundary conditions of Dirichlet, Neumann, and Fourier, the model surfaces are covered with small electrodes $e$ separated from each other by narrow insulating spaces.

Each electrode $e$, which corresponds to an elementary area $\delta S$ of the boundary, can thus take on a value of electrical potential localized to that electrode alone. This potential may be imposed at a previously fixed value by means of a potentiometer. This is what is done when the boundary condition is of the Dirichlet type; this potential then represents (to within a scale factor) the given value of the function $\varphi(M)$ at the point $M$ of the boundary which corresponds to the midpoint of the elementary area $\delta S$.

When the potential has thus been fixed the electric current $I$ which feeds the electrode can be measured, thus giving the value of the normal derivative $d\varphi(M) \div dn$ of the function $\varphi$ at this point; the following relation holds, if $\varphi$ be identified directly with $V$:

$$I = -\sigma(d\varphi/dn)\,\delta S \qquad (1)$$

where $\sigma$ is the conductivity of the electrical model.

Inversely, if the boundary condition is of the Neumann type, Eq. (1) indicates that a current $I$ which is proportional to the value of $d\varphi/dn$, considered as known, must be sent into the model. The measurement of the electrical potential then taken by the electrode determines the value of $\varphi(M)$ which is sought.

Finally, in the case of a Fourier boundary condition [linear relation between $\varphi(M)$ and $d\varphi(M)/dn$] of the type

$$\varphi = a(d\varphi/dn) + \bar{\varphi} \qquad (2)$$

where $a(M)$ and $\bar{\varphi}(M)$ are known functions, it can easily be verified that each electrode $e$ must be fed by connecting between it and its potentiometer (which is set at the value $\bar{\varphi}$) a resistance $R$ having a value of $a(M)/\sigma\delta S$, as seen by Eq. (1).

## Direct Plotting of a Velocity Field

(1) The procedure usually used in the rheoelectric analogy method to represent the two-dimensional flow of a perfect incompressible fluid consists in identifying the velocity potential $\varphi(x, y)$ or the stream function $\psi(x, y)$ with the electrical potential in a plane tank. In the former case, the model of an obstacle in the flow is insulating; in the latter case, it is conducting with a constant potential.

In order to obtain the value of the velocity at a point of the flow the electrical gradient must be determined at the corresponding point in the tank. This is obtained by using a system of two very closely spaced probes (double probe) which must be correctly oriented and between which the potential difference is measured. This potential difference is always very small, and it is necessary to amplify it considerably; only a carefully designed apparatus, such as that used at ONERA[2] will provide correct results.

In all cases, measurements along the contour of the object placed in the tank are delicate, and the small imperfections in the fabrication of the analog model can give rise to fairly large errors. These errors can be partially avoided if the essential geometric characteristics, such as slopes or curvatures, be introduced in the form of electrical data.

In order to do this the real or imaginary part of the complex velocity $w = \varphi'_x - i\varphi'_y$ can be represented *directly* in the electric tank, or, what is more convenient, its logarithm

$$\log w = \log V - i\theta$$

where $V$ designates the absolute value of the velocity and $\theta$ its argument. The functions $\log V$ and $\theta$ are harmonic and therefore can be represented analogically in a plane tank or by means of Teledeltos paper.

The contour of the object (which will here be taken as an airfoil) is a streamline and, when its geometrical form is given, the function $\theta(s)$ is known ($s$ being the arc length along the contour). The analog representation is very simple: the function $\theta(x, y)$ is identified with the electrical potential of the plane model. The boundary conditions are of the Dirichlet type; $\theta(s)$ is specified along the contour and has a discontinuity of $\pi$ at the

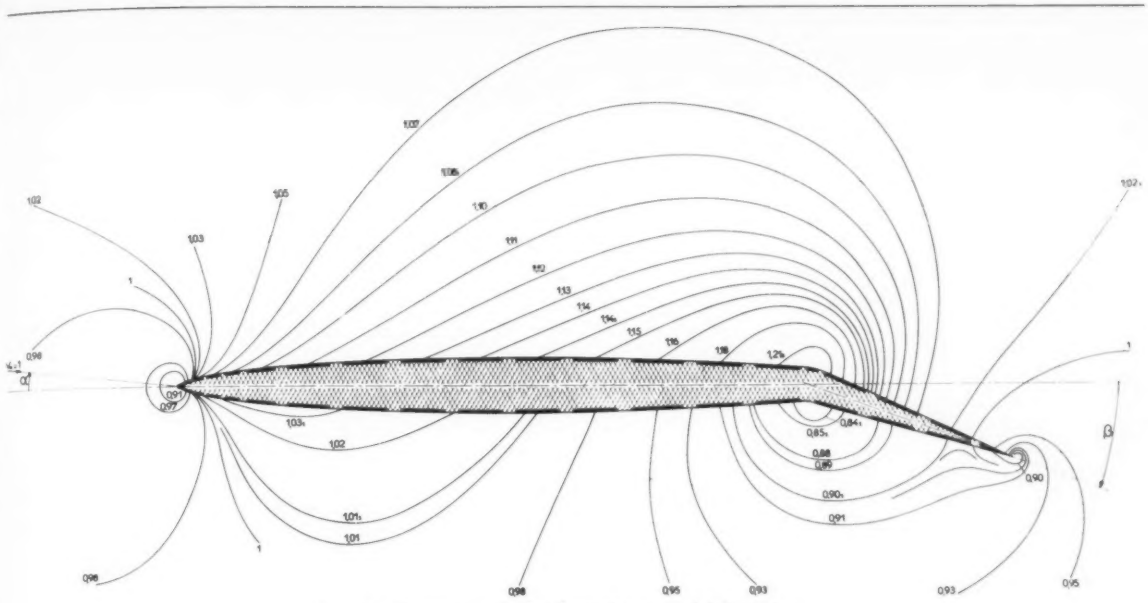

FIG. 1. Constant velocity lines about an airfoil section.

stagnation point and another discontinuity at the trailing edge, this latter value depending on the trailing-edge angle. The imposing of these Dirichlet conditions is carried out as was described above by covering the contour of the airfoil with small electrodes $e$ (about 40, for example) each one of which is raised to the known electrical potential value $\theta(s)$.

Once the potentials of the electrodes $e$ have been adjusted to the correct values, the classical plotting of the equipotential lines of the analog model (either tank or conducting paper) can be carried out. Thus are obtained the lines of constant argument $\theta$ of the velocity field. The current passing through each electrode $e$ can also be measured and the normal derivative $d\theta/dn$ calculated by Eq. (1). The function $\log V$ being conjugate to $\theta$ ($d/ds \log V = d\theta/dn$), the integration of $d\theta/dn$ in the $s$-direction allows the velocity distribution along the airfoil contour to be determined.

The field of the function $\log V$ can also be represented in the electric tank, either by making use of the results of the preceding experiment which gives $\log V$ on a contour of the object (one is then led to satisfy a condition of the Dirichlet type) or in observing directly that

$$-(d/dn) \log V = (d\theta/ds) = C(s)$$

where $C(s)$ is the curvature of the airfoil section at the point $s$. One is thus led to impose directly the values of the curvature $C(s)$ in the form of electrical currents feeding the small contour electrodes. At the stagnation point it is necessary to provide a *point* electrode in order to account for the logarithmic singularity at this point; the same thing occurs at the trailing edge. Plotting the electrical equipotential lines gives, in this case, the lines of constant velocity—i.e., the isobars of the flow.

The analog procedure described above can also be used in the case where several obstacles in the flow field are in proximity to each other—for example, an airfoil with slotted flap, or cascades of airfoils as were studied by G. Renard, who employed the periodic character of the velocity field to make a rheoelectric setup limited to a single band of the field with a width equal to the pitch of the cascade.

The study of a slight modification of the curvature of an airfoil can also be carried out with this experimental setup. In this case it is advantageous to impose in the tank the curvature difference $\delta C = C_1 - C$ between the modified and unmodified section profiles; one then directly obtains the change in the velocity field with respect to the initial field.

G. Renard,[3] of the CNRS laboratory, made use of this method to determine the isobars around airfoil sections of various forms. Fig. 1 gives an example of an airfoil with flap deflected; it will be noticed that a variation of the flap angle $\beta$ affects the curvature of the object only in the region of the hinge. The corresponding electrical manipulations therefore concern only this region.

(2) This method is useful for determining jet lines. Consider, for example, the flow about two symmetrically located wedges having wakes of the Riabouchinsky type (see Fig. 2). Along the jet line BB′ the velocity is constant and the stagnation points are at A and A′ on the axis of symmetry Ox. Along the plate AB(A′B′) the normal derivative $(d/dn) \log V$ is zero. The symmetry is taken into account by limiting the analog representation to one quarter of the field; the model (made of Teledeltos paper, for example) is electrically fed through a point electrode at A and another electrode which covers $BB_1$, the remainder of the contour being

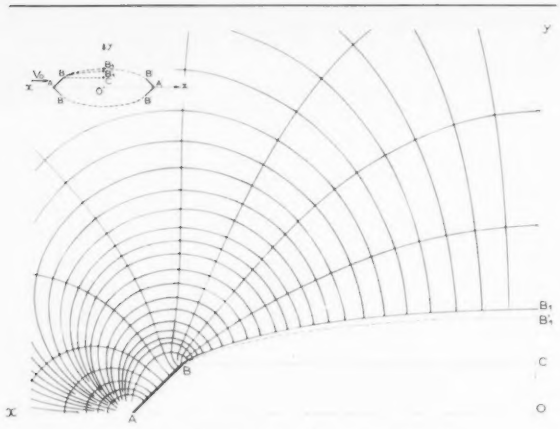


FIG. 2. Velocity field—flow with line jet.

insulating. The field of constant velocity lines is obtained in this way.

If, on the other hand, an electrode is placed along xA and another on AB, the lines of constant argument are determined; in this case the portion $BB_1$ is insulating. This experiment permits the definition by successive iterations of the form of the jet line $\overset{\frown}{BB_1}$, this latter being supposed unknown at first. It suffices, in fact, to start with the straight line form $\overline{BC}$ as a first approximation; reading off the electrical potential along BC then gives a first approximation for $\theta(s)$ which, by integration, furnishes an approximate jet line $\overset{\frown}{BB'_1}$. Next, the paper is cut along this new jet line and the experiment is repeated. This procedure is very rapid, for the second approximation gives almost the exact jet line. This successive approximation technique can be applied in numerous flow problems wherein jet lines are involved and their forms are unknown a priori.

(3) A final application of this method deals with the determination of the lines of constant modulus in conformal mapping. The analog setups used to define the point correspondence between a simply connected region and the surface of a rectangle have been described elsewhere.[2] In the complex plane $z = x + iy$ an analytic function $f(z) = \varphi + i\psi$ is defined, the real and imaginary parts $\varphi$ and $\psi$ of which take on constant values along complementary arcs.

The preceding method can be used to obtain the moduli of the transformation by representing analogically the modulus of $\log df/dz$, the normal derivative of which is known along the contour when the curvature distribution is given (Neumann type condition). Plotting the equipotential lines of the electrical model thus gives directly the lines of constant modulus of the conformal transformation.

Fig. 3 shows, at the left, the orthogonal network of lines of constant $\varphi$ and $\psi$ which defines the conformal correspondence between an ellipse cut by a chord and a rectangle. On the right of Fig. 3 are shown the lines of constant modulus. This Figure is a photograph of the two models made of Teledeltos conducting paper.

(4) In the electric tank, as in the wind tunnel, the presence of walls is occasionally troublesome. When it

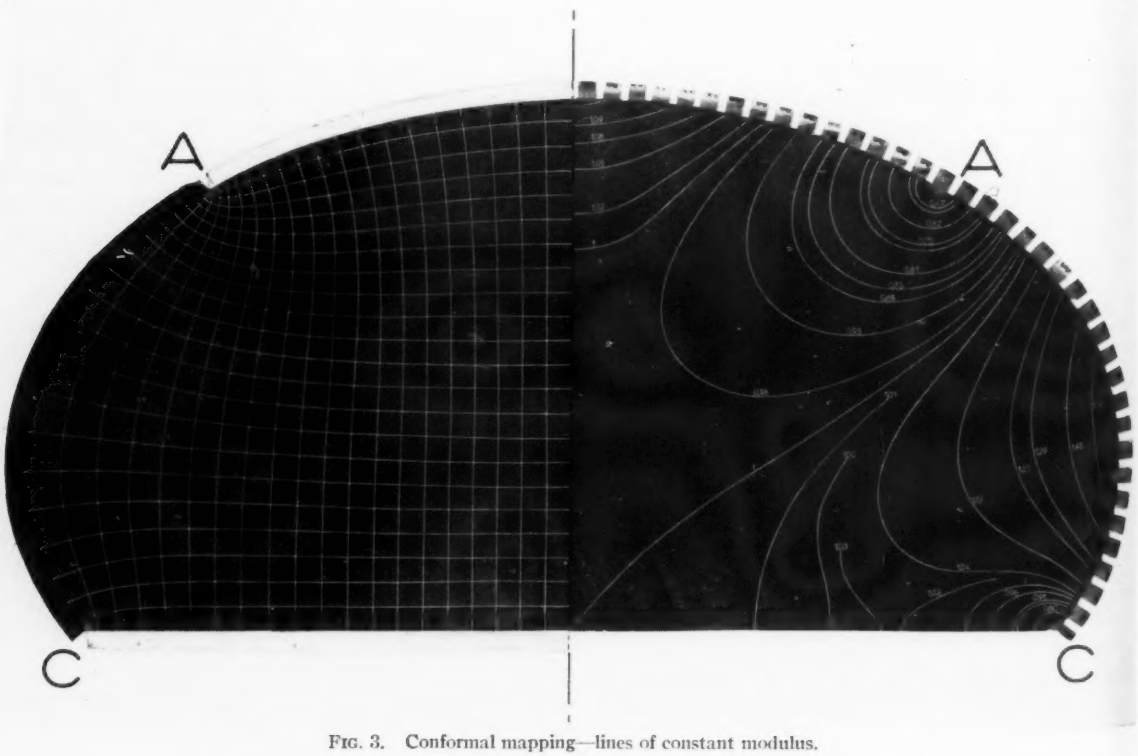


FIG. 3. Conformal mapping—lines of constant modulus.

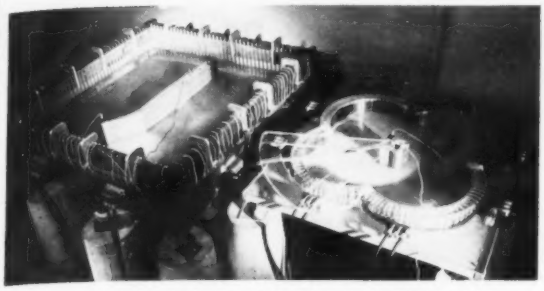

FIG. 4. Electric tanks for fields of unlimited dimensions.

is necessary to represent an infinite field (as in the case of the examples described under 1 and 2 above) a system of two associated tanks is used; one tank represents the useful part of the field, and the other represents that part of the field which lies outside the first, this latter being brought, by inversion, into the finite region of the auxiliary tank. The photograph in Fig. 4 shows such an experimental arrangement; the useful part of the field is represented directly in the square tank, the region external to this square corresponding to the interior of the auxiliary tank at the right which has somewhat the shape of a four-leaf clover: a square, increased on each side by the area of the semicircle described on the side. Homologous points located along the edges of the tank are electrically interconnected. The arrangement described above thus constitutes a tank of infinite extent.

### WING WITH TRAILING EDGE BLOWING

(1) Among the theoretical studies[4, 5, 6] made in recent years to take account of blowing at the trailing edge of an airfoil, simple linear representation has been proposed, independently it appears, by different authors[7, 8, 9]. In spite of the simplifications adopted, this representation appears to reflect the actual phenomenon[11] in a satisfactory way; it also allows of a simple analog interpretation by the rheoelectric method. Fortunately, this interpretation makes it possible to extend the study to lifting surfaces.

The jet furnished by the blowing is supposed to extend indefinitely downstream, and its effect on the external flow is considered to be that of a line of velocity discontinuity or of vortex distribution, as in the case of a thin airfoil. In the linearized theory this jet line is taken as identical with its projection on the $x$-axis. As Fig. 5 shows, the airfoil lies along the segment $[-(c/2), +(c/2)]$ of this axis, and the jet lies along the segment from $+(c/2)$ to infinity. The velocity $V_0$ of the stream is parallel to the $x$-axis.

If the jet velocity is great with respect to $V_0$, it may be assumed that its value remains practically constant along the jet line and equal to the jet velocity $V_j$. The pressure difference $\delta p$ between the two boundaries of the jet considered as a stream tube having a mass flow $Q$ and a local radius of curvature $\mathcal{R}$ is then equal to

$$\delta p = Q\, V_j/\mathcal{R} = (1/2)\rho V^2{}_0 C_j c/\mathcal{R} \qquad (3)$$

where $\rho$ is the density of the external fluid and $C_j$ is the momentum coefficient

$$C_j = 2QV_j/\rho V_0{}^2 c$$

This pressure difference $\delta p$ is also manifested in the external fluid at two points located opposite each other on either side of the jet. Under the given assumptions, this pressure difference is proportional to the difference between velocities measured at the corresponding points. Therefore, if $u$ and $v$ are the components of the perturbation velocity, it is found that $\delta p = 2\rho V_0 u$ along the segment $(+c/2, +\infty)$. (Since $u$ and $v$ are, respectively, odd and even functions of $y$, the study of the velocity perturbation field may be limited to a half plane, the upper half of the $xy$-plane, for example.)

If it be observed finally that $V_0/\mathcal{R} \approx \partial v/\partial x$—i.e., that the external fluid is tangent to the jet and that the curvature $1/\mathcal{R}$ is small—Eq. (3) leads to the condition

$$u = (cC_j/4)(\partial v/\partial x) \qquad \text{or} \qquad u = (cC_j/4)(\partial u/\partial y) \quad (4)$$

which holds at every point of the segment $(+c/2, +\infty)$ for $y > 0$.

If it is desired to obtain the perturbation velocity potential which will here be designated by $\varphi(x, y)$, integration of Eq. (4) will define the condition to be satisfied by this potential along $(+c/2, +\infty)$. The result is

$$\varphi = (cC_j/4)(\partial\varphi/\partial y) + \bar{\varphi} \qquad (5)$$

where the unknown constant of integration $\bar{\varphi}$ can be determined when the jet outflow angle $\Theta$ has been fixed. The necessary relation is

$$\bar{\varphi} - \varphi_{\text{T.E.}} = (cC_j/4)\, V_0\Theta \qquad (6)$$

where $\varphi_{\text{T.E.}}$ is the value of $\varphi$, at the trailing edge $(x = c/2)$.

In the analytical studies it is the induced velocities which are generally sought, and what is usually done is

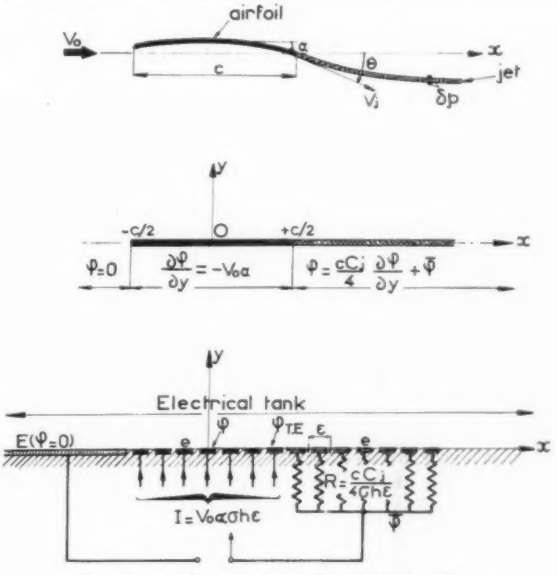


FIG. 5. Analog representation of the jet flap.

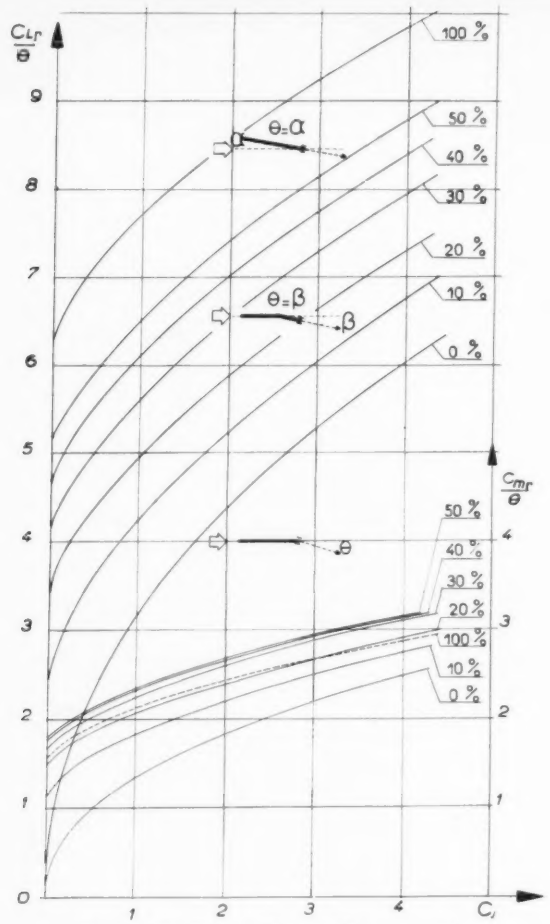


FIG. 6. Coefficients $C_{L_\Gamma}$ and $C_{m_\Gamma}$ versus $C_j$.

to consider the intensity of the vortex distribution along $(+c/2, +\infty)$ so that conditions (4) and (5) become integral relations concerning the vortex intensity. The mathematical formulation of this integral relation is unnecessary in obtaining a solution by rheoelectrical analogy. The functions $u(x, y)$ and $\varphi(x, y)$ are in fact harmonic, and therefore one or the other can be identified with the electrical potential of a plane tank which represents the $(x, y)$-plane, one of the tank sides coinciding with the $x$-axis (see Fig. 5).

(2) The present discussion will be limited to analog representations for $\varphi(x, y)$. When the form of the airfoil section is given, its slope $-\alpha(x)$ along the segment $[-(c/2), +(c/2)]$ defines the normal derivative $\partial\varphi/\partial y = -V_0\alpha$; the corresponding boundary condition is of the Neumann type. It may also be remarked that the condition (6) on the jet is of the Fourier type. In the analogy, then, it is only necessary to distribute small electrodes $e$ along the $x$-axis side of the tank, with an interspacing of $\epsilon$, from $-c/2$ to infinity. The currents flowing out of these electrodes are set at the values $I(x) = V_0\alpha\sigma h\epsilon$ on the interval $[-(c/2), +(c/2)]$ ($h$ being the liquid depth: $\delta S = h\epsilon$). Equal resistances of $R = cC_j/4\sigma h\epsilon$ are employed on the interval $(+c/2, +\infty)$, as shown in Fig. 5. Finally, the interval $(-\infty, -c/2)$ is covered with a single, long electrode $E$ the potential of which is fixed at zero since $\varphi$, being an odd function of $y$, is zero along this part of the $x$-axis.

The measurement of the electrical potential $\varphi_{T.E.}$ at the point $x = c/2$ (trailing edge) gives the circulation about the airfoil, $\Gamma = 2\varphi_{T.E.}$, and the corresponding lift coefficient is $C_{L_\Gamma} = 4\varphi_{T.E.}/V_0c$, that is, if Eq. (6) be used:

$$C_{L_\Gamma} = [\varphi_{T.E.}/(\bar{\varphi} - \varphi_{T.E.})]C_j\theta$$

The overall lift coefficient is obtained by adding to $C_{L_\Gamma}$ the reaction component $C_j\theta$, or, what is evidently the same thing, by taking the circulation $2\bar{\varphi}$ about the lumped system of profile and jet together.

$$C_L = C_{L_\Gamma} + C_j\theta = [\bar{\varphi}/(\bar{\varphi} - \varphi_{T.E.})]C_j\theta$$

The center of lift is obtained by measuring the potential distribution $\varphi(x)$ along the airfoil, and, by differentiation, the pressure distribution is obtained. Finally, the form of the jet is easily calculated from the potential distribution measured along the segment $(+c/2, +\infty)$.

The rheoelectric method was applied by J. Revuz[10] to the following practical cases concerning a straight line airfoil:

(a) Plate at an angle of attack $\alpha$, with *regular* blowing in the direction of the extension of the airfoil rearward: $\theta = \alpha$.

(b) Plate at zero angle of attack, with flap set at an angle $\beta$; *regular* blowing. If $x_1$ is the abscissa of the flap hinge point, $\partial\varphi/\partial y = 0$ for $-c/2 < x < x_1$ and $\partial\varphi/\partial y = -V_0\beta$ for $x_1 < x < c/2$; and at the trailing edge, $\theta = \beta$.

(c) Plate at zero angle of attack, with *singular* blowing: the jet is ejected in a direction making an angle $-\theta$ with the $x$-axis. On the segment $(-c/2, +c/2)$, $\partial\varphi/\partial y = 0$, and on the analog model the corresponding part is insulating; $\theta = \theta$ at the trailing edge.

The results are presented in Fig. 6, where, for these three cases, the hypercirculatory lift coefficient $C_{L_\Gamma}$ is plotted vs. $C_j$. For an arbitrary configuration $(\alpha, \beta, \theta)$ it is then possible to make a linear combination of these effects to obtain finally the lift coefficient $C_L$, adding in also the reaction effect $C_j(\alpha + \beta + \theta)$. The hypercirculatory moment coefficients $C_{m_\Gamma}$ are also shown. (The moments are taken about the leading edge.)

The agreement between these theoretical results and the experimental results obtained at ONERA by Poisson-Quinton and Jousserandot is good. The comparisons made were in the lift coefficient $C_{L_\Gamma}$, in the variation of the center of lift, in the pressure distribution over the airfoil, and in the downstream form of the jet. When the jet is ejected tangentially from a slot located at the hinge line of the deflected flap, it can be assumed, for the theory, that the jet slips along the surface and finally leaves the trailing edge of the flap at the angle that the upper surface of the flap makes with the velocity $V_0$. Wind-tunnel results appear to confirm this hypothesis.

(3) The rheoelectric method which has just been described can evidently be used to treat other jet problems, such as interaction problems when, for example, an airfoil with blowing is near the ground, or where a cascade of airfoils has a rearward jet, or where a flow is deviated by a jet, etc. Studies are currently being conducted on these questions.

The most interesting extension of the method concerns lifting surfaces having a jet ejected along all or part of the trailing edge. The scheme of the linearized theory developed for the case of the two-dimensional airfoil can be retained by supposing that, in the three-dimensional case, each stream tube of the surface of discontinuity constituting the jet remains in a plane parallel to the $xy$-plane (Fig. 7). In particular, then, it is necessary that the velocities $V_j$ of the emergent jet satisfy this condition. It is thus implicitly assumed that the width of the jet surface in the $y$-direction remains the same behind the wing.

The reasoning employed in Section (1) of this part of the paper can then be applied to each stream tube in the jet. The wing is thus extended rearward by a surface of pressure discontinuity, and therefore of velocity discontinuity, which lies in the $xy$-plane and has a width equal to the span if the jet is ejected all along the wing. At every point of this band, the relation

$$u = (cc_j/4)(\partial u/\partial z)$$

holds, but here, $c$ and $c_j$ are functions of $y$, and, in particular, $c_j(y)$ defines a local coefficient the value of which is determined by the momentum ejected at the trailing edge of the wing section having ordinate $y$ and chord $c(y)$. The overall coefficient, based on the surface $S$ of the wing, will be given by

$$C_j = (1/S)\int_{-L}^{+L} c_j c\, dy$$

(where $2L$ is the span).

If attention is focused on the perturbation potential $\varphi(x, y, z)$ the corresponding condition on the surface of discontinuity is:

$$\varphi = (cc_j/4)(\partial\varphi/\partial z) + \bar{\varphi} \qquad (7)$$

for $y$ constant, though the constant $\bar{\varphi}$ is a function of $y$.

On the wing $S$ the condition is once more of the

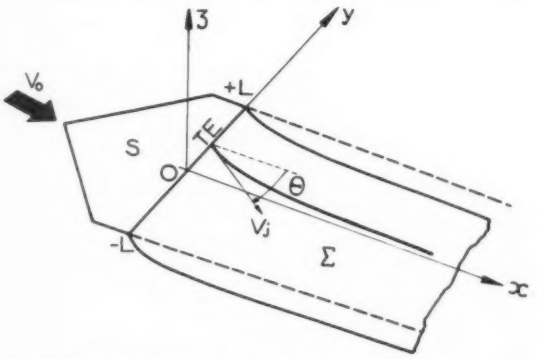


FIG. 7. Trailing edge blowing on a lifting surface.

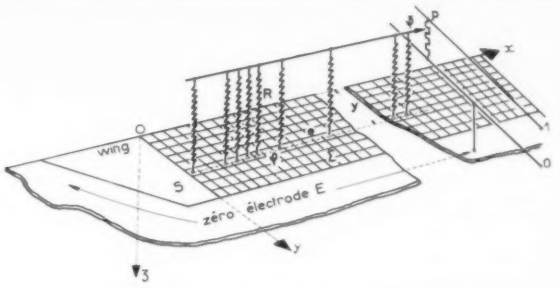


FIG. 8. Rheoelectric model of a lifting surface with blowing.

Neumann type:

$$\partial\varphi/\partial z = -V_0\alpha(x, y)$$

where $-\alpha(x, y)$ is the slope of the lifting surface at the point $(x, y)$.

The analog experiment is carried out in a large deep tank wherein the free liquid surface is taken as the $xy$-plane $z = 0$, the $z$-axis is directed downward into the tank, and $\varphi$, being an odd function of $z$, is zero in the plane $z = 0$ outside the wing $S$ and outside the wake $\Sigma$. Hence, a large electrode $E_0$, maintained at zero electrical potential, covers the region where $\varphi = 0$.

The analog setup is indicated in Fig. 8 for the simplest case, singular blowing [$\alpha(x, y) = 0$]; in this case the model which represents the wing plan form is insulating. The model for the jet wake surface $\Sigma$ is covered with small electrodes. All the electrodes in a line $y$ = constant are electrically fed through resistances proportional to the product $c \cdot c_j$ by means of a potentiometer $p$ which fixes the value $\bar{\varphi}(y)$ in such a way as to regulate the jet angle $\Theta(y)$ at the exit

$$\bar{\varphi}(y) - \varphi_{T.E.}(y) = (cc_j/4)V_0\Theta(y)$$

Once the potentiometers are set, measurement of the electrical potential distribution over the wing model and over the wake furnishes all necessary aerodynamic information (load distribution over the wing).

The general case of an arbitrary lifting surface can be treated without difficulty [$\alpha(x, y)$ being given] by maintaining electric current inflows over $S$ which are proportional locally to $\alpha(x, y)$. If the jet outflow takes place only over a portion of the trailing edge the other parts of the region $\Sigma$ are occupied only by free vortices. These are represented in the analogy in the usual fashion by long, narrow electrodes parallel to the $x$-axis[2] and for which the potentials are adjusted so as to satisfy the Kutta-Joukowsky condition at the trailing edge.

The induced drag can be calculated by measuring the potential distributions $\varphi_\infty(y)$ and the normal derivatives $\partial\varphi_\infty/\partial y$ on the surface $\Sigma$ at infinity downstream—i.e., in the electric tank as far as possible behind the wing model. In several of the cases considered the $\varphi_\infty(y)$ distribution is found to be almost elliptic; in these cases it is easy to write down a simple expression for the induced $C_{Di}$ as a function of aspect ratio.

In concluding this section, the author would like to express his thanks to Maurice Roy, Director of ONERA, for his kind cooperation in authorizing presentation of the above-mentioned results obtained in the ONERA electrical analogy laboratories.

## The Annular Wing

### (1) *Theory*

The theory of the annular wing can be considered within the framework of the linear approximation when the perturbations caused by the presence of this wing in the flow are small. The effects due to its thickness can be represented by source-sink distributions; the incidence and camber effects are obtained, as in thin airfoil and lifting surface theory, by replacing the annular wing and its wake of free vortices by a suitable vortex distribution. Under the linear theory these various effects can be separated out and studied individually.

From a geometrical viewpoint, the annular wing is a body of revolution of which a meridian section has the form of an airfoil section (see Fig. 9). This airfoil section can be characterized by (1) the angle $\alpha$ between the chord line and the axis of symmetry (conicity), (2) a mean camber line which defines the curvature of the airfoil, and (3) a thickness distribution.

When the axis of symmetry of the annular wing is parallel to the general stream velocity $V_0$, the flow is axially symmetric and the analysis of the effects due to conicity, to curvature, and to thickness, is simplified. The wing lift is zero, but it is interesting to know what force is exerted on the airfoil section lying in a meridian plane and what the pressure distributions over the contour are.

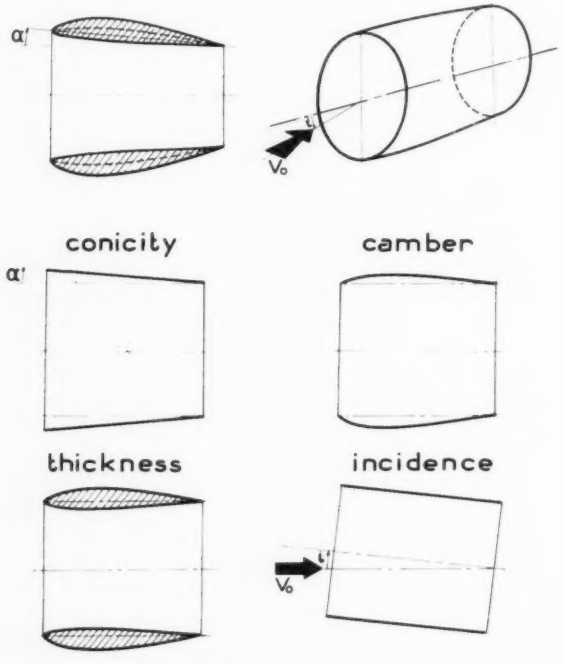


Fig. 9. Annular wing—various effects.

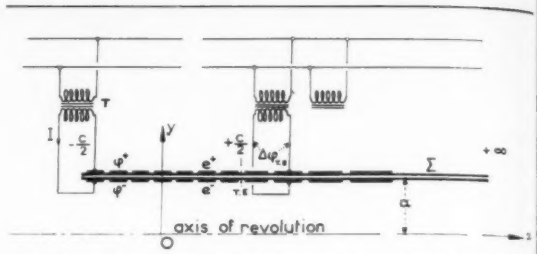


Fig. 10. Rheoelectric model for the study of conicity effect.

If the axis of symmetry of the annular wing is inclined at an angle $i$ to the wind at infinity, the flow is of the general three-dimensional type, and the aerodynamic characteristics vary from one meridian section to another. In order to determine the lift due to incidence the wing is schematically represented by a cylindrical surface of revolution which may be considered as a lifting surface followed by a wake of free vortices. These different effects have been studied by the rheoelectric method in the CNRS laboratory by G. Hacques.

### (2) *Axially Symmetric Flows About the Annular Wing*

The simplest analog representation concerns the conicity effect. The straight line airfoil of chord $c$ is placed at an angle of attack $\alpha$ and is identified with its projection upon a line parallel to the axis at a distance $a$ from it—i.e., $a$ is the radius of the wing.

The flow study is carried out by making use of the perturbation potential $\varphi(x, y)$ defined in a meridian $xy$-plane wherein the $x$-axis coincides with the axis of symmetry. This potential is not uniform around the airfoil because of the circulation $\Gamma$.

The rheoelectric image of this flow is obtained in an inclined tank by placing a thin insulating strip parallel to the axis of symmetry and separated from it by a distance $a$. This strip (see Fig. 10) is covered with electrodes $(e^+, e^-)$ mounted in opposing pairs. The electrode-carrying strip represents a cut made in the $xy$-plane corresponding to the airfoil $(-c/2, +c/2)$ and to its rearward extension $(+c/2, +\infty)$.

On the airfoil the boundary condition is $\partial\varphi/\partial y = -V_0\alpha$. The potential difference $\Delta\varphi = \varphi^+ - \varphi^-$ between two opposite points of the cut defines the local circulation; the value of the circulation about the airfoil is obtained by measuring this difference at the trailing edge: $\Gamma = \Delta\varphi_{T.E.}$.

In order to realize these conditions electrically a current $I = V_0\alpha\sigma h\epsilon$ must be sent into the electrodes $e$ in such a way that it enters the electrode $e^-$ and flows out of $e^+$. To accomplish this, independent electrical feed is effected by means of a transformer $T$. Behind the airfoil, on the segment $(+c/2, +\infty)$ the potential difference between two opposed electrodes $(e^+, e^-)$ remains constant and equal to $\Delta\varphi_{T.E.}$. This potential difference can also be set up for each pair of electrodes by means of transformers. The circulation $\Gamma$ being supposed unknown to begin with, it is determined by

the Kutta-Joukowsky condition at the trailing edge, which requires that

$$(\partial/\partial x)(\Delta\varphi)_{\text{T.E.}} = 0$$

This condition assures that the correct values of the potential differences $\Delta\varphi$ are established along the wake $(+c/2, +\infty)$. The measurement of this value gives the circulation $\Gamma$ and therefore the force acting on the airfoil. The velocity distributions $u^+$, $u^-$ are obtained, by differentiation, from the measurement of $\varphi^+$ and $\varphi^-$ along the segment $(-c/2, +c/2)$.

Fig. 11 gives some results for perturbation velocity distributions along the airfoil for various values of the ratio $\lambda = 2a/c$ ($\lambda_\infty$ corresponds to two-dimensional flow). The absolute values of the velocity $u$ are higher on the inner surface than on the outer, and the dissymmetry becomes more and more pronounced as $\lambda$ decreases. The force on the airfoil increases very rapidly as $\lambda$ decreases. The presence of a central cylindrical body of indefinite length placed along the axis of the annular wing increases considerably the value of this force by increasing the inner surface pressures, but this causes only an insignificant change in the negative pressures on the outer surfaces.

The effects of curvature can be calculated in the same way by adjusting the currents $I(x)$ to be proportional to the slopes $\alpha(x)$ of the airfoil. In this way, the effect of an annular flap deflected through a given angle, and having a flap chord length of various percentages of airfoil chord has been determined. The circulation $\Gamma$ due to the effect of curvature may also be determined directly from the effect of conicity (for fixed $\lambda$) by the rule of inverse flows.

In this way the following problem can be solved: Determine the camber to be given to an airfoil in order to obtain a given pressure distribution. For the study of this case it is advantageous to represent the pressure potential $u(x, y)$ in the electric tank. This potential is in fact uniform about the airfoil and does not require the prolongation of the cut to infinity downstream.

The problem is generally treated for the ideal angle of attack—i.e., that angle for which the velocity remains finite for the leading edge as well for the trailing edge. It is then easy to set up the potential difference corresponding to the given difference $\Delta u = u^+ - u^-$ on either side of the cut occupying the segment $(-c/2, +c/2)$. The measurement of the electrical current $I$ passing between $e^+$ and $e^-$ gives $\partial u/\partial y$. The value of the slope $\alpha(x)$ at a point $x$ of the airfoil is finally obtained by calculating the integral

$$\alpha(x) = \int_{-\infty}^{x} (\partial u/\partial y)dx$$

(Ahead of the airfoil, the gradient $\partial u/\partial y$ is measured in the electric tank by means of a double probe.)

In the experiments which were carried out, the different cambers needed in an airfoil section of an annular wing in order to obtain some classical velocity distributions $u$ were determined. The example shown in Fig. 12 corresponds, for $\lambda = 1$, to the linear distribution (NACA, $a = 0$). The result obtained by analogy gave a mean camber line which in appearance resembled closely the two-dimensional case, though the curvature is less pronounced. It will be noticed that the velocity distributions $u^+(x)$ and $u^-(x)$ differ from each other and are not linear, even though the imposed velocity difference possesses this linear property.

The rheoelectric representation of thickness effects is carried out in a similar manner, the perturbation velocity potential $\varphi(x, y)$ being employed. However, in this case, the derivative $\partial\varphi/\partial y$ taken at a point of the segment $(-c/2, +c/2)$ changes sign from one side to the other of the cut (the slope having opposite signs on inner and outer surfaces of the airfoil).

The analogy was used in this case to determine the deformation to be given to an airfoil in order to maintain the same velocity distribution on the contour for various values of $\lambda$. Fig. 13 gives an example of this: in order to keep the same velocity distribution as that obtained in two-dimensional flow about a lenticular airfoil, it is necessary to bulge out the outer surface and to flatten the inner more and more as the parameter $\lambda$ decreases.

### (3) *The Annular Wing at Incidence*

The annular wing, considered as a lifting surface having the form of a cylinder of revolution, is extended rear-

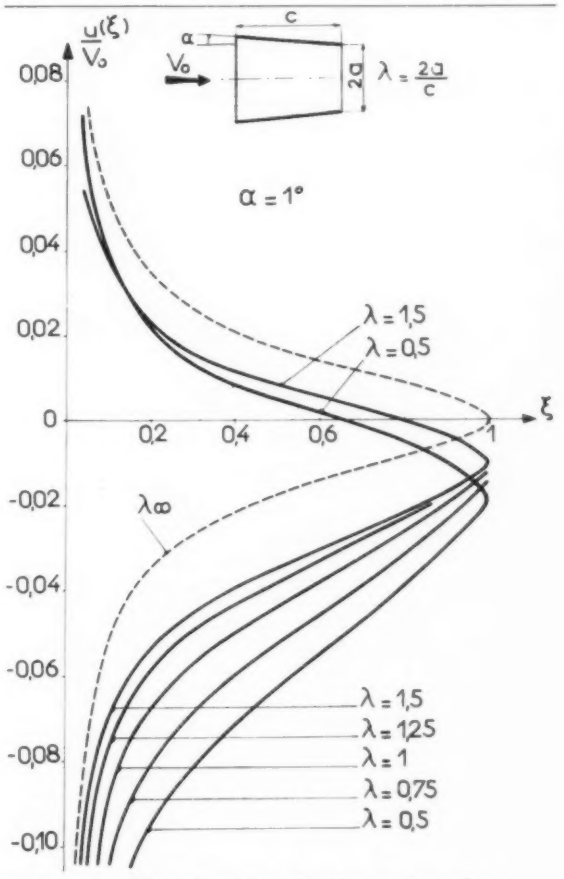


FIG. 11. Effect of conicity—distribution of velocity $u$.

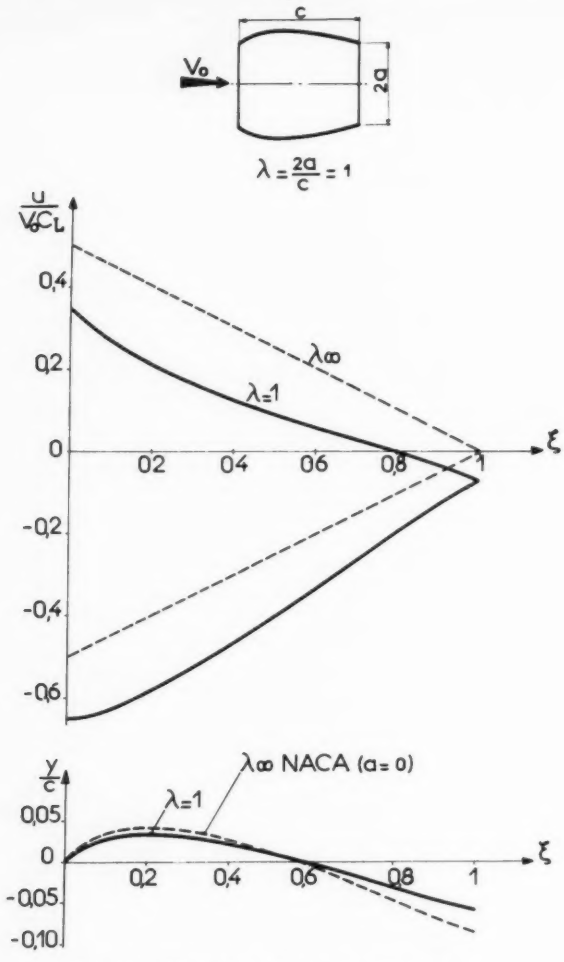


FIG. 12. Effect of camber for an annular wing.

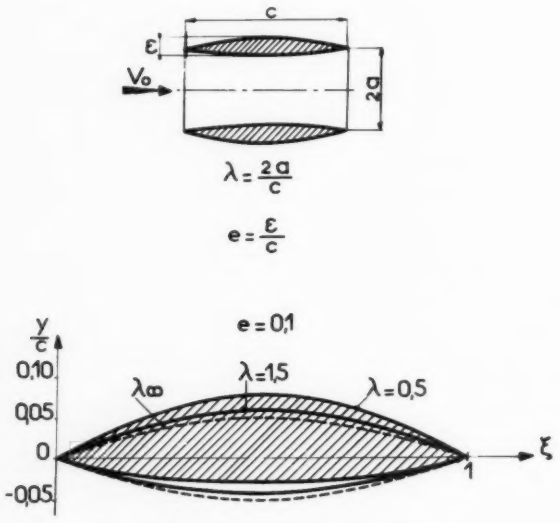


FIG. 13. Effect of thickness for an annular wing.

ward by means of a cylindrical surface of discontinuity having the same diameter and constituting the wake of free vortices (see Fig. 14).

Pressure equilibrium over this surface implies that at every point $u^+ - u^- = 0$. The corresponding condition on the velocity potential $\varphi$ is then:

$$\Delta\varphi = \varphi^+ - \varphi^- = \text{constant}$$

on each generating line of $\Sigma$. The value of this constant varies from one generator to another; it also defines the circulation $\Gamma(\theta)$ about the section of the annular wing defined by a meridian plane of polar angle $\theta$. The distribution of circulation $\Gamma(\theta)$ is at first unknown; it is determined by satisfying the Kutta-Joukowsky condition at the trailing edge, that is: $(\partial\Gamma/\partial x)_{T.E.} = 0$.

On the wing the boundary condition for $\varphi$ is obtained by writing that the fluid is tangent to the surface—i.e., that

$$d\varphi/dn = -V_0 i \cos(\widehat{n, z})$$

In order to simplify the analog model as much as possible it is interesting to consider an auxiliary potential $\Phi(x, y, z)$ which is defined by:

$$\Phi(x, y, z) = \varphi(x, y, z) - V_0 iz$$

that is, by subtracting from the potential $\varphi(x, y, z)$ which is sought a uniform flow of velocity $-V_0 i$ parallel to the $z$-axis, which is equivalent to studying the annular wing in the transversal flow field $V_0 i$. On the wing and in the wake the differences $\Delta\Phi$ and $\Delta\varphi$ are equal and the circulation remains the same.

To sum up, the boundary conditions for $\Phi$ are as follows: (a) on the wing, $d\Phi/dn = (d\varphi/dn) - V_0 i \cos(\widehat{n, z}) = 0$; (b) in the wake, the difference $\Delta\Phi = \Phi^+ - \Phi^- = \Delta\varphi$ is constant along a given generator, and its value $\Gamma(\theta)$ is determined by the condition (c); (c) at the trailing edge, $(\partial/\partial x)(\Delta\Phi)_{T.E.} = 0$; (d) for $z = \infty$, $\Phi$ reduces to the uniform field $-V_0 iz$; and finally, (e) in the plane $z = 0$, $\Phi = \varphi = 0$.

The rheoelectric image of the field of the function $\Phi(x, y, z)$ is obtained in a deep tank (see Fig. 14). The condition (a) is satisfied by representing the annular wing by means of a portion of an insulating cylinder (a thin, curved sheet of Plexiglas). The wake $\Sigma$ is constructed in the same way but carries on its two sides pairs of opposed electrodes between the electrodes of which are set up the potential differences $\Delta\Phi(\theta)$ by means of transformers T. All the primaries of these transformers T which feed electrodes distributed along the same generator, are connected to a potentiometer P which is adjusted to the right value of potential for satisfying condition (c). Finally, to satisfy conditions (d) and (e), two large parallel electrodes $E_1$ and $E_0$ cover, one the bottom of the tank, the other, the free water surface which coincides with the $xy$-plane. If the distance $H$ which separates these electrodes is large with respect to the diameter $2a$ of the wing, the potential difference between $E_0$ and $E_1$ corresponds to $-V_0 iH$ and the corresponding electric field represents the transversal flow $-V_0 iz$.

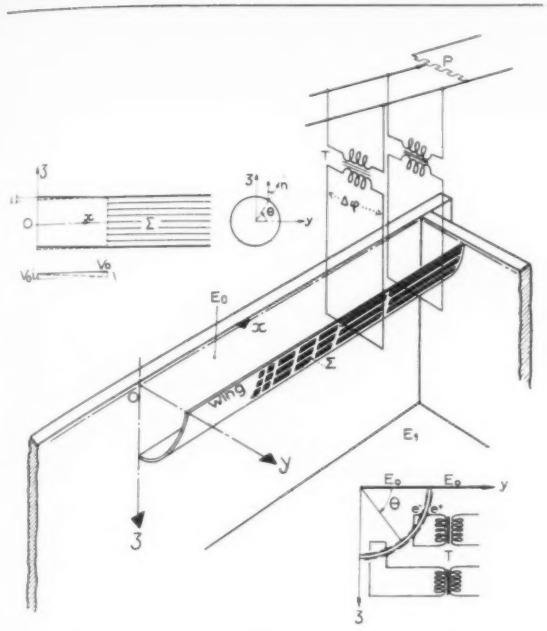


FIG. 14. Rheoelectric model of the annular wing with incidence.

Once these electrical adjustments have been carried out, the differences $\Delta\Phi(\theta)$ which give the circulation distribution $\Gamma(\theta)$ are measured. The potential $\Phi$ can also be measured on the inner and outer surfaces of the Plexiglas insulating model and the pressure distribution over the whole of the annular wing can thus be determined.

The analog experiments carried out by Hacques on a preliminary model of this type are presently being completed, and the results for various values of $\lambda$ are being prepared for publication. The method described permits a rather complete analysis of the properties of the annular wing in the subsonic domain. It is probable also that use of the pressure potential will make it possible to take into account the effect of a propeller placed inside the wing.

Finally, an analog setup somewhat comparable to that described in the preceding section concerning the plane lifting surface, will make possible the representation of the effect of blowing at the trailing edge of the annular wing.

## CONCLUSION

The three problems examined above—direct plotting of velocity fields, trailing edge blowing, and the annular wing—give an idea of possible applications of the rheoelectric analogy method. These applications are not limited solely to aerodynamics, and the same procedures and instruments can be used to solve other problems of mathematical physics of interest to aeronautics.

Rheoelectric calculation, which may in addition be advantageously associated with other analog procedures, such as *resistive networks*, requires only simple, economical means. Its flexibility in application allows easy passage, using the same experimental materials, from one type of problem to another; thus, the user will not hesitate to employ it for a rapid test intended to clarify certain aspects of a complicated theoretical analysis. The influence of the various parameters of a problem, entering as they do in the form of physical quantities in the analogy, is more easily traced out than through a purely numerical calculation. In fact, analog experimentation often brings out certain theoretical difficulties which had passed unnoticed in the early stages of the study of the problem.

To sum up, this method is a means of study as well as a means of calculation. Viewed from this angle it bears, in relation to the large calculating machines, the same relation that a small laboratory wind tunnel bears to the large wind tunnel destined for industrial use.

## REFERENCES

[1] Pérès, J., *Les méthodes d'analogies en mécanique appliquée*, Fifth International Congress of Applied Mechanics, Cambridge, Mass., September, 1938.

[2] Malavard, L., *The Use of Rheoelectrical Analogies in Aerodynamics*, AGARDograph No. 18, North Atlantic Treaty Organization, Advisory Group for Aeronautical Research and Development, Palais de Chaillot, Paris, August, 1956.

[3] Renard, G., *Determination directe des gradients par analogies électriques*, Neuvième Congrès International de Mécanique Appliquée, Bruxelles, September, 1956.

[4] Roy, M., *Principe d'étude de l'aile à jet*, La Recherche Aéronautique (ONERA) No. 52, July–October, 1956.

[5] Legendre, R., *Etude théorique du soufflage près du bord de fuite d'un profil d'aile*, Note intérieure ONERA 12/1308/A, April, 1954.

[6] Legendre, R., *Influence de l'émission d'un jet au bord de fuite d'un profil sur l'écoulement autour de ce profil*, C. R. Acad. Sc. t. 242, p. 2438–2440, May 14, 1956.

[7] Malavard, L., *Contribution à l'étude théorique du soufflage au bord de fuite d'un profil d'aile*, Note intérieure ONERA 4/1727-A, December, 1954.

[8] Helmbold, H. B., *The Lift of a Blowing Wing in a Parallel Stream*, Journal of the Aeronautical Sciences, Vol. 22, No. 5, p. 341, May, 1955.

[9] Spence, D. A., *A Treatment of the Jet Flap by Thin-Aerofoil Theory*, R. A. E. Report No. Aero 2568, November, 1955.

[10] Revuz, J., *Etude analogique du soufflage au bord de fuite d'un profil d'aile*, Proceedings of the International Analogy Computation Meeting, Bruxelles, October, 1955.

[11] Malavard, L., Poisson-Quinton, Ph., and Jousserandot, P., *Recherches théoriques et expérimentales sur le contrôle de circulation par soufflage appliqué aux ailes d'avions*, ONERA, Note Technique No. 37, June, 1956.

# The Plastic Bending of an Eccentrically Loaded Column†

WILLIAM E. BOYCE*

*Brown University*

SUMMARY

This paper treats the behavior of a rigid, work-hardening column compressed by eccentric axial loads. A piecewise linear theory of plasticity is used to analyze the lateral displacements which occur as the loads are slowly increased. In particular, a sudden stiffening effect shortly after the onset of plastic flow is noted and explained.

## (1) INTRODUCTION

THE STUDY of problems dealing with the stability of axially loaded columns has a long and interesting history, starting with the work of Euler[1-3] in the mid-eighteenth century. Euler derived the formula,

$$P = \pi^2 EI/L^2 \tag{1.1}$$

for the buckling load of an initially straight, simply supported, elastic column compressed by central axial end loads.

A similar study of plastic columns was deferred for more than a century. After some exploratory work by Considère[4] and Engesser,[5] von Kármán[6] derived an expression for an "effective" or "reduced" modulus which would replace Young's modulus in Eq. (1.1), thus extending the validity of this formula beyond the elastic range. A convenient summary of this theory has been given by Timoshenko.[7]

The classical approach to stability problems, employed universally by the authors cited above, consists of determining whether a column can pass from the straight to a bent equilibrium configuration when subjected to a prescribed axial load. The smallest axial load for which such a transition is possible is the "buckling load" given by the Euler - von Kármán formula.

Eventually, careful experiments revealed significant discrepancies between observed values of the buckling loads and those predicted on the basis of the classical theory. To explain this phenomenon, Shanley[8, 9] suggested that the point of view underlying the classical theory is not appropriate for stability problems involving plastic effects. His recommendation was essentially this: that it would be more realistic to determine the smallest load at which the column can assume a bent, as well as the straight, equilibrium configuration, rather than to determine the smallest load at which the column can pass from the straight to a bent equilibrium configuration. In the elastic range the two problems have the same solution; however, in the plastic range, their solutions may differ, the critical load for the second problem being generally less than that for the first, and hence more in line with experimental observations.

More recently Ziegler[10] carefully distinguished several classes of stability problems, and discussed the methods which might be applied to them. He noted in particular that the classical theory, with its static stability criterion, has been frequently applied to problems for which it is actually not valid. Drucker and Onat[11] have discussed the inapplicability of the classical theory to inelastic systems.

The present paper considers an initially straight column subjected to eccentric axial end loads, which are thought of as increasing slowly from zero. Since both bending moments and axial forces are present in such a system, it would be more properly called a "beam-column." For brevity, however, the term "column" is used here.

The classical notion of stability is closely linked to the concept of a conservative system and thus is unsuited to the discussion of buckling outside the elastic range. An investigation of buckling in the work-hardening range should include both the elastic and the plastic components of the deformation, thus taking full account of the conservative and the nonconservative aspects of the problem. In the following analysis, however, a sandwich column made of a *rigid, work-hardening* material is considered, because the neglect of all conservative effects is believed to provide a better insight into the nature of nonconservative effects.

In the next section the problem is described more precisely, and some basic concepts are reviewed. Section (3) contains a discussion of the problem in qualitative terms, based on a simplified column in which the ability to bend is concentrated in a single element. A detailed analysis of the more general column is given in Section (4).

Received June 28, 1956.

† The results presented in this paper were obtained while the author was a Universal Match Foundation Fellow in Applied Mathematics at Brown University.

The author would like to express his appreciation to Prof. W. Prager for his advice on many occasions during this investigation and to Prof. D. C. Drucker for several helpful suggestions. The author is also indebted to Mrs. R. C. Alverson of the Brown University Computing Laboratory for the computations, which were carried out as part of the research sponsored by the Office of Naval Research under Contract Nonr-562(10) with Brown University.

* Research Associate, Division of Applied Mathematics.

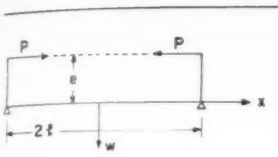


FIG. 1.

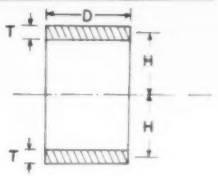


FIG. 2.

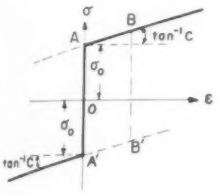


FIG. 3.

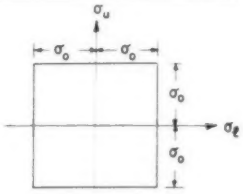


FIG. 4.

## (2) DESCRIPTION OF PROBLEM

Consider an initially straight column of length $2l$ subjected to compressive end loads $P$, which are parallel to the axis of the column but act at a distance $e$ from it (see Fig. 1). Suppose that the column is of a sandwich type, consisting of two identical thin flanges carrying all direct stresses, and a central layer supporting only shear stresses. The cross section of the column is shown in Fig. 2; the width and thickness of the flanges are denoted by $D$ and $T$, respectively, and the height of the cross section from center flange to center flange by $2H$. It will be assumed that the flanges are made of a rigid-plastic material with the stress-strain diagram shown in Fig. 3. The heavy lines in this diagram correspond to loading in tension or compression starting from the virgin state O. The specimen is supposed to remain rigid until the yield stress $\sigma_0$ is reached in tension or compression; thereafter, the absolute value of the stress $\sigma$ increases linearly with the absolute value of the strain $\epsilon$ as long as the loading process is continued. After the state B has been reached in tension, let the specimen be unloaded and then loaded in compression. Since elastic effects are neglected, the strain $\epsilon$ remains constant during the unloading and the subsequent loading in compression until the new yield limit in compression is reached at B′. To include a kind of Bauschinger effect in the analysis, it will be assumed that the vertical segment BB′ has the same length $2\sigma_0$ as the corresponding segment AA′ in the virgin state. This particular assumption regarding the Bauschinger effect was adopted because it affords some simplification of the mathematical work, and yet constitutes a sufficiently accurate description of the actual behavior of structural metals to justify the hope that the following analysis will yield a qualitatively correct picture of the plastic deformations of the sandwich column.

A discussion of the corresponding yield condition and flow rule for a generic element of the column has been given by Prager;[12] his development will be summarized here. The states of stress and strain at a generic cross section of the column are specified by the stresses $\sigma_u$, $\sigma_l$ and the strains $\epsilon_u$, $\epsilon_l$ in the upper and lower flanges. In Fig. 4, $\sigma_u$ and $\sigma_l$ are used as rectangular coordinates of the "stress point" which represents the state of stress in the cross section. Since the column element remains rigid as long as the stresses in both flanges remain below the yield limit, the initial yield condition for the column element is represented by the square yield locus in Fig. 4. When the stress point reaches, for instance, the upper side of this square at some point other than the endpoints, the upper flange is ready to yield in tension while the lower flange remains rigid. As the upper flange work-hardens, the stress point continues to move upwards. The assumption made regarding the Bauschinger effect (see Fig. 3) then implies that the square yield locus in Fig. 4 undergoes a translation by $C\epsilon_u$ in the direction of the positive $\sigma_u$ axis. Accordingly, the following model represents the mechanical behavior of the column element.

Consider the square rigid frame shown in Fig. 5 which is assumed to be mounted so that it can perform any translation in its plane. A perfectly smooth pin Q is free to move within the frame, and imparts motion to it only when in contact with one of the sides or corners of the frame. Initially, the frame and pin are both centered at the origin O. As the frame is displaced by the moving pin the vector from O to the center C of the frame has the components $C\epsilon_l$, $C\epsilon_u$, while the vector from O to the center of the pin Q has the components $\sigma_l$, $\sigma_u$.

From Fig. 6 it is easily seen that the axial force $N$ and bending moment $M$ are given by

$$M = TDH(\sigma_l - \sigma_u) \qquad N = TD(\sigma_l + \sigma_u) \quad (2.1)$$

Similarly, from Fig. 7 it is apparent that the extension $\epsilon$ and curvature $\kappa$ of the centerline are given by

$$\epsilon = (1/2)(\epsilon_l + \epsilon_u) \qquad \kappa = (1/2H)(\epsilon_l - \epsilon_u) \quad (2.2)$$

Eqs. (2.1) and (2.2) establish that the oblique axes in

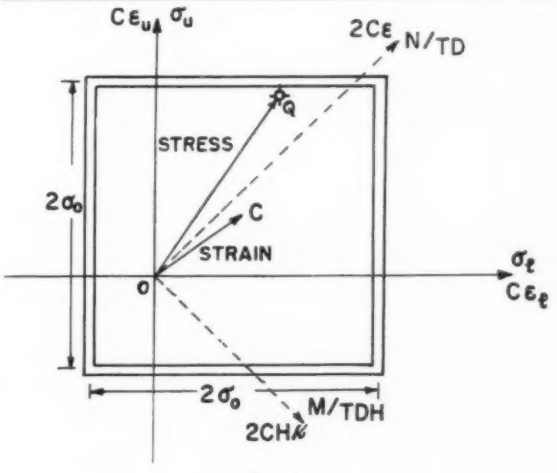


FIG. 5.

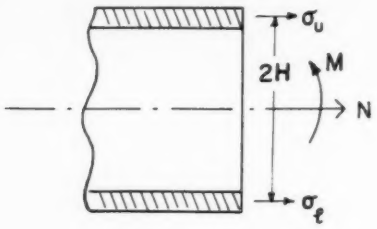


FIG. 6

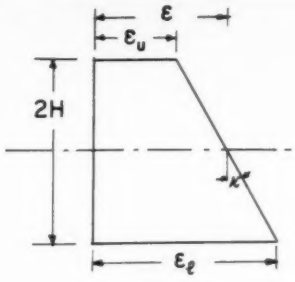


FIG. 7

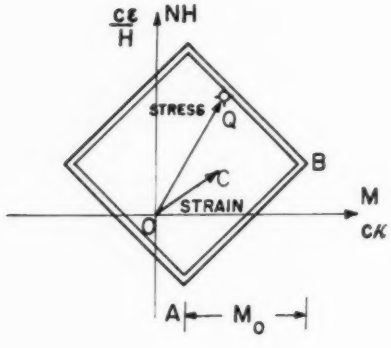


FIG. 8

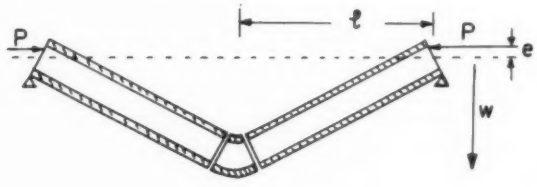


FIG. 9

Fig. 5 may be used to obtain the relation among the generalized stresses and strains, $M$, $N$, $\epsilon$, and $\kappa$. In fact, it is readily verified that the proper pairs of variables are $M$ and $c\kappa$, $NH$ and $c\epsilon/H$, where

$$c = 2CDTH^2 \tag{2.3}$$

It may be more convenient to use the orientation of Fig. 8. The yield moment in pure bending $M_0$ and the yield force in simple tension $N_0$ satisfy

$$M_0 = N_0 H = 2\sigma_0 TDH \tag{2.4}$$

### (3) Qualitative Discussion

Before launching into a detailed analysis, a brief qualitative discussion of the expected behavior of the column may help to indicate the course to be followed. This discussion may be simplified by considering a column in which the flexibility is concentrated in a single element of infinitesimal length located at the center. That is, the column is thought of as consisting of two rigid bars joined by a sort of work-hardening hinge (see Fig. 9). This way of obtaining a qualitative picture of column behavior in the plastic range was first adopted by Shanley,[9] although in conjunction with a different stress-strain law. It is most convenient to phrase the discussion in terms of Fig. 10, where $\sigma_u$ and $\sigma_l$ now represent the stresses in the upper and lower flanges of the bending element, or hinge. As the rest of the column is assumed to remain always rigid, these are the only relevant stresses.

Initially, for $P = 0$, $\sigma_u = \sigma_l = 0$; the stress point is at the origin O. As $P$ increases, the stress point moves

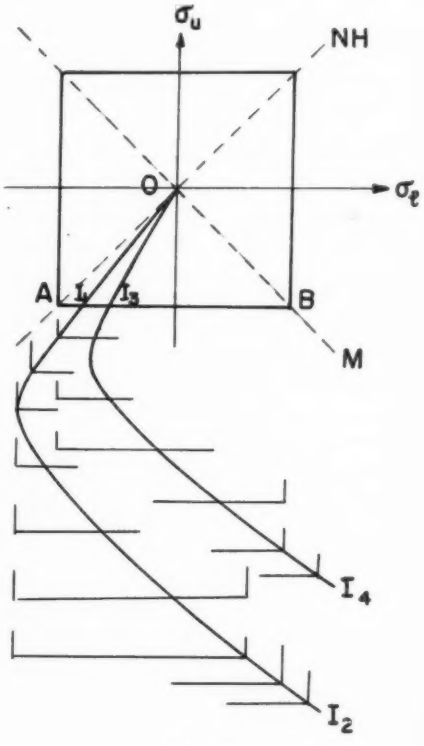


FIG. 10.

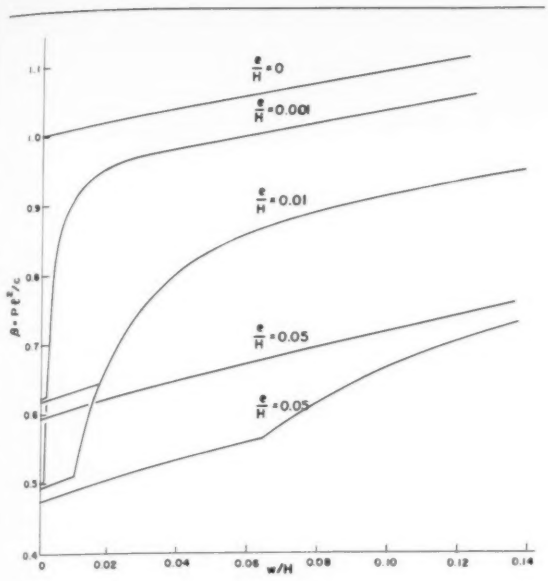


FIG. 11.

out from O along a straight line such as $OI_1$, the slope of which depends on the eccentricity of loading; eventually, for a load $P = P_1$, this line intersects the yield locus at some point on AB. Physically, this means that the upper flange has become plastic in compression, although the lower flange remains rigid. Only now, of course, may the hinge bend. As $P$ exceeds $P_1$, the stress point continues to move out from the origin, causing a movement of the frame along the normal to AB. This vertical displacement of the frame is proportional to the compressive strain in the upper flange.

Once bending has been initiated in the column, further increases in the applied load serve to increase the "effective eccentricity" of the load. The effective eccentricity, denoted by $e^*$, is defined to be the distance from the centerline of the hinge to the line of action of the load $P$. Hence

$$e^* = e + w \tag{3.1}$$

where $w$ is the lateral displacement of the hinge. Clearly, an increase in $e^*$ tends to reduce the compressive stress in the lower flange. On the other hand, as long as $e^* \leq H$, an increase in $P$ acts directly to increase the compressive stress in the lower flange. It is the magnitude of $e^*$ which primarily governs the relative importance of these two factors. When $e^* \ll H$, which is normally the case in the first stages of plastic deformation, the effect of an increase in $e^*$ is small compared to the direct effect of the added load. Hence the stress in the lower flange is increased in magnitude. Later on, for substantially larger values of $e^*$, the reverse is true, and an increase in $P$ decreases the compressive stress in the lower flange. Clearly, at some intermediate point in the loading program, $\sigma_l$ is stationary with respect to $P$; at this time a stress reversal occurs in the lower flange. Since elastic strains are neglected, it is not accompanied by a strain reversal, as would otherwise be the case. Depending on the magnitude of $\sigma_0$, the lower flange may or may not become plastic before the stress reversal takes place. The behavior of the hinge is quite different in the two cases.

First, suppose that the lower flange does become plastic, at a load $P = P_2$, before the stress reversal. This corresponds to the entry of the stress point into the corner A of the yield locus, as the stress point follows a path such as $OI_2I_2$. From this instant the motion of the frame is identical with that of the pin. This abrupt change in the direction of motion of the frame is translated into a discontinuity in the slope of the load-deflection curve, a point which will be elucidated shortly. If the load is further increased, the lower flange will experience a stress reversal, say at $P = P_3$. In the stress plane this is represented by the return of the stress point from the corner A to the side AB of the yield locus. The direction of motion of the frame varies continuously during this transition.

Alternatively, the stress point may follow a path such as $OI_3I_4$ in Fig. 10, never becoming engaged in corner A. In this case stress reversal occurs before $\sigma_l$ reaches the yield limit, and the lower flange does not become plastic in compression. Consequently, there is no discontinuity in the direction of motion of the frame.

In any event, under still further increases in load, the lower flange will first become stress-free (when $e^* = H$), and then start to load again, this time in tension. Eventually $\sigma_l$ will reach the tensile yield limit, corresponding to the entry of the stress point into corner B of the yield locus. By this time a fairly large lateral displacement will have occurred, which presumably would render the column useless as a structural member.

An analysis of the load-displacement relation for this simple column has been carried out, based on the foregoing remarks. Although much simpler, it closely parallels the treatment of the more general column contained in the next section; for this reason the details are omitted. However, the results are shown in Fig. 11 in the form of a plot of the load parameter, $Pl^2/c$, versus the normalized deflection of the hinge, $w/H$. Three non-zero values of the ratio $e/H$ were used together with two values of the yield stress $\sigma_0$. The limiting case of zero eccentricity is also plotted. The principal feature of the set of curves is the discontinuity in slope at $P = P_2$, which occurs in a majority of them. This represents a sudden stiffening of the column, and coincides with the discontinuous change in the direction of the flow vector (displacement of the frame) as the lower flange becomes plastic in compression. Physically, the explanation is as follows.

Bending, and thus a lateral displacement, must occur in the hinge, in order to preserve the continuity of the material, whenever there is a difference in the rate of shortening per unit load in the two flanges. For $P > P_1$, the rate of shortening in the upper flange will always exceed that in the lower flange, due to the effective eccentricity of loading. Moreover, except at

$P = P_2$, both rates vary continuously with the applied load; hence their difference, which is the rate of excess shortening in the upper flange, varies continuously. Consequently, the rate of bending, or of lateral displacement, varies continuously, and the load-displacement curve has a continuously turning tangent. However, at $P = P_2$, when the lower flange first becomes plastic, the rate of shortening in the lower flange has a jump discontinuity. Hence, the rate of excess shortening in the upper flange and the rate of bending decrease discontinuously. The sharp decrease in the rate of bending is equivalent to a sudden stiffening of the column, and manifests itself in the discontinuity in the slope of the load-deflection curve at $P = P_2$. The smaller the effective eccentricity at this instant, the more marked will be this effect.

### (4) The General Column

A rigid, work-hardening column, free to bend at any cross section, behaves much like the very special column discussed in the previous section, at least in principle. Mathematical difficulties arise, however, from the fact that the stress point for each cross section may follow a different path. Consequently, at a given time all parts of the column may not be in the same plastic regime, so that different sets of equations must be applied to different portions of the column.

Equilibrium considerations, always valid, imply that

$$M = P(e + w) \qquad N = -P \tag{4.1}$$

where $w(x)$ is the transverse displacement of a generic point of the column's centerline. The curvature $\kappa$ of the center line is given in terms of $w(x)$ by

$$\kappa = -d^2w/dx^2 \tag{4.2}$$

Plastic flow at a cross section begins at a load $P = P_1$, when the stress point for that cross section contacts the yield locus along the side AB, where

$$M - NH = M_0 \tag{4.3}$$

Since the stress state is uniform along the column as long as $w \equiv 0$, every column element becomes plastic at the same load $P_1$, which is found by substituting Eq. (4.1) into Eq. (4.3);

$$P_1 = (M_0/H)/[1 + (e/H)] \tag{4.4}$$

In terms of the dimensionless quantities

$$\alpha = M_0l^2/cH \qquad \beta = Pl^2/c \tag{4.5}$$

the yield load is

$$\beta_1 = \alpha/[1 + (e/H)] \tag{4.6}$$

For loads exceeding the yield load, the entire column will initially be in regime AB. Hence, throughout the column,

$$cd\kappa = -c(d\epsilon/H) \tag{4.7}$$

which expresses the fact that the flow vector $[cd\kappa, c(d\epsilon/H)]$ is in the direction of the exterior normal to side AB of the yield locus. Furthermore, since the stress point must remain in contact with the yield locus, the projections of the stress increment vector $(dM\ HdN)$ and the flow vector onto the exterior normal to AB must be equal. That is,

$$dM - HdN = cd\kappa - c(d\epsilon/H) \tag{4.8}$$

Combining Eqs. (4.7) and (4.8) yields

$$dM - HdN = 2cd\kappa \tag{4.9}$$

which must be integrated using the conditions at $P = P_1$ as initial conditions. These are

$$M_1 = P_1e \qquad N_1 = -P_1 \qquad \kappa_1 = 0 \tag{4.10}$$

so that carrying out the indicated integration, substituting from Eqs. (4.1), (4.2), and (4.5), and introducing the dimensionless variables $w/H$ and $x/l$ finally furnishes the differential equation

$$(w/H)'' + (1/2)\beta(w/H) = -(1/2)[1 + (e/H)] \times (\beta - \beta_1) \tag{4.11}$$

primes denote differentiation with respect to $x/l$. Since by virtue of symmetry only half of the column need be considered, the boundary conditions are

$$(w/H)'(0) = (w/H)(1) = 0 \tag{4.12}$$

The integration is easily carried out, and

$$w/H = [1 + (e/H) - (\alpha/\beta)] \times \{[\cos \sqrt{\beta/2}(x/l)/\cos \sqrt{\beta/2}] - 1\} \tag{4.13}$$

As long as every point of the column remains in regime AB, Eq. (4.13) expresses the deflection. However, a given point enters regime A, that is, the lower flange becomes plastic, when

$$M + NH = -M_0 \tag{4.14}$$

or

$$(e/H) + (w/H) - 1 + (\alpha/\beta) = 0 \tag{4.15}$$

there. Clearly this condition is first satisfied at the end of the column $x = l$. The load $\beta = \beta_2$ at which this point enters regime A is found to be

$$B_2 = \{[1 + (e/H)]/[1 - (e/H)]\}\beta_1 = \alpha/[1 - (e/H)] \tag{4.16}$$

For loads exceeding $\beta_2$ a central portion of the column remains in regime AB where Eq. (4.11) prevails. The rest of the column, however, has entered regime A. There the flow vector is equal to the stress increment vector. That is

$$dM = cd\kappa \qquad HdN = c(d\epsilon/H) \tag{4.17}$$

Only the first of these equations is needed. It appears that this equation must be integrated using as initial conditions the situation at each cross-section at the time it entered regime A. This would vary from point to point. However, the final result does not depend on the time at which regime A was entered,* and hence the values of the variables at $\beta = \beta_1$ may be used as initial conditions,

* See reference 13 for a discussion of this statement.

$$M_1 = \kappa_1 = 0 \tag{4.18}$$

Therefore, the integration of the first Eq. (4.17) yields

$$M = c\kappa \tag{4.19}$$

which is equivalent to the differential equation

$$(w/H)'' + \beta(w/H) = -\beta(e/H) \tag{4.20}$$

The boundary conditions are still given by Eq. (4.12); the one at the center applies to the solution of Eq. (4.11), the other to the solution of Eq. (4.20). The moving transition point $x = \sigma$ between regimes AB and A is determined from the fact that Eq. (4.14) is always satisfied there. The displacements are then given by

$$\frac{w}{H} = \frac{\sqrt{2}\left[1 - \frac{\alpha}{\beta} + \sqrt{2}\,\frac{e}{H}\,\frac{\cos\sqrt{\beta}\,(\sigma/l)}{\sin\sqrt{\beta}}\cot\sqrt{\frac{\beta}{2}}\,\frac{\sigma}{l} + \frac{e}{H}\,\frac{\sin\sqrt{\beta}\,(\sigma/l)}{\sin\sqrt{\beta}}\right]\frac{\cos\sqrt{\beta/2}(x/l)}{\sin\sqrt{\beta/2}(\sigma/l)}}{\sqrt{2}\cot\sqrt{\beta/2}(\sigma/l) - \tan\sqrt{\beta}\,[1 - (\sigma/l)]} -$$

$$\sqrt{2}\,\frac{e}{H}\,\frac{\cos\sqrt{\beta}\,(\sigma/l)}{\sin\sqrt{\beta}}\,\frac{\cos\sqrt{\beta/2}(x/l)}{\sin\sqrt{\beta/2}(\sigma/l)} - \left(1 + \frac{e}{H} - \frac{\alpha}{\beta}\right), \qquad 0 \le x \le \sigma \tag{4.21}$$

$$\frac{w}{H} = \frac{\left[1 - \frac{\alpha}{\beta} + \sqrt{2}\,\frac{e}{H}\,\frac{\cos\sqrt{\beta}\,(\sigma/l)}{\sin\sqrt{\beta}}\cot\sqrt{\frac{\beta}{2}}\,\frac{\sigma}{l} + \frac{e}{H}\,\frac{\sin\sqrt{\beta}\,(\sigma/l)}{\sin\sqrt{\beta}}\right]}{\sqrt{2}\cot\sqrt{\beta/2}(\sigma/l) - \tan\sqrt{\beta}\,[1 - (\sigma/l)]} \times$$

$$\frac{\sin\sqrt{\beta}\,[1 - (x/l)]}{\cos\sqrt{\beta}\,[1 - (\sigma/l)]} - \frac{e}{H}\left[1 - \frac{\sin\sqrt{\beta}\,(x/l)}{\sin\sqrt{\beta}}\right], \qquad \sigma \le x \le l \tag{4.22}$$

The relation between $\beta$ and $\sigma/l$ is

$$\frac{e}{H}\,\frac{\cos\sqrt{\beta}\,(\sigma/l)}{\sin\sqrt{\beta}}\tan\sqrt{\beta}\left(1 - \frac{\sigma}{l}\right) + \frac{e}{H}\,\frac{\sin\sqrt{\beta}\,(\sigma/l)}{\sin\sqrt{\beta}} +$$

$$\sqrt{2}\left(1 - \frac{\alpha}{\beta}\right)\tan\sqrt{\beta}\left(1 - \frac{\sigma}{l}\right)\tan\sqrt{\frac{\beta}{2}}\,\frac{\sigma}{l} - \left(1 - \frac{\alpha}{\beta}\right) = 0 \tag{4.23}$$

It may happen that the entire column eventually enters regime A. The load $\beta = \beta_3$ at which this occurs is obtained from Eq. (4.23) by setting $\sigma/l = 0$. This gives the equation

$$(e/H) - [1 - (\alpha/\beta_3)]\cos\sqrt{\beta_3} = 0 \tag{4.24}$$

which may or may not have a relevant solution. If it does, then for $\beta > \beta_3$ the column is entirely in regime A, so that Eq. (4.20) holds throughout the column. Carrying out the integration and applying both boundary conditions results in

$$w/H = (e/H)\{[\cos\sqrt{\beta}(x/l)/\cos\sqrt{\beta}] - 1\} \tag{4.25}$$

Alternatively, if Eq. (4.24) has no relevant solution, then the column is never entirely in regime A.

During the preceding derivation, several assumptions have been tacitly made which should be clarified. In the first place, it was assumed that the lower flange becomes plastic in compression at the end before it becomes plastic in tension at the center. In other words, the stress point for the end section enters corner A of the yield locus before that for the center section enters corner B. This is to be expected for small eccentricities and has been verified numerically. Furthermore, the solution represented by Eqs. (4.21)–(4.25) is valid only as long as no stress reversal in the lower flange has taken place. If the column is entirely in regime A then stress reversal occurs when

$$dM/d(PH) = 0 \tag{4.26}$$

If this equation is satisfied for $\beta = \beta_4$, then it can be cast into the form

$$(e/H)[1 + (1/2)\sqrt{\beta_4}\tan\sqrt{\beta_4}] = \cos\sqrt{\beta_4} \tag{4.27}$$

If, however, the column is partly in regime AB and partly in regime A when stress reversal occurs, then $\beta_4$ is found from the condition

$$d(\sigma/l)/d\beta = 0 \tag{4.28}$$

where $d(\sigma/l)/d\beta$ is calculated from Eq. (4.23). This equation expresses the fact that the transition point $\sigma$ between regimes AB and A is stationary at the instant of stress reversal.

It seems impractical to carry the analysis further. After stress reversal has taken place, integration of the flow equations requires the use of initial conditions which vary from point to point. This, in turn, results in differential equations for $w/H$ with nonconstant coefficients. While in principle these could be integrated, the resulting expressions would be extremely cumbersome. Actually, experiments indicate that when strain reversal (or stress reversal) occurs, failure of the column is at hand. Consequently, little is lost by discontinuing the analysis at this point.

Of particular interest is the situation as $e/H \to 0$. In this case, Eqs. (4.6), (4.16), and (4.24) show that $\beta_1$, $\beta_2$, and $\beta_3$ all approach $\alpha$ as $e/H \to 0$. This means that as soon as the column becomes plastic, every part of it enters regime A. Hence the governing equation is (4.25), which implies that there is no bending until

$$\sqrt{\beta} = \pi/2 \tag{4.29}$$

at which time the right-hand side becomes indeterminate. However, Eq. (4.27) states that

$$\sqrt{\beta_4} = \pi/2 \tag{4.30}$$

These results show that, as soon as the column starts to bend, the lower flange begins to unload, so that the theory given here cannot be used to obtain the load-deflection relation for loads greater than $\beta_4$. It is interesting to note that Eq. (4.30) gives

$$P_4 = \pi^2 c/4l^2 \tag{4.31}$$

as the load at which a centrally loaded column starts to bend. This is the tangent modulus load of the classical theory, provided $c$ is identified with the plastic flexural rigidity.

Computations have been carried out based on the equations of this section; the results appear in Fig. 12 in the form of a plot of the load parameter, $\beta$, versus the normalized central deflection, $w(0)/H$. The same set of values of $e/H$ is employed as for the simple model, and two values of $\alpha$ are used. The curves are quite similar to those of Fig. 11.

The stiffening effect produced when the lower flange becomes plastic is more complicated in this case than before, because the lower flange does not become plastic everywhere at once. Rather, there is a sort of traveling wave of plasticity, with its front at $x = \sigma$, which sweeps down the column, beginning at $x = l$.

There are two distinct effects of this so-called "wave." The first is a gradual stiffening exhibited by an element before the "wave" arrives; this is due to the fact that some portion of the lower flange is plastic in compression, although the element under inspection is not. The second is a sudden stiffening, characterized by a discontinuity in the slope of the load-deflection curve,

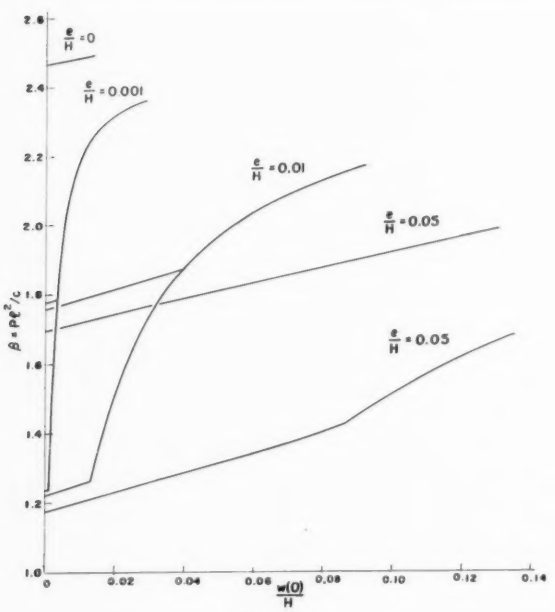


FIG. 12.

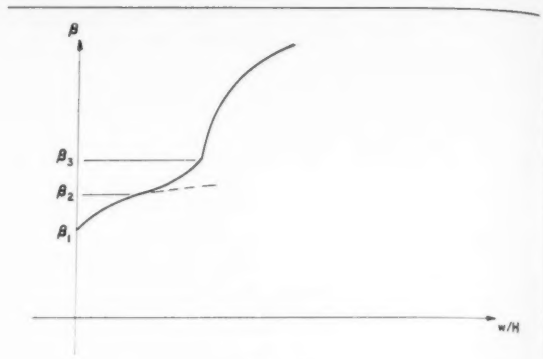


FIG. 13.

which occurs as the "wave front" reaches the column element in question. The latter effect will not always occur, since there are circumstances under which stress reversal in the lower flange will begin before any given element of the lower flange becomes plastic.

Both effects are illustrated in Fig. 13, which shows a typical load-deflection curve. The dotted curve is a continuation of the one from $\beta_1$ to $\beta_2$; it is found solely from the equations of regime AB. The actual situation, involving both regimes A and AB, is represented by the solid curve. The increase in load necessary to produce a given deflection is the gradual stiffening noted above. This effect increases continuously with $\beta$ as more and more of the lower flange becomes plastic. The discontinuity in slope at $\beta = \beta_2$ is due to the sudden stiffening which accompanies the front of the "plastic wave." Of course, in a real material this stiffening will not be characterized by an actual discontinuity in slope, but rather by a small zone in which the slope increases rapidly. This is due to the fact that the stress-strain law assumed here has a discontinuity in slope at the beginning of plastic flow (in Fig. 3, point A, for example), whereas in reality the stress-strain law is represented by a smooth curve. Furthermore, the presence of elastic strains will tend to obscure the effect.

Nevertheless, experimental verification of this type of behavior has recently been given by Baker, Horne, and Heyman.[14] Although they deal with a somewhat different problem, the sudden stiffening is very noticeable in their empirical curves, which resemble some of those in Figs. 11 and 12.

### (5) Conclusion

The results presented here suggest that some care must be used in any experimental determination of the "buckling load" for sandwich-type plastic columns under eccentric loads. Some lateral displacement occurs from the moment at which the upper flange becomes plastic; however, for small eccentricities the total displacement before the lower flange also becomes plastic will be small, in many cases small enough so that the column will remain serviceable. After both flanges are plastic, the resultant stiffening of the column prevents further appreciable displacements

(*Continued on page 362*)

# Theory of the Finite-Span Blowing Wing

H. B. HELMBOLD*

*Fairchild Engine and Airplane Corporation*

SUMMARY

The essential features of two-dimensional flow around a blowing wing are briefly outlined. The flow around the finite-span blowing wing is investigated under the simplifying assumption of undisturbed static pressure at infinity downstream. The effects of finite span are induced drag, and losses of jet thrust and jet-induced lift. The induced drag results from circulation around the wing and jet sheet, the loss of jet thrust from final jet deflection, and the loss of jet-induced lift from loss of jet-sheet curvature. The forces on the finite-span jet wing are functions of the induced angle which is determined either graphically from a sixth-degree equation or by a second-order approximation for moderate induced angles. The jet coefficients are finally represented as functions of jet-power coefficient and jet-sheet thickness ratio.

SYMBOLS

| | |
|---|---|
| $S$ | = wing area |
| $b$ | = wing span |
| $A$ | = $b^2/S$ = aspect ratio |
| $c$ | = wing chord |
| $h$ | = thickness of the jet sheet ($h_0 = h$ at midspan) |
| $R$ | = radius of curvature of the jet sheet |
| $\rho$ | = density |
| $V$ | = undisturbed velocity |
| $q$ | = $\rho V^2/2$ = dynamic pressure |
| $V_j$ | = jet velocity at undisturbed pressure |
| $\delta_{te}$ | = jet-deflection angle at the trailing edge |
| $\Delta p_j$ | = pressure discontinuity across the jet sheet |
| $\Delta p_t$ | = excess total pressure of the jet |
| $\epsilon$ | = discontinuity of the velocity across the jet sheet |
| $m_j$ | = mass flux of the jet sheet |
| $\Delta m_j$ | = increase of jet-mass flux through fixed jet thickness (slot width) |
| $J_0$ | = $m_j V$ = incoming momentum flux of the jet sheet |
| $J$ | = $m_j V_j$ = jet-momentum flux at undisturbed pressure |
| $\Delta J$ | = excess jet-momentum flux for fixed jet-sheet thickness (slot width) |
| $\Delta J_y$ | = $\Delta J \sin \delta_{te}$ |
| $T_j$ | = jet thrust |
| $T_{le}$ | = leading-edge thrust |
| $T_{te}$ | = trailing-edge thrust |
| $F_j$ | = resultant pressure force on the jet sheet |
| $L_0$ | = basic circulation lift (two-dimensional) |
| $\Delta L$ | = jet-induced lift |
| $L_p$ | = $L_0 + \Delta L$ = circulation lift on the airfoil |
| $\lambda$ | = "centrifugal thickness" of the jet sheet |
| $d\Delta E/ds_j$ | = excess energy per unit length of the jet sheet |
| $C_\mu$ | = $J/qS$ = jet-momentum coefficient |
| $C_E$ | = $\Delta J/qS$ = excess jet-momentum coefficient |
| $C_Q$ | = $m_j/\rho VS$ = quantity coefficient |
| $C_L$ | = $L/qS$ = lift coefficient |
| $C_{L_0}$ | = $L_0/qS$ = basic lift coefficient |
| $\Delta C_L$ | = $\Delta L/qS$ = jet-induced lift coefficient |
| $C_{Tj}$ | = $T_j/qS$ = jet thrust coefficient |
| $\delta_\infty$ | = downwash angle at infinity downstream |
| $m$ | = additional virtual mass of the trailing vortex system |
| $L_J$ | = impulse lift |
| $L_C$ | = total circulation lift on airfoil plus jet |
| $L'_C$ | = total pressure force on airfoil plus jet |
| $w'$ | = absolute velocity near jet surface at infinity downstream |
| $D_i$ | = induced drag |
| $\alpha_i$ | = induced angle of airfoil plus jet |
| $\Delta J'_y$ | = pressure lift on jet sheet |
| $F_w$ | = pressure force on airfoil |
| $L'_0$ | = contribution of basic airfoil circulation force to $L'_C$ |
| $C_{L'C}$ | = $L'_C/qS$ = coefficient of total pressure force |
| $\Delta C_{L'C}$ | = nondimensional contribution of jet-induced force to $C_{L'C}$ |
| $\Delta C_{Tj}$ | = nondimensional induced loss of jet thrust |
| $P_j$ | = jet power |
| $C_{Pj}$ | = $P_j/qVS$ = jet power coefficient |
| $V_{j0}$ | = static jet velocity |

Received July 20, 1956.

* Research Scientist, Fairchild Aircraft Division.

## INTRODUCTION

THE BLOWING WING was first conceived as a boundary-layer controlled wing. A jet blown tangentially to the upper surface into the boundary layer served to keep the flow attached or to reattach the separated flow at high angles of attack and at high flap deflections. A certain minimum jet strength was needed to obtain the lift coefficient predicted by potential flow theory. However, further increase of the jet strength produced a further increase of lift which originally was thought of as the upward component of the direct jet reaction. Actually, an experiment by G. B. Schubauer[1] on an elliptical airfoil section at zero angle of attack with a jet blowing downward from the trailing edge showed that the lift was much greater with a positive wind-tunnel speed than with zero speed. This fact, however, went unnoticed for many years. A similar experiment by H. Hagedorn and P. Ruden[2] met the same fate. These authors already recognized clearly the physical principle of jet-induced lift by stating that with a blowing jet there exists a pressure discontinuity at the trailing edge and by suggesting that this pressure discontinuity continues downstream along the jet sheet and serves to deflect the jet sheet into the direction of the parallel stream and that consequently, the pressure distribution on the airfoil becomes "fuller" and the lift greater. There remained only to explain the experience of reference 1. A mathematical formulation of the problem was first presented in reference 3 and a theoretical proof that the jet-induced lift must exceed the upward component of direct jet reaction was given in reference 4. Along similar lines of thought the problem was formulated independently by R. Legendre[5] and solved numerically by L. Malavard.[6] A method for analytical solution was outlined by D. A. Spence.[7] To date the theoretical work has been

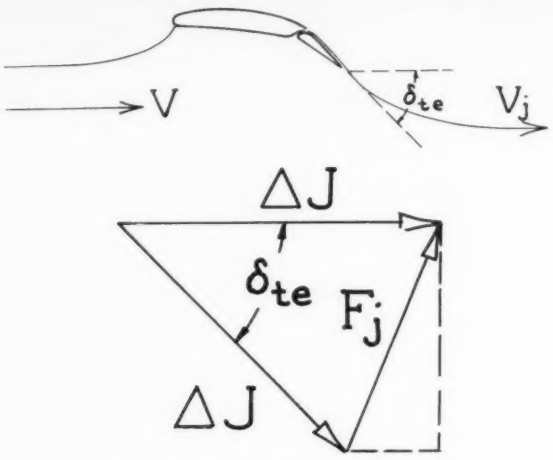


FIG. 1a. *Top.* FIG. 1b. *Bottom.*

concentrated on the two-dimensional problem. The three-dimensional problem of the finite-span blowing wing is the subject of the present study.

## (1) REVIEW OF THE TWO-DIMENSIONAL PROBLEM

Before attacking the more complex three-dimensional case it will be necessary to clearly recognize the unaccustomed features of the two-dimensional problem.

A thin jet sheet is blown downward from the trailing edge of the airfoil at an angle $\delta_{te}$ with respect to the undisturbed velocity $V$. The basic flow turns the jet sheet gradually into the direction of this velocity $V$. The turning force is provided by a pressure discontinuity $\Delta p_j$ across the jet sheet which must be in equilibrium with the excess of centrifugal acceleration in the jet,

$$\Delta p_j = \rho\,(V_j^2 - V^2)\,(h/R) = 2\Delta p_t(h/R) \qquad (1)$$

Here $\rho$ denotes the density, $V_j$ the jet velocity, $h$ the thickness, and $R$ the radius of curvature of the jet sheet, while $\Delta p_t$ is the excess total pressure of the jet. The pressure discontinuity vanishes if $V_j$ becomes equal to $V$ (no jet). On the other hand, the pressure discontinuity requires a discontinuity $\epsilon$ of the velocity across the jet sheet, since

$$\Delta p_j = \rho V \epsilon \qquad (2)$$

Eqs. (1) and (2) are written as first-order approximations. Combining these equations, the lifting vorticity of the jet sheet is obtained as

$$\epsilon = 2(\Delta p_t/\rho V)\,(h/R) = [(V_j^2 - V^2)/V]\,(h/R) \qquad (3)$$

Its effects on the airfoil will be presently discussed. The resultant of the pressure distribution $\Delta p_j$ is the force $F_j$ which rotates the vector of the excess jet-momentum flux $\Delta J = \rho bh(V_j^2 - V^2)$ through the angle $\delta_{te}$ into the direction of $V$ (see Fig. 1). It is assumed that the static pressures are equal at infinity upstream, at infinity downstream, and at the trailing edge, so that the magnitude of the excess jet-momentum flux $\Delta J$ is equal at the trailing edge and at infinity downstream. The components of the turning force are a lift and a drag. The lift arrests the downward excess momentum flux of the jet sheet and is therefore equal to $\Delta J_y = \Delta J \sin \delta_{te}$; the drag increases the horizontal momentum flux and equals $\Delta J(1 - \cos \delta_{te})$. The jet thrust is the excess of horizontal jet-momentum flux at infinity downstream over the horizontal jet-momentum flux at infinity upstream,

$$T_j = J - J_0 = m_j(V_j - V), \qquad (4)$$

where $m_j = \rho bh V_j$ denotes the jet-mass flux, and $b$ is the span. The lifting vorticity of the jet sheet induces an upwash velocity and an increase of horizontal velocity on the airfoil. In order to maintain the tangency condition on the airfoil the circulation around the airfoil must be increased.[3] This additional circulation produces an additional lift $\Delta L$ which may be called the jet-induced lift. Because of the jet-induced upwash angle on the airfoil, a thrust force $T_{te}$ is produced which may be called the leading-edge thrust.

The next step is to consider the resultant of the pressure forces on the airfoil-jet combination, excluding the jet thrust $T_j$ which is an impulse force. According to the Kutta-Joukowski theorem, this resultant must be a pure lift force because the velocity of the basic flow is horizontal at infinity downstream as well as at infinity upstream. Its magnitude is

$$L = \Delta J_y + L_p = \Delta J \sin \delta_{te} + L_0 + \Delta L \qquad (5)$$

The horizontal component of the resultant under consideration is zero. That means the leading-edge thrust and the drag component of the turning force are opposite and equal, $T_{te} = \Delta J(1 - \cos \delta_{te})$. In a physical flow, the pressure lift $L_p$ and the leading-edge thrust $T_{te}$ can be seriously impaired by leading-edge separation, whereas the direct jet reaction with its components $\Delta J_y$ and $T_{te}$ remains indestructible (reaction equal to action).

Now we are prepared to discuss the forces acting on the airfoil (see Fig. 2). The direct reaction on the airfoil of the jet-momentum flux is composed of a lift equal to $\Delta J_y = \Delta J \sin \delta_{te}$ and of a thrust equal to the excess of the jet thrust over the leading-edge thrust

$$T_{te} = T_j - T_{le} = J - J_0 - \Delta J(1 - \cos \delta_{te}) = \Delta J \cdot \cos \delta_{te} - \Delta m_j \cdot V \qquad (6)$$

which may be called trailing-edge thrust. Here $\Delta m_j = \rho bh(V_j - V)$. With high jet-deflection angles $\delta_{te}$ this thrust becomes negative. The pressure distribution on the airfoil contour results in a pressure force $F_W$ which is composed of a pressure lift $L_p$ (consisting of the initial lift $L_0$ of the airfoil without jet and the jet-induced lift $\Delta L$) and of the leading-edge thrust $T_{te}$.

The two-dimensional problem involves two characteristic lengths, namely the wing chord $c$ and, according to Eq. (3), the centrifugal thickness $\lambda$ of the jet sheet[4] where

$$\lambda \equiv [(V_j^2 - V^2)/V^2]h = 2(\Delta p_t/\rho V^2)h$$

is supposed to be constant from the trailing edge downstream. Hence $\lambda/c$, or its double value,

$$C_E \equiv 2(\lambda/c) = 2[(V_j^2 - V^2)/V^2](h/c) \qquad (7)$$

is a characteristic nondimensional parameter of the problem. The subscript $E$ refers to the fact that $\Delta p_t \cdot bh$ is the excess energy per unit length of the jet sheet, as is demonstrated by

$$dE/ds_j = (dt/ds_j)\,(d\Delta E/dt) = (1/V_j)\,(d\Delta E/dt) = (\Delta p_t \cdot bhV_j)/V_j = \Delta p_t \cdot bh$$

Dividing Eq. (6) by $qS$, where $q = \rho V^2/2$ denotes the free-stream dynamic pressure and $S = bc$ the wing area, we obtain the lift coefficient,

$$C_L = C_E \sin \delta_{te} + 2\pi \sin \alpha + f(C_E) \sin \delta_{te} \qquad (8)$$

consisting of these three terms:

$$(\Delta J/qS) \sin \delta_{te} = C_E \sin \delta_{te}$$

$$C_{L_0} \equiv L_0/qS = 2\pi \sin \alpha$$

where $\alpha$ is the angle of attack referred to the zero-lift direction of the airfoil section without jet, and

$$\Delta C_L = \Delta L/qS = f(C_E) \sin \delta_{te}$$

This last term represents the lift on the wing induced by the lifting vorticity of the jet sheet (jet-induced lift). The function $f(C_E)$ has been computed by L. Malavard[6] for a flat plate at zero angle of attack with a jet leaving the trailing edge under a small deflection angle. His result may be roughly approximated by $f(C_E) = \pi\sqrt{C_E}$.

The jet thrust coefficient, according to Eq. (4), is

$$C_{T_j} \equiv T_j/qS = 2(h/c)\,(V_j/V)\,[(V_j - V)/V] \qquad (9)$$

## (2) The Three-Dimensional Problem: State of Flow at Infinity Downstream

For sake of clarity and simplicity it will be supposed that the airfoil is an aerodynamically untwisted wing of elliptical plan form and that $V_j/V$, $h/c$, and $\delta_{te}$ are constant spanwise along the trailing edge, so that $C_E$ and $C_{T_j}$ are also constant spanwise. Then the spanwise lift distribution will be elliptical, and if cross-sectional deformations of the jet sheet are excluded, the elliptical cross section of the jet sheet at infinity downstream will move downward normally to its span like a solid body. The jet sheet carries on its surface a system of longitudinal vortices, the equivalent of the well known free vortex sheet downstream of a finite-span wing without blowing jet. The downward motion of the jet sheet is the result of the lift acting on the jet mass and the additional virtual mass of the longitudinal vortex system. The momentum theorem applied to a control surface far distant from the blowing wing and normal to the undisturbed parallel stream at infinity downstream states that the lift is equal to the change of vertical momentum flux from infinity upstream to infinity downstream.[3]

$$L = m_j V_j \sin \delta_\infty + m\,V \sin \delta_\infty \qquad (10)$$

Here $m_j = \rho b(\pi/4)h_0 V_j$ denotes the jet-mass flux and $m = \rho(\pi/4)b^2 V$ the additional virtual mass flux of the longitudinal vortex system; $h_0$ is the thickness of the jet sheet in the center of the span and $\delta_\infty$ is the downwash angle at infinity downstream. $V_j \sin \delta_\infty$ and $V \sin \delta_\infty$ are the downwash velocities inside and immediately outside of the jet sheet. It has been assumed that the static pressure at infinity downstream is everywhere equal to the static pressure of the undisturbed parallel stream, so that the velocity along the jet sheet outside of the jet equals the undisturbed velocity $V$. From Eq. (10) it follows that

$$\sin \delta_\infty = L/(m_j V_j + mV) = (L/b)/[\rho(\pi/4)\,(h_0 V_j^2 + bV^2)] \qquad (11)$$

This expression includes some interesting limiting cases. If $L/b$ is finite and the span $b$ becomes infinite the downwash angle $\delta_\infty$ vanishes,[3] as has been admitted in discussing the two-dimensional problem. If the parallel stream vanishes, $V = 0$, the pressure lift $L_p$ on the wing vanishes too and only $J_y = J \sin \delta_{te} = \rho b(\pi/4)h_0 V_j^2 \sin \delta_{te}$ remains, so that $\sin \delta_\infty = \sin \delta_{te}$ and the jet sheet becomes straight (elliptical cylinder).

The first consequence of a positive downwash angle at infinity downstream is a loss of useful jet thrust since now, instead of Eq. (4),

$$T_j = J \cos \delta_\infty - J_0 = m_j\,(V_j \cos \delta_\infty - V) \qquad (12)$$

or, in nondimensional form,

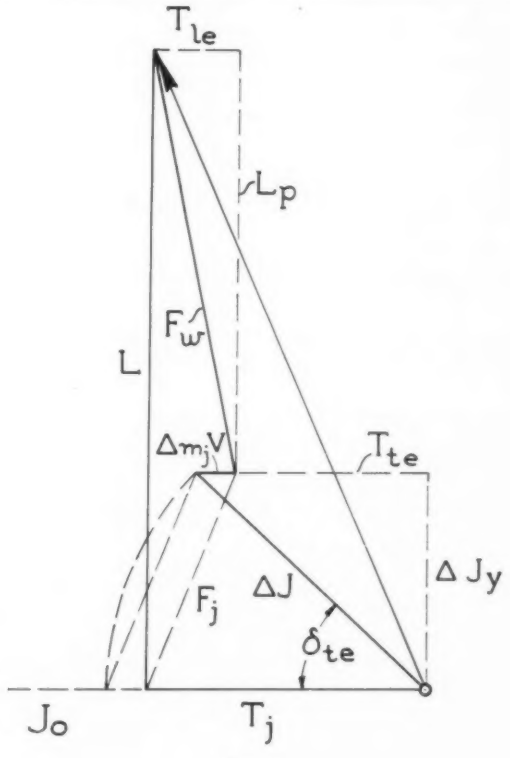


Fig. 2.

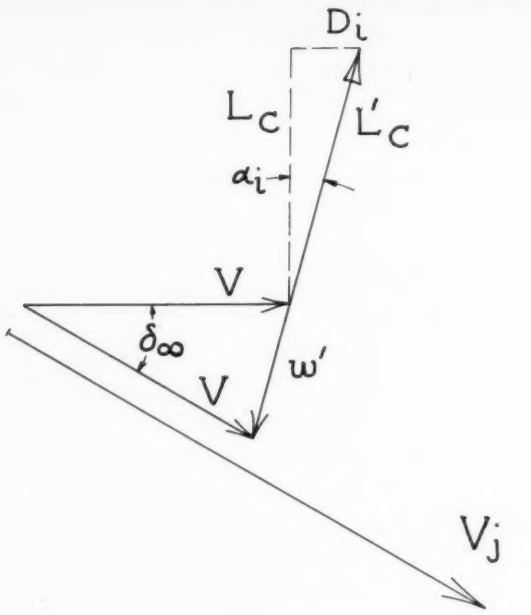


FIG. 3.

$$C_{T_j} = 2(h/c)\,(V_j/V)\,[(V_j \cos \delta_\infty - V)/V] = C_\mu \cos \delta_\infty - 2(h/c)\,(V_j/V) \quad (13)$$

where

$$C_\mu \equiv J/qS = 2(h/c)\,(V_j/V)^2$$

The second consequence is the occurrence of induced drag which will be discussed presently.

First, however, we must go back to Eq. (10) and note the essential difference between the two terms on its right-hand side. The term $L_J = m_j V_j \sin \delta_\infty$ represents the reaction of vertical jet-momentum flux at infinity downstream and may be called impulse lift. Its price is a loss of useful jet thrust, namely $m_j V_j(1 - \cos \delta_\infty)$. The other term, $L_c = mV \sin \delta_\infty$, represents the reaction of the vertical momentum flux in the flow surrounding the jet sheet and may be called total circulation lift because it is connected to the system of longitudinal vortices, which, in turn, is determined by the total circulation around the wing-jet combination. It is quite an unfamiliar feature that the growth of longitudinal vortices is not terminated at the trailing edge but continues along the jet sheet according to the downstream decay of jet sheet vorticity. The price of total circulation lift is the induced drag or, in other words, the induced drag is caused by the above defined total circulation lift only.[4]

Under the assumption that the static pressure is equal at infinity upstream and downstream the magnitude of the velocity of the surrounding flow along the jet sheet is equal to the undisturbed velocity. There is, however, a vectorial difference between that velocity and the undisturbed velocity; it may be denoted by $w'$ (see Fig. 3). Its magnitude is $w' = 2V \sin (\delta_\infty/2)$ and its inclination toward the vertical is $\delta_\infty/2$.

The vectorial change of momentum flux in the basic flow causes a reaction $L'_c = mw'$ opposite to $w'$. The kinetic energy left in the absolute motion around the jet sheet equals the work of the induced drag,

$$m(w'^2/2) = L'_c(w'/2) = D_i V \quad (14)$$

Hence,

$$D_i/L'_c = w'/2V = \sin (\delta_\infty/2) = \sin \alpha_i$$

The induced angle of attack is half the downwash angle at infinity downstream. The reaction force $L'_c$ is the resultant pressure force on the wing-jet combination. With the blowing wing of finite span it is inclined backward by the induced angle of attack and consists of a vertical component, the circulation lift $L_c = L'_c \cos \alpha_i$, and a horizontal component, the induced drag $D_i = L'_c \sin \alpha_i$. Note that the term "induced angle of attack" no longer denotes the inclination to the vertical of the pressure force on the wing itself but the inclination of the resultant pressure force on the wing-jet combination.

### (3) The Three-Dimensional Problem: Force Vectors on the Blowing Wing

By the occurrence of downwash angle $\delta_\infty$ and induced angle $\alpha_i$, the force-vector diagram, Fig. 2, of the two-dimensional case is essentially modified and takes a configuration like Fig. 4 in the three-dimensional case. In the first case the lift $L$ was pure circulation lift. Now the total lift $L$ is the sum of circulation lift $L_c$ and impulse lift $L_J$. The useful thrust is no longer the jet thrust $T_j$, but the difference $T_j - D_i$, which may be called the net thrust. Since now the jet sheet is turned only through the angle $\delta_{te} - \delta_\infty$, the vertical

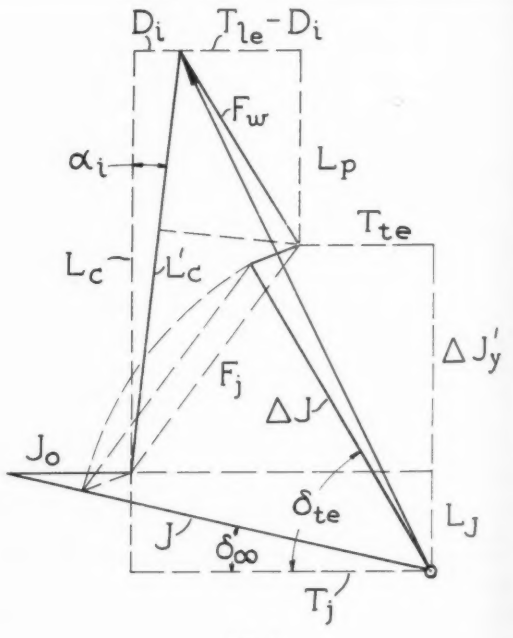


FIG. 4.

and horizontal components of the turning force $F_j$ become $\Delta J'_y = \Delta J(\sin \delta_{te} - \sin \delta_\infty)$ and $T_{te} = \Delta J(\cos \delta_\infty - \cos \delta_{te})$, respectively. Hence, the direct reaction on the airfoil of the jet-momentum flux is composed of a lift equal to

$$\Delta J_y = L_J + \Delta J'_y = J \sin \delta_\infty + \Delta J (\sin \delta_{te} - \sin \delta_\infty) = \Delta J \sin \delta_{te} + \rho b(\pi/4) h_0 V^2 \sin \delta_\infty$$

and of the trailing-edge thrust

$$T_{te} = T_j - T_{te} = J \cos \delta_\infty - J_0 - \Delta J(\cos \delta_\infty - \cos \delta_{te}) = \Delta J \cos \delta_{te} + \rho b(\pi/4) h_0 V^2 \cos \delta_\infty - J_0 = \Delta J \cos \delta_{te} - \Delta m_j V$$

where $\Delta m_j = \rho b(\pi/4) h_0 (V_j - V \cos \delta_\infty)$. The force vector unnamed in Fig. 4 and connecting the vectors $\Delta J(\delta_{te})$ and $F_W$ represents the direct reaction on the airfoil of the incoming jet-momentum flux; its horizontal and vertical components are $\Delta m_j \cdot V$ and $\rho b(\pi/4) h_0 V^2 \sin \delta_\infty$, respectively.

In order to apply the information about the two-dimensional problem to the three-dimensional problem, it becomes necessary to break down the force $L'_c$ into its physical elements. These are the projections of the pressure forces $F_j$ and $F_W$ on the direction of $L'_c$. The projection of $F_j$ is

$$\Delta J'_y \cos \alpha_i + T_{te} \sin \alpha_i = \Delta J[(\sin \delta_{te} - \sin \delta_\infty) \times \cos \alpha_i + (\cos \delta_\infty - \cos \delta_{te}) \sin \alpha_i] = \Delta J[\sin (\delta_{te} - \alpha_i) - \sin \alpha_i] \quad (15)$$

as can be read from Fig. 4. This is the contribution of the jet to the circulation force $L'_c = \sqrt{L_c^2 + D_i^2}$. The projection of $F_W$ is the contribution of the wing to the circulation force $L'_c$. It consists of a contribution of the wing without jet and a jet-induced force, and it requires special consideration because now the flow around the wing-jet combination is inclined by the induced angle $\alpha_i$ and because the curvature of the jet sheet is diminished. The contribution of the wing without jet becomes

$$L'_0 = 2\pi \sin \alpha_\infty \cdot qS = 2\pi \sin (\alpha - \alpha_i) \cdot qS \quad (16)$$

instead of $L_0 = 2\pi \sin \alpha \cdot qS$. The significance of jet-sheet curvature is recognized by inspection of Eq. (3). The lifting vorticity $\epsilon$ on the jet sheet is proportional to the jet-sheet curvature. It is this vorticity which induces an upwash at the wing and consequently an additional circulation. In the three-dimensional case the jet sheet is turned through the angle $\delta_{te} - \delta_\infty$ only, instead of $\delta_{te}$. This indicates clearly a loss of curvature and, in the last consequence, a loss of jet-induced lift.

In order to obtain an estimate of the correction necessary to account for the effect of diminished curvature we start from a case where the distribution of jet-sheet vorticity as present with two-dimensional flow and its change by the effect of finite span can be clearly distinguished. With a weak jet, where $C_E$ is small, curvature and vorticity of the jet sheet are essentially concentrated within a distance from the trailing edge comparable to the wing chord. Now if the aspect ratio is high, the change in curvature and vorticity is small and is mainly concentrated within a distance from the trailing edge comparable to wing span. In this case the effect of finite span on the jet-induced force is diminished for two reasons—because of smallness of the change in vorticity and because of the greater distances of the vorticity difference from the wing. Then it will be justified to assume (a) that that part of the turning which causes the jet-induced lift is practically completed within a distance from the wing where the inclination of the flow is not yet appreciably different from the induced angle $\alpha_i$, and (b) that the following turning from the inclination $\alpha_i$ to the final value $\delta_\infty$ is so small and it occurs at such a far distance that its effect on the wing becomes negligible. This consideration suggests replacing, as a first step, the term $\Delta C_L = f(C_E) \cdot \sin \delta_{te}$ of Eq. (8) by $\Delta C_{L'C} = f(C_E) \sin (\delta_{te} - \alpha_i)$. If, on the other hand, $C_E$ becomes very large the angle $\delta_\infty = 2\alpha_i$ approaches $\delta_{te}$ and the jet sheet tends to become straight, irrespective of aspect ratio, until finally $\Delta C_{L'C}/f(C_E)$ vanishes completely. [This contention will be justified in connection with Eq. (20)]. Both extreme cases can be combined in one equation which becomes reasonably determined by additionally demanding that it should be as simple as possible and that the function $f(C_E)$ should be taken over from the two-dimensional solution,

$$C_{L'C} = f(C_E) \{\sin (\delta_{te} - \alpha_i) - [(\sin^{n+1} \alpha_i)/\sin^n (\delta_{te}/2)]\} \quad (17)$$

where $n$ is expected to be equal to or greater than 2. When the aspect ratio becomes infinite the induced angle vanishes and the bracket term becomes $\sin \delta_{te}$, and when $C_E$ tends to infinity the induced angle $\alpha_i = \delta_\infty/2$ tends to $\delta_{te}/2$ and the bracket term vanishes.

The force $L'_c$ is the sum of the terms described by Eqs. (15) to (17),

$$L'_c = \Delta J'_y \cos \alpha_i + T_{te} \sin \alpha_i + L'_0 + \Delta L'_c \quad (18)$$

where $\Delta L'_c = \Delta C_{L'C} qS$. On the other hand,

$$L'_c = mw' = \rho(\pi/4) b^2 V \cdot 2V \sin \alpha_i = q \cdot \pi b^2 \sin \alpha_i \quad (19)$$

Combining Eqs. (18) and (19) we obtain, after dividing by $qS$ and rearranging, an equation for determination of $\sin \alpha_i$,

$$2\pi (\sin \alpha \cos \alpha_i - \cos \alpha \sin \alpha_i) + [C_E + f(C_E)] (\sin \delta_{te} \cos \alpha_i - \cos \delta_{te} \sin \alpha_i) - C_E \sin \alpha_i - f(C_E) [(\sin^{n+1} \alpha_i)/\sin^n (\delta_{te}/2)] = \pi A \sin \alpha_i \quad (20)$$

where $A = b^2/S$ denotes the aspect ratio. If $f(C_E) \sim \sqrt{C_E}$ describes correctly the behavior of $f(C_E)$ for $C_E \to \infty$, it is justified to write $C_E \sim f^2(C_E)$. Then, with $f(C_E) \to \infty$, Eq. (20) states that the sum of the terms proportional to $f^2(C_E)$ and $f(C_E)$ is finite for finite aspect ratio. This is possible only if the factors of $C_E$ and $f(C_E)$ vanish for infinite $f(C_E)$. Hence, $\delta_\infty = 2\alpha_i \to \delta_{te}$ in this limiting case. Within the finite

sum of the terms proportional to $f^2(C_E)$ and $f(C_E)$ the relative contribution of the term proportional to $f(C_E)$ is small of the order $1/f(C_E)$. In other words, the limiting value of Eq. (17) for infinite $C_E$ becomes zero.

### (4) The Three-Dimensional Problem: an Approximate Solution

Eq. (20) represents a sixth or higher degree equation in $\sin \alpha_i$ which could be solved graphically. An approximation sufficient for moderate values of $\sin \alpha_i$, say, smaller than 0.4, is obtained by omitting all terms of higher than the second degree in $\sin \alpha_i$,

$$M \sqrt{1 - \sin^2\alpha_i} = N \sin \alpha_i \tag{21}$$

where

$$M \equiv 2\pi \sin \alpha + [C_E + f(C_E)] \sin \delta_{te}$$
$$N \equiv 2\pi \cos \alpha + \pi A + C_E(1 + \cos \delta_{te}) + f(C_E) \cos \delta_{te}$$

with the solution

$$\sin \alpha_i = M / \sqrt{M^2 + N^2} \tag{22}$$

The total lift is the sum of circulation lift $L_c = L'_c \cos \alpha_i$ and impulse lift $L_J = J \sin \delta_\infty$. Hence, by Eq. (19) and $\delta_\infty = 2\alpha_i$,

$$L = q \cdot \pi b^2 \sin \alpha_i \cos \alpha_i + \rho V_j^2 (\pi/4) b h_0 \cdot 2 \sin \alpha_i \cos \alpha_i$$

or, after division by $qS$,

$$C_L = (\pi A + 2C_\mu) \sin \alpha_i \cos \alpha_i \tag{23}$$

The jet-thrust coefficient is, according to Eq. (13),

$$C_{T_j} = C_\mu(1 - 2 \sin^2\alpha_i) - 2C_Q \tag{24}$$

where $C_Q \equiv m_j/\rho VS = (V_j/V)\ (h/c)$ is the quantity coefficient. The induced drag is $D_i = L'_c \sin \alpha_i = q \cdot \pi b^2 \cdot \sin^2 \alpha_i$ and its nondimensional coefficient

$$C_{D_i} \equiv D_i/qS = \pi A \sin^2 \alpha_i \tag{25}$$

The induced drag may be combined with the induced loss of jet thrust,

$$\Delta C_{T_j} = C_{T_j} - (C_\mu - 2C_Q) = 2C_\mu \sin^2 \alpha_i \tag{26}$$

resulting in

$$C_{D_i} + \Delta C_{T_j} = (\pi A + 2C_\mu) \sin^2 \alpha_i \tag{27}$$

This is the total induced loss of net thrust for a finite blowing wing. By comparison with the total lift, Eq. (23), we obtain the intuitive result

$$C_{D_i} + \Delta C_{T_j} = C_L \tan \alpha_i \tag{28}$$

It is acknowledged that the present treatment of the three-dimensional problem can lead only to a simple first approximation because of the simplifying assumptions involved—namely, (a) constant static pressure at infinity downstream, (b) undeformed jet sheet, and (c) summary account for the effect of curvature loss by finite aspect ratio. An estimate of the error caused by the assumptions (a) and (b) cannot be made until the final configuration of the rolled-up jet sheet and its proper velocity is known. The problem of the rolled-up vortex sheet behind a plain wing without blowing jet has been treated in a note to the Readers' Forum of this Journal.[8]

### (5) Jet-Power Requirements

The power necessary to produce a jet sheet of mass flux $m_j$ and jet velocity $V_j$ at the flight speed $V$ is

$$P_j = m_j[(V_j^2 - V^2)/2] = \rho b \cdot (\pi/4) h_0 V_j [(V_j^2 - V^2)/2] \tag{29}$$

if $V_j$ is the jet velocity at a static pressure equal to the static pressure of the undisturbed flow. Since the static pressure at the trailing edge is sufficiently close to the undisturbed static pressure, $V_j$ may be interpreted as the jet velocity at the trailing edge. By putting $V = 0$ in Eq. (29), the static jet velocity

$$V_{j_0} = [2P_j/\rho b \cdot (\pi/4) h_0]^{1/3} \tag{30}$$

is obtained. By dividing Eq. (29) by $\rho b \cdot (\pi/4) h_0 V^3/2$ a cubic equation for the nondimensional jet velocity results,

$$(V_j/V)^3 - (V_j/V) = (V_{j_0}/V)^3 \tag{31}$$

Since in all practical cases $V/V_{j0}$ is considerably smaller than one, the solution of this equation is very satisfactorily approximated by

$$\frac{V}{V_j} = \frac{(V/V_{j_0})}{1 + (1/3)\ (V/V_{j_0})^2} \tag{32}$$

which is still a good approximation for $V/V_{j_0} < 1$. It is convenient to define a nondimensional jet-power coefficient as

$$C_{P_j} = P_j/qVS = (h/c)\ (V_j/V) \times [(V_j^2 - V^2)/V^2] \quad \text{where } S = b \cdot (\pi/4) c_c \tag{33}$$

With this notation the nondimensional static jet velocity becomes

$$V_{j_0}/V = [C_{P_j}/(h/c)]^{1/3} \tag{34}$$

(The subscripts 0 with $h$ and $c$ have been omitted because $h/c$ is constant along the span.) For engineering purposes it is desirable to express the jet coefficients as functions of $C_{P_j}$ and $h/c$. These functions are

$$C_Q = (h/c)\ (V_j/V) = (h/c) \left\{ [C_{P_j}/(h/c)]^{1/3} + (1/3)\ [(h/c)/C_{P_j}]^{1/3} \right\} \tag{35}$$

$$C_\mu = 2(h/c)\ (V_j/V)^2 = 2(h/c) \left\{ [C_{P_j}/(h/c)]^{1/3} + (1/3)\ [(h/c)/C_{P_j}]^{1/3} \right\}^2 \tag{36}$$

$$C_E = 2\frac{h}{c}\frac{V_j^2 - V^2}{V^2} = 2C_{P_j}\frac{V}{V_j} = \frac{2C_{P_j}\left(\frac{h/c}{C_{P_j}}\right)^{1/3}}{1 + \frac{1}{3}\left(\frac{h/c}{C_{P_j}}\right)^{2/3}} \tag{37}$$

all for $V/V_{j_0} = [(h/c)/C_{P_j}]^{1/3} < 1$.

(Continued on page 370)

# Dissociation Effects in Hypersonic Viscous Flows†

Y. H. KUO*
*Cornell University*

SUMMARY

The problem of boundary-layer flow is formulated for a gaseous mixture, resulting from the dissociation of a single perfect diatomic gas. Under the assumption that the mixture is in dissociative equilibrium, the flow quantities, such as surface temperature and skin-friction and heat-transfer coefficients, are evaluated, and the importance of the transport coefficients—namely, the viscosity, conductivity, and diffusion coefficient—are examined. It is shown that under the condition of equilibrium dissociation the effects of dissociation on the transfer coefficients are not large at very high speed.

## (1) INTRODUCTION

IN RECENT YEARS the growing interest in high-speed flight has led to the study of the flow phenomena prevailing at Mach Numbers in the hypersonic range. One of these problems concerns the flow of air past a body with either sharp or blunt nose in the limit of very large Mach Numbers. The problem has usually been formulated under the assumptions that air is a slightly viscous, heat-conducting, continuous medium but obeys the laws of a perfect gas. In the low Mach Number range the theory is well founded and has yielded results fully in accord with experiments. In the hypersonic range, however, the temperature of the gas may reach a point that makes the simple hypothesis of perfect gas untenable because under the existing temperature conditions some molecules are split up under the strong bombardment of the fast-moving particles. When this process affects a considerable proportion of the gas molecules, the gas is said to be *dissociated*.

After dissociation has taken place, part of the kinetic energy of the molecules, which would have been stored in the gas as heat energy, is lost in decomposing the molecules. As a result, the temperature of the gas drops. This difference of temperature between the real dissociated and ideal undissociated gases grows rapidly as the process of dissociation proceeds at higher and higher temperatures. In the problem of hypersonic flow over a body, the calculations have been made on the basis of the information obtained previously without including the effect of dissociation. Since the effects generated by the viscous thickening of the boundary layer depend greatly on the temperature field, an error made in temperature will ultimately be manifested in every other calculated quantity.

In view of the increasing importance of high-speed flow, it is imperative that the basis of the classical theory be further broadened to adapt it to the new situation in which polyatomic gases would dissociate, in order to lend reality to the theoretical conclusions. This paper, as a first attempt, proposes to formulate the boundary-layer problem at high temperature under the suppositions that (1) the fluid in the main stream is a simple diatomic gas, and (2), when dissociated, the resulting mixture is in dissociative equilibrium. The justification for these assumptions lies in the fact that the main objective in such preliminary investigation is first to be able to express the dissociation effects in terms of convenient physical parameters and estimate them effectively for the case of a single gas. As air is almost 80 per cent nitrogen, its thermodynamic properties will certainly be overwhelmingly dominated by nitrogen. Hence, any information gained for nitrogen can be helpful toward the understanding of the phenomena observed in air.

## (2) THERMODYNAMIC FUNCTIONS OF A GASEOUS MIXTURE

It is assumed that the gaseous mixture to be considered below results from the dissociation of some molecules $A_2$ in an originally pure diatomic gas and that the constituents $A_2$ and $A$ of the mixture are in chemical equilibrium and react reversibly according to

$$A_2 \rightleftarrows 2A \tag{2.1}$$

under given temperature and pressure. For this mixture, the relative amount of the constituents $A_2$ and $A$ can be conveniently characterized by the *degree of dissociation*, defined as the fraction of the original gas $A_2$ transformed in the reaction. Let the total number of molecules $A_2$ before dissociation takes place be $N_0$. The number of molecules $A_2$ and atoms $A$ in the mixture is then, respectively, $N_0(1 - \epsilon)$ and $2N_0\epsilon$. It can be verified that in the present case the mass fraction of $A$ becomes identically the same as the degree of dissociation.

In the mixture, let the partial pressures of the gases $A_2$ and $A$ be, respectively, $p_{A_2}$ and $p_A$. In the case of perfect gases, they are related to the density $\rho$ and temperature $T$ of the mixture by

Received June 18, 1956.

† This work was carried out at the Graduate School of Aeronautical Engineering under the sponsorship of the Mechanics Branch, Office of Naval Research. Reproduction in whole or in part is permitted for any purpose of the United States Government. The author has enjoyed and greatly profited by the frequent discussions with Dr. Frank E. Marble during his stay at Cornell University.

* Professor, Graduate School of Engineering.

$$\left.\begin{aligned} p_A &= 2\epsilon R\rho T \\ p_{A_2} &= (1-\epsilon)R\rho T \end{aligned}\right\} \tag{2.2}$$

where $R$ is the gas constant referred to unit mass of the original gas. The total pressure of the mixture, according to Dalton's law, will be the sum of $p_A$ and $p_{A_2}$—namely,

$$p = \{1+\epsilon\}R\rho T \tag{2.3}$$

Similarly, let the specific heat content of the pure gases $A$ and $A_2$ be, respectively, $H_A$ and $H_{A_2}$. In the temperature range considered, the translational and rotational motions of the particles are fully excited but the vibrational and electronic states are partially excited. To the first approximation, if the molecule $A_2$ rotates like a rigid rotator and, independently, vibrates like a harmonic oscillator with frequency $\nu$ with the lowest energy zero, the statistical-mechanical calculations give

$$\left.\begin{aligned} H_A &= c(A)2\epsilon RT \\ H_{A_2} &= c(A_2)(1-\epsilon)RT \end{aligned}\right\} \tag{2.4}$$

where $c(A)$ and $c(A_2)$ are defined by

$$\begin{aligned} c(A) &= (5/2) + \left[\sum_n g_n\mathcal{E}_n(A)e^{-\mathcal{E}_n(A)}/\sum_n g_n e^{-\mathcal{E}_n(A)}\right] \\ c(A_2) &= (7/2) + [(h\nu/kT)/(e^{h\nu/kT}-1)] + \\ &\quad \left[\sum_n g_n\mathcal{E}_n(A_2)e^{-\mathcal{E}_n(A_2)}/\sum_n g_n e^{-\mathcal{E}_n(A_2)}\right] \end{aligned} \tag{2.5}$$

with

$$\mathcal{E}_n(A) = E_n(A)/kT \qquad \text{and} \qquad \mathcal{E}_n(A_2) = E_n(A_2)/kT$$

In the above expressions, 5/2 and 7/2 are easily recognized as the classical values for specific heat at constant pressure; the term $(h\nu/kT)/(e^{h\nu/kT}-1)$ is the vibrational energy of a diatomic molecule $A_2$ and, finally, the last term in both cases represents the contributions from the electronic excitations. The constants $g_n$, $h$, and $k$ are, respectively, the number of electronic states of energy $E_n$ of which the ground state is chosen to be zero, Planck's constant, and Boltzmann's constant. For a given particle, the values of $g_n$ and $E_n$ can be calculated either theoretically or by spectroscopic analysis.

With the temperature held much below that of complete dissociation, the above approximation is adequate and the sums in each case can be replaced by the first few terms. If the temperature goes beyond the range 10,000°K., say, then high-order effects such as anharmonicity of the oscillations, the coupling between oscillation and rotation, etc., should be considered. A calculation of this type has been made by H. A. Bethe.[1]

If the energy of dissociation per molecule is $D$, the total heat content per unit mass of the mixture is

$$H = [c(A_2)(1-\epsilon) + c(A)2\epsilon + (D/kT)\epsilon]RT \tag{2.6}$$

Here the first two terms inside the square bracket can be called the thermodynamic heat content and the last term which arises from the heat absorbed by the reaction (2.1) can be called chemical heat content. It will be noted that, in an aerodynamic problem of this nature, the total heat content, instead of the partial heat content, will appear as the convenient thermodynamic variable.

## (3) Chemical Equilibrium

It is seen from the preceding section that for a two-component mixture, the thermodynamic functions contain not only thermal variables $T$ and $p$ but also the concentration of one of the constituents. In a mixture in which there is chemical reaction, the determination of this quantity requires knowledge of the law that governs the rate of chemical reaction, like the case of a combustion process. In cases where the reaction, under given temperature and pressure, cannot proceed indefinitely, an equilibrium state will ultimately be established. If this condition is satisfied, the partial pressures $p_A$ and $p_{A_2}$ will be such that

$$K_p = p_A{}^2/p_{A_2} \tag{3.1}$$

where $K_p$ is constant for given temperature and is known as the equilibrium constant.

From the definition of partial pressures of Eq. (2.2), it follows that

$$K_p = [4\epsilon^2/(1-\epsilon^2)]p \tag{3.2}$$

In thermodynamics, the condition of equilibrium such as defined above can be expressed by the fact that, holding the temperature and pressure constant, the thermodynamic potential of the system cannot be changed by any variation of the partial pressures. With this principle, statistical mechanics[2] gives the result

$$K_p = \Lambda[Z^2(A)/Z(A_2)]T^{3/2}e^{-D/kT} \tag{3.3}$$

where $Z(A)$ and $Z(A_2)$, known as the sum-over-states, or partition function, denote

$$\left.\begin{aligned} Z(A) &= \sum_n g_n e^{-\mathcal{E}_n(A)} \\ Z(A_2) &= (1-e^{-h\nu/kT})^{-1}\sum_n g_n e^{-\mathcal{E}_n(A_2)} \end{aligned}\right\} \tag{3.4}$$

and the constant $\Lambda$ is

$$\Lambda = [2(2\pi k)^{3/2}/h^3](m_A/2)^{3/2}(h^2/8\pi^2 I) \tag{3.5}$$

Here $m_A$ is the mass of the particle $A$, and $I$ is the moment of inertia of the molecule $A_2$.

Knowing $K_p$ as a function of temperature, the equilibrium degree of dissociation can then be calculated from Eq. (3.2)—namely,

$$\epsilon = [K_p/(4p+K_p)]^{1/2} \tag{3.6}$$

This relation can finally express the enthalpy $H$ in terms of the thermodynamic variables $T$ and $p$.

## (4) Boundary-Layer Equations

Consider a two-dimensional steady flow of a diatomic gas past a fixed semi-infinite flat plate. In a Cartesian

system $(x, y)$, let $y = 0$ and $0 \leq x$ be the plate and let $u$ and $v$ be, respectively, the $x$- and $y$-components of the velocity of the fluid. By the boundary-layer theory, the equations of motion reduce to

$$\rho u(\partial u/\partial x) + \rho v(\partial u/\partial y) = -(dp/dx) + (\partial/\partial y)[\mu(\partial u/\partial y)] \quad (4.1)$$

$$(\partial/\partial x)(\rho u) + (\partial/\partial y)(\rho v) = 0 \quad (4.2)$$

where $\mu$ is the viscosity coefficient of the gaseous mixture.

For a binary mixture, the energy equation, by the same approximation, assumes the form:

$$\rho u(\partial H/\partial x) + \rho v(\partial H/\partial y) = u(dp/dx) + (\partial/\partial y) \times [\lambda(\partial T/\partial y) + (H_A - H_{A_2})\rho\mathfrak{D}(\partial\epsilon/\partial y)] + \mu(\partial u/\partial y)^2 \quad (4.3)$$

where $H$ denotes the total specific heat content of the mixture defined by (2.6); $\lambda$ and $\mathfrak{D}$ are, respectively, the thermal conductivity and binary diffusion coefficients. The second term in the square bracket represents the heat flux transported by diffusion. The effects of thermal diffusion are generally small and, therefore, are neglected. Since the composition of the mixture varies in the flow field, the mass fraction of the individual species is required to satisfy

$$\rho u(\partial\epsilon/\partial x) + \rho v(\partial\epsilon/\partial y) = (\partial/\partial y)[\rho\mathfrak{D}(\partial\epsilon/\partial y)] + \Phi \quad (4.4)$$

where $\Phi$ is the amount of $A_2$ dissociated per unit volume per unit time. These equations, together with the equation of state (2.3), constitute the complete mathematical problem of the flow of a binary gaseous mixture in the boundary layer.

For the present, it will be assumed that the mixture in the flow is always in dissociative equilibrium. This is equivalent to saying that the rate of the reaction is fast in comparison with the process of diffusion. Under this condition, the degree of dissociation as a function of temperature and pressure is completely determined as shown in Section (3); and the equation of diffusion is made simply to be a relation defining the reaction rate $\Phi$ and, consequently, requires no further consideration.

To simplify the energy equation in the case of equilibrium, let the heat capacity at constant pressure be defined by[3]

$$c_p = (\partial H/\partial T)_p \quad (4.5)$$

In accordance with the assumptions of dissociative equilibrium and boundary-layer approximations, the energy equation can be written as

$$\rho u(\partial H/\partial x) + \rho v(\partial H/\partial y) = u(dp/dx) + (\partial/\partial y) \times \{(\mu/Pr)\{1 + [(H_A - H_{A_2})/c_p]Le(d\epsilon/dT)\}(\partial H/\partial y)\} + \mu(\partial u/\partial y)^2 \quad (4.6)$$

where $Pr\ (= c_p\mu/\lambda)$ and $Le(= \rho\mathfrak{D}c_p/\lambda)$ are, respectively, the Prandtl and Lewis Numbers.

## (5) An Approximate Method of Solution

Let the stream function $\Psi$, the heat content $H$ and the pressure $p$ be nondimensionalized as follows:

$$\left.\begin{aligned} \Psi &= \rho_\infty U_\infty L\sqrt{C/Re}\,\psi(\xi, \eta) \\ H &= c_p^{(0)} T_\infty \chi(\xi, \eta) \\ p &= \rho_\infty U_\infty^2 P(\xi) \end{aligned}\right\} \quad (5.1)$$

where $U_\infty$, $\rho_\infty$, and $T_\infty$ are, respectively, the velocity, density, and temperature of the free stream; $c_p^{(0)}$ denotes the specific heat at constant pressure of the undissociated gas $A_2$; $L$ an arbitrary length; $Re$ the Reynolds Number, defined by $\rho_\infty U_\infty L/\mu_\infty$; and $C$ a constant defined in Eq. (5.5). The nondimensional variables $\xi$ and $\eta$ are related to the physical variables $x$ and $y$ by the transformation

$$\left.\begin{aligned} x &= L\xi \\ y &= L\sqrt{C/Re}\int_0^\eta [dz/(\rho/\rho_\infty)] \end{aligned}\right\} \quad (5.2)$$

From the transformations (5.1) and (5.2), it follows that

$$\left.\begin{aligned} u &= U_\infty \psi_\eta \\ \rho v &= -U_\infty \rho_\infty \sqrt{C/Re}[\psi_\xi + L\eta_x\psi_\eta] \end{aligned}\right\} \quad (5.3)$$

The elimination of the velocities according to Eq. (5.3) from Eqs. (4.1) and (4.6) leads to

$$\left.\begin{aligned} &\frac{\partial\psi}{\partial\eta}\frac{\partial^2\psi}{\partial\xi\partial\eta} - \frac{\partial\psi}{\partial\xi}\frac{\partial^2\psi}{\partial\eta^2} = -\frac{\rho_\infty}{\rho}\frac{dP}{d\xi} + \frac{\partial}{\partial\eta}\left[\frac{\mu\rho}{C\mu_\infty\rho_\infty}\frac{\partial^2\psi}{\partial\eta^2}\right] \\ &\frac{\partial\psi}{\partial\eta}\frac{\partial\chi}{\partial\xi} - \frac{\partial\psi}{\partial\xi}\frac{\partial\chi}{\partial\eta} = (\gamma - 1)M^2 \times \left[\frac{\rho_\infty}{\rho}\frac{\partial\psi}{\partial\eta}\frac{dP}{d\xi} + \frac{\mu\rho}{C\mu_\infty\rho_\infty}\left(\frac{\partial^2\psi}{\partial\eta^2}\right)^2\right] + \frac{\partial}{\partial\eta}\frac{\mu\rho}{C\mu_\infty\rho_\infty}\frac{1}{Pr}\left[1 + \frac{H_A - H_{A_2}}{c_p}Le\frac{d\epsilon}{dT}\right]\frac{\partial\chi}{\partial\eta} \end{aligned}\right\} \quad (5.4)$$

where $\gamma$ is the ratio of the specific heats of the undissociated gas $A_2$, and $M$ the Mach Number defined by $U_\infty/\sqrt{\gamma p_\infty/\rho_\infty}$.

In these variables, it is seen that the problem is further simplified by the appearance in both equations of a quantity $\mu\rho$. In view of the fact that $\rho$ and $\mu$ vary with temperature in opposite directions, the rate of variation of the product $\mu\rho$ with temperature will be greatly reduced. This was found true in the case of a pure gas or nonreacting gaseous mixture when the temperature is moderately high. In the case of a reacting mixture, the heat of reaction involved may alter the transport properties to an extent that $\mu\rho$ may change appreciably with temperature. However, if the mixture is in dissociative equilibrium, the effect of the heat release on the mean-free path will be small and the viscosity coefficient for such a mixture

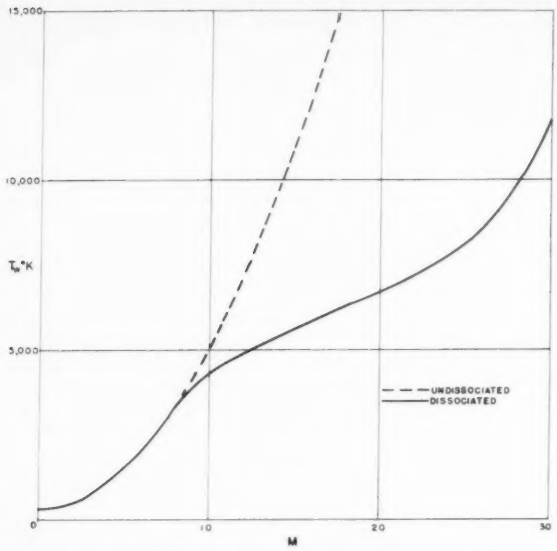


FIG. 1. Adiabatic wall temperature vs. flight Mach Number for dissociated and undissociated nitrogen at $p_\infty = 1$ atm., $T_\infty = 300$°K., and $Pr = 0.72\sigma$.

can be considered, to the first approximation, to be the same as that of a nonreacting mixture.

For a binary mixture of nonreacting gases, according to the kinetic theory, the viscosity coefficient can be expressed, to a first approximation, in terms of the viscosities of the constituent gases, the ratios of concentrations and constants, depending on the character of interaction between particles. If the force between particles varies inversely as some power of the distance between them, the viscosity then varies, like that of a single gas, with temperature according to a power law $T^\omega$, $\omega$ being a constant varying slightly with concentration of the mixture.[4] Also, at constant temperature, the variation of viscosity with concentration is, on the whole, very small. It can, therefore, be concluded that, as in the single gas, the product $\mu\rho$ must also vary slowly with temperature. By the same argument, the Lewis Number must vary with temperature in a similar manner as in a nonreacting mixture.

On the other hand, one observes that the Prandtl Number depends on the ratio of heat capacity $c_p$ to the thermal conductivity $\lambda$ both of which are strongly dependent on the heat of reaction. In the case of a mixture in dissociative equilibrium, the heat capacity $c_p$ can be calculated from Eqs. (2.6) and (3.6) in terms of the degree of dissociation $\epsilon$ and heat of dissociation $D$. As for the thermal conductivity coefficient $\lambda$, it can be shown approximately that it varies very nearly as $c_v\mu$, $c_v$ being the heat capacity at constant volume.[5] It is, therefore, not difficult to verify that the Prandtl Number is also insensitive to change of temperature. By a slightly different argument, C. F. Hansen has arrived at the same conclusion.[6]

Moreover, it can be shown that the ratio of the heat flux transported by diffusion to that by conduction in the case of dissociative equilibrium is approximately

$$Le\,\frac{[(D/2kT) - 2]\epsilon(1-\epsilon^2)(D/kT)}{\epsilon + 9 + [(1/2) + (D/kT)]\epsilon(1-\epsilon^2)(D/kT)}$$

when the vibrational states are fully excited. The most important factor in this expression is evidently $D/kT$ for nonvanishing $\epsilon$. When the first term in the denominator becomes unimportant, the ratio reduces to the value 0.5. It is clear that, over a wide range of temperature, the ratio must vary slowly with temperature. In the case of nitrogen, it has the values of 0.26 at 5,000°K., 0.29 at 6,000°K. and 0.23 at 8,000°K.

Following the accepted practice in the compressible boundary-layer theory for a nonreacting gas, the following approximations are proposed:

$$\left.\begin{aligned} \mu\rho &= C\mu_\infty\rho_\infty \\ Pr &= \text{constant} \\ Le &= \text{constant} \\ \sigma &= 1 + Le \times \\ &\quad \frac{[(D/2RT) - 2]\epsilon(1-\epsilon^2)(D/kT)}{\epsilon + 9 + [(1/2) + (D/kT)]\epsilon(1-\epsilon^2)(D/kT)} \\ &= \text{constant} \end{aligned}\right\} \tag{5.5}$$

On account of Eqs. (5.5), Eqs. (5.4) reduce to

$$\left.\begin{aligned} &\frac{\partial\psi}{\partial\eta}\frac{\partial^2\psi}{\partial\xi\partial\eta} - \frac{\partial\psi}{\partial\xi}\frac{\partial^2\psi}{\partial\eta^2} = -\frac{\rho_\infty}{\rho}\frac{dP}{d\xi} + \frac{\partial^3\psi}{\partial\eta^3} \\ &\frac{\partial\psi}{\partial\eta}\frac{\partial\chi}{\partial\xi} - \frac{\partial\psi}{\partial\xi}\frac{\partial\chi}{\partial\eta} = (\gamma-1)M^2 \times \\ &\qquad \left[\frac{\rho_\infty}{\rho}\frac{\partial\psi}{\partial\eta}\frac{dP}{d\xi} + \left(\frac{\partial^2\psi}{\partial\eta^2}\right)^2\right] + \frac{\sigma}{Pr}\frac{\partial^2\chi}{\partial\eta^2} \end{aligned}\right\} \tag{5.6}$$

The problem thus is reduced to that of incompressible boundary layer with an equivalent Prandtl Number $\sigma/Pr$ and pressure gradient $(\rho_\infty/\rho)dP/d\xi$. The aerodynamic effects of dissociation can thereby be investigated without integrating the differential system (5.4).

### (a) *Insulated Flat Plate*

In the case of insulated plate $dP/d\xi = 0$, with the Blasius solution $f(\zeta)$ given, $\zeta$ being the similarity parameter $\eta/\sqrt{\xi}$, the energy equation can be readily integrated in terms of $f$, first shown by Pohlhausen. On the plate $\zeta = 0$, $\chi$ reduces to

$$\chi(T_w/T_\infty) = 1 + [(\gamma-1)/2]M^2\sqrt{Pr/\sigma} \tag{5.7}$$

where $T_w$ denotes the temperature of the plate. For an undissociated gas, $\chi(T_w/T_\infty)$ is identically $T_w/T_\infty$. Now, on account of Eqs. (2.6) and (3.6), it is a rather complex function of both $T$ and $p$. At standard temperature and pressure, the temperature of the plate for nitrogen $N_2$ is plotted against $M$ and is shown in Fig. 1. For comparison, the plate temperature for undissociated $N_2$ is also given. It is seen that at one atmospheric pressure and $T_\infty = 300$°K., dissociation starts at about 3,500°K., corresponding to a Mach

Number of about 8, and nearly completes at about 10,000°K. with Mach Number of around 28. In this temperature range, the difference in temperature for dissociated and undissociated gases is large; for instance, when dissociation is half completed at 6,000°K., the temperature for the undissociated gas would have been 14,000°K. This clearly demonstrates how far in error the predictions can be if this effect is ignored at high temperature.

On account of the fact that the surface temperature has been considerably reduced by dissociation of the gas, there will be less expansion of the streamlines in the normal direction than that of the undissociated gas at the same Mach Number and, hence, a corresponding decrease of the boundary-layer thickness and the velocity $v$. For, as $\zeta = \infty$, its asymptotic value is

$$v = U_\infty \sqrt{C/Re_x} \left\{ 0.860 + (1/2) \int_0^\infty \times [(1 + \epsilon)(T/T_\infty) - 1]\, d\zeta \right\} \quad (5.8)$$

It is known that at high Mach Number the second term inside the brace predominates and, from Fig. 1, the value of the integral will be much smaller if dissociation of the gases is allowed.

To investigate the effect of dissociation on the skin friction, let the constant $C$ be chosen by the same convention as that adopted in the case of undissociated gas. Namely, the assumed viscosity-temperature law agrees with true value of $\rho\mu$ at the surface where the temperature is the highest. That is, at $\zeta = 0$,

$$C = (\mu\rho/\mu_\infty\rho_\infty)_w \quad (5.9)$$

From this value of $C$, it follows that the ratio of the skin-friction coefficient $c_f$ to that $c_f^{(0)}$ of the undissociated gas is

$$c_f/c_f^{(0)} = \sqrt{(\rho\mu/\rho^{(0)}\mu^{(0)})_w} \quad (5.10)$$

This result shows that if the quantity $\rho\mu$ in both cases is held constant but has the correct value at the highest point of the temperature field, then the change of the skin friction by dissociation, at the same Reynolds and Mach Numbers, can be expressed in terms of the change of $\rho\mu$ by dissociation. In the case of undissociated gas, the quantity $\rho^{(0)}\mu^{(0)}$ can be calculated with reasonable accuracy at high temperature from the knowledge of the viscosity at normal temperature. When dissociation takes place, the situation will be entirely different. Although the quantity $\rho\mu$ behaves much like that of a neutral mixture (as argued in the previous discussion), quantitatively it is quite another matter. It is known from the kinetic theory that the viscosity of a nonreacting mixture depends upon the viscosities of all the constituents. In the present problem, one of the species is a monatomic gas which exists only at high temperature, and the calculation of its viscosity will be very different from that of nonreacting particles at normal temperature. Under these circumstances, the very question of the nature of interaction between particles, namely whether the interaction is attraction or repulsion, depends on the state of excitation of the colliding particles. As far as is known, this type of calculation has not yet been made.

There is evidence that these effects do exist. For instance, when atomic hydrogen diffuses into molecular nitrogen, the calculated diffusion coefficient by the kinetic theory agrees with the value measured by experiments. However, when hydrogen atoms diffuse into molecular hydrogen, the measured diffusion coefficient is about 4 times as large as has been calculated.[7] If this abnormal increase in diffusion coefficient is observed in the case of hydrogen atoms diffusing through hydrogen molecules, there must be a similar increase in other transport coefficients. For this reason, the numerical verification of Eq. (5.10) cannot be given.

### (b) *Cooled Flat Plate*

From the above results, it is observed that if the plate is thermally insulated, the surface temperature will generally be high enough to melt (even to vaporize) steel, for a flight Mach Number greater than 6 at sea level. It is clear that if high-speed flight is to be possible, the heat generated by friction must be removed by means of cooling. Let the surface temperature be $T_w$ and the ambient temperature $T_\infty$. The solution satisfying these conditions is

$$\chi = 1 + [(\gamma - 1)/2]M^2\theta_1(\zeta) + \{\chi_w - 1 - [(\gamma - 1)/2]M^2\sqrt{Pr/\sigma}\}\theta_2(\zeta) \quad (5.11)$$

where $\theta_1$ and $\theta_2$ are functions of the similarity parameter $\zeta$. These functions, like the Blasius function $f(\zeta)$, are tabulated for different values of $Pr/\sigma$ (see reference 8).

For nitrogen at $M = 20$, $Pr = 0.72\sigma$, $Le = 0.72$, $T_\infty = 300$°K., and $p_\infty = 1$ atmosphere, the temperature distribution is presented in Fig. 2 for a wall temperature of 1,200°K. Under these conditions, the temperature reaches a maximum of about 4,200°K. in the neighborhood of the plate. Since nitrogen begins to dissociate at 3,500°K. at one atmosphere, there is a sizable portion of the high temperature zone

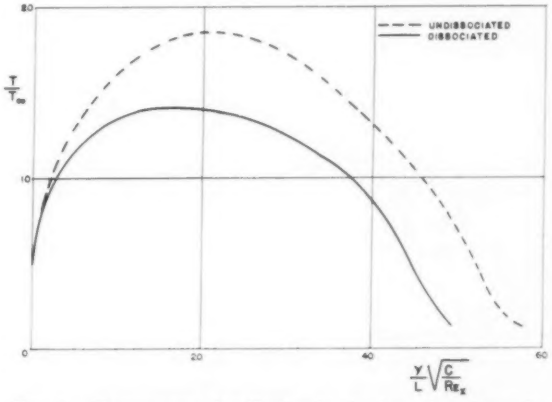


FIG. 2. Temperature distribution in the boundary layer for dissociated and undissociated nitrogen at $p_\infty = 1$ atm., $T_\infty = 300$°K., $M = 20$, and $Pr = 0.72$.

in which the gas is partially dissociated. For comparison, the temperature field with no dissociation taken place, is also plotted for the same constant $C$. It is noted that one of the effects of dissociation is to reduce the boundary-layer thickness.

In the present case where the surface is cooled, it is learned from the calculations of compressible boundary layer that if the constant $C$ is chosen to correspond to the true value of $\rho\mu/\rho_\infty\mu_\infty$ at the neighborhood of the maximum temperature instead of at the surface as in the previous case, the skin friction and the heat transferred to the surface can be similarly calculated. In the case where the gas is in dissociative equilibrium, the heat flux across the surface is given by

$$q = -[\lambda(\partial T/\partial y) + \rho\mathfrak{D}(H_A - H_{A_2})(d\epsilon/dT)(\partial T/\partial y)]_w \quad (5.12)$$

On account of Eqs. (5.1), (5.2), (5.5), and (5.11), the heat flux $q$ can be written as

$$q = q^{(0)} \left(\frac{\sigma Pr^{(0)}}{Pr}\right)^{2/3} \sqrt{\frac{C}{C^{(0)}}} \times \frac{1 + [(\gamma - 1)/2]M^2\sqrt{Pr/\sigma} - \chi_w}{1 + [(\gamma - 1)/2]M^2\sqrt{Pr^{(0)}} - T_w} \quad (5.13)$$

where $q^{(0)}$ denotes the heat flux in the case of the undissociated gas and $Pr^{(0)}$ and $C^{(0)}$, the corresponding constants as defined in Eqs. (5.5). When the Mach Number is very large and the wall temperature is low, the ratio of the heat fluxes is approximately

$$q/q^{(0)} = (\sigma Pr^{(0)}/Pr)^{1/6}\sqrt{C/C^{(0)}} \quad (5.14)$$

It can be concluded from this result that, unless the change of Prandtl Number is large due to dissociation, the effect of dissociation on the heat flux due to change of Prandtl Number is small; and, like the skin-friction coefficient, the ratio of the heat fluxes is sensibly proportional to $(\mu\rho/\mu^{(0)}\rho^{(0)})^{1/2}$. As in the case of cooling, the difference of temperature between dissociated and undissociated gases is greatly reduced, the ratio $(\mu\rho/\mu^{(0)}\rho^{(0)})^{1/2}$ cannot be much different from unity. Generally, it seems that if the surface temperature is low, the effect of dissociation cannot be large, even if the Mach Number is high.

Of course, it must be emphasized that these conclusions have been reached on the assumptions that the mixture is in dissociative equilibrium. When this restriction is dropped by including such phenomena as relaxation and recombination, the results may well be considerably modified.

## References


[1] Bethe, H. A., *The Specific Heat of Air up to 25,000°K.*, Department of Commerce, Report PB-27307, 1942.

[2] Tolman, Richard C., *The Principles of Statistical Mechanics*, p. 610; Oxford University Press, 1938.

[3] Epstein, Paul S., *Textbook of Thermodynamics*, p. 316; John Wiley & Sons, Inc., New York, 1937.

[4] Chapman, Sydney, and Cowling, T. G., *The Mathematical Theory of Non-uniform Gases*, p. 232; Cambridge University Press, 1939.

[5] Rossini, Frederick D., (Ed.), *High Speed Aerodynamics and Jet Propulsion*, Vol. I, "Thermodynamics and Physics of Matter," p. 411; Princeton University Press, 1955.

[6] Hansen, C. Frederick, *Note on the Prandtl Number for Dissociated Air*, Journal of Aeronautical Sciences, Vol. 20, No. 11, p. 789, November, 1953.

[7] Langmuir, Irving, *Phenomena, Atoms and Molecules*, pp. 189, 200–201, Philosophical Library, 1950.

[8] Low, George M., *The Compressible Laminar Boundary Layer with Heat Transfer and Small Pressure Gradients*, NACA TN 3028, 1953.



## Notice to Contributors

Manuscripts submitted for publication *must* be double- or triple-spaced originals. There should be wide margins on all sides of the sheets and triple spacing around formulas to allow for the marking of directions for the printer.

Original drawings (jet black India ink on white paper or tracing cloth) should accompany the manuscript. *(Blueprints are not acceptable.)* Photographs *must* be on glossy white paper. The smallest lettering on 8- by 10-in. figures should be no less than 1/4 in. high.

Only the simplest formulas should be typewritten; all others should be carefully written in pen and ink. The difference between capital and lower-case letters and Greek symbols should be clearly distinguished.

***See Inside Back Cover of this issue for further details***

# Buckling of Thin-Walled Circular Cylinders Under Axial Compression and Internal Pressure

Y. C. FUNG* AND E. E. SECHLER*

*The Ramo-Wooldridge Corporation and California Institute of Technology*

SUMMARY

Theoretical studies show that the effect of internal pressure on the buckling of thin-walled circular cylinders under axial compression depends on the dimensionless parameter $\bar{p} = (p/E)(R/t)^2$ where $p$ is the internal pressure, $E$ the modulus of elasticity, $R$ the cylinder radius, and $t$ the wall thickness of the cylinder. The theoretical treatment of Lo indicates that the critical buckling stress should increase with increasing values of $\bar{p}$ up to a value of $\bar{p} \approx 0.169$, after which the buckling stress remains constant at a value equal to that given by the small deflection theory. Since previous experimental data were limited to values of $\bar{p}$ less than 0.10, additional experimental data were obtained up to $\bar{p} \approx 2.0$ to check the theoretical values. The present tests show that Lo's theory, with certain significant modifications in interpretation, is in fair agreement with the experimental results. A proposed design method is presented which, it is believed, will give conservative values for the buckling stress of such cylinders.

A series of photographs showing the variation of the buckling pattern with the internal pressure is one of the most interesting features revealed by the present series of experiments.

SYMBOLS

| | | |
|---|---|---|
| $E$ | = | Young's modulus, psi |
| $K$ | = | another conventional symbol for $\bar{\sigma}_{cr}$ |
| $L$ | = | length of cylinder, in. |
| $p$ | = | internal pressure, psi |
| $\bar{p}$ | = | nondimensional internal pressure $= (p/E)(R/t)^2$ |
| $p_B$ | = | pressure in loading bellows, psi |
| $P_{cr}$ | = | total compressive load at buckling, lbs. |
| $R$ | = | radius of cylinder, in. |
| $t$ | = | cylinder wall thickness, in. |
| $\sigma_{cr}$ | = | critical compressive stress at buckling, psi |
| $\bar{\sigma}_{cr}$ | = | nondimensional buckling stress $= (\sigma_{cr}/E)(R/t)$ |
| $\bar{\sigma}_{cr_0}$ | = | $K_0$ = value of $\bar{\sigma}_{cr}$ at zero internal pressure |
| $\Delta\bar{\sigma}_{cr}$ | = | $\bar{\sigma}_{cr} - \bar{\sigma}_{cr}$ |

## INTRODUCTION

THE EARLIEST WORK on the effect of internal pressure on the buckling of thin-walled cylinders under axial compression is due to Prescott[1] who indicates that the interaction depends on the dimensionless parameter $\bar{p} = (p/E)(R/t)^2$, where $p$ is the internal pressure, $E$ is the Young's modulus, $R$ is the radius of the cylinder, and $t$ is the wall thickness. His result indicates a parabolic increase of the critical bucking stress with $\bar{p}$. On the other hand, Flügge's[2] exhaustive study in 1932, based on the small-deflection theory, indicates a negligible effect of the internal pressure on the buckling load. Based on some observed contradiction of experimental results with Flügge's conclusion, Lo, Crate, and Schwartz[3] constructed a large-deflection theory, using the method of von Kármán and Tsien,[4] to show that the buckling load increases with increasing values of $\bar{p}$ up to $\bar{p} \approx 0.169$, and then remains constant for $\bar{p} > 0.169$. The theoretical constant value for large values of $\bar{p}$ is the classical buckling load of the small deflection theory. The parameter $\bar{p}$ was introduced explicitly by Lo, et al.

Previous experimental results support Lo's theory for $\bar{p} < 0.1$. Experimental data for $\bar{p} > 0.1$ were not available. In order to determine the buckling behavior of cylinders subject to internal pressures corresponding to larger values of $\bar{p}$, experiments were performed for which results are presented herein.

## APPARATUS AND PROCEDURES

### *Test Specimens*

The specimens used for the tests were cylinders, 11.0 in. long with a 3.5 in. inside diameter, made of 24S-H (condenser foil) aluminum alloy sheets of three thicknesses: 0.001, 0.002, and 0.003 in. The material was furnished by Alcoa, and the cylinders were made by the Task Corporation, Pasadena. The cylinders were made by cementing the sheets together. After experimenting with various kinds of cements, the most satisfactory was found to be the Radio Service Cement, made by General Cement Co., Ill. Lap joints were used for the longitudinal seam. The two ends were attached to rings which provide a seal for internal pressure and becomes part of the loading system (see Fig. 1).

### *Loading System*

Two types of buckling tests were made—loading by dead weight, and loading by pressure bellows. The apparatus for dead weight loading was very simple. The cylinder was sealed at both ends by 1/2 in. brass plates with silicone rubber O-rings. Pressure and manometer leads were placed in the lower end plate. The cylinders were tested in the upright position and load was applied on the top plate by means of a lever system.

Because of the poor control at the critical buckling condition in the dead weight loading system, the mortality rate of the cylinders was high and comprehensive data were gathered only for the 0.003 in. thick cylinder. Some results, however, were obtained by a similar setup using paper cylinders.

Received August 1, 1956.

*Consultants, Aeromechanics Section, The Ramo-Wooldridge Corporation; Associate Professor and Professor of Aeronautics, respectively, California Institute of Technology.

Most of the experimental results were obtained by means of the pressure-bellows system shown in Fig. 1. The cylinder was sealed at the front end by O-rings and at the rear end by a flexible bellow. The front ring of the cylinder was rigidly constrained by the central shaft and the nose cap. The rear end is a floating body. Pressurization of the cylinder was made by compressed air which was led into the hollow shaft.

TABLE 1
Results of Model No. 1. 0.001 in. Skin. Pressure-Bellows Loading. $\bar{\sigma}_{cr_0} = 0.104$ from Eq. 5.

| $\bar{p}$ (cm.Hg.) | $\bar{p}_{B_{cr}}$ (psi) | $P_{cr}$ (lbs.) | $\bar{p}$ | $\bar{\sigma}_{cr}$ | $\Delta\bar{\sigma}_{cr}$ | Picture No. | Remarks |
|---|---|---|---|---|---|---|---|
| 0 | 4 | 4 | 0 | 0.063 | — | Fig. 5 | |
| 0.4 | 5 | 4.5 | 0.0298 | 0.071 | — | | |
| 0.8 | 11.5 | 11.0 | 0.0476 | 0.175 | 0.070 | | |
| 2.0 | 15 | 13.1 | 0.119 | 0.208 | 0.103 | | |
| 3.2 | 17 | 13.8 | 0.190 | 0.219 | 0.114 | | |
| 4.2 | 20 | 15.9 | 0.250 | 0.253 | 0.148 | | |
| 5.2 | 23 | 17.8 | 0.309 | 0.283 | 0.178 | Fig. 6 | (1) |
| 7.0 | 24 | 16.7 | 0.416 | 0.265 | 0.160 | | |
| 7.6 | 25 | 17.1 | 0.451 | 0.272 | 0.167 | | |
| 8.6 | 26 | 16.9 | 0.510 | 0.269 | 0.164 | Fig. 7 | |
| 10.2 | 30 | 19.2 | 0.606 | 0.306 | 0.201 | | (2) |
| 13.2 | 33 | 18.8 | 0.785 | 0.297 | 0.192 | | |
| 15.2 | 36 | 19.6 | 0.903 | 0.312 | 0.207 | | |
| 16.6 | 38 | 20.0 | 0.985 | 0.318 | 0.213 | | |
| 18.0 | 41 | 21.4 | 1.07 | 0.340 | 0.235 | Fig. 8 | (3) |
| 19.8 | 42 | 20.4 | 1.18 | 0.324 | 0.219 | | |
| 21.0 | 45 | 22.0 | 1.25 | 0.350 | 0.245 | | (4) |
| 22.2 | 47 | 22.7 | 1.32 | 0.361 | 0.256 | | |
| 23.2 | 49 | 22.8 | 1.38 | 0.362 | 0.257 | | (5) |
| 24.2 | 49 | 21.6 | 1.44 | 0.344 | 0.239 | | |
| 25.8 | 50 | 21.7 | 1.53 | 0.345 | 0.240 | | |
| 27.6 | 52 | 21.6 | 1.64 | 0.344 | 0.239 | | |
| 28.7 | 56 | 24.5 | 1.71 | 0.390 | 0.285 | | |
| 29.8 | 55 | 22.2 | 1.77 | 0.353 | 0.248 | | (6) |
| 30.4 | 56 | 22.5 | 1.81 | 0.358 | 0.253 | | |
| 31.8 | 59 | 24.0 | 1.89 | 0.382 | 0.277 | Fig. 9 | |
| 32.2 | 60 | 24.6 | 1.91 | 0.392 | 0.287 | | |
| 33.8 | 61 | 23.8 | 2.01 | 0.378 | 0.273 | | |
| 34.8 | 62 | 23.6 | 2.06 | 0.375 | 0.270 | | |
| 33.2 | 60 | 23.5 | 1.98 | 0.374 | 0.269 | | |
| 31.6 | 56 | 21.0 | 1.87 | 0.334 | 0.229 | | |
| 29.6 | 55 | 22.4 | 1.76 | 0.356 | 0.251 | | |
| 27.2 | 53 | 23.3 | 1.62 | 0.371 | 0.266 | | (7) |
| 25.4 | 50 | 22.2 | 1.51 | 0.353 | 0.248 | | |
| 23.4 | 48 | 22.5 | 1.39 | 0.356 | 0.251 | | |
| 21.2 | 46 | 23.0 | 1.26 | 0.366 | 0.261 | | |
| 19.6 | 42 | 20.7 | 1.16 | 0.329 | 0.224 | | |
| 17.0 | 41 | 22.6 | 1.01 | 0.360 | 0.255 | | |
| 15.2 | 38 | 21.8 | 0.90 | 0.346 | 0.241 | | |
| 12.6 | 35 | 21.6 | 0.75 | 0.344 | 0.239 | | |
| 11.0 | 32 | 20.4 | 0.65 | 0.324 | 0.219 | | |
| 9.0 | 26 | 16.4 | 0.53 | 0.261 | 0.156 | | |
| 6.4 | 24 | 18.5 | 0.38 | 0.294 | 0.189 | | |
| 4.2 | 21 | 16.9 | 0.25 | 0.269 | 0.164 | | |

(1) Diamonds 12 by 6 mm. (short dimension was axial).
(2) Diamonds 7 by 3 mm.
(3) Gradually change to rings.
(4) Diamonds 12 by 3 mm.
(5) Diamonds 34 by 3 mm.
(6) Bellows-shaped buckles all around circumference.
(7) Diamonds began to be visible in rings.

TABLE 2
Results of Model No. 5. 0.003 in. Skin. Dead Weight Loading. $\bar{\sigma}_{cr_0} = 0.199$ from Eq. 5.

| $\bar{p}$ (cm. Hg.) | Wt. (lbs.) | $P_{cr}$ | $\bar{p}$ | $\bar{\sigma}_{cr}$ | $\Delta\bar{\sigma}_{cr}$ |
|---|---|---|---|---|---|
| 0 | 36.5 | 81.1 | 0 | 0.143 | — |
| 5.6 | 50 | 97.6 | 0.037 | 0.172 | — |
| 7.6 | 55 | 103.9 | 0.050 | 0.184 | — |
| 9.6 | 60 | 110.1 | 0.063 | 0.195 | — |
| 11.8 | 65 | 116.1 | 0.077 | 0.205 | 0.006 |
| 13.8 | 70 | 122.3 | 0.091 | 0.216 | 0.017 |
| 16.0 | 75 | — | — | Model failed | |

Compressive load was applied to the cylinder by means of four bellows contained in the body to the rear of the cylinder. The rear ends of the four bellows were fixed, and the front ends were free to move. When the bellows were pressurized, they extended and transmitted the force through rigid rods into the rear ring of the cylinder. Nitrogen bottles were used for the pressurization of the bellows.

Strain gages were attached to a 0.002 in. skin and a 0.003 in. skin to measure the strain in the longitudinal direction, with locations as shown in Fig. 1.

## Test Procedure

In the pressure-bellows loading tests, the internal pressure $p$ (compressed air) was measured by a manometer and the bellows pressure $p_B$ (nitrogen) was measured by a pressure gage. The strains were recorded by standard electric strain-gage equipment. Generally, very careful adjustment of the cylinder installation was necessary to avoid initial buckles for the 0.001 in. skin, but for the 0.002 in. skin the installation was quite simple. Since the size of buckle decreased with increasing internal pressure, the buckling test was usually started with some medium value of the internal pressure $p$. For each fixed $p$, the bellows pressure $p_B$ was gradually increased until buckling occurred. The values of $p$ and $p_B$ were then recorded simultaneously. The load was then decreased until the buckles disappeared. The internal pressure was then increased a desired amount and the process repeated. After the maximum allowable internal pressure was reached, downward steps were taken until $p = 0$.

A few records of the strain-load relationship were obtained in the post-buckling range with $p_B$ considerably in excess of the critical buckling value.

In the dead weight testing, the cylinder was first pressurized, then the weight was applied and the internal pressure was allowed to decrease slowly until buckling occurred.

## Experimental Results

Table 1 gives a set of typical experimental results for pressure-bellows loading tests on a 0.001 in. skin. Table 2 gives the typical results for dead weight tests in 0.003 in. skins. These, and other experimental results, are presented also in Figs. 2, 3, and 4.

The occurrence of diamond shaped buckles were usually unmistakable; most of them appeared with a clicking noise. For the 0.001 in. skins, and for one 0.002 in. skin, however, ring shaped buckles with a rather small wave length appeared when the internal pressure, $p$, was sufficiently high. Further increase in compressive load gradually created alternative dimples in these rings which finally developed into a diamond pattern. The diamonds at low values of internal pressure, $p$, were more or less square, those at higher internal pressure were elongated, sometimes with a wave length in the circumferential direction ten times longer than that in the axial direction. At intermediate values of

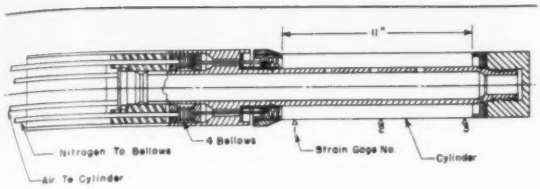


FIG. 1. Test specimen, loading system, and strain-gage positions.

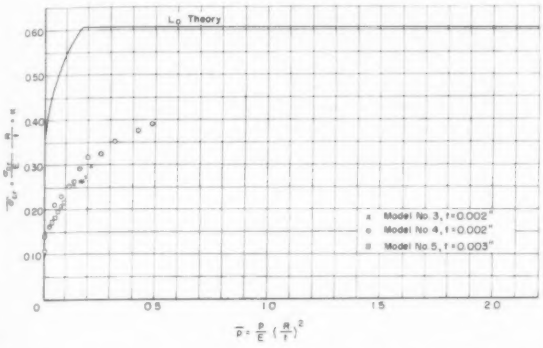


FIG. 2. Experimental results for models with $t = 0.002$ in. and $t = 0.003$ in.

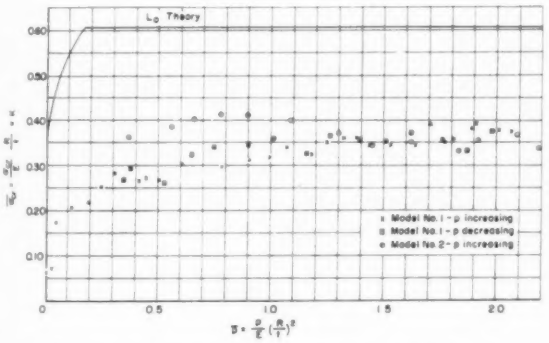


FIG. 3. Experimental results for models with $t = 0.001$ in.

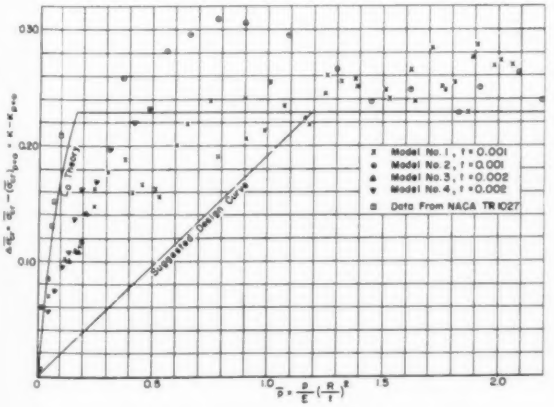


FIG. 4. Incremental buckling stress due to pressure.

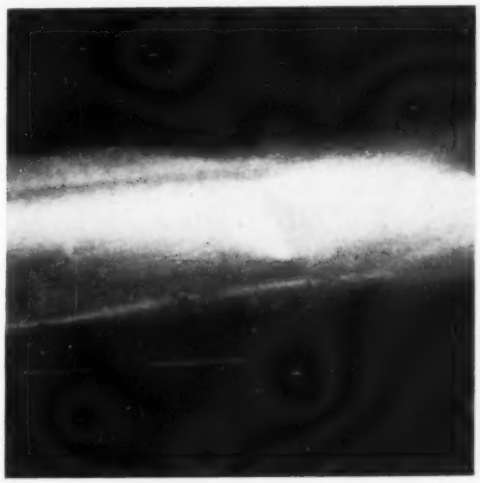

FIG. 5. Buckling pattern at zero internal pressure. Diamond-shaped buckles were isolated. $t = 0.001$ in., $\bar{p} = 0$, $\bar{\sigma}_{cr} = 0.063$.

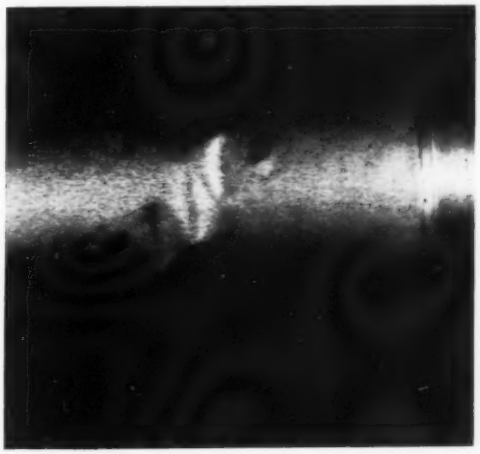

FIG. 6. Buckling pattern at small internal pressure. Note the arrangement of consecutive buckles. $t = 0.001$ in., $\bar{p} = 0.309$, $\bar{\sigma}_{cr} = 0.283$.

FIG. 7. Buckling pattern at intermediate internal pressure. $t = 0.001$ in., $\bar{p} = 0.510$, $\bar{\sigma}_{cr} = 0.269$.

TABLE 3
General Relationships for Data Reduction

Model: length = 11.0 in.
diameter = 3.5 in.
Pressure-Bellows Loading:
(a) Correction for internal pressure:
Area acted upon: O.D. = 3.5 in. I.D. = 2.125 in.
Area = $(\pi/4)(3.5^2 - 2.125^2) = 6.06$ sq.in.
(b) Effective total bellows-area = 1.04 sq.in.
(c) Critical buckling load:
$P_{cr} = 0.14\, p_{Bcr}(\text{psi}) - 6.06 \times 0.1934 \times p\,(\text{cm. Hg.})$

internal pressure the diamond buckles formed a ray running at an angle of approximately 25° with the longitudinal axis. At higher values of $\bar{p}$ the buckles usually occurred over a symmetrical section, including 4 or 5 waves in the axial direction. These changes of buckling pattern were photographed on one model and are presented herein in Figs. 5 through 9.

The ring shaped buckles mentioned above resembled the sinusoidal waves assumed in the classical small-deflection theory. The occurrence of such symmetrical buckles did not represent the ultimate collapse load of the cylinder. Furthermore, their occurrence was very gradual; no critical compressive load could be determined visually. On the other hand, strain gage records did often show a temporary discontinuity in the load-strain relationship. However, it was not possible to correlate this break in the strain records with visual observation of the symmetrical buckles. It must be remembered also that for such thin-walled cylinders the stress level was so low that the experimental scatter in the electric strain gage readings was large.

Figs. 10 and 11 show the typical load-strain curves. It is seen that when a gage was far away from the diamond buckles the load-strain relationship remained nearly linear at the critical regime and in the post-buckling range. Since it was not the purpose of the strain gage measurements to determine the local buckling stress, the recorded value was the overall compressive load.

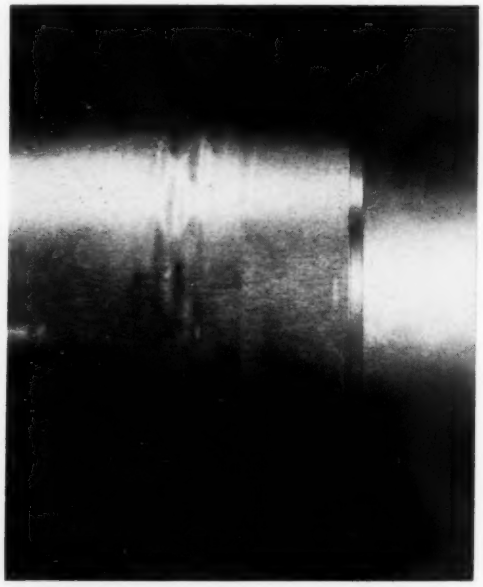

FIG. 8. Buckling pattern at higher intermediate internal pressure. Note elongation of the diamond-shaped buckles. $t = 0.001$ in., $\bar{p} = 1.07$, $\bar{\sigma}_{cr} = 0.340$.

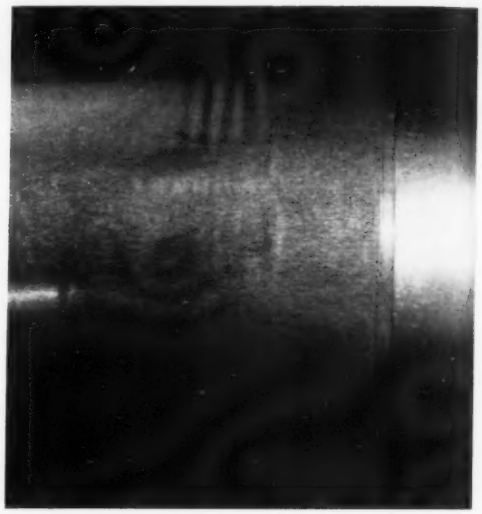

FIG. 9. Buckling pattern at high internal pressure. Bellows-shaped buckles. $t = 0.001$ in., $\bar{p} = 1.89$, $\bar{\sigma}_{cr} = 0.382$.

The results are plotted in terms of the two dimensionless parameters introduced by Lo, Crate, and Schwartz,[3]

$$\bar{\sigma}_{cr} = (\sigma_{cr}/E)(R/t) = P_{cr}/2\pi Et^2 \quad (1)$$

$$\bar{p} = (p/E)(R/t)^2 \quad (2)$$

where $P_{cr}$ is the buckling load and the other terms are as previously defined. Data reduction information are given in Table 3.

## BUCKLING STRESS WITHOUT INTERNAL PRESSURE

Previous experimental data have shown that the value of the critical buckling stress without internal pressure can be expressed as

$$\sigma_{cr_0} = K_t E(t/R) \quad (3)$$

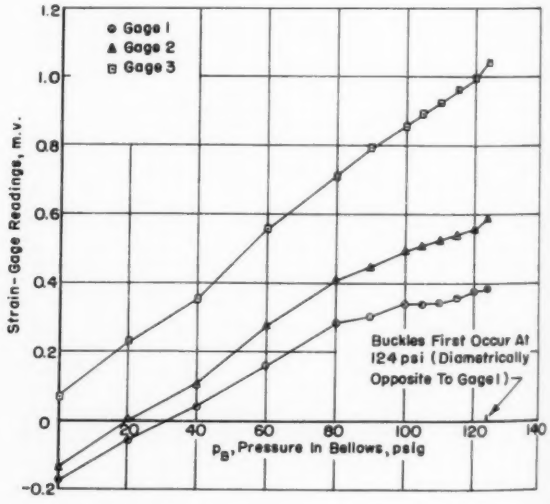


FIG. 10. Typical load-strain curves for 0.002 in. skin. Internal pressure approximately 5.4 psi.

where the classical small deflection theories give $K_0 \approx 0.6$. However, a large number of tests on thin-walled cylinders show that the experimental value of $K_0$ is usually lower than 0.6 and that it decreases with increasing $R/t$. The reasons for this have been discussed by Donnell and others but it is sufficient for our purposes to take the experimental data for cylinders having various geometric parameters and establish an empirical value for $K_0$ which is compatible with common manufacturing processes in making such cylindrical structures. This was done by Kanemitsu and Nojima[5] and the empirical equation which they proposed is

$$\sigma_{cr_0}/E = 9(t/R)^{1.6} + 0.16(t/L)^{1.3} \quad (4)$$

where $L$ is the length of the cylinder.

If this is put into the usual form—namely, Eq. (3)—we find a relationship between $K_0$ and the cylinder dimensions as follows:

$$K_0 = (R/t)[9(t/R)^{1.6} + 0.16(t/L)^{1.3}] = (\sigma_{cr_0}/E)(R/t) = \bar{\sigma}_{cr_0} \quad (5)$$

showing a decrease in $K_0$ as $R/t$ increases for any given value of $L$. A typical set of curves plotted for various values of $R/t$ and $L/R$ is given in Fig. 12.

## Comparison of Experimental Data With Lo's Analysis

The data from the current tests have been plotted in Figs. 2 and 4, inclusive. As shown on these curves, Lo's theory gives a curve that starts at $\bar{\sigma}_{cr} = 0.376$ for $\bar{p} = 0$ and rises until it reaches $\bar{\sigma}_{cr} = 0.605$ at $\bar{p} = 0.169$. For all higher values of $\bar{p}$ the value of $\bar{\sigma}_{cr}$ remains constant at 0.605. Flügge's theory would be a horizontal line at $\bar{\sigma}_{cr} = 0.605$ at all values of $\bar{p}$.

It will be noticed that all the experimental values of $\bar{\sigma}_{cr}$ are much lower than the predicted values from theory. However, the general trend of variation of $\bar{\sigma}_{cr}$ with pressure is as predicted by Lo—i.e., the tendency is for $\bar{\sigma}_{cr}$ to increase with increasing $\bar{p}$ and to reach a constant value at higher values of $\bar{p}$.

In reference 3, it is recommended that the increment of $\bar{\sigma}_{cr}$, the $\Delta\bar{\sigma}_{cr}$, be plotted against $\bar{p}$, where

$$\Delta\bar{\sigma}_{cr} = \bar{\sigma}_{cr} - \bar{\sigma}_{cr_0} \quad (6)$$

and $\bar{\sigma}_{cr_0}$ is the value of $\bar{\sigma}_{cr}$ at zero pressure. When this is done in the above reference, good agreement is shown with the theoretically predicted results. This same procedure has been carried out for the present tests in Fig. 4. Since the value of $\bar{\sigma}_{cr}$ at $p = 0$ was difficult to obtain with any degree of accuracy, the value given by Eq. (5) was used for this initial value. As can be seen from Fig. 4, this procedure gives reasonable agreement, at least with the trends predicted by Lo's theory and it should, therefore, be possible to use this method for design of such cylinders. The test data for the dead weight tests of the 0.003 in. thick cylinders all appear to be low and this is probably due to not fully developing the true buckling load in these cylinders. The values given for $\bar{\sigma}_{cr}$ in Table 2 correspond to the first visible

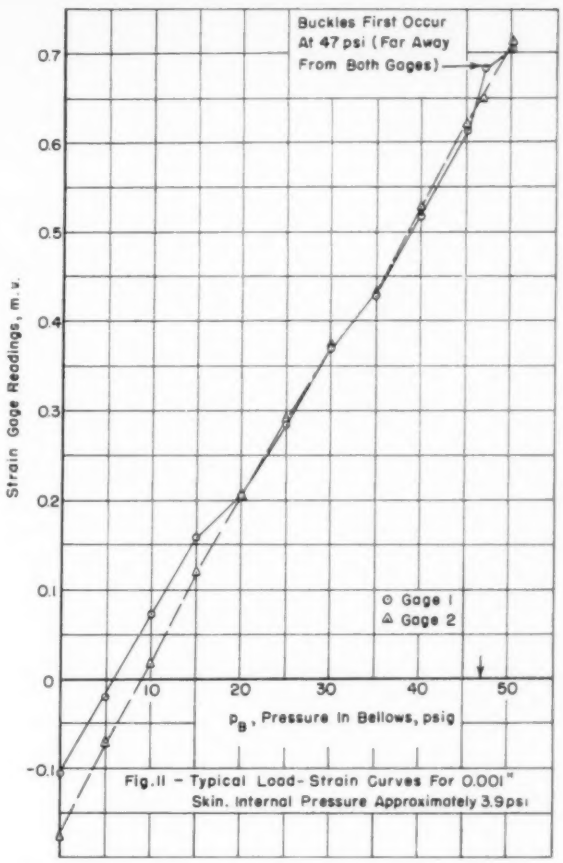


Fig. 11 – Typical Load-Strain Curves For 0.001" Skin. Internal Pressure Approximately 3.9 psi

enlargement of initial dimples in the skin and were probably considerably lower than the true buckling stress. This ultra-conservative technique was used to avoid complete collapse of the cylinder under dead weight loading.

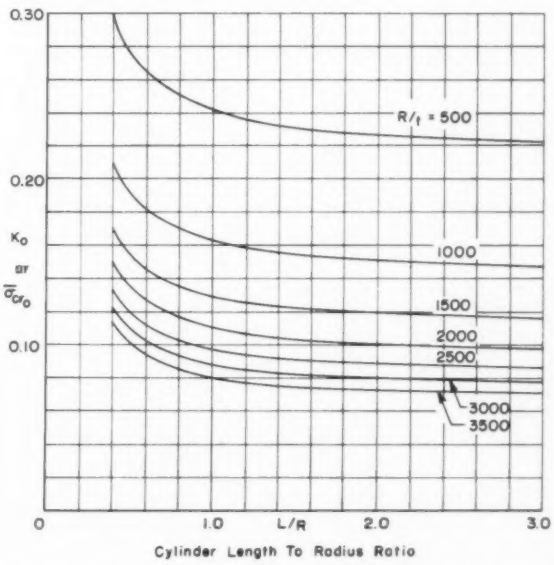


FIG. 12. Values of $K_0 = \bar{\sigma}_{cr_0}$ in the equation $\bar{\sigma}_{cr} = K_0 E(t/R)$. $K_0 = 9(t/R)^{0.6} + 0.16(R/L)^{1.3}(t/R)^{0.3} = \bar{\sigma}_{cr_0}$

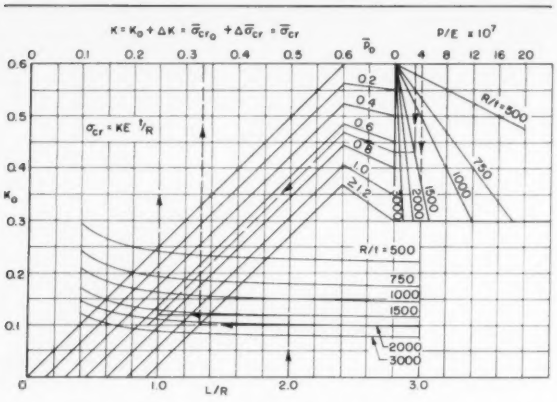


FIG. 13. A nomogram.

## PROPOSED DESIGN METHOD

For thin-walled cylinders subjected to both internal pressure and axial compressive loads, the following design technique is recommended:

(1) Determine the value of $\bar{\sigma}_{cr_0}$ or $K_0$ for zero internal pressure by using Eq. (5) (see Fig. 12).

(2) For values of $\bar{p}$ between 0 and 1.20, use a linear increase in $\Delta\bar{\sigma}_{cr}$ from zero at $\bar{p} = 0$ to $\Delta\bar{\sigma}_{cr} = 0.229$ at $\bar{p} = 1.20$. For all values of $\bar{p} > 1.20$ use $\Delta\bar{\sigma}_{cr} = 0.229$.

On the basis of currently available information, the above design procedure should give a conservative (but not ultra-conservative) value for the buckling stress of such cylinders.

Using the above procedure, Fig. 13 has been drawn. This sets up the method in nomographic form for rapid use by the designer. Its use will be illustrated by the two examples below.

### *Example 1*

Consider an unstiffened cylindrical section which has the following dimensions and properties:

$$R = 30 \text{ in.} \quad L = 60 \text{ in.} \quad t = 0.020 \text{ in.}$$
$$E = 10^7 \text{ psi} \quad p = 3 \text{ psi}$$

from which

$$R/t = 1{,}500 \quad L/R = 2.0 \quad p/E = 3 \times 10^{-7}$$

Entering the right-hand portion of Fig. 13 with $p/E = 3 \times 10^{-7}$ and dropping to the $R/t = 1{,}500$ line we obtain $\bar{p} = 0.675$. This value is transferred to the left-hand side of the curve. Then, going from $L/R = 2.0$ vertically to the $R/t = 1{,}500$ curve, then horizontally, we intersect the $\bar{p} = 0.675$ line at a value of $K = 0.250$. If it is desired, the value of $K_0$ can also be found from the extreme left-hand scale which gives $K_0 = 0.119$, indicating that the $\Delta K$ due to pressure is equal to 0.131.

The critical axial buckling stress is, therefore,

$$\sigma_{cr} = 0.250 \times 10^7 \times (1/1{,}500) = 1{,}667 \text{ psi}$$

### *Example 2*

Consider the following cylinder:

$$R = 30 \text{ in.} \quad L = 60 \text{ in.} \quad t = 0.015 \text{ in.}$$
$$E = 3 \times 10^7 \text{ psi} \quad p = 12 \text{ psi}$$

this gives

$$R/t = 2{,}000 \quad L/R = 2.0 \quad p/E = 4 \times 10^{-7}$$

From the right-hand side of Fig. 13 we see that the intersection of the $R/t = 2{,}000$ line with the $p/E = 4 \times 10^{-7}$ line would occur at a value of $\bar{p} > 1.20$. Therefore, the $\bar{p} = 1.20$ line is used for the rest of the solution. Going from $L/R = 2.0$ to $R/t = 2{,}000$, then horizontally to $\bar{p} = 1.20$, we find that $K_0 = 0.100$ and $K = 0.328$ giving a value of $\Delta K = 0.228$ due to pressure.

The design critical buckling stress is

$$\sigma_{cr} = 0.328 \times 3 \times 10^7 \times (1/2{,}000) = 4{,}920 \text{ psi}$$

Any more accurate design method must necessarily await the development of a more complete theoretical treatment of the pressurized cylinder problem.

## REFERENCES

[1] Prescott, J., *Applied Elasticity*, 1924. Reprinted by Dover Publications, New York, 1946.

[2] Flügge, W., *Die Stabilität der Kreiszylinderschale*, Ing.-Archiv, III, 463–506, December, 1932.

[3] Lo, H., Crate, H., and Schwartz, E. B., *Buckling of Thin-Walled Cylinder under Axial Compression and Internal Pressure*, NACA Report 1027, 1951.

[4] Von Kármán, T., and Tsien, H. S., *The Buckling of Thin Cylindrical Shells under Axial Compression*, Journal of the Aeronautical Sciences, Vol. 8, pp. 303–312, June, 1941.

[5] Kanemitsu, S., and Nojima, H., *Axial Compression Tests of Thin Circular Cylinders*, M. S. Thesis, Guggenheim Aeronautical Laboratory, California Institute of Technology, 1939.

An Authorized Binding for
Journal of the Aeronautical Sciences

Arrangements have been made by the Institute of the Aeronautical Sciences for members and subscribers to have their Journals bound carefully and economically. Simply write for details to:

Publishers' Authorized Bindery Service

5809 West Division St. Chicago 51, Ill.

# The Aerodynamic Variable Nozzle†

A. I. MARTIN*

*The Bristol Aeroplane Company, Limited*

SUMMARY

If a thin layer of high-pressure air is injected into the main stream of a nozzle, then two types of flow are possible. Either the air jet will mix with the main stream or it will be separated from the main stream by means of a vortex sheet. By using the theory of one-dimensional gas flow, this paper gives first-order approximations to the aerodynamic quantities relating to such a nozzle in the case where no heat exchange occurs between the jet and main stream. Both types of flow are worked out, and some of the results compared with experiment.

SYMBOLS

Capital letters refer to main-stream quantities
Small letters refer to secondary flow (jet-current)
Subscript 0 denotes stagnation values
Subscript 1 denotes upstream values
Subscript 2 denotes downstream values

$A_1$ = initial radius of flow
$A_2$ = final radius of flow (total flow in mixing process)
$b_1$ = initial thickness of jet flow (small) *just* before contact with main stream
$b_2$ = final thickness of jet flow (small). Void in mixing process
$F$ = total thrust
$K$ = an expression involving Mach Numbers given by Eq. (4.3)
$\mathfrak{M}$ = $w/W$
$M$ = Mach Number referred to sonic velocity at stagnation
$M_1$ = initial Mach Number of main stream
$M_2$ = final Mach Number of main stream. Also final Mach Number of jet in mixing process
$m_1$ = Mach Number of jet *just* before contact with main stream
$m_2$ = Mach Number of jet way downstream. Void in mixing process
$P$ = pressure of main stream at $M$
$P_0$ = pressure of main stream at stagnation
$p_0$ = pressure of jet at stagnation
$R$ = characteristic gas constant
$T$ = absolute temperature of main stream at M
$T_0$ = absolute temperature of main stream at stagnation
$t_0$ = absolute temperature of jet at stagnation
$W$ = mass flow of main stream
$W_N$ = mass flow of main stream when no jet current is admitted
$w$ = mass flow of jet
$x$ = $W_N/W$
$\beta$ = $b_1/A_1$
$\gamma$ = ratio of specific heats (approximately 1.4 for air)
$\mu$ = local Mach Number
$\Pi$ = final or atmospheric pressure
$\mathrm{P}$ = density of main stream at $M$
$\mathrm{P}_0$ = density of main stream at stagnation
$\rho_0$ = density of jet at stagnation
$\phi$ = "angle of inclination" of initial direction of motion of jet to centerline of main stream

Equation of isentropic law; $P\mathrm{P}^{-\gamma} = P_0\mathrm{P}_0{}^{-\gamma}$
Equation of perfect state; $P^{-1}\mathrm{P}T = P_0{}^{-1}\mathrm{P}_0T_0$

Received August 9, 1956.

† This work was carried out at The Bristol Aeroplane Company in connection with the Olympus engine. The author wishes to take this opportunity to express his gratitude to Dr. S. G. Hooker.

* Formerly, Senior Engineer. Now, Aerodynamicist, Weapon Research Division, A. V. Roe & Company, Limited.

## (1) INTRODUCTION

A METHOD of obtaining a nozzle with a variable throat is to inject secondary air into the main stream. If the air jet and main stream belong to the same isentropic line then no heat exchange takes place between the two flows. This will be the case, for example, if the secondary air is obtained from the main stream by isentropic compression. Such a nozzle is of use in controlling the performance of a jet engine at different operating conditions. The secondary air may be bled from the high-pressure stage of the compressor and can be regarded as being injected into the main stream through a circumferential passageway situated near the throat of the nozzle. By varying its mass flow, reasonable control may be obtained for the thrust and flow in the main stream.

The problem is one on the "mixing" of two fast air streams, and is considered here from the point of view of one-dimensional gas analysis. A similar procedure may be expected to give results for the injection of atomized fuel into a main air stream.

## (2) SIMPLIFICATION

The general problem of the injection of a jet of air into a main stream would be very difficult to discuss in a complete manner. There are several possible types of distinct flow for any given arrangement of the boundary walls. If the total heads of the main stream and jet current are initially equal, and if the fluid is incompressible, then the flow could follow either of two classical arrangements in hydrodynamics. One side of the jet current being divided from the main flow by a certain stream surface, the other side might or might not separate from the walls of the channel. In the case of two-dimensional motion, these two arrangements have been discussed in reference 1 by means of the Helmholtz-Kirchhoff method of conformal transformation. If the total heads are not initially equal then either the jet is separated from the main flow by means of a vortex sheet or it will mix with the main flow in some turbulent fashion.‡ Most likely, in practice, both these effects will take place in this order as we follow a particle of fluid during its motion through the secondary flow.

‡ This mixing may have unsteady, rotational, and viscous effects. It seems more likely to take place by turbulence than by vortex diffusion arising from viscosity.

When the order of magnitude of the total head in the jet is large in comparison with that in the main stream, it may be anticipated that approximately correct results will be obtained by assuming the sole existence of a vortex sheet without turbulent mixing. We then have separate equations of continuity for the two flows, and Bernoulli's law may be supposed to hold along any stream line. However, when the two total heads are of about the same order of magnitude,* we might expect approximately correct results to be obtained by assuming that early turbulent mixing quickly gives rise to the particles of fluid from the jet being completely diffused into the main stream and thereby yielding constant aerodynamic quantities over a cross section. This will be true for the average values of aerodynamic quantities even if the motion itself is not entirely steady. For this case, we have a single equation of continuity expressing the fact that the final stream is derived from that of the main stream and jet current, and Bernoulli's law will not hold along the jet current although it may be supposed to hold along the center line of the main stream. Such simplifications give results which agree fairly well with actual fact.

### (3) Approximate Equations

It is found to be convenient to work in terms of Mach Numbers referred to the velocity of sound at stagnation.† Thus, Bernoulli's law for isentropic flow of a perfect gas is given by the equations

$$\left.\begin{aligned} P &= P_0\{1 - (1/2)(\gamma - 1)M^2\}^{\gamma/(\gamma-1)} \\ \mathrm{P} &= \mathrm{P}_0\{1 - (1/2)(\gamma - 1)M^2\}^{1/(\gamma-1)} \\ T &= T_0\{1 - (1/2)(\gamma - 1)M^2\} \end{aligned}\right\} \quad (3.1)$$

For the vortex sheet case, Eqs. (3.1) will hold along any streamline, but for the mixing process they will fail except along the centerline of the nozzle.

In order to simplify the work still further and yet start from a view as elementary as possible, it will be assumed that continuity holds at the initial *points of contact* of the jet and main stream (see points C and D in Figs. 1 and 2), and that the latter is instantaneously at rest at these points. Thus, we suppose the entry pressure and temperature of the jet to be the same as the corresponding stagnation values in the main stream. This pressure relation is similar to that which occurs in well-known classical models in hydrodynamics. Continuity of temperature avoids heat exchange, and is equivalent to saying that the two flows belong to the same isentropic line. It then follows that we also have continuity of density whenever the two characteristic gas constants are equal. Admitting to such argument, we have the equations

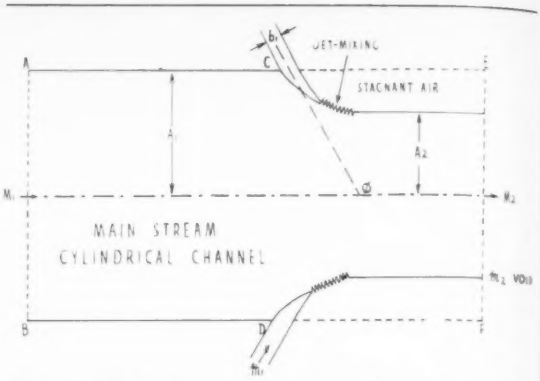


FIG. 1. Mixing process—final flow consists of main stream and jet mixed together so that aerodynamic quantities are constant across circular cross section of radius $A_2$.

$$\left.\begin{aligned} p_0\{1 - (1/2)(\gamma - 1)m_1^2\}^{\gamma/(\gamma-1)} &= P_0 \\ \rho_0\{1 - (1/2)(\gamma - 1)m_1^2\}^{1/(\gamma-1)} &= \mathrm{P}_0 \\ t_0\{1 - (1/2)(\gamma - 1)m_1^2\} &= T_0 \end{aligned}\right\} \quad (3.2)$$

It is true that these equations are restrictive and, perhaps, unrealistic. They represent an ideal case from which we propose to start. It is not suggested that they are satisfied in an actual engine nozzle, but that the restriction they impose leads to an approximately correct choice of dependence of variables for such a nozzle.

We next write down equations of continuity and overall momentum for the two types of flow. The thickness of flow of the jet *just* before it comes in contact with the main stream is supposed to be small.

#### (a) *Mixing Process*

There is a single equation of continuity which may be set in the form

$$(A_2/A_1)^2 M_2\{1 - (1/2)(\gamma - 1)M_2^2\}^{1/(\gamma-1)} = M_1\{1 - (1/2)(\gamma - 1)M_1^2\}^{1/(\gamma-1)} + 2\beta m_1\{1 - (1/2)(\gamma - 1)m_1^2\}^{-(1/2)} \quad (3.3)$$

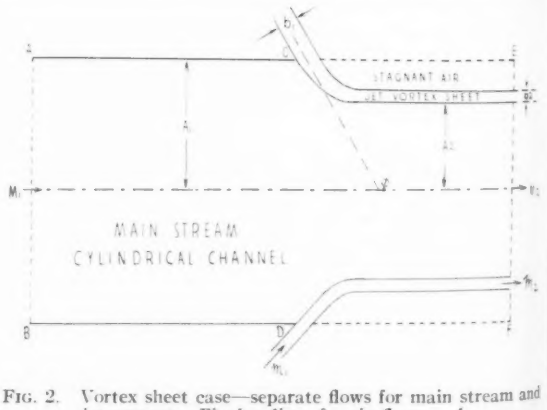


FIG. 2. Vortex sheet case—separate flows for main stream and jet current. Final radius of main flow = $A_2$.

* The total head in the jet is in this case somewhat larger than that in the main stream in order to ensure that the jet completely fills its own passageway.

† This makes the final equations slightly simpler than the corresponding ones involving local Mach Numbers. In any case, a Mach Number $M$ referred to the velocity of sound at stagnation is related to the local Mach Number $\mu$ by the formula

$$\{1 - (1/2)(\gamma - 1)M^2\}\{1 + (1/2)(\gamma + 1)\mu^2\} = 1$$

To carry out numerical computations it is convenient to make this transformation and use standard flow tables (see reference 4, Table 14, and reference 5, Table I.1).

In the derivation of this equation, we may obtain the ratio $p_0\rho_0/P_0\rho_0$ of two sonic velocities by using the first and second equations in (3.2). The two terms on the right-hand side are obtained from the initial rates of flow of the main stream and jet, densities being expressed in terms of Mach Numbers by equations of the same type as the second equation in (3.1), and the area of the jet passageway being taken as $2\pi.1_1b_1$. The left-hand side represents the final total rate of flow.*

Consideration of the whole fluid contained within the cylinder ABEF (see Fig. 1) yields the equation for the rate of change of overall momentum. It may be set in the form

$$\begin{aligned}\{1-(1/2)(\gamma-1)M_1^2\}^{\gamma/(\gamma-1)}+\\ \gamma M_1^2\{1-(1/2)(\gamma-1)M_1^2\}^{1/(\gamma-1)}-\\ 2\beta\gamma m_1^2\{1-(1/2)(\gamma-1)m_1^2\}^{-1}\cos\phi=\\ \{1-(1/2)(\gamma-1)M_2^2\}^{\gamma/(\gamma-1)}+\\ \gamma(A_2/A_1)^2M_2^2\{1-(1/2)(\gamma-1)M_2^2\}^{1/(\gamma-1)}\end{aligned}\tag{3.4}$$

The first terms on the two sides are derived from pressure forces, the remaining terms come from fluxes of momentum. For the first term on the right, an appeal has been made to Bernoulli's law applied along the whole centerline of the main stream—this forming the only streamline passing through the "mixing region" along which we may suppose the law to hold. Use has also been made of the first equation in (3.2).

The important point to be observed in the above procedure is that we have not supposed a Bernoulli law to hold along the jet current after it comes in contact with the main stream. Indeed, the jet mixing may well be unsteady and rotational provided that it does not too much upset that part of the main stream in the neighborhood of the centerline.

Given any two Mach Numbers, Eqs. (3.3) and (3.4) enable calculations to be made for the third Mach Number and the ratio of contraction $A_2/A_1$.

### (b) *Vortex Sheet Case*

There are now two equations of continuity, one for the main stream and one for the jet, given by

$$\begin{aligned}M_1\{1-(1/2)(\gamma-1)M_1^2\}^{1/(\gamma-1)}=\\ (A_2/A_1)^2M_2\{1-(1/2)(\gamma-1)M_2^2\}^{1/(\gamma-1)}\end{aligned}\tag{3.5}$$

and

$$\begin{aligned}m_1\{1-(1/2)(\gamma-1)m_1^2\}^{1/(\gamma-1)}=\\ (A_2b_2/A_1b_1)m_2\{1-(1/2)(\gamma-1)m_2^2\}^{1/(\gamma-1)}\end{aligned}\tag{3.6}$$

Continuity of pressure far downstream also gives

$$\begin{aligned}p_0\{1-(1/2)(\gamma-1)m_2^2\}^{\gamma/(\gamma-1)}=\\ P_0\{1-(1/2)(\gamma-1)M_2^2\}^{\gamma/(\gamma-1)}=\Pi\end{aligned}\tag{3.7}$$

It is here that we have used Bernoulli's law along the jet current.

From Eqs. (3.2) and (3.7),

$$\left.\begin{aligned}1-(1/2)(\gamma-1)m_2^2=\{1-(1/2)(\gamma-1)m_1^2\}\times\\ \{1-(1/2)(\gamma-1)M_2^2\}\end{aligned}\right\}\tag{3.8}$$

or

$$m_2^2=m_1^2+M_2^2\{1-(1/2)(\gamma-1)m_1^2\}$$

The equation of overall momentum may be set in the form

$$\begin{aligned}\{1-(1/2)(\gamma-1)M_1^2\}^{\gamma/(\gamma-1)}+\gamma M_1^2\{1-(1/2)\times\\ (\gamma-1)M_1^2\}^{1/(\gamma-1)}-2\beta\gamma m_1^2\{1-(1/2)(\gamma-1)\times\\ (\gamma-1)m_1^2\}^{-1}\cos\phi=\{1-(1/2)(\gamma-1)\times\\ M_2^2\}^{\gamma/(\gamma-1)}+\gamma M_1M_2\{1-(1/2)(\gamma-1)\times\\ M_1^2\}^{1/(\gamma-1)}+2\beta\gamma m_1m_2\{1-(1/2)\times\\ (\gamma-1)m_1^2\}^{-1}\end{aligned}\tag{3.9}$$

Several terms in this equation are seen to be of the same type as corresponding terms in Eq. (3.4). By Eq. (3.5), the second term on the right of Eq. (3.9) is of the same type as that on the right of Eq. (3.4). The additional term in Eq. (3.9) is derived from the outward flux of momentum of the jet current. The equation is most easily obtained by considering the whole fluid in the cylinder ABEF (see Fig. 2), and using Eqs. (3.1), (3.2), (3.5), (3.6), and (3.7).

Given any two of the four Mach Numbers, Eqs. (3.8) and (3.9) enable calculations to be made for the remaining two. The ratio of contraction is then given by Eq. (3.5).

Some may prefer to obtain the final set of equations by starting out from assumptions other than those contained in Eqs. (3.2), but then the latter may be inferred by working backwards. It is to be realized that Eqs. (3.2) are only strictly supposed to hold along a circumference of points, and in an ideal case. Values at particular points can only correctly be taken as average values at points far up or downstream. If we wished to allow for a "relatively large" difference in entry temperatures of the jet and main stream, (heat exchange), then the final results would contain an additional independent variable.

## (4) Mass Flow Characteristics of the Jet

The mass flow of the jet is

$$w=2\pi.1_1b_1\sqrt{\gamma p_0\rho_0}\cdot m_1\{1-(1/2)(\gamma-1)m_1^2\}^{1/(\gamma-1)}$$

Hence, using $p_0^{-1}\rho_0t_0=$ a constant $R$, we have†

$$\begin{aligned}w\sqrt{t_0}/p_0=2\pi.1_1b_1\sqrt{\gamma/R}\cdot m_1\{1-(1/2)\times\\ (\gamma-1)m_1^2\}^{1/(\gamma-1)}\end{aligned}\tag{4.1}$$

Also, by the first equation in (3.2),

$$p_0/\Pi=(P_0/\Pi)\{1-(1/2)(\gamma-1)m_1^2\}^{-[\gamma/(\gamma-1)]}\tag{4.2}$$

These two equations hold either for the mixing process or the vortex sheet case. Given the nozzle pressure

* One of the editorial reviewers has pointed out that Eq. (3.3) assumes that the average stagnation pressure and temperature of the final mixed stream are the same as for the initial main stream, and that this is not strictly true but probably introduces a negligible error. The author admits that he has considered variation along particular stream lines and then extended the results to average values over the cross sections far up or downstream.

† Here, $p_0$ is in absolute units. Engineers' units have been used for plotting Figs. 3, 4, and 5.

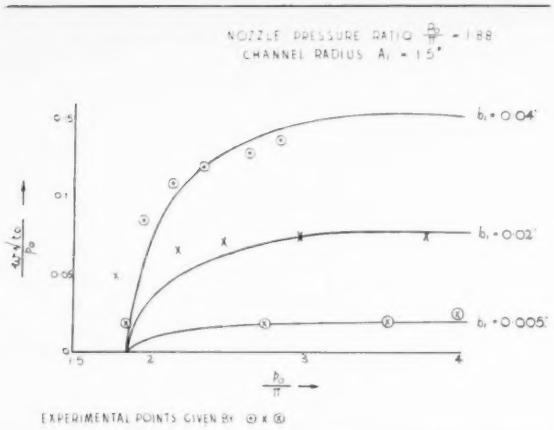


FIG. 3. Jet mass flow characteristics—comparison between theory and experiment. $w$ = jet mass flow, lbs./sec.; $p_0$ = jet pressure at stagnation, lbs./in.²; $t_0$ = jet temperature at stagnation, °C. abs.

ratio $P_0/\Pi$, they enable graphs* to be plotted which show the relationship between $w\sqrt{t_0}/p_0$ and $p_0/\Pi$ (see Fig. 3). The elimination of the parameter $m_1$ may be carried out by using well-known aerodynamic curves, or standard flow tables. Fig. 3 shows comparison between theory and experiment in the case when $P_0/\Pi = 1.88$, $A_1 = 1.5$ in., $b_1 = 0.005$ in., 0.02 in., and 0.04 in. In experiments $p_0$ is taken as jet entry pressure, the fair agreement shows that in the pressure equation in (3.2) $p_0$ may be taken as an approximately correct average value over the jet cross section in the case of thin jet layers. It will be noticed that as the stagnation pressure in the jet approaches that in the main stream the experimental and theoretical results tend to disagree. This is to be expected since the jet will then start to "break away" from its boundary walls, no allowance being made in the theory for this effect.

For slow subsonic or incompressible flow the right-hand sides of Eqs. (4.1) and (4.2) may be expanded by the binomial theorem, and powers of $m_1$ higher than two neglected. We then obtain the parabolic law

$$p_0 = P_0\{1 + (R/8\pi^2 A_1^2 b_1^2)\ (w\sqrt{t_0}/p_0)^2\}$$

## (5) Relationship Between the Jet and Main Stream Mass Flows

The mass flow of the main stream is

$$W = \pi A_1^2 \sqrt{\gamma P_0 \rho_0} \cdot M_1\{1 - (1/2)\ (\gamma - 1)M_1^2\}^{1/(\gamma-1)}$$

Let $W_N$ be the mass flow in the main stream when *no* jet is admitted, the reservoir and exit conditions remaining the same—i.e., $P_0$, $\rho_0$, $T_0$, and $\Pi$ have the same values for $W_N$ as for $W$. Bernoulli's law applied along the centerline of the channel shows that the Mach Number at exit is unaltered. Hence,

$$W_N = \pi A_1^2 \sqrt{\gamma P_0 \rho_0} \cdot M_2\{1 - (1/2)\ (\gamma - 1)M_2^2\}^{1/(\gamma-1)}$$

The mass flow $w$ of the jet has already been given in the previous section. Let $\mathfrak{M} = w/W$, and $x = W_N/W$. Then, by the first two equations in (3.2), we have

$$\left.\begin{aligned} \mathfrak{M} &= 2\beta\, \frac{m_1\{1 - (1/2)\ (\gamma - 1)m_1^2\}^{-(1/2)}}{M_1\{1 - (1/2)\ (\gamma - 1)M_1^2\}^{1/(\gamma-1)}} \\ \text{and} \\ x &= \frac{M_2\{1 - (1/2)\ (\gamma - 1)M_2^2\}^{1/(\gamma-1)}}{M_1\{1 - (1/2)\ (\gamma - 1)M_1^2\}^{1/(\gamma-1)}} \end{aligned}\right\} \quad (5.1)$$

The relation between $\mathfrak{M}$ and $x$ can then be determined from Eqs. (3.3) and (3.4), or Eqs. (3.8) and (3.9).

### (a) *Mixing Process*

We have, from Eqs. (3.3) and (3.4), the ratio of contraction $A_2/A_1 = \sqrt{(1 + \mathfrak{M})/x}$. Substitution of this equation, together with those of Eqs. (5.1), in Eq. (3.4), yields

$$\begin{aligned} \{1 - (1/2)\ (\gamma - 1)M_1^2\}^{\gamma/(\gamma-1)} + \gamma M_1^2\{1 - (1/2) \times \\ (\gamma - 1)M_1^2\}^{1/(\gamma-1)} - (\gamma \cos\phi/2\beta) \cdot (\mathfrak{M}^2/x^2) \times \\ M_2^2\{1 - (1/2)\ (\gamma - 1)M_2^2\}^{2/(\gamma-1)} = \{1 - (1/2) \times \\ (\gamma - 1)M_2^2\}^{\gamma/(\gamma-1)} + \gamma \cdot [(1 + \mathfrak{M})/x] \cdot M_2^2\{1 - (1/2) \times \\ (\gamma - 1)M_2^2\}^{1/(\gamma-1)} \end{aligned}$$

This is a quadratic equation for $\mathfrak{M}$, the appropriate root being given by

$$\mathfrak{M} = \{1 - (1/2)\ (\gamma - 1)M_2^2\}^{-[1/(\gamma-1)]} \times \frac{\sqrt{\{x^2 + [(\cos\phi)/\beta]K^2\}} - x}{[(\cos\phi)/\beta]} \quad (5.2)$$

where

$$\begin{aligned} K = \sqrt{2/\gamma} \cdot (x/M_2)\ [\{1 - (1/2)\ (\gamma - 1)M_1^2\}^{\gamma/(\gamma-1)} - \\ \{1 - (1/2)\ (\gamma - 1)M_2^2\}^{\gamma/(\gamma-1)} - \gamma M_1 \times \\ (M_2 - M_1)\{1 - (1/2)\ (\gamma - 1)M_1^2\}^{1/(\gamma-1)}]^{1/2} \end{aligned} \quad (5.3)$$

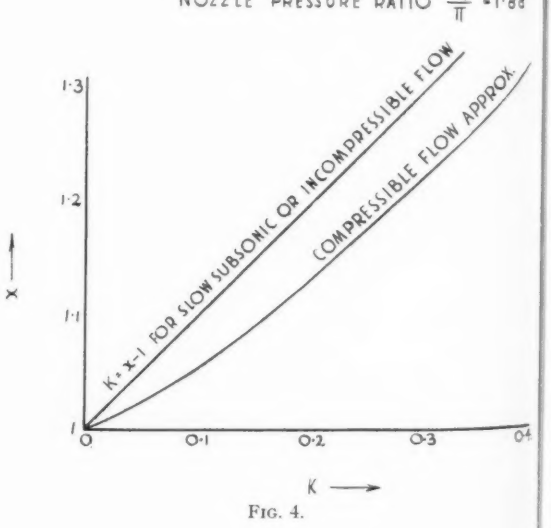


FIG. 4.

* For the experimental results, the author is grateful to B. Blackwell of the Performance and Aerodynamics Department of the Bristol Aeroplane Company.

With the pressure ratio approximately equal to 1.88, there is, of course, sonic velocity at the throat of the nozzle.

In obtaining the expression for $K$ use has again been made of the second equation in (5.1).

Given the nozzle pressure ratio $P_2/\Pi$, $M_2$ is obtained from (3.7). The second equation in (5.1) then gives $M_1$ in terms of $x$. Thus (5.3) determines $K$ as a function of $x$. For the case when $P_0/\Pi = 1.88$, the corresponding curve is shown in Fig. 4.

For slow subsonic or incompressible flow $M_1 = x^{-1}M_2$, $K = x - 1$ and the relation between $\mathfrak{M}$ and $x$ is independent of the stagnation pressure $P_0$.

### (b) *Vortex Sheet Case*

Eq. (3.5) shows that the ratio of contraction is now $A_2/A_1 = 1/\sqrt{x}$. To obtain the relation between $\mathfrak{M}$ and $x$, let $m_1\{1 - (1/2)(\gamma - 1)m_1^2\}^{-(1/2)} = M_2\nu_1$. Then Eqs. (3.8) and (3.9) are equivalent to $(m_2/m_1)^2 = (\nu_1^2 + 1)/\nu_1^2$, and $(K/x)^2 = 4\beta\nu_1^2(m_2/m_1 + \cos\phi)$ where $K$ is again given by (5.3). Elimination of $m_2/m_1$ yields an equation which can be solved for $\nu_1$, $\mathfrak{M}$ then being obtained by dividing the first equation in (5.1) by the second. The final result is

$$\mathfrak{M} = \{1 - (1/2)(\gamma - 1)M_2^2\}^{-[1/(\gamma-1)]} \cdot (2^{1/2} \cdot \beta \cdot x/\sin\phi) \times \sqrt{[1 + (K^2/\beta x^2)\cos\phi + (K^4/4\beta^2x^4)]^{1/2} - 1 - (K^2/2\beta x^2)\cos\phi} \quad (5.4)$$

Fig. 5 compares certain results from Eqs. (5.2) and (5.4) with values obtained from experiment on a nozzle having $A_1 = 1.5$ in., $b_1 = 0.03$ in. and $\phi = 70°$, the nozzle pressure ratio again being 1.88.

For fast jet injection, $\nu_1$ will be large, and hence so also will $K/x$. In this case (5.4) reduces to

$$\mathfrak{M} = \{1 - (1/2)(\gamma - 1)M_2^2\}^{-[1/(\gamma-1)]} \times \sqrt{\beta/(1 + \cos\phi)} \cdot K$$

For incompressible flow this further reduces to

$$x - 1 = f \cdot \mathfrak{M} \quad (5.5)$$

where $f = \sqrt{(1 + \cos\phi)/\beta}$ is constant for a given nozzle.* Even for compressible flow Fig. 5 shows that $x$ and $\mathfrak{M}$ are very nearly related by a linear equation of the type (5.5).

## (6) Failure of Mixing Process

If $\phi$ is an obtuse angle the equation (5.2) becomes imaginary whenever $x$ exceeds the root of the equation $x^2 + K^2\cos\phi/\beta = 0$. The corresponding jet mass flow is given by

$$(\mathfrak{M}/x)W_N = -\{1 - (1/2)(\gamma - 1)M_2^2\}^{-[1/(\gamma-1)]} \times (\beta W_N/\cos\phi) = -(\pi A_1^2\beta/\cos\phi)\, M_2\sqrt{\gamma P_0 \rho_0}$$

It may be inferred that the main stream and jet current will fail to mix whenever $w$ exceeds this critical value.

* If the density of the jet is different from that in the main stream then the ratio of these two densities occurs under the square root sign in the equation for $f$.

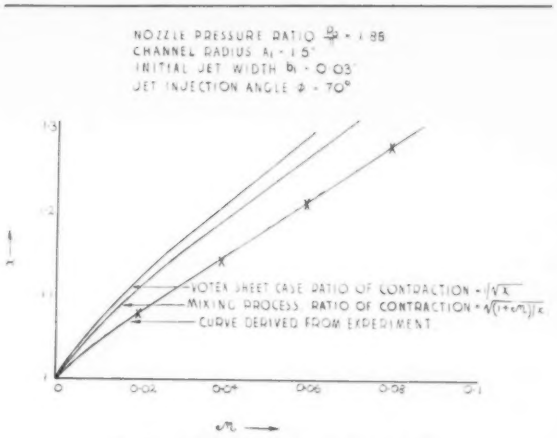


FIG. 5. Relation between mass flows.

## (7) Thrust Characteristics—Best Angle of Jet Injection

For the mixing process, consideration of the rate of change of momentum at exit shows that the total thrust $F$ is given by

$$F = \pi\gamma A_2^2 P_0 M_2^2\{1 - (1/2)(\gamma - 1)M_2^2\}^{1/(\gamma-1)}$$

Use of equations in Section (5) then shows that†

$$F/W\sqrt{T_0} = \sqrt{\gamma R} \cdot M_2 \cdot (1 + \mathfrak{M}) \quad (7.1)$$

This equation enables thrust characteristics to be plotted. The left-hand side may be called the thrust coefficient. In particular, the equation shows that such characteristics are independent of the initial jet width and angle of injection.

The thrust coefficient assumes its maximum value whenever $\mathfrak{M}$ does so. If $\phi$ is an obtuse angle, then, provided we insist on keeping to the mixing process, $\mathfrak{M}$ is bounded above by a critical value; otherwise $\mathfrak{M}$ is unlimited. Thus, to obtain a large thrust coefficient, $\phi$ should not exceed 90°. Furthermore, it may easily be seen that the derivative with respect to $\cos\phi/\beta$ of the right-hand side of (5.2) is negative. Hence, for fixed $x$, $\mathfrak{M}$ increases with $\phi$. It follows that the best thrust characteristics will be obtained for a nozzle in which the jet is injected at right angles to the main stream. In practice, it is found that the best angle of injection is slightly less than a right angle.

Eq. (7.1) shows that

$$F/(W + w)\sqrt{T_0} = \sqrt{\gamma R} \cdot M_2$$

Hence, for a given nozzle pressure ratio the thrust coefficient relative to the total flow is a constant. This result has also been confirmed by experiment.

For the vortex sheet case the total thrust is

$$F = \pi\gamma A_2^2 P_0 M_2^2\{1 - (1/2)(\gamma - 1)M_2^2\}^{1/(\gamma-1)} + 2\pi\gamma A_2 b_2 p_0 m_2^2\{1 - (1/2)(\gamma - 1)m_2^2\}^{1/(\gamma-1)}$$

Use of equations in Section (5) shows that correspond-

† For engineers' units replace $R$ by $R/g$.

ing to (7.1) we then have

$$F/W\sqrt{T_0} = \sqrt{\gamma R}\cdot M_2(1 + k\mathfrak{M}) \qquad (7.2)$$

where $k = \sqrt{1 + \nu_1^2}$ depends on $\beta$ and $\phi$, and

$$\nu_1 = M_2^{-1}m_1\{1 - (1/2)(\gamma - 1)m_1^2\}^{-(1/2)} = \{1 - (1/2)(\gamma - 1)M_2^2\}^{1/(\gamma-1)}\cdot(\mathfrak{M}/2\beta x)$$

For given $x$, it can be shown that $k$ assumes its greatest value when $\phi = 180°$, at least in the case of small jet flows. Thus, in the vortex sheet case, the total thrust will be greatest when the jet current is not injected into the main stream at all, but flows parallel to it. This result may have been expected, of course.

Since $k > 1$, comparison of Eq. (7.1) with Eq. (7.2) shows that the vortex sheet case always gives slightly better thrust characteristics than the mixing process. Thus, for given flows, mixing is only obtained at the cost of a slight reduction in thrust.

### References


[1] Ehrich, F. F., *Penetration and Deflection of Jets Oblique to a General Stream*, Journal of the Aeronautical Sciences, Vol. 20, No. 2, pp. 99–104, February, 1953.

[2] Durand, W. F., (Ed.), *Aerodynamic Theory*, Vol. III; Springer, Berlin, 1935.

[3] Howarth, L., (Ed.), *Modern Developments in Fluid Dynamics—High Speed Flow*, Vol. I, Ch. VI; Oxford, 1953.

[4] Shapiro, A. H., Hawthorne, W. R., and Edelman, G. M., *The Mechanics and Thermodynamics of Steady One-Dimensional Gas Flow With Tables for Numerical Solutions*, Meteor, Massachusetts Institute of Technology, Guided Missiles Program, 1947. See Table 14.

[5] *A Selection of Tables for Use in Calculations of Compressible Airflow*, prepared by Compressible-Flow-Tables-Panel, Oxford, 1952. See Table II.


## The Plastic Bending of an Eccentrically Loaded Column

(*Continued from page 338*)

until a considerably higher load is reached. Only at this higher load does the column become useless due to lateral instability. It should be noted that this load is not sharply defined; however, a determination of the buckling load as that load which *first* produces lateral deflections would result in an unreasonably low value, at least when the eccentricity is small. On the other hand, the tangent modulus load is somewhat too high, being approached only in the limit as the eccentricity vanishes.

### References


[1] Euler, L., *Methodus inveniendi lineas curvas maximi minimive proprietate gaudentes. Additamentum I: De curvis elasticis*, p. 267, Lausanne, 1744.

[2] Euler, L., *Histoire de l'Académie*, Vol. 13, pp. 252–282; Berlin, 1757.

[3] Timoshenko, S. P., *Theory of Elastic Stability*, p. 64; McGraw-Hill Book Company, Inc., New York, 1936.

[4] Considère, A., *Résistance des Pièces Comprimées*, Congrès International des Procédés de Construction, Annexe, Librairie Polytechnique, p. 371; Paris, 1891.

[5] Engesser, F., *Über Knickfragen*, Schweizerische Bauzeitung, Vol. 26, No. 4, p. 24, 1895.

[6] Von Kármán, T., *Untersuchungen über Knickfestigkeit*, Mitteilungen über Forschungsarbeiten auf dem Gebiete des Ingenieurwesens, Verein Deutscher Ingenieure, Heft 81, Berlin, 1910.

[7] Timoshenko, S. P., loc. cit., p. 156.

[8] Shanley, F. R., *The Column Paradox*, Journal of the Aeronautical Sciences, Vol. 13, No. 12, p. 678, December, 1946.

[9] Shanley, F. R., *Inelastic Column Theory*, Journal of the Aeronautical Sciences, Vol. 14, No. 5, pp. 261–268, May, 1947.

[10] Ziegler, H., *Linear Elastic Stability: A Critical Analysis of Methods*, Zeit. für angewandte Mathematik und Physik, Vol. 4, pp. 89–121, 167–185, 1953.

[11] Drucker, D. C., and Onat, E. T., *On the Concept of Stability of Inelastic Systems*, Journal of the Aeronautical Sciences, Vol. 21, No. 8, pp. 543–548, August, 1954.

[12] Prager, W., *The Theory of Plasticity: A Survey of Recent Achievements*, James Clayton Lecture, Proceedings, Institution of Mechanical Engineers, Vol. 169, pp. 41–57, 1955.

[13] Boyce, W. E., *The Bending of a Work-Hardening Circular Plate by a Uniform Transverse Load*, Quart. Appl. Math., Vol. 14, pp. 277–288, 1956.

[14] Baker, J. F., Horne, M. R., and Heyman, J., *The Steel Skeleton: Plastic Behavior and Design*, Ch. 13; Cambridge University Press, 1956.



# IAS Twenty-Sixth Annual Meeting

## *Hotel Sheraton-Astor, New York City, January 27–30, 1958*

The Meetings Committee plans to schedule sessions on Aerodynamics, Aeroelasticity, Design, Electronics, Flight Propulsion, Instruments, Rotating Wing Aircraft, Safety in Flight, Structures, Air Transportation, etc.

Members or organizations wishing to have papers considered for presentation at this meeting should submit outlines or short abstracts to the Meetings Committee, 2 East 64th St., New York 21, N.Y., no later than August 1, 1957.

# The Balance Method Applied to Swept-Wing Stress Analysis†

LUIGI BROGLIO*
*University of Rome*

SUMMARY

This paper presents preliminary results of an investigation dealing with the stress analysis of the variable cross-section swept wing, reinforced by many stringers, having elastic ribs, and with cover sheets carrying also tension or compression.

The paper is divided into two parts. In Part I the fundamental relationships are derived that lead to the mathematical statement of the problem. They consist of the equations of "equilibrium," with which no special difficulties are encountered, and of the equations of "elasticity," for which a particular choice of the parameters of strain appeared to be most advantageous.

In Part II the solution of the problem is obtained by the balance method, an original method of computation introduced by the author in 1934. This is a procedure that can be applied to many important problems of applied mechanics and physics according to a general and uniform technique described in detail in reference 1.

As a consequence of the general physical concepts on which it is based, the balance method leads to a fundamental transformation of the problem in the case of the swept wing, as well as in any other application. From a mathematical viewpoint, this transformation leads to a simplification of the equations obtained in Part I and to their solution by a quite simple and convergent method of successive approximations.

In this first application of the balance method to swept-wing structural problems, attention was focused on the quantities that are most interesting from a practical viewpoint, such as the stress concentration in the rear spar and the bending-torsion interaction. This permitted a reduction in the numbers of parameters which are assumed to define satisfactorily the motion of the various points belonging to the same wing-section.

## PART I

### (1) DESCRIPTION

THE SWEPT WING is referred to the three coordinate axes $x$, $y$, $z$. The angle subtended by the $x$- and $y$-axes is $(\pi/2) - \Lambda$, where $\Lambda$ is the sweep angle (see Fig. 1). All the stringers are parallel to the $y$-axis, and all the ribs are parallel to the $xz$-plane.

The generic section of the structure corresponding to a $y$ = const. plane is also shown in Fig. 1. It is symmetric with respect to the $x$-axis. Along the two sides $b$ of the rectangle, the sheet, of thickness $t$, is reinforced by a continuous and uniform distribution of stringers of cross-sectional area $\bar{\beta}t/\cos\Lambda$ per unit length in the $x$-direction and by two cap strips of cross-section A′ and A″. Along the two sides $c$ the sheet is of thickness $t_v'$ and $t_v''$.

The ribs are assumed to be uniformly and continuously spaced, the rib caps have the cross-sectional area $\bar{\alpha}t/\cos\Lambda$ per unit length in the $y$-direction, and the sheet has a thickness $t_r/\cos\Lambda$ per unit length in the $y$-direction (see Fig. 1).

### (2) STRESS-STRAIN RELATIONSHIPS

The stress-strain relationships are written by using (1) the orthogonal projections $u$, $v$, $w$ of the total displacement on the axes $x$, $y$, $z$ (the values of $v$, $w$ at $x = 0$ and $x = b$ are denoted by $v'$, $w'$, and $v''$, $w''$, respectively—see Fig. 1); (2) the strain components $\epsilon_x = \partial u/\partial x$; $\epsilon_y = \partial v/\partial y$; $\gamma = (\partial v/\partial x) + (\partial u/\partial y)$; (3) the stresses $\sigma_x$, $\sigma_y$, $\tau$, in the $x$ and $y$ directions of the cover sheet, and the unit forces $p_x = t\sigma_x + E\bar{\alpha}t\epsilon_x$; $p_y = t\sigma_y + E\bar{\beta}t\epsilon_y$; $q = t\tau$ acting on the cover sheet plus stringers and rib caps (see Fig. 1); and (4) the axial forces $\bar{N}'$ and $\bar{N}''$ and the shear flows $q_v'$ and $q_v''$ in the two spars. The shear flow in the rib is denoted by $q_r$.

The relationships obtained are (see Appendix A)

$$\left.\begin{aligned} p_x/tE^* &= (1+\alpha)\epsilon_x + \nu^*\epsilon_y - m\gamma \\ p_y/tE^* &= \nu^*\epsilon_x + (1+\beta)\epsilon_y - m\gamma \\ q/tE^* &= -m(\epsilon_x + \epsilon_y) + \mu\gamma \end{aligned}\right\} \tag{1}$$

$$(\partial^2\epsilon_x/\partial y^2) + (\partial^2\epsilon_y/\partial x^2) = \partial^2\gamma/\partial x\partial y \tag{2}$$

where

$$\left.\begin{aligned} &E/E^* = \alpha/\bar{\alpha} = \beta/\bar{\beta} = (1-\nu^2)\cos^2\Lambda \\ &m = \sin\Lambda \qquad \nu^* = \sin^2\Lambda + \nu\cos^2\Lambda \\ &\mu = \sin^2\Lambda + (1/2)(1-\nu)\cos^2\Lambda \end{aligned}\right\} \tag{3}$$

$$\left.\begin{aligned} &\bar{N}'/EA' = dv'/dy \qquad \bar{N}''/EA'' = dv''/dy \\ &q_v'/Gt_r' = (dw'/dy) - (2v'/c) \\ &q_v''/Gt_v'' = (dw''/dy) - (2v''/c) \\ &q_r/Gt_r = (\partial w/dx) - (2u/c) \end{aligned}\right\} \tag{4}$$

### (3) EQUATIONS OF EQUILIBRIUM

The external loading is represented in Fig. 2a—it consists of the distributed loads $P'\,dy$ on the front spar and $P''\,dy$ on the rear spar. In Fig. 2b the swept wing is loaded by a special type of loading that will be used in the analysis of Part II. This special loading consists of two self-balancing systems at each rib. One of them consists of two equal and opposite moments $Hc\,dy$ in the plane of the rib and the other of

Presented at the Structures Session, Twenty-Third Annual Meeting, IAS, New York, January 24–27, 1955.

We wish to express our sincere appreciation to Dr. N. J. Hoff of the Polytechnic Institute of Brooklyn for his assistance in editing this paper—ED.

† Work developed under Contract AF61(514)-422, sponsored by the ARDC of USAAF, through its European Office to the School of Aeroengineering, Rome University.

* Professor, School of Aeronautical Engineering.

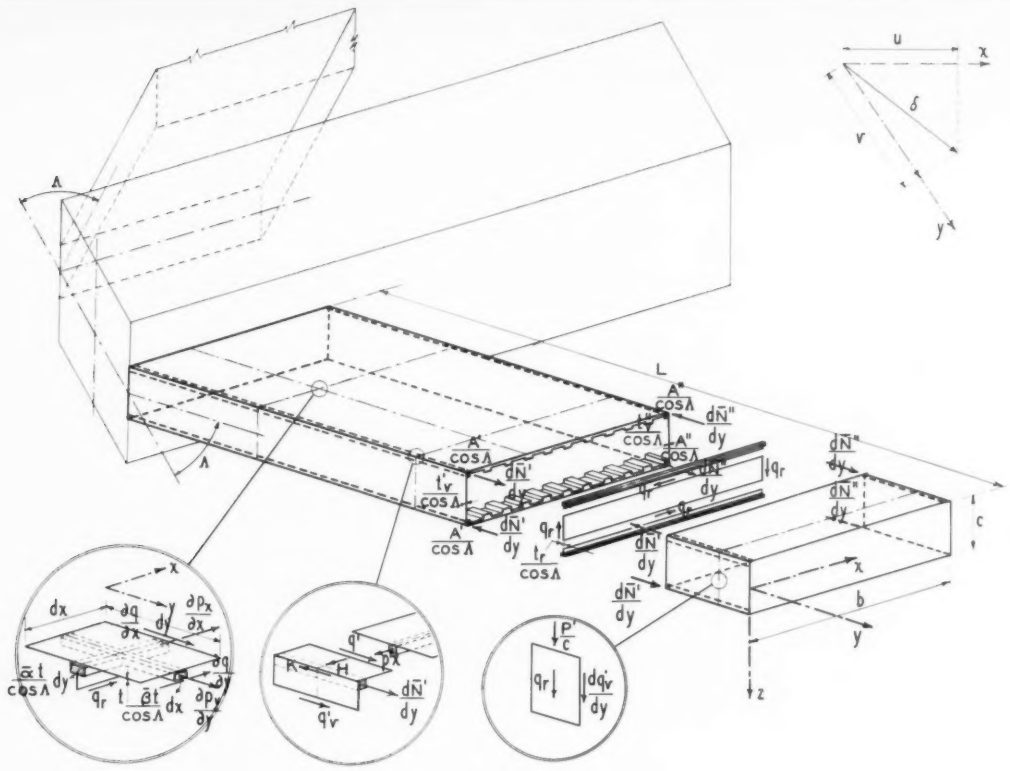


FIG. 1.

two equal and opposite moments $Kc\,dy$ in the planes of the spars.

For the sake of generality, the equations of equilibrium are written for the case in which the two loadings of Figs. 2a and 2b are applied to the structure at the same time (Fig. 2c).

The equations of equilibrium for the top reinforced sheet are (see Fig. 1)

$$\left.\begin{aligned}(\partial p_x/\partial x) + (\partial q/\partial y) + q_r &= 0\\ (\partial p_y/\partial y) + (\partial q/\partial x) &= 0\end{aligned}\right\} \tag{5}$$

with the boundary conditions (see Fig. 1):

$$\left.\begin{aligned}p_x' &= p_x'' = H\\ q_v' + q' - K + (d\bar{N}'/dy) &= 0\\ q_v'' - q'' + K + (d\bar{N}''/dy) &= 0\end{aligned}\right\} \tag{6}$$

where $p_x'$, $q'$ and $p_x''$, $q''$ denote the values of $p_x$ and $q$ at $x = 0$ and $x = b$, respectively.

The remaining conditions of equilibrium refer to the rib web and to the spar web. They are (see Fig. 1)

$$\left.\begin{aligned}\partial q_r/\partial x = 0 \qquad (P'/c) + (dq_v'/dy) + q_r &= 0\\ (P''/c) + (dq_v''/dy) - q_r &= 0\end{aligned}\right\} \tag{7}$$

In order to solve the general problem of the swept wing, Eqs. (1), (2), (4), (5), (6), and (7) can be used. The boundary conditions at $y = 0$ prescribe that all the displacements are zero: at $y = L$ (with $L$ the length of the structure) they prescribe that all the stresses vanish.

## PART II

### (1) Purpose of the Balance Method

It is known that a system of linear algebraic equations can be quickly solved by successive approximations if, in the matrix of the coefficients, the principal diagonal elements predominate over the other elements. This is the case in structural problems only when the effect of each of the forces, of which the external loading consists is strongly localized,—that is, if this effect decreases rapidly with the distance from the point of application of the force (see reference 2, p. 14). But it follows from the St. Venant principle that each of the self-balancing systems of moments in Fig. 2b must have its effect sensibly confined to a region near the rib to which the self-balancing system is applied; whereas the same cannot be said of the loads $P'$ and $P''$ (see Fig. 2a). The essential purpose of the balance method is to reduce the solution of the problem shown in Fig. 2a to the solution of a problem of the type shown in Fig. 2b, and to provide a procedure of uniformly and rapidly convergent approximations for problems of the type 2b.

### (2) The Problem to be Solved

The case of symmetric structure will be studied, for which $A' = A'' = A$, and $r_v' = r_v'' = r_v$. It would be

particularly profitable to apply the balance method to the general problem considered in Part I, because the advantages of the method in comparison with standard methods increase with the complexity of the structure. However, for the sake of simplicity, the paper is confined to problems in which the displacements $u$, $v$, $w$ can be adequately expressed as

$$\left.\begin{aligned} u &= u_0(y) + u_1(y)\ (2\xi - 1) \\ v &= v_0(y) + v_1(y)\ (2\xi - 1) \\ w &= w_0(y) + (b/c)u_0(y)\ (2\xi - 1) - \\ &\qquad (2b/c)u_1(y)\xi(1 - \xi) \end{aligned}\right\} \tag{8}$$

where $\xi = x/b$.

Eqs. (8) express the motion of each rib by the five parameters $u_0$, $v_0$, $w_0$, $u_1$, $v_1$. Of these, $u_0$, $v_0$, $w_0$ define the rigid motion of the rib, whereas the remaining two parameters $u_1$ and $v_1$, called "distortion parameters" (see p. 18 of reference 1), define the flexibility of the rib in its plane and the warping of the rib.

Through introduction of Eqs. (8) in Eqs. (1) and (4), the stress-strain relationships become

$$\left.\begin{aligned} p_x &= \bar{p}(y) + 6\bar{\bar{p}}(y)\ (2\xi - 1) \\ p_y &= p_0(y) + 6p_1(y)\ (2\xi - 1) \\ q &= q_0(y) + 6q_1(y)\ (2\xi - 1) \end{aligned}\right\} \tag{9}$$

(For the values of $\bar{p}$, $p_0$, $q_0$, $\bar{\bar{p}}$, $p_1$, $q_1$, see Appendix B.)

$$\left.\begin{aligned} q_x' + q_x'' &= 2Gt_x[(dw_0/dy) - 2(v_0/c)] \\ q_x' - q_x'' &= 2Gt_x[(2v_1/c) - (b/c)\ (du_0/dy)] \\ \bar{N}' &= EA[(dv_0/dy) - (dv_1/dy)] \\ \bar{N}'' &= EA[(dv_0/dy) + (dv_1/dy)] \end{aligned}\right\} \tag{10}$$

In order to determine the five functions $u_0$, $v_0$, $w_0$, $u_1$, $v_1$ five relationships derived from the general conditions of equilibrium (see reference 1) can be used (see Appendix C).

$$(d/dy)\ (\bar{N}' + \bar{N}'' + p_0 b) + q_x' + q_x'' = 0 \tag{11}$$

$$(1/c)\ (P' + P'') + (d/dy)\ (q_x' + q_x'') = 0 \tag{12}$$

$$(1/c)\ (P'' - P') + (d/dy)\ (q_x'' - q_x') + 2(dq_0/dy) = 0 \tag{13}$$

$$b(dq_1/dy) - p + H = 0 \tag{14}$$

$$b(dp_1/dy) + (1/2)\ (q_x'' - q_x') + (1/2)\ (d/dy)\ (\bar{N}'' - \bar{N}') - q_0 + K = 0 \tag{15}$$

The problem is to find the five functions $u_0$, $v_0$, $w_0$, $u_1$, $v_1$ that satisfy Eqs. (9), (10), (11), (12), (13), (14), and (15) with appropriate boundary conditions. This is the problem to which the balance method will be applied.

### (3) Technique of the Balance Method

According to the general rules of the balance method given in reference 1, first the rigid motion parameters ($u_0$, $v_0$, $w_0$) are eliminated from the equations, and all the stresses are expressed in terms of the distortion parameters ($u_1 v_1$) and of the resultants of the external loading. The latter are the shear force,

$$V = \int_y^L (P' + P'')\, dy$$

$[(H + H^*)/E^*t]$ the bending moment,

$$M = \int_y^L V\, dy$$

and the twisting moment,

$$T = (b/2) \int_y^L (P'' - P')\, dy$$

From Eqs. (11), (12), and (13) one gets

$$\left.\begin{aligned} k(du_0/dy) &= m(M/bcE^*t) + (1 + \beta^*) \times \\ &\quad (T/bcE^*t) + 2m(u_1/b)\ (1 + \beta^* - \nu^*) + \\ &\quad 2(v_1/b)\ [m^2 + (1 + \beta^*)\ (\lambda - \mu)] \\ k(dv_0/dy) &= (\lambda + \mu)\ (M/bcE^*t) + \\ &\quad m(T/bcE^*t) + 2(u_1/b)\ [m^2 - \nu^*(\lambda + \mu)] + \\ &\quad 2(v_1/b)\ (2m\lambda) \\ (c/b)\ (dw_0/dy) &= 2(v_0/b) + (V/2\lambda cE^*t) \end{aligned}\right\} \tag{16}$$

where

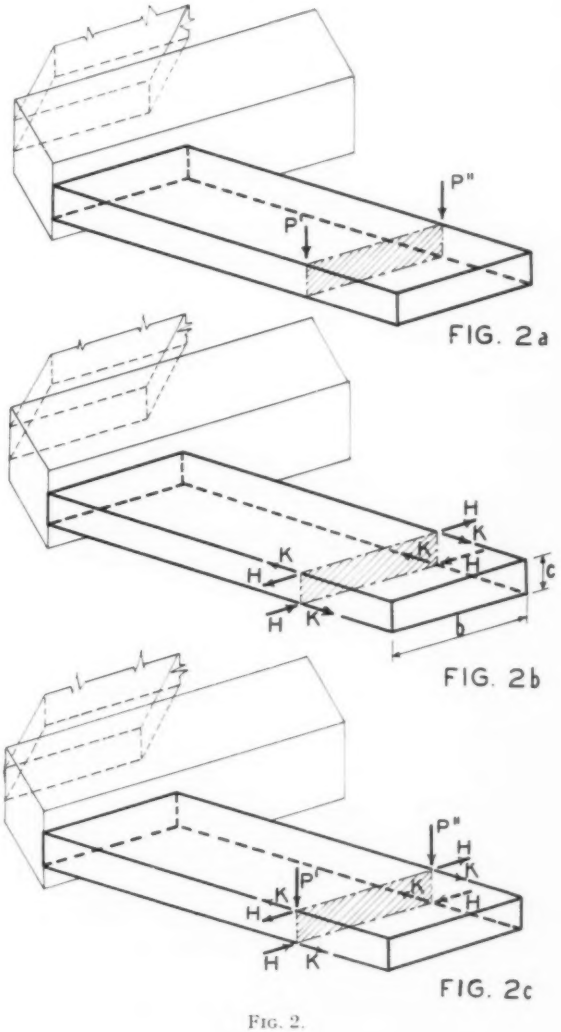


FIG. 2a

FIG. 2b

FIG. 2c

FIG. 2.

$$\left.\begin{aligned}\beta^* &= \beta + 2(EA/btE^*) \qquad \lambda = (b/c)\,(Gt_c/E^*t)\\ k &= (1+\beta^*)(\lambda+\mu) - m^2\end{aligned}\right\} \quad (17)$$

Introduction of Eqs. (16) into Eqs. (14) and (15) leads to

$$[(H+H^*)/E^*t]\,(L^2/b^2) + (1/t)\,(d/d\eta)\times \{t[\mu(d\theta/d\eta) - m(d\varphi/d\eta)]\} + fm\varphi - f_1\theta = 0 \quad (18)$$

$$[(K+K^*)/E^*t]\,(L^2/b^2) + (1/t)\,(d/d\eta)\times \{t[(1+\rho^*)(d\varphi/d\eta) - m(d\theta/d\eta)]\} + fm\theta - f_2\varphi = 0 \quad (19)$$

Here, $u_1$, $v_1$, $y$, are replaced by the following nondimensional quantities:

$$\theta = u_1/6b \qquad \varphi = v_1/6b \qquad \eta = y/L$$

Moreover,

$$\rho^* = \beta + 6(EA/btE^*)$$

$$(b^2/L^2)f = (24\lambda/k)\,[1+\beta^*-\nu^*]$$

$$(b^2/L^2)f_1 = (12/k)\,[\alpha k + (1+\beta^*-\nu^{*2})\times(\lambda+\mu-m^2) - m^2(1-\nu^*)^2]$$

$$(b^2/L^2)f_2 = (48\lambda/k)\,[\mu(1+\beta^*) - m^2]$$

$$H^* = \{[m^2 - \nu^*(\lambda+\mu)]/k\}\,(M/bc) + [m(1+\beta^*-\nu^*)/k]\,(T/bc) \quad (20)$$

$$K^* = (2m\lambda/k)\,(M/bc) + \{[m^2 + (\lambda-\mu)(1+\beta^*)]/k\}\,(T/bc) \quad (21)$$

The boundary conditions of Eqs. (18) and (19) are

$$\left.\begin{aligned}&\theta = \varphi = 0 \quad \text{when} \quad \eta = 0\\ \text{and} \quad &d\theta/d\eta = d\varphi/d\eta = 0 \quad \text{when} \quad \eta = 1\end{aligned}\right\} \quad (22)$$

If $\varphi$ and $\theta$—that is, $u_1$ and $v_1$—are obtained from Eqs. (18) (19), and (22), $u_0$, $v_0$, $w_0$ are readily given by Eqs. (16) (since $u_0 = v_0 = w_0$ for $\eta = 0$). Finally, all the stresses in the swept wing are readily obtained in terms of $u_0$, $v_0$, $w_0$, $u_1$, $v_1$ [see Eqs. (9) and Appendix B]. Consequently, the whole problem is reduced to the integration of Eqs. (18) and (19) with the boundary conditions (22).

From Eqs. (20) and (21) it is seen that $H^*$ and $K^*$ are known quantities depending upon $M$ and $T$ only—i.e., independent of $H$ and $K$.

Eqs. (18) and (19) refer to the general case of loading of Fig. 2c (loads $P'P''$ and balanced moments $Hc$, $Kc$, acting at the same time). For the problem of Fig. 2a ($H = 0$, $K = 0$), the equations become

$$(H^*/E^*t)\,(L^2/b^2) + (1/t)\,(d/d\eta)\times \{t[\mu(d\theta/d\eta) - m(d\varphi/d\eta)]\} + fm\varphi - f_1\theta = 0 \quad (18')$$

$$(K^*/E^*t)\,(L^2/b^2) + (1/t)\,(d/d\eta)\times \{t[(1+\rho^*)(d\varphi/d\eta) - m(d\theta/d\eta)]\} + fm\theta - f_2\varphi = 0 \quad (19')$$

whereas, for the problem of Fig. 2b ($P' = 0$, $P'' = 0$), the general equations (18) and (19) give

$$(H/E^*t)\,(L^2/b^2) + (1/t)\,(d/d\eta)\times \{t[\mu(d\theta/d\eta) - m(d\varphi/d\eta)]\} + fm\varphi - f_1\theta = 0 \quad (18'')$$

$$(K/E^*t)\,(L^2/b^2) + (1/t)\,(d/d\eta)\times \{t[(1+\rho^*)(d\varphi/d\eta) - m(d\theta/d\eta)]\} + fm\theta - f_2\varphi = 0 \quad (19'')$$

Eqs. (18′), (19′) hold for arbitrary values of $P'$ and $P''$, that is, $H^*$ and $K^*$. Eqs. (18″), (19″) hold for arbitrary values of $H$ and $K$.

Eqs. (18″) and (19″) become identical with Eqs. (18′) and (19′), respectively, when $H$ and $K$ in Fig. 2b are related to $P'$ and $P''$ of Fig. 2a through the equations $H = H^*$, $K = K^*$ (where $H^*$ and $K^*$ are expressed by Eqs. (20) and (21) in terms of $P'$, $P''$—i.e.,

$$H = \{[m^2 - \nu^*(\lambda+\mu)]/k\}\,(M/bc) + m[(1+\beta^*-\nu^*)/k]\,(T/bc) \quad (23)$$

$$K = (2m\lambda/k)\,(M/bc) + \{[m^2 + (\lambda-\mu)\times(1+\beta^*)]/k\}\,(T/bc) \quad (23')$$

where

$$T = \int_y^L (P' + P'')\,dy$$

$$M = \int_y^L T\,dy \qquad \int_y^L (b/2)\,(P'' - P')\,dy$$

As Eqs. (18′) and (19′) have the same boundary conditions (20) as Eqs. (18″) and (19″), this result proves that Eqs. (18′) and (19′) are those ruling the problem of Fig. 2b, provided $H$ and $K$ have the values specified by Eqs. (23) and (23′). The purpose of the balance method is thus reached; the solution of the actual problem of Fig. 2a (swept wing subjected to loads $P'$ and $P''$) is reduced to the solution of the problem of Fig. 2b (swept wing subjected to self-balancing systems).

The third and final step of the balance method is to solve the problem of Fig. 2b (with $H = H^*$, $K = K^*$) by means of Eqs. (18″) and (19″). No special difficulties arise in this final step. Indeed, the St. Venant principle ensures the convergence of any conventional method of successive approximations applied to Eqs. (18″) and (19″).

Moreover, from such equations it appears that any approximation used for $\theta$ and $\varphi$ leads to residuals which are still self-balancing systems of the same nature as the starting $H$ and $K$. This provides a uniform and objective technique of operations every step of which is the same; consequently, the computations can easily be carried out by inexperienced personnel, and they can easily be programed for machine computation.

The basic difference between the balance method and conventional methods is also pointed out by Eqs. (18″), (19″). Conventional methods generally lead to equations in which all the displacements (as unknowns) and all the external loads $P'$ and $P''$ (as known terms) appear simultaneously. The balance method leads to Eqs. (18″), (19″)—that is, to equations in which only distortion parameters (as unknowns) and only self-balancing systems (as known terms) are present.

The procedure given above can be applied without

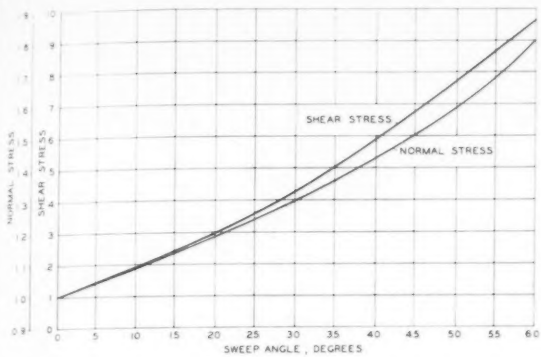


FIG. 3a. Rear spar stress (referred to straight wing stress), constant section wing.

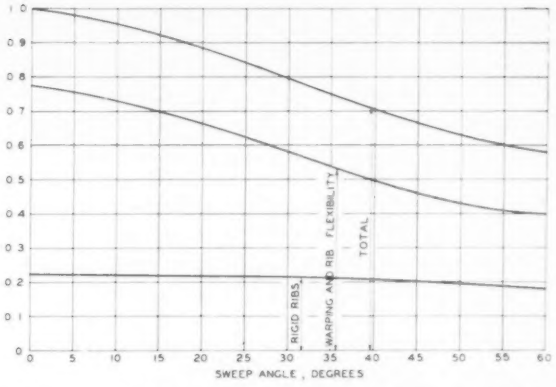


FIG. 3b. Angle of twist due to a torque (referred to straight wing angle of twist), constant section wing.

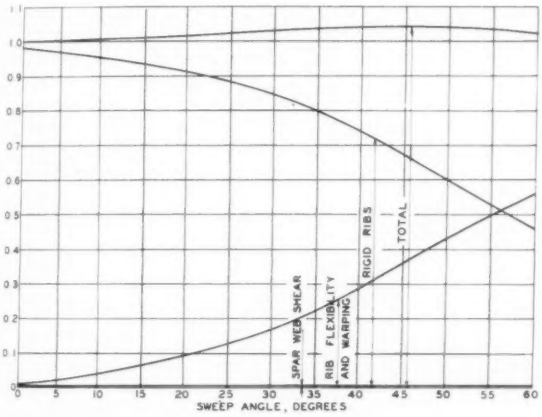


FIG. 3c. Vertical displacement due to a bending force at the free end (referred to straight wing vertical displacement), constant section wing.

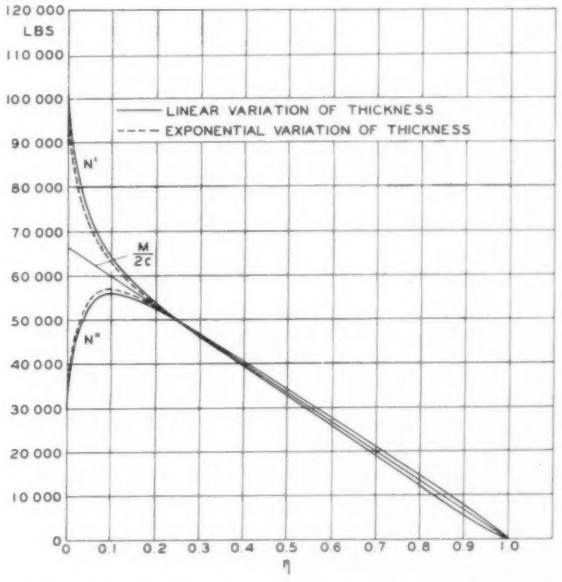


FIG. 4a. Variable section wing ($\lambda = 45°$) normal forces spanwise distribution.

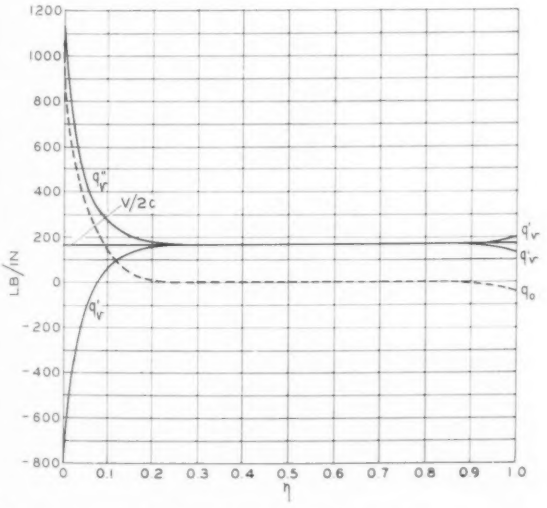


FIG. 4b. Linearly variable section wing ($\Lambda = 45°$) shear flows spanwise distributions.

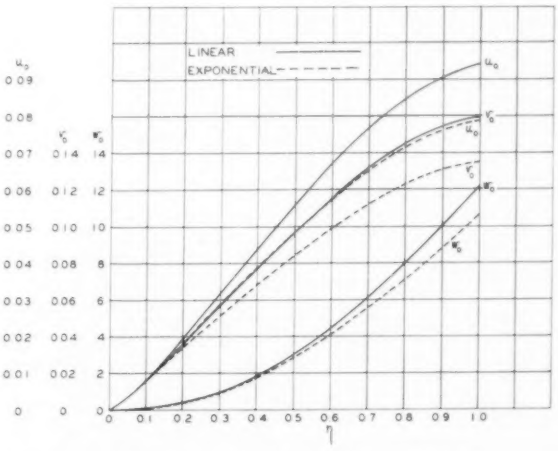


FIG. 4c. Variable section wing ($\Lambda = 45°$) spanwise displacement distributions.

any essential modification to a great variety of problems in the field of applied mechanics. If attention is confined to the analysis of aeronautical structures, it can be shown that, for any type of wing or fuselage, the equations of the problem can be written in such a way that, for each section, only the distortion parameters (as unknowns) and only self-balancing systems (as known terms) appear, so that a uniform and objective technique of successive approximations can always be used for numerical computations.

### *Numerical Examples*

The above analysis, with the analytical results of Appendix D, was applied to some numerical examples.

(a) *Constant Section Wing*—The constant section wing is defined by the following geometrical data:

$A = 1.5625$ sq.in. $\quad b = 50$ in. $\quad \bar{\alpha} = 0.9375$
$t = 0.125$ in. $\quad c = 6$ in. $\quad \bar{\beta} = 1.40625$
$t_r = 0.250$ in. $\quad L = 400$ in.

For this shell the rear spar normal and shear stress due to two equal forces of 1,000 lb., applied to the rear and front spars (pure bending), for various angles of sweep, was considered; for the same structure, the tip displacement $w_0$, and the tip rotation due to a torque also were calculated.

The results, referred to the values of the straight wing are presented in Figs. 3a, 3b, and 3c.

(b) *Linearly Varying Section*—The calculation was performed for a shell for which $\Lambda = 45°$ and

$$t = 0.05\eta + 0.200\ (1 - \eta)\ \text{in.}$$

and, for which all the other dimensions (excepting $L$, $b$, and $c$ that are still 400 in., 50 in., 6 in., respectively) are obtained from those of section (a) above by a variation proportional to $t$. The spanwise distribution of $q_r' q_r'' N' N''$, and of the displacements are shown in Figs. 4a, 4b, and 4c. Here $N'$ and $N''$ denote the forces in the front and rear caps that are vectorially equivalent to all the normal forces on the top panel plus stringers.

Table 1 shows the routine of computation by successive approximations (described in detail in reference 1). Note the rapidity of the convergence which permits a solution through a very small number of iterations.

(c) *Exponentially Varying Section*—Calculations were carried out for a structure for which

$$t = t_0 e^{-F\eta}$$

(where $t_0 = 0.200$; $F = \lg_e 4$). All the other dimensions, excepting $L$, $b$, $c$, that are still 400 in., 50 in., and 6 in., respectively, are changed in the same proportion as $t$ with respect to the values of section (a) under *Numerical Examples* above. The results are presented in Figs. 4a, 4b, and 4c. It is shown in Appendix D that for such a structure an exact solution is also possible.

## Appendix A

Let $\bar{y}$ (see Fig. 1) be the direction parallel to the $x$-axis. Denote by $u$, $V$, $\epsilon_1$ $\epsilon_2$ $\gamma_{12}$, and $\sigma_1$ $\sigma_2$ $\tau_{12}$, the displacements, the strains, and the stresses with respect to the orthogonal axes $x$ and $\bar{y}$. One has

$$\begin{cases} u = u \\ v = u \sin\Lambda + V\cos\Lambda \end{cases}$$

$$\begin{cases} \epsilon_x = \epsilon_1; \qquad \epsilon_y = \epsilon_1 \sin^2\Lambda + \epsilon_2 \cos^2\Lambda + \gamma_{12}\sin\Lambda\cos\Lambda \\ \gamma = \gamma_{12}\cos\Lambda + 2\epsilon_1 \sin\Lambda \end{cases}$$

$$\begin{cases} E\epsilon_1 = \sigma_1 - \nu\sigma_2 \\ E\epsilon_2 = \sigma_2 - \nu\sigma_1 \\ E\gamma_{12} = 2(1+\nu)\tau_{12} \end{cases}$$

$$\begin{cases} \sigma_1 \cos\Lambda = \sigma_x + \sigma_y \sin^2\Lambda + 2\tau\sin\Lambda \\ \sigma_2 = \sigma_y \cos\Lambda \\ \tau_{12} = \tau + \sigma_y \sin\Lambda \end{cases}$$

Hence,

$$\begin{cases} (E\cos\Lambda)\epsilon_x = \sigma_x + (\sin^2\Lambda - \nu\cos^2\Lambda)\sigma_y + 2\tau\sin\Lambda \\ (E\cos\Lambda)\epsilon_y = (\sin^2\Lambda - \nu\cos^2\Lambda)\sigma_x + \sigma_y + 2\tau\sin\Lambda \\ (E\cos\Lambda)\gamma = 2(\sigma_x + \sigma_y)\sin\Lambda + 2(1 + \sin^2\Lambda + \nu\cos^2\Lambda)\tau \end{cases}$$

or

$$\begin{aligned} \sigma_x/E^* &= \epsilon_x + \nu^*\epsilon_y - m\gamma \\ \sigma_y/E^* &= \nu^*\epsilon_x + \epsilon_y - m\gamma \\ \tau/E^* &= -m(\epsilon_x + \epsilon_y) + \mu\gamma \end{aligned}$$

whence Eqs. (1) are obtained.

## Appendix B

$$\bar{p} = [2(1+\alpha)\ (u_1/b) - 2m(v_1/b) + \nu^*(dv_0/dy) - m(du_0/dy)]E^*t$$

$$\bar{\bar{p}} = (E^*t/6)\ [\nu^*(dv_1/dy) - m(du_1/dy)]$$

$$p_0 = E^*t[2\nu^*(u_1/b) - 2m(v_1/b) + (1+\beta)\ (dv_0/dy) - m(du_0/dy)]$$

$$p_1 = (E^*t/6)\ [(1+\beta)\ (dv_1/dy) - m(du_1/dy)]$$

Table 1
Routine of Computation by Successive Approximations

| | | | | | | | | | |
|---|---|---|---|---|---|---|---|---|---|
| 0.028818 | 0.031361 0.028699 | 0.031477 0.028552 | 0.031611 0.028380 | 0.031785 0.028158 | 0.031998 0.027871 | 0.032272 0.027485 | 0.032639 0.026936 | 0.033153 0.026097 | 0.059003 |
| −0.26054 | −0.23158 | −0.20261 | −0.17363 | −0.14464 | −0.11564 | −0.08661 | −0.05753 | −0.02834 | −0.00306 |
| −0.00726 | −0.00751 −0.00838 | −0.00865 −0.00549 | −0.00579 −0.00480 | −0.00493 −0.00370 | −0.00407 −0.00280 | −0.00322 −0.00189 | −0.00238 −0.00094 | −0.00155 −0.00018 | −0.00074 |
| −0.00726 | −0.01389 | −0.01214 | −0.01039 | −0.00863 | −0.00687 | −0.00511 | −0.00332 | −0.00173 | −0.00074 |
| −0.00044 | −0.00021 −0.00038 | −0.00040 −0.00033 | −0.00035 −0.00027 | −0.00030 −0.00022 | −0.00024 −0.00017 | −0.00019 −0.00011 | −0.00014 −0.00006 | −0.00009 −0.00004 | −0.00005 |
| −0.00044 | −0.00059 | −0.00073 | −0.00062 | −0.00052 | −0.00041 | −0.00030 | −0.00020 | −0.00013 | −0.00005 |
| −0.00002 | −0.00001 −0.00002 | −0.00002 −0.00002 | −0.00002 −0.00002 | −0.00002 −0.00001 | −0.00002 −0.00001 | −0.00001 −0.00001 | −0.00001 0 | −0.00001 0 | 0 |
| −0.00002 | −0.00003 | −0.00004 | −0.00004 | −0.00003 | −0.00003 | −0.00003 | −0.00002 | −0.00001 | −0.00001 |
| −0.26826 | −0.24609 | −0.21552 | −0.18468 | −0.15382 | −0.12295 | −0.09204 | −0.06106 | −0.03021 | −0.00385 |

$$q_0 = E^*t[-2m(u_1/b) + 2\mu(v_1/b) + \mu(du_0/dy) - m(dv_0/dy)]$$

$$q_1 = (E^*t/6)[\mu(du_1/dy) - m(dv_1/dy)]$$

## Appendix C

By integrating the first of Eqs. (5) and taking into account Eqs. (7), one gets Eq. (13).

By multiplying the first of Eqs. (5) by $\xi - (1/2)$, integrating, and taking into account the first of Eqs. (6), one gets Eq. (14).

By integrating the second of Eqs. (5), and adding the second and third of Eqs. (6), one has Eq. (11). By multiplying the second of Eqs. (5) by $\xi - (1/2)$, integrating, and taking into account Eqs. (6), one has Eq. (15). Finally, Eq. (12) is obtained by summing the second and third of Eqs. (7).

## Appendix D

First, the two simultaneous linear equations (18″) and (19″) with the boundary conditions

$$\theta = \varphi = 0 \quad \text{when } \eta = 0$$
$$d\theta/d\eta = d\varphi/d\eta = 0 \quad \text{when } \eta = 1$$

can be reduced to two independent second-order linear differential equations. For this purpose multiply Eq. (18″) by an indeterminate coefficient $\kappa$ and add it to Eq. (19″), and let

$$Z = (L^2/b^2E^*t)(\kappa H + K)$$

If $\kappa$ is such that

$$m[f\mu - f_1]\kappa^2 + [(1 + \rho^*)f_1 - \mu f_2]\kappa + m[f_2 - f(1 - \rho^*)] = 0 \quad (24)$$

by letting

$$\omega^2 = (f_2 - mf\kappa)/(1 + \rho^* - m\kappa)$$
$$\Phi = (1 + \rho^* - m\kappa)\varphi + (\mu\kappa - m)\theta$$

one obtains the equation

$$(1/t)(d/d\eta)[t(d\phi/d\eta)] - \omega^2\phi + Z = 0 \quad (25)$$

The boundary conditions are

$$\left.\begin{aligned} \phi &= 0 \quad \text{when} \quad \eta = 0 \\ d\phi/d\eta &= 0 \quad \text{when} \quad \eta = 1 \end{aligned}\right\} \quad (26)$$

Eq. (24) has two roots $\kappa_I$ and $\kappa_{II}$, to which two values of $\omega$ ($\omega_I$ and $\omega_{II}$) and two functions $\phi_I$ and $\phi_{II}$ correspond. When the functions $\phi_1$ and $\phi_{II}$—defined by Eqs. (25) (26)—are known, $\varphi$ and $\theta$ can be determined from

$$\varphi = a_{11}\phi_I + a_{12}\phi_{II} \qquad \dot{\varphi} = a_{11}\dot{\phi}_I + a_{12}\dot{\phi}_{II}$$
$$\theta = a_{21}\phi_I + a_{22}\phi_{II} \qquad \dot{\theta} = a_{21}\dot{\phi}_I + a_{22}\dot{\phi}_{II}$$

where

$$a_{11} = (\mu\kappa_{II} - m)/\epsilon$$
$$a_{12} = -[(\mu\kappa_I - m)/\epsilon]$$
$$a_{21} = -[(1 + \rho^* - m\kappa_{II})/\epsilon]$$
$$a_{22} = (1 + \rho^* - m\kappa_I)/\epsilon$$

and

$$\epsilon = (1 + \rho^* - m\kappa_I)(\mu\kappa_{II} - m) - (\mu\kappa_I - m)(1 + \rho^* - m\kappa_{II})$$

The problem is thus reduced to the integration of the two linear differential equations (25) and (26) for the two different values of $\kappa$($\kappa_I$ and $\kappa_{II}$).

Second, the differential system (25), (26) is of the same type as that discussed in detail in reference 2, p. 121.

For the most general type of variation of the functions $t$ and $Z$, the reduction of the differential system (25), (26) to an algebraic one to be solved by successive approximations is indicated. Here only the results are summarized, in order to apply them for practical purposes. The successive operations are:

(a) Choose $n + 1$ stations $\eta_i$ ($i = 0, 1 \ldots n$) along the wing.

(b) Introduce a new variable defined by

$$\zeta = t^* \int_0^\eta (d\eta/t) \quad \text{with} \quad (1/t^*) = \int_0^1 (d\eta/t)$$
$$(0 \le \zeta \le 1)$$

and calculate the value of $\zeta$ at the $n$ stations (0, $\zeta_1$, $\zeta_2$, . . . $\zeta_{n-1}$, 1) and the length of the various intervals in the new variable $\Delta_i = \zeta_i - \zeta_{i-1}$

(c) For every interval calculate

$$\omega_i = (t_{m,i}/t^*)\omega\Delta_i$$

($t_{m,i}$ being the mean value of $t$ in the $i$th interval).

(d) The coefficients and known terms of the set of linear algebraic equations are

$$s_i = \frac{\dfrac{\omega_i}{\Delta_i \sinh \omega_i}}{\dfrac{\omega_i}{\Delta_i \tanh \omega_i} + \dfrac{\omega_{i+1}}{\Delta_{i+1} \tanh \omega_{i+1}}}$$

$$d_i = \frac{\dfrac{\omega_{i+1}}{\Delta_{i+1} \sinh \omega_{i+1}}}{\dfrac{\omega_i}{\Delta_i \tanh \omega_i} + \dfrac{\omega_{i+1}}{\Delta_{i-1} \tanh \omega_{i+1}}}$$

$$Q_i = (t^*/\Delta_i)\{(Z_{i-1}/\omega^2)[1 - (\omega_i/\sinh \omega_i)] + (Z_i/\omega^2)[(\omega_i/\tanh \omega_i) - 1]\} + (t^*/\Delta_{i+1})\{(Z_i/\omega^2)[(\omega_{i+1}/\tanh \omega_{i+1}) - 1] + (Z_{i+1}/\omega^2)[1 - (\omega_{i+1}/\sinh \omega_{i+1})]\}$$

and the system to be solved is

$$x_i - s_{i+1}x_{i+1} - d_{i-1}x_{i-1} = Q_i \quad (27)$$

where

$$x_i = \phi_i\{(t^*/\Delta_i) \tanh \omega_i + (t^*/\Delta_{i+1}) \tanh \omega_{i+1}\}$$

and $Z_i$, $t_i$, $\phi_i$ are the values of $Z$, $t$, $\phi$ at the station $\zeta_i$ ($i = 0, 1, 2, \ldots n$), respectively.

The system (27) can be quickly solved by successive approximations, as is shown in reference 1, page 132 and page 164.

When the $\phi_i$'s are known, the $(d\phi_i/d\eta)$'s can be easily obtained as

$$\frac{t_i}{t^*}\frac{d\phi_i}{d\eta} = \frac{1}{\Delta_{i+1}}\left\{\phi_{i+1}\frac{\omega_{i+1}}{\sinh\omega_{i+1}} - \phi_i\frac{\omega_{i+1}}{\tanh\omega_{i+1}} + \frac{Z_i}{\omega^2}\left(\frac{\omega_{i+1}}{\tanh\omega_{i+1}} - 1\right) + \frac{Z_{i+1}}{\omega^2}\left(1 - \frac{\omega_{i+1}}{\sinh\omega_{i+1}}\right)\right\} = \frac{1}{\Delta_i}\left\{\phi_i\frac{\omega_i}{\sinh\omega_i} - \phi_{i-1}\frac{\omega_i}{\tanh\omega_i} - \frac{Z_{i-1}}{\omega^2}\left(1 - \frac{\omega_i}{\sinh\omega_i}\right) - \frac{Z_i}{\omega^2}\left(\frac{\omega_i}{\tanh\omega_i} - 1\right)\right\}$$

One has thus a simple control of the operations being performed.

Third, for particular distribution of $t$, exact analytical solutions are possible. Some of them are explicitly given here.

(a) Constant section. If $t$ = const., for two equal loads $P$ applied at the free end, one gets

$$\phi = \frac{L^2}{b^2}\frac{2PL}{kbcE^*t}\left[2m\lambda + \kappa\{m^2 - \nu^*(\lambda+\mu)\}\right]\times \frac{1}{\omega^2}\left\{1 - \eta + \frac{\sinh\omega\eta}{\omega\cosh\omega} - \frac{\cosh\omega(1-\eta)}{\cosh\omega}\right\}$$

For the case of a torque $T$ applied at the free end,

$$\phi = \frac{L^2}{b^2}\frac{T}{kbcE^*t^*}\left\{m^2 + (\lambda-\mu)(1+\beta) + \kappa m(1+\beta^*-\nu^*)\right\}\left\{1 - \frac{\cosh\omega(1-\eta)}{\cosh\omega}\right\}$$

(b) If $t$ is expressible as

$$t = t_0 e^{-F\eta}$$

an exact solution is also possible.

For the case of two equal loads $P$ applied at the free end, one gets

$$\frac{\phi}{(L^2/b^2)(2PL/kbcE^*t^*)\left\{2m\lambda + \kappa[m^2 - \nu^*(\lambda+\mu)]\right\}} = e^{(F/2)\eta}\left\{\frac{1}{\omega^2}\frac{e^{F/2}[1 + (F^2/\omega^2)]}{(F/2)\sinh\sigma + \sigma\cosh\sigma}\sinh\sigma\eta - \frac{1}{\omega^2}\left(1 - \frac{F}{\omega^2}\right)\frac{(F/2)\sinh\sigma(1-\eta) + \sigma\cosh\sigma(1-\eta)}{(F/2)\sinh\sigma + \sigma\cosh\sigma} + \frac{1}{\omega^2}\left\{1 - \frac{F}{\omega^2} - \eta\right\}e^{F\eta}\right.$$

where $\sigma^2 = \omega^2 + (F^2/4)$.


REFERENCE

[1] Broglio, Luigi, *Balance Method in Engineering Science*, Technical Report No. 1, under Contract AF61(514)-422, ARDC, WADC, USAF.


## Theory of the Finite-Span Blowing Wing

(*Continued from page 344*)


REFERENCES

[1] Schubauer, G. B., *Jet Propulsion with Special Reference to Thrust Augmentors*, NACA TN 442, January, 1933.

[2] Hagedorn, H., and Ruden, P., *Windkanal—Untersuchungen an einem Junkers-Doppelflügel*, LGL—Bericht A64, 1938.

[3] Helmbold, H. B., *On the Lift of a Blowing Wing in a Parallel Stream*, University of Wichita, Engineering Study 110, August, 1953.

[4] Helmbold, H. B., *On the Lift of a Blowing Wing in a Parallel Stream (revised)*, University of Wichita, Engineering Study 135, April, 1954. Excerpts: Journal of the Aeronautical Sciences, Vol. 22, No. 5, pp. 341, 342, May, 1955; Ingenieurarchiv, Vol. 23, p. 209, 1955.

[5] Legendre, R., *Étude théorique du soufflage près du bord de fuite d'un profil d'aile*, Note intérieure ONERA 12/1308A, April 20, 1954.

[6] Malavard, L., *Contribution a l'étude théorique du soufflage au bord de fuite d'un profil d'aile*, Note intérieure ONERA 4/1727A, December, 1954.

[7] Spence, D. A., *On the Lift of a Blowing Wing in a Parallel Stream*, Journal of the Aeronautical Sciences, Vol. 23, No. 1, pp. 92–94, January, 1956.

[8] Helmbold, H. B., *Limitations of Circulation Lift*, Readers' Forum, Journal of the Aeronautical Sciences, Vol. 24, No. 3, p. 237, March, 1957.



## Change of Address

Since the Post Office Department does not as a rule forward magazines to forwarding addresses, it is important that the Institute be notified of changes in address 30 days in advance of publishing date to ensure receipt of every issue of the JOURNAL and REVIEW.

Notices should be printed legibly and sent directly to:

Institute of the Aeronautical Sciences, Inc.
2 East 64th Street, New York 21, N.Y.

# Correlation of Cone-Cylinder Normal Force and Pitching Moment Data by the Hypersonic Similarity Rule

WILLIAM H. DORRANCE* AND ROBERT G. NORELL**

*Convair, A Division of General Dynamics Corporation*

(1) SUMMARY

Experimental data taken from tests of cone cylinders at a range of supersonic Mach Numbers in the Naval Ordnance Laboratory 40 cm. by 40 cm. wind tunnel are correlated in this paper using the Hypersonic Similarity Rule. The uniqueness of this rule was experimentally established for cone cylinders by taking measurements on hypersonically related bodies at different Mach Numbers. Once uniqueness was experimentally established, it was possible to correlate data taken for a wide variety of cone cylinders in such a way as to provide charts for estimating normal force, normal force distribution and pitching moment for cone cylinders for Mach Numbers greater than 1.5, cone semi-vertex angles up to 14°, and angles of attack up to 15°, providing laminar flow exists over the body.

(2) SYMBOLS

| | |
|---|---|
| $c_M$ | $= M/qS_bl$; positive for restoring moment about nose tip |
| $c_N$ | $= N/qS_b$ |
| $c_0$ | = velocity of sound in free stream |
| $K_t$ | $= \beta t/l_n$ = hypersonic similarity parameter |
| $K_\alpha$ | $= \beta\alpha$ = hypersonic similarity parameter; $\alpha$ in degrees as used herein |
| $l$ | $= l_n + l_a$ = total body length; see Fig. 1 |
| $l_a$ | = length of afterbody; see Fig. 1 |
| $l_n$ | = length of nose; see Fig. 1 |
| $M$ | = pitching moment |
| $M_o$ | = free-stream Mach Number |
| $N$ | = any number, also normal force in $c_N$ |
| $q$ | = free-stream dynamic pressure |
| $S_b$ | $= \pi t^2/4$ = reference area |
| $t$ | = body thickness; see Fig. 1 |
| $x$ | = distance from tip of cone; see Fig. 1 |
| $x_{c.p.}$ | = distance to center of pressure from tip of nose |
| $\alpha$ | = angle of attack |
| $\beta$ | $= [M_0^2 - 1]^{1/2}$ |

(3) INTRODUCTION

In 1946, Tsien,[1] using the fundamental equations for two-dimensional isentropic compressible flow about thin bodies, found a similarity parameter relating hypersonic flows about similar bodies. This powerful rule properly used would then relate the lift and drag due to pressure stresses acting on a given thin two-dimensional body at a given hypersonic Mach Number to the lift and drag due to pressure stresses acting on a thin two-dimensional body with identical thickness distribution at a different hypersonic Mach Number related to the given Mach Number by the similarity parameters. This version of the similarity rule has been used with considerable success to obtain two-dimensional airfoil force and moment coefficients.[2, 3]

Later, Hayes[4] indicated the rule could be extended to include three-dimensional bodies and could be used for nonisentropic, nonviscous flows with vorticity present. The similarity parameters for three-dimensional bodies were explicitly derived in references 5 and 6. It was suggested in reference 5 that the viscous cross force contribution to normal force may possibly be correlated by the hypersonic similarity rule also. The similarity parameters for the most general class of thin bodies were now defined and available for application.

The senior author of the present paper decided late in 1951 to test the similarity law for a commonly used aerodynamic body, the cone cylinder. If the similarity parameters, as applied to this shape, proved to be unique, as shown by experimental data, then a series of charts could be prepared from data taken on a systematically-chosen set of cone angles and afterbody lengths at a variety of supersonic Mach Numbers. These charts could be used to estimate normal force coefficients, pitching moment coefficients, and their axial distributions on any cone cylinder falling within the range of parameters covered by the charts. Reference 7 presents the correlation scheme suggested and used in the present paper.

One other contribution was essential to the correlation scheme proposed. In 1951 Van Dyke[8] showed that a simple modification of the hypersonic similarity parameters would extend the range of the rule down into the Mach Number range generally considered to be supersonic rather than hypersonic. This modification entailed replacing $M_o$ with $\beta$ whenever $M_o$ appeared in hypersonic similarity parameters. This contribution led the present authors to believe that wind-tunnel tests at Mach 1.5 and above could be used to prepare the design charts. The Naval Ordnance Laboratory 40 cm. by 40 cm. blowdown supersonic tunnel provided Mach Numbers in this range and was selected for the tests.

### (a) *The Hypersonic Similarity Rule for Three-Dimensional Bodies*

The hypersonic similarity law can be stated as follows. The normal force and pitching moment on two bodies are related and their flow fields similar, providing they have the same thickness distribution and identical values of the similarity parameters. This

Received June 29, 1956.

* Assistant to the Director of Scientific Research.

** Aerodynamics Engineer.

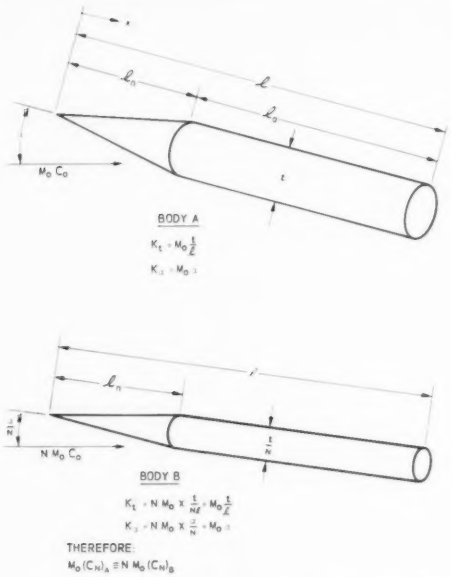


FIG. 1. Illustration of hypersonic similarity law for cone cylinders.

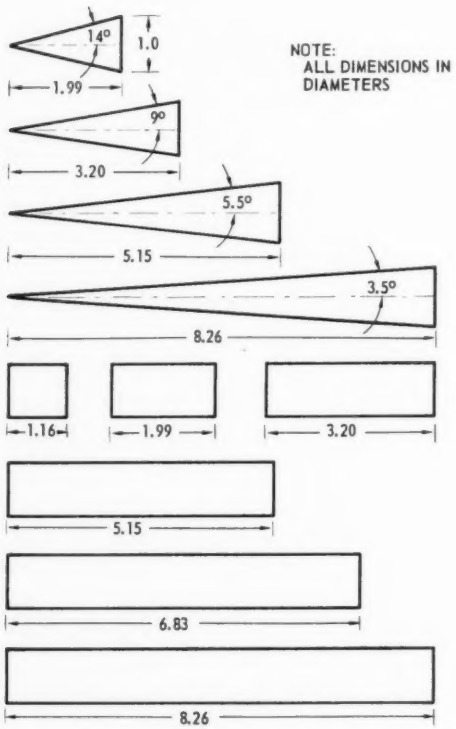


FIG. 2. Cone-cylinder combinations tested in Naval Ordnance Laboratory wind tunnel.

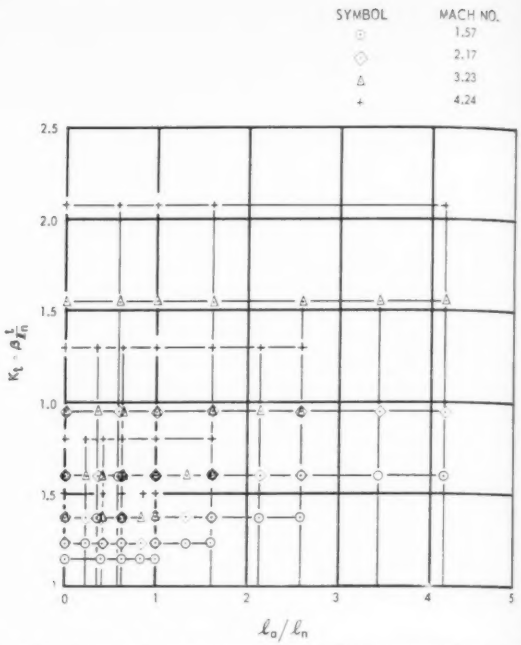


FIG. 3. Range of parameters $K_t$ and $l_a/l_n$ covered by Naval Ordnance Laboratory tests of cone cylinders.

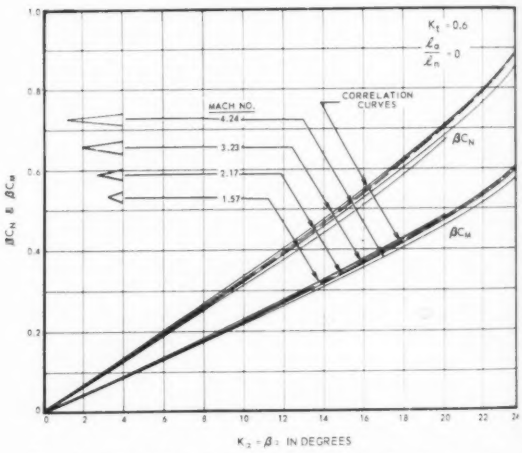


FIG. 4. Test of hypersonic similitude for slender cones.

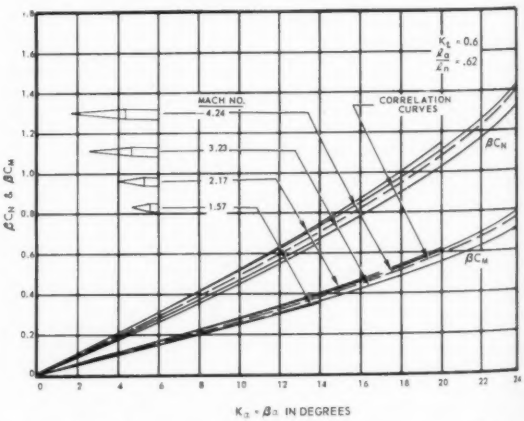


FIG. 5. Test of hypersonic similitude for slender cone cylinders.

law is illustrated in Fig. 1 for cone-cylinder bodies. In Fig. 1,

$$(l_a/l_n)_A = (l_a/l_n)_B$$

hence, the thickness distributions are identical. Also,

$$(K_t)_A = (K_t)_B$$

$$(K_\alpha)_A = (K_\alpha)_B$$

therefore, according to the similarity law,

$$M_o(C_N)_A = NM_o(C_N)_B$$

$$M_o(C_M)_A = NM_o(C_M)_B$$

This is the rule as outlined in references 5 and 6.

### (b) *Similarity Parameters Chosen for Cone-Cylinder Tests and Correlations*

Recalling that Van Dyke in reference 8 showed that replacing $M_o$ with $\beta$ in the similarity parameters whenever $M_o$ appeared would extend the Mach Number range of applicability of the parameters, the present authors planned to use this modified form of the parameter in this investigation. Also, because the requirement for identical thickness distributions is implicit in applying the similarity law, it was necessary to introduce an additional parameter to account for this. For cone cylinders this is very simple since two cone cylinders will have the same thickness distribution if the ratio of nose length to afterbody length is the same for both. Therefore, our similarity parameters are

$$K_t = \beta t/l_n$$

$$K_\alpha = \beta\alpha$$

and, for cone cylinders, $l_a/l_n$ is an additional parameter. $\beta C_N$ and $\beta C_M$ could be plotted versus $l_a/l_n$ with $K_\alpha$ (or $K_t$) as a parameter for different constant values of $K_t$, (or $K_\alpha$) if satisfactory uniqueness of the rule were shown by measurements.

### (c) *Range of Parameters in the Wind-Tunnel Tests*

The purpose of the proposed wind-tunnel tests was twofold: (1) to test the uniqueness of the hypersonic similarity rule for cone cylinders, and (2) having satisfactorily determined uniqueness, to obtain data for preparation of normal force and pitching moment coefficient charts which could then be used for *any* cone cylinder falling within the range of parameters of the charts.

The Naval Ordnance Laboratory 40 cm. by 40 cm. blowdown supersonic tunnel was selected for these tests. The test Mach Numbers were 1.57, 2.17, 3.23, and 4.24. A series of cone-cylinder bodies was chosen to systematically vary the parameters $K_\alpha$, $K_t$ and $l_a/l_n$ as well as to provide tests at different Mach Numbers on bodies having identical values of these parameters. Fig. 2 shows these bodies.

Fig. 3 shows the range of variation of the parameters $K_t$ and $l_a/l_n$ at different Mach Numbers. Note that

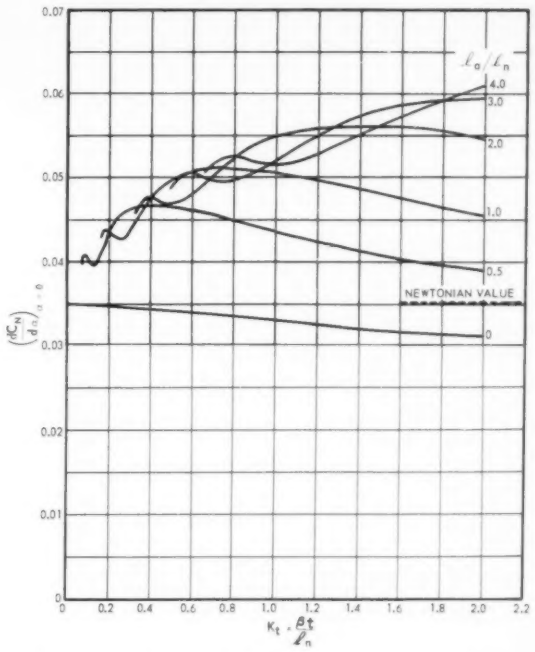


FIG. 6. Normal force coefficient slope at zero angle of attack.

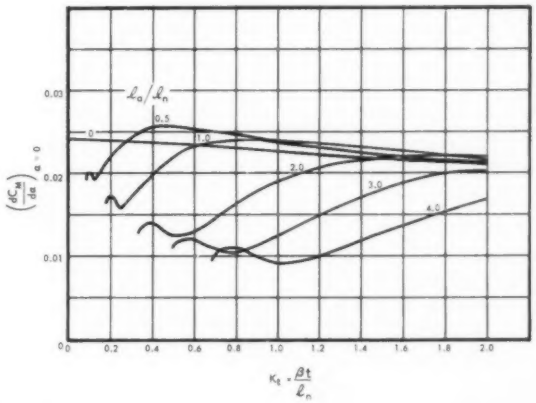


FIG. 7. Pitching moment coefficient slopes at zero angle of attack.

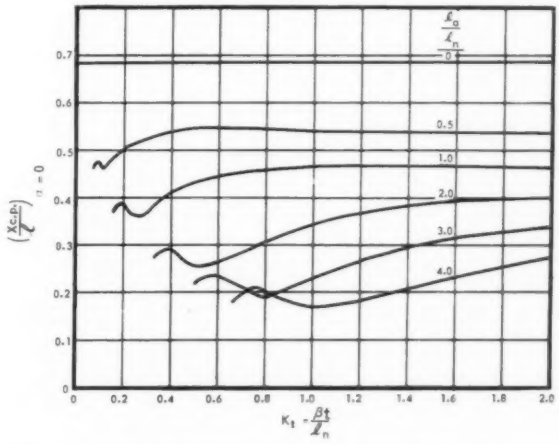


FIG. 8. Center of pressure location at zero angle of attack.

identical values of $K_t$ and $l_a/l_n$ were obtained at two or more Mach Numbers in no less than 18 different cases.

The range of parameters covered by these tests is

$$0 \leq K_\alpha \leq 42.5°$$

$$0.145 \leq K_t \leq 2.07$$

and

$$0 \leq l_a/l_n \leq 4.15$$

Because the 40 cm. by 40 cm. tunnel is the blow-down type, the reservoir pressure is atmospheric pressure and test section Reynolds Numbers are low. In most cases the boundary-layer flow over the models was laminar. For this reason the data and charts presented herein apply only to the case of laminar flow over cone cylinders. The authors have extended these charts to include an estimated change in the viscous cross force for turbulent cross flow but decided to eliminate the resulting charts in the present paper because of the additional uncertainty for this case. References 9 and 10 report the data taken during these tests.

## (4) Discussion

### (a) *Results of Experimental Uniqueness Test*

As shown in Fig. 3, measurements were made on several cone cylinders at different Mach Numbers for which the values of $K_t$ and $l_a/l_n$ were constant. These models would then be related to each other in the manner shown in Fig. 1. If the Hypersonic Similarity Law is valid, then plots of $\beta C_N$ and $\beta C_M$ versus $K_\alpha$ should superimpose in order to demonstrate uniqueness.

Figs. 4 and 5 illustrate this uniqueness test for cones ($l_a/l_n = 0$) and cone cylinders ($l_a/l_n = 0.62$) respectively at a value of $K_t = 0.60$. Uniqueness is shown to reasonable accuracy. In each case, the results for the lowest test Mach Number of 1.57 show least agreement, as would be expected as a consequence of the existence of lower Mach Number bound of applicability of the Hypersonic Similarity Rule. Also, at this Mach Number, transition to turbulent flow occurred on the longest of the cone-cylinder afterbodies.

### (b) *Charts for Normal Force and Pitching Moment Coefficient Slopes and Center of Pressure at Zero Angle of Attack*

Curves of the slopes of the normal force and pitching moment coefficients and center of pressure location at zero angle of attack for cone cylinders were prepared by correlating the measured data.

Fig. 6 shows $dC_N/d\alpha$ plotted versus $K_t$ with $l_a/l_n$ as a parameter. These curves reveal two trends. (1) for a given body ($l_a/l_n$ = constant, $t/l_n$ = constant), as $\beta$ increases, $dC_N/d\alpha$ can pass through several maximums and minimums, and (2) for a given nose and Mach Number ($K_t$ = constant) increasing the afterbody length (or $l_a/l_n$) at first increases $dC_N/d\alpha$, then decreases $dC_N/d\alpha$, then increases $dC_N/d\alpha$ and may repeat this cycle beyond the range of these data. Thus, it is possible that, for some ranges of afterbody length, the normal force of a cone cylinder at a small angle of attack can be decreased by extending the afterbody length. That is, there are regions of negative normal force distribution along long afterbodies following cone noses at small angle of attack. This behavior follows the trend predicted by linearized theory for pointed bodies.

Figs. 7 and 8 show $dC_M/d\alpha$ and $x_{c.p.}/l$ measurements at zero angle of attack correlated in a similar manner.

### (c) *Charts for Normal Force and Pitching Moment at Angles of Attack*

A large number of correlation charts giving $\beta C_N$ and $\beta C_M$ versus $l_a/l_n$ for different values of $K_\alpha$ were prepared for given constant values of $K_t$. However, in the interest of brevity, only a minimum number will be presented here. Extrapolation for inbetween values of $K_t$ will give reasonable accuracy.

Figs. 9, 10, 11, and 12 gives $\beta C_N$ versus $l_a/l_n$ for different values of $K_\alpha$ for constant values of $K_t = 0.25$, 0.50, 1.0, and 2.0, respectively. Figs. 13, 14, 15, and 16 give the corresponding correlations of $\beta C_M$ versus $l_a/l_n$ for the same values of $K_\alpha$ and $K_t$.

### (d) *Charts for Normal Force Coefficient Distribution Along the Afterbody*

Figs. 9 through 12 give curves of $\beta C_N$ versus $l_a/l_n$ for constant values of $K_\alpha$ and $K_t$. It is apparent that the slopes of these curves are related to the distribution normal force coefficient with increasing afterbody length. In fact, if $K_\alpha$ and $K_t$ are held constant,

$$\beta^2[dC_N/d(l_a/l)] = K_t[d(\beta C_N)/d(l_a/l_n)] \qquad (1)$$

where the right-hand side of Eq. (1) is obtained by measuring the slopes of lines of constant $K_\alpha$ on Figs. 9, 10, 11, and 12.

Figs. 17, 18, 19, and 20 show values of the normal force coefficient distribution parameter plotted versus $l_a/l_n$ for different values of $K_\alpha$ at values of $K_t = 0.25$, 0.50, 1.0, and 2.0, respectively. Examination of Figs. 17 and 18 reveal that for low values of $K_\alpha$ there are indeed areas of negative normal force along the afterbody for a given fixed value of nose angle, angle of attack, and Mach Number ($K_\alpha$, $K_t$ and $\beta$ held constant, $l_a/l_n$ varying).

### (e) *Accuracy of the Charts*

The accuracy of the charts was tested by comparing coefficients obtained from the correlation charts with measured data. Fig. 21 shows a comparison of $dC_N/d\alpha$ and $dC_M/d\alpha$ at zero angle of attack as obtained from the correlation charts of Figs. 6 and 7 with measured data for cone cylinders at $K_t = 0.60$. As shown on Fig. 3, data from $M_o = 1.57$, 2.17, and 3.23 are available for comparison for cone cylinders with several values of $l_a/l_n$. The agreement between correlation and measurement is satisfactory.

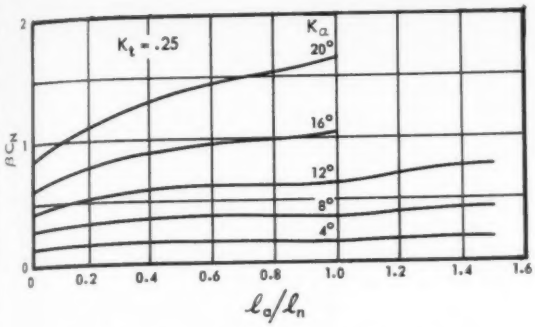


FIG. 9. Normal force coefficient for $K_t = 0.25$.

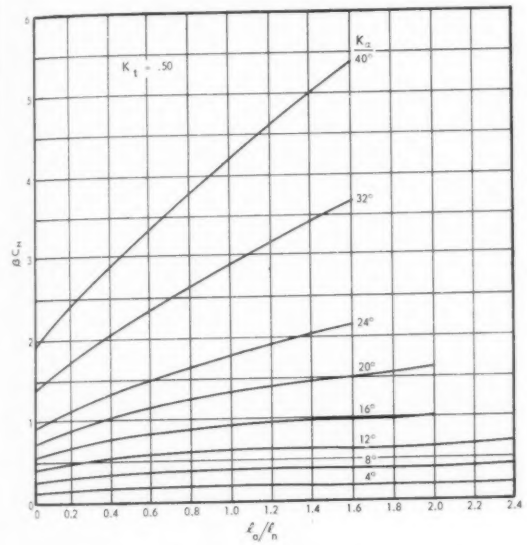


FIG. 10. Normal force coefficient for $K_t = 0.50$.

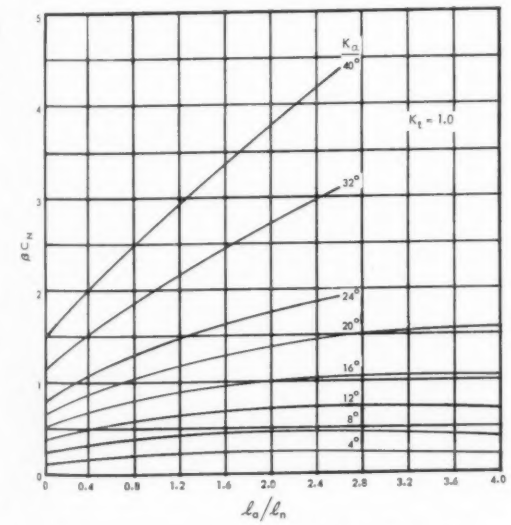


FIG. 11. Normal force coefficient for $K_t = 1.0$.

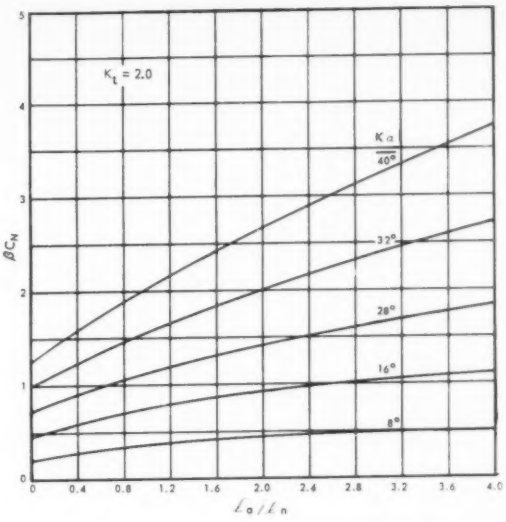


FIG. 12. Normal force coefficient for $K_t = 2.0$.

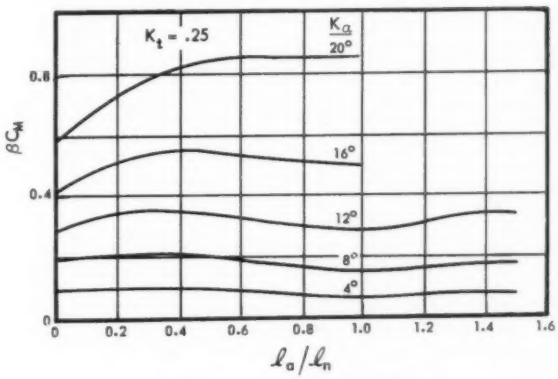


FIG. 13. Pitching moment coefficient for $K_t = 0.25$.

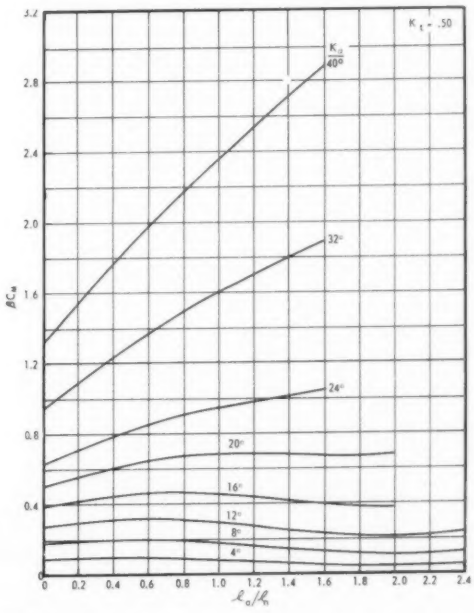


FIG. 14. Pitching moment coefficient for $K_t = 0.50$.

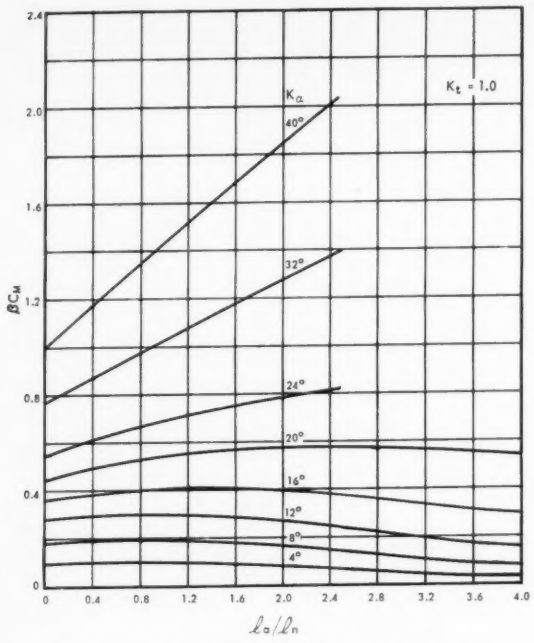


FIG. 15. Pitching moment coefficient for $K_t = 1.0$.

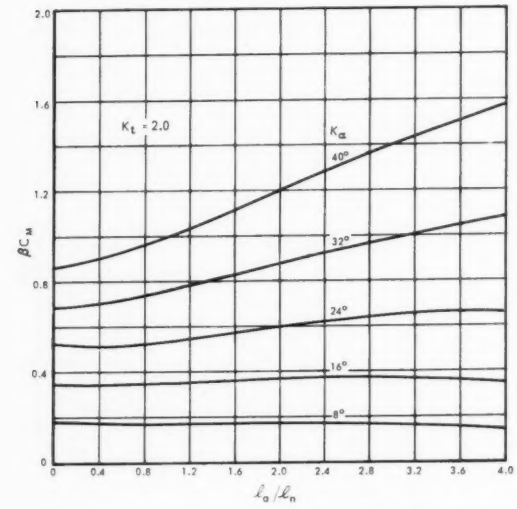


FIG. 16. Pitching moment coefficient for $K_t = 2.0$.

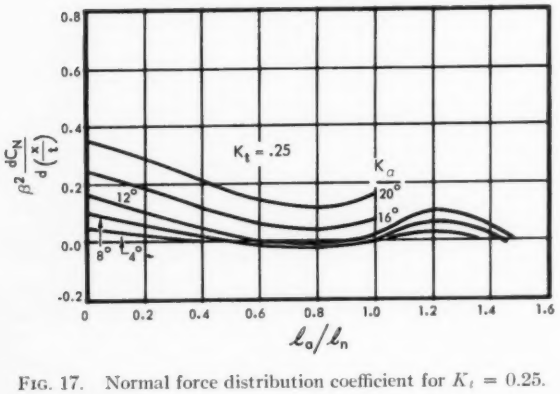


FIG. 17. Normal force distribution coefficient for $K_t = 0.25$.

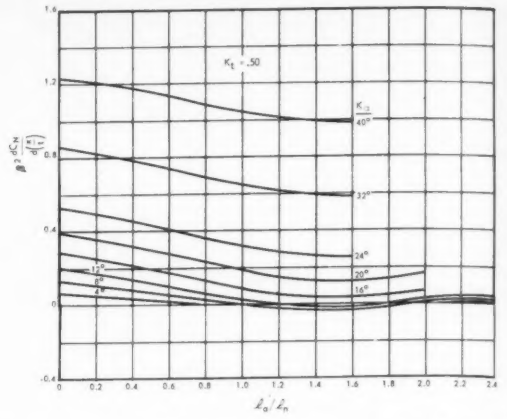


FIG. 18. Normal force coefficient distribution for $K_t = 0.50$.

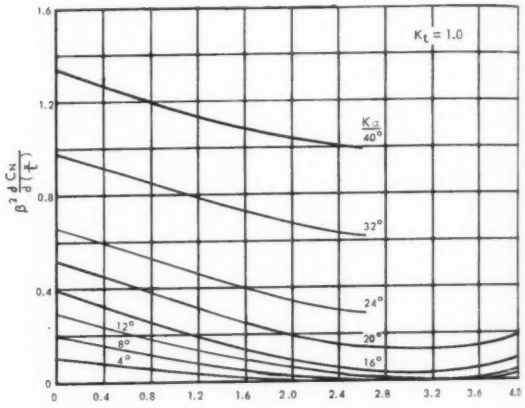


FIG. 19. Normal force coefficient distribution for $K_t = 1.0$.

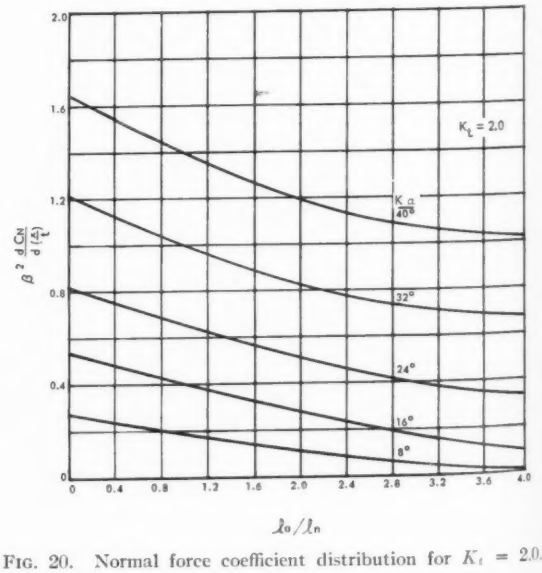


FIG. 20. Normal force coefficient distribution for $K_t = 2.0$.

## (5) Conclusions

Wind tunnel test data for normal force and pitching moment coefficients for cone cylinders have been correlated using the Hypersonic Similarity Rule and satisfactory uniqueness of the rule was demonstrated for cone cylinders.

Correlation plots were prepared using the wind tunnel data which can be used to obtain normal force and pitching moment coefficients, center of pressure and normal force distribution for any cone cylinder at any angle of attack and Mach Number within the range of the parameters of the plot. These limitations are, first,

$$M_o \leq 1.5$$

second,

$$l_n/t \leq 2.0$$

third,

$$\alpha \leq 42.5°/\beta$$

The charts apply for the case of laminar flow over the cone cylinders.

## Appendix—Use of the Correlation Charts

In general, for air-frame stability and air load analysis it is desirable to present aerodynamic data in terms of $C_N$ and $C_M$ versus $\alpha$ and $dC_N/dx$ versus $x$ at a constant Mach Number. Since the data in the correlation charts is presented in terms of the similarity parameters, it is desirable to outline how the conventional representation can be obtained from the correlation charts.

### (a) *Normal Force and Pitching Moment Coefficients at a Constant Mach Number*

The procedure for obtaining $C_N$ or $C_M$ versus $\alpha$ is described as follows.

(1) For the Mach Number and cone cylinder of interest determine $l_a/l_n$ and $K_t$.

(2) Enter Figs. 9 through 12 (or 13 through 16 for $\beta C_M$) at the proper value of $l_a/l_n$ for three values of $K_t$, two of which bracket the $K_t$ of interest.

(3) Read off values of $\beta C_N$ (or $\beta C_M$) for various values of $K_\alpha$ for the three values of $K_t$ at the proper value of $l_a/l_n$. Plot $\beta C_N$ (or $\beta C_M$) versus $K_t$ for different values of $K_\alpha$.

(4) Enter the plot of $\beta C_N$ (or $\beta C_M$) versus $K_t$ for various values of $K_\alpha$ prepared under step (3) at the proper value of $K_t$ to obtain $\beta C_N$ versus $K_\alpha$ for the body under consideration. The conversion to $C_N$ versus $\alpha$ is obvious.

### (b) *Normal Force Distribution Along the Afterbody at a Constant Mach Number*

The procedure for obtaining normal force coefficient distribution along the afterbody from the correlation charts for a given cone cylinder at a given Mach Number is as follows.

(1) For the cone cylinder and Mach Number under consideration determine $K_t$ and $l_a/l_n$. For various afterbody stations determine the appropriate values of $l_a/l_n$.

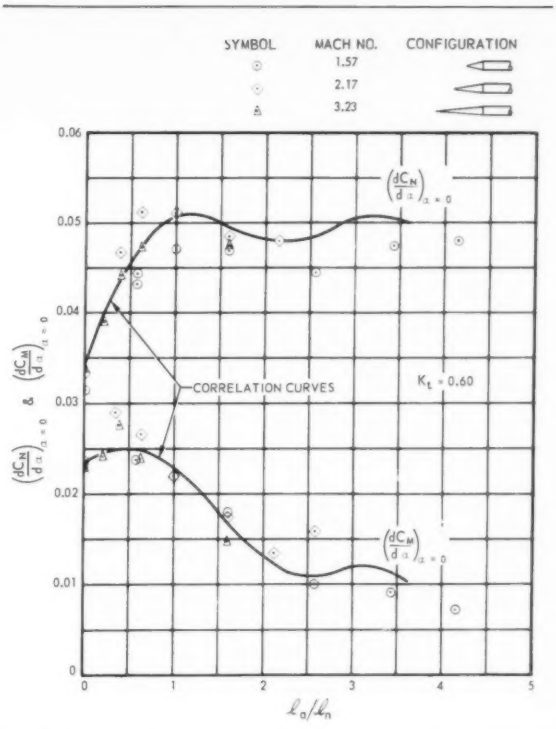


Fig. 21. Comparison of correlation curves with experimental data for $K_t = 0.60$.

(2) Enter Figs. 17 through 20 at the selected values of $l_a/l_n$ picked under step (1) on three charts for three values of $K_t$, two of which bracket the value of $K_t$ of interest. Read off values of $\beta^2[dC_N/d(l_a/t)]$ for various values of $K_\alpha$ and plot $\beta^2[dC_N/d(l_a/t)]$ versus $K_t$ for several $K_\alpha$ and the selected values of $l_a/l_n$.

(3) Enter plots prepared under step (2) at values of $K_t$ under consideration and obtain $\beta^2[dC_N/d(l_a/t)]$ versus $K_\alpha$ for selected values of $l_a/l_n$.

(4) $dC_N/d(l_a/t)$ can now be plotted versus $l_a/t$ for several values of $\alpha$ from step (3).

(5) For the cone nose, since pressure is constant along a meridian of the cone, $dC_N/d(x/t) = 8C_N(x/t)\tan^2\theta_n$, where $C_N$ is obtained from the plots in the manner described previously for $l_a/l_n = 0$.

If the normal force coefficient distribution is to be plotted over the entire length of the cone cylinder with the origin at the cone tip, the values of $dC_N/d(l_a/t)$ determined for the afterbody should be displaced a distance $l_n/t$ from the tip—i.e.,

$$(x/t) = (l_n/t) + (l_a/t) \qquad \text{for} \qquad x \geq l_n \qquad (2)$$

where $x$ is distance from cone tip.

## References

[1] Tsien, H. S., *Similarity Laws of Hypersonic Flows*, Journal of Mathematics and Physics, Vol. XXV, No. 3, p. 247, October, 1946.

(*Continued on page 392*)

# Readers' Forum

*BRIEF REPORTS of investigations in the aeronautical sciences and discussions of papers published in the JOURNAL are presented in this special department. Entries must be restricted to a maximum of 1,300 words or the equivalent of one JOURNAL page including formulas and illustrations. Publication is completed as soon as possible after receipt of the material. The Editorial Committee does not hold itself responsible for the opinions expressed by the correspondents.*

## Contents


**Subsonic Oscillatory Control Surface Coefficients Computed by the Method of Reissner and Haskind** ..... HENRY E. FETTIS 378

**The Heated Vertical Plate at High Prandtl Number** ..... K. STEWARTSON AND L. T. JONES 379

**Flow in the Forward Stagnation Region of Blunt Bodies** ..... ROBERT W. TRUITT 380

**On the Flutter of Infinitely Long Panels on Many Supports** ..... ROBERT W. LEONARD AND JOHN M. HEDGEPETH 381

**A Note on Steady-State Aeroelasticity** .. ALAN H. WICKENS 383

**The Buckling of Triangular or Skew Plates** ..... VICTOR I. WEINGARTEN 384

**On Complex Roots of an *n*th Degree Equation** ..... C. A. M. VAN DER LINDEN 384

**On the Prediction of Gust and Buffet Response of Wings and Airfoils** ..... ALBERT S. RICHARDSON, JR. 385

**Experiment on the Variation of Airfoil Properties With Reynolds Number** ..... A. F. CHARWAT 386

**Comments on the Lagrangian Multiplier in Drag Minimization** ..... ROBERT T. STANCIL 388

**Thermal Buckling of Clamped Cylindrical Shells** ..... WILLIAM ZUK 389

**A Simple Relation Between the Shock and Expansion Pressure Coefficients for Two-Dimensional Hypersonic Flow** ..... J. L. RAYMOND AND E. P. WILLIAMS 389

**A Note on Cone Base Pressures in Hypersonic Flow** ..... RICHARD D. LINNELL 390

**An Extension of Donnell's Equation for a Circular Cylindrical Shell** ..... TSU-TAO LOO 390

**Real Part of the Square Root of a Complex Number** ..... E. V. LAITONE 391

**Note on the Change From Multi-Cell to Single-Cell Rotating Stalls** ..... F. CHEERS 392


## Subsonic Oscillatory Control Surface Coefficients Computed by the Method of Reissner and Haskind*


Henry E. Fettis

*Mathematician, Aeronautical Research Laboratory, Wright Air Development Center, ARDC, Wright-Patterson AFB, Ohio*



December 7, 1956


IN A PREVIOUS NOTE by the author and G. Blanch,[11] values were given for coefficients of total lift and moment at Mach Number 0.7, for a two-dimensional airfoil oscillating in translation and pitch. The present values represent a by-product of these calculations, obtained by evaluating the partial integrals of the pressure distribution and its first moment. The resulting values give the force and moment on a control surface attached to an airfoil oscillating in translation and pitch. The corresponding coefficients are defined (as in reference 9) such that

$$\text{total force on control surface} = \pi\rho b^3\nu^2\{P_h(h/b) + P_\alpha(\alpha)\}$$

$$\text{total moment about control surface leading edge} = \pi\rho b^4\nu^2\{T_h(h/b) + T_\alpha(\alpha)\}$$

where $\nu$ is the frequency of oscillation. From these coefficients it is then possible to obtain coefficients of total lift and moment due to translational and rotational motions of the control surface, as defined in reference 9. The relations employed are given in reference 10. The computations were made for Mach Number 0.7 and for the following values of reduced frequency and control surface chord:

$$\omega = 0.02(0.02)0.1(0.1)0.7,\ 2.94,\ 3.643$$
$$c = -0.9(0.1)0.9$$

They may be obtained from the author by request. In the present note only representative values are given for the purpose of comparison with the results by other methods, obtained from the following sources (see Table 1): (a) Turner and Rabinowitz[6, 7] (approximate solution of Possio's integral equation), (b) Fettis[7] (approximate solution of Possio's integral equation), and (c) Timman and Van de Vooren[12] (exact solution employing Mathieu functions). The correspondence between the present coefficients and those of reference 12 is as follows:

$$\omega^2 T_h = n_a' + in_a''$$
$$\omega^2 T_\alpha = [n_b' + (1/2)n_a'] + i[n_b' + (1/2)n_a'']$$
$$\omega^2 L_\beta = k'_c + ik''_c$$
$$\omega^2 M_\beta = [m_c' + (1/2)k_c'] + i[m_c'' + (1/2)k_c'']$$

Comparison of the four sets of values indicates good agreement throughout, although the two sets of results based on the exact theory do not agree as well when $\omega < 0.1$. This discrepancy is undoubtedly due to the fact that the coefficients do not lend


* The author is indebted to Dr. Gertrude Blanch for her assistance in formulating the problem and to Lt. Francis T. Cryan for programing and carrying out the computations on the E.R.A. 1103 automatic digital computer.

TABLE 1

$e = .6\ (\tau = .2)$

$\omega^2 T_h = n'_a + i\, n''_a$

| $\omega$ | I | II | III | IV |
|---|---|---|---|---|
| .04 | -.0000612 -.0006151 i | -.000062 -.000615 i | -.000061 -.000615 i | -.00006 -.00062 i |
| .08 | -.0000579 -.0010966 i | -.000059 -.001096 i | -.000059 -.001101 i | -.00006 -.00109 i |
| .20 | +.0007029 -.0023152 i | .000700 -.002315 i | .000670 -.002364 i | .00071 -.00232 i |
| .40 | +.0043684 -.0045589 i | .00438 -.00457 i | .00400 -.00484 i | .00437 -.00454 i |

$\omega^2 T_a = (n'_b + 1/2\, n'_a) + i(n''_b + 1/2\, n''_a)$

| $\omega$ | I | II | III | IV |
|---|---|---|---|---|
| .04 | -.015445 -.0000292 i | -.01544 -.0000261 i | -.01546 -.0000261 i | -.01546 -.00006 i |
| .08 | -.013792 -.002260 i | -.01378 -.00224 i | -.01385 -.002241 i | -.01380 -.00226 i |
| .20 | -.011029 -.010585 i | -.01104 -.01057 i | -.01131 -.01042 i | -.01104 -.01058 i |
| .40 | -.007878 -.025241 i | -.00790 -.02528 i | -.00885 -.02401 i | -.00759 -.02522 i |

$\omega^2 L_\beta = k'_c + i\, k''_c$

| $\omega$ | I | II | III | IV |
|---|---|---|---|---|
| .04 | -1.30498 .30089 i | -1.3055 +.3006 i | -1.3048 +.3008 i | -1.3116 +.3047 i |
| .08 | -1.12491 .37107 i | -1.1251 +.3709 i | -1.1244 +.3708 i | -1.1291 +.3733 i |
| .20 | -.84865 .36572 i | -.8484 +.3660 i | -.8466 +.3638 i | -.8488 +.3660 i |
| .40 | -.65350 .31076 i | -.6832 +.3123 i | -.6790 +.3000 i | -.6834 +.3106 i |

$\omega^2 M_\beta = (m'_c + 1/2\, k'_c) + i\,(m''_c + 1/2\, k''_c)$

| $\omega$ | I | II | III | IV |
|---|---|---|---|---|
| .04 | -.57540 -.01736 i | ------- ------ | -.5755 -.0173 i | -.5743 -.0176 i |
| .08 | -.58330 -.02926 i | ------- ------ | -.5829 -.0291 i | -.5825 -.0294 i |
| .20 | -.60826 -.049678 i | ------- ------ | -.6046 -.0491 i | -.6084 -.0497 i |
| .40 | -.65061 -.057094 i | ------- ------ | -.6318 -.0602 i | -.6506 -.0571 i |

$\omega^2 T_\beta = n'_c + i\, n''_c$

| $\omega$ | I | II | III | IV |
|---|---|---|---|---|
| .04 | ----- ------ | ------ ------ | -.0316 +.000346 i | -.03157 +.00035 i |
| .08 | ----- ------ | ------ ------ | -.0307 -.000596 i | -.03067 -.00060 i |
| .20 | ----- ------ | ------ ------ | -.0295 -.00433 i | -.02964 -.00440 i |
| .40 | ----- ------ | ------ ------ | -.0291 -.01022 i | -.02994 -.01048 i |

Key: Column I: **Present Values**
Column II: Dietze
Column III: **AFTR 6688**
Column IV: Timman and Van de Vooren

themselves to interpolation in that interval. For $\omega < 0.1$, the coefficients computed by the two approximate methods[6, 7] agree very well with those obtained by the formulation of Reissner and Haskind, while for $\omega > 0.1$ the coefficients obtained by the method of Dietze agree better with those found by the two exact formulations than do those of reference 7. This latter discrepancy is to be expected, in view of the fact that the linear approximation to the kernel of the Possion integral equation is a very crude one for $\omega > 0.1$.

To date, no values have been obtained by the present exact method for the hinge moment coefficient, $T_\beta$, due to control surface motion, since computation of this coefficient requires a complete reformulation of the problem.

## References


[1] Reissner, E., and Sherman, S., *Compressibility Effects in Flutter*, Curtiss-Wright Research Laboratory Report No. SB-240-S-1, 1944.

[2] Haskind, M. D., *Oscillations of a Wing in a Subsonic Gas Flow*, Prikl. Mat. I. Mekh. (Moscow), Vol. XI, No. 1, pp. 129–146, 1947 (in Russian). Also available as Translation No. A 9-T-22, Air Materiel Command and Brown University.

[3] Reissner, E., *On the Application of Mathieu Functions in the Theory of Subsonic Compressible Flow Past Oscillating Airfoils*, NACA TN 2363, May, 1951.

[4] Timman, R., and van de Vooren, A. I., *Theory of the Oscillating Wing with Aerodynamically Balanced Control Surface in a Two-Dimensional, Subsonic, Compressible Flow*, Report F. 54, National Aeronautical Research Institute, Amsterdam, 1949.

[5] Dietze, F., *The Air Forces of the Harmonically Vibrating Wing in a Compressible Medium at Subsonic Velocity*, Part I, AF Translation #F-TS-506RS, August 9, 1946, and F-TS-948-RE, March, 1947; Part II, AF Translation #F-TS-948RE, March, 1947, and Chance Vought Report No. GTR-65, June, 1947.

[6] Turner, M. J., and Rabinowitz, S., *Aerodynamic Coefficients for an Oscillating Airfoil with Hinged Flap, with Tables for a Mach Number of 0.7*, NACA TN 2213, 1950.

[7] Fettis, Henry E., *Tables of Lift and Moment Coefficients for an Oscillating Wing Aileron Combination in Two-Dimensional Subsonic Flow*, Air Force Technical Report No. 6688, Supp. No. 1, October, 1954.

[8] Blanch, Gertrude, *Tables of Lift and Moment Coefficients For Oscillating Airfoils in Subsonic Compressible Flow*, National Bureau of Standards Report No. 2260, February 6, 1953.

[9] Smilg, Ben, and Wasserman, Lee S., *Application of Three Dimensional Flutter Theory to Aircraft Structures*, Air Force Technical Report No. 4798, July 9, 1942.

[10] Fettis, Henry E., *Reciprocal Relations in the Theory of Unsteady Flow Over Thin Airfoil Sections*, Proceedings of The Second Midwestern Conference on Fluid Mechanics, The Ohio State University, March, 1952.

[11] Blanch, Gertrude, and Fettis, Henry E., *Subsonic Oscillatory Aerodynamic Coefficients Computed by the Method of Reissner and Haskind*, Readers' Forum, Journal of the Aeronautical Sciences, Vol. 20, No. 12, pp. 851–853, December, 1953.

[12] Van de Vooren, A. I., *Aerodynamic Coefficients of an Oscillating Airfoil with Control Surface in Two-Dimensional Subsonic Flow*, Journal of the Aeronautical Sciences, Vol. 20, No. 3, pp. 153–159, March, 1953. (Corrected values appear in N.L.L. Report No. F-151.)


## The Heated Vertical Plate at High Prandtl Number


K. Stewartson and L. T. Jones*

*Reader and Research Student, Respectively, in Applied Mathematics, Bristol University, England*



December 12, 1956


IN A RECENT PAPER, Morgan and Warner[1] considered several problems of heat transfer at high Prandtl Number $\sigma$. For the laminar convection about a heated vertical plate, they used an order of magnitude argument to find the dependence of Nusselt Number and skin friction on $\sigma$, determining the coefficients from some numerical calculations of Ostrach.[2] It is possible, however, to solve this problem independently; the results are also of interest because the boundary layer is divided into two parts, of which the inner is *independent* of the outer. Using the notation in reference 1 we have to solve

$$\left.\begin{aligned} f''' + 3ff'' - 2f'^2 + h &= 0 \\ h'' + 3\sigma f h' &= 0 \end{aligned}\right\} \qquad (1)$$

where $f' = df/d\zeta$ etc., $\sigma$ is large, and

$$f(0) = f'(0) = h(0) - 1 = f'(\infty) = h(\infty) = 0 \qquad (2)$$

Here $f$ defines the stream function and $h$ the temperature.

Now write[1]

$$\eta_1 = (3\sigma)^{1/4}\zeta, \quad f(\zeta) = (3\sigma)^{-3/4} f_1(\eta), \quad h(\zeta) = h_1(\eta) \qquad (3)$$

and, in the limit $\sigma \to \infty$, Eqs. (1) reduce to

$$f_1''' + h_1 = 0, \quad h_1'' + f_1 h_1' = 0 \qquad (4)$$

The relevant boundary conditions are now

$$f_1(0) = f_1'(0) = h_1(0) - 1 = h_1(\infty) = f_1''(\infty) = 0 \qquad (5)$$

* Now at Atomic Weapons Research Establishment, Aldermaston, England.

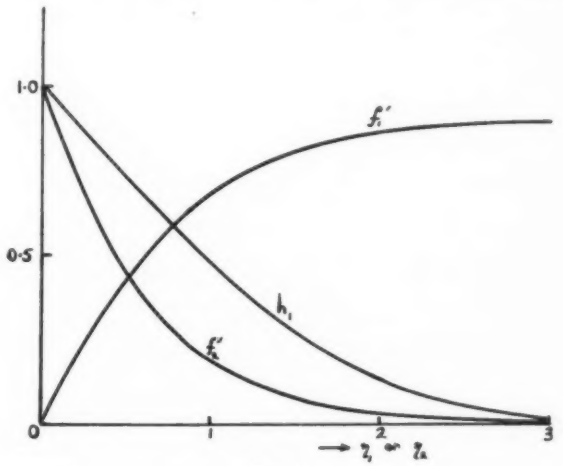


FIG. 1.

and the appropriate solutions for $f_1'$ and $h_1$ are displayed in Fig. 1. From the numerical computation it is found that

$$f_1''(0) = 1.087, \quad h_1'(0) = -0.540, \quad f_1'(\infty) = +0.892 \quad (6)$$

Thus, after emerging from this inner layer which we may call the temperature boundary layer, $h$ is exponentially small, $f = 0(\sigma^{-3/4})$, $f'' = o(\sigma^{-1/4})$, and $f' = 0(\sigma^{-1/2})$. A velocity boundary layer must now be introduced to reduce $f'$ to zero. In it we write

$$\eta_2 = (0.892)^{1/2}(3\sigma)^{-1/4}\zeta, \quad f(\zeta) = (0.892)^{1/2}(3\sigma)^{-1/4} f_2(\eta) \quad (7)$$

and neglect $h$ so that

$$f_2''' + 3f_2f_2'' - 2f_2'^2 = 0 \quad (8)$$

From a comparison between Eqs. (7) and (3) it follows that in the limit $\sigma \to \infty$ the boundary conditions satisfied by $f_2$ must be

$$f_2(0) = 0, \quad f_2'(0) = 1, \quad f_2'(\infty) = 0 \quad (9)$$

while $f_2''(0)$ need not vanish.

The appropriate function $f_2'$ is sketched in Fig. 1, and from the numerical computation it is found that

$$f_2''(0) = -1.541, \quad f_2(\infty) = 0.599 \quad (10)$$

Thus there are two boundary layers—one of thickness $0(\sigma^{-1/4})$ in which the temperature difference $h$ is brought to zero, and one of thickness $0(\sigma^{1/4})$ in which the component of velocity parallel to the plate is brought to zero again.

Combining the results we have

$$\left.\begin{aligned} f''(0) &= 0.826\sigma^{-1/4}, \quad h'(0) = -0.711\sigma^{1/4}, \\ f(\infty) &= 0.430\sigma^{-1/4} \end{aligned}\right\} \quad (11)$$

when $\sigma$ is large. The constants in the formulas for $f''(0)$ and $h'(0)$ are slightly higher than those in reference 1, the second being nearer the approximate value $-0.718$ obtained by Eckert.[3] Comparison of $f(\infty)$ with Ostrach's results is difficult because he does not explicitly give it, but it is inferred from his tables that $f(\infty)\sigma^{1/4} = 0.437$, 0.426, and 0.470 at $\sigma = 10$, 100, and 1,000, respectively.

### References


[1] Morgan, G. W., and Warner, W. H., *On Heat Transfer in Laminar Boundary Layers at High Prandtl Number*, Journal of the Aeronautical Sciences, Vol. 23, No. 10, pp. 937–948, October, 1956.

[2] Ostrach, S., *An Analysis of Laminar Free-Convection Flow and Heat Transfer About a Flat Plate Parallel to the Direction of the Generating Body Force*, NACA Rep. 1111, 1953.

[3] Eckert, E., *Einführung in der Wärme und Stoffaustausch*, p. 116; Springer-Verlag, Berlin, 1949.


## Flow in the Forward Stagnation Region of Blunt Bodies


Robert W. Truitt

*Professor of Aeronautical Engineering, Virginia Polytechnic Institute, Blacksburg, Va.*


December 15, 1956

### Introduction

Acknowledge of the flow in the forward stagnation region of blunt bodies is important in the aerodynamic heating problem. The velocity $u_\delta$ varies with $x$ along the surface in the stagnation region—i.e., $u_\delta = \beta x$[1]. For incompressible flow, the velocity gradient $\beta$ has the value of $4U/D$ for cylinders and $3U/D$ for spheres, where the $D$'s are the respective diameters and $U$ is the velocity of the undisturbed stream.

### Supersonic Flow

In the case of supersonic flow, a shock wave stands in front of the blunt body and forms a region of subsonic (nearly incompressible) flow around the stagnation region. It is anticipated that in the stagnation region, $\beta$ for supersonic flow could be predicted closely by potential theory, using as free-stream conditions those behind the center of the detached shock wave. If, for the potential-flow theory, use is made of the solution for the blunt body in a uniform stream at *true* infinity, the values thus obtained for $\beta$ are found by experiment to be entirely inadequate. The reason is that, at high supersonic speeds, the proximity of the detached shock wave alters considerably the potential flow in the stagnation region. For example, a body with a hemispherical (or cylindrical) nose moving at hypersonic speeds would be enclosed, over the nose region, by a "sphere (or cylinder) of silence." This means that the character of the low-speed flow in the vicinity of the nose region is very nearly equivalent to the incompressible flow about a sphere (or cylinder) due to the movement of a concentric spherical (or cylindrical) shell. These potential-flow solutions have been given by Stokes as[2]

$$\phi_{\text{sphere}} = [a^3U/(b^3 - a^3)][r + (b^3/2r^2)] \cos\theta + Ur\cos\theta \quad (1)$$

for the sphere, and

$$\phi_{\text{cyl}} = [Ua^2/(b^2 - a^2)][r + (b^2/r)] \cos\theta + Ur\cos\theta \quad (2)$$

for the cylinder, where $\phi$ is the scalar potential, $a$ is the radius of the sphere (or cylinder), $b$ is the radius of the concentric shell, $r$ is the radial distance ($a \leq r \leq b$) at the angle $\theta$, and $U$ is the "free-stream" velocity at $r = b$, $\theta = 0°$. (See Fig. 1.)

Appropriate derivatives of Eqs. (1) and (2) will give, of course, the velocity components in the flow field ($a \leq r \leq b$) and thus provide a complete description of the embedded incompressible flow near the stagnation region. The tangential (resultant) velocity on the surface ($r = a$) is of particular interest and is given as

$$-\frac{1}{r}\frac{\partial\phi}{\partial\theta} = q_{\theta_{\text{sphere}}} = \left[1 + \frac{2 + (b/a)^3}{2[(b/a)^3 - 1]}\right] U\sin\theta \quad (3)$$

for the sphere, and

$$q_{\theta_{\text{cyl}}} = \left[1 + \frac{(b/a)^2 + 1}{(b/a)^2 - 1}\right] U\sin\theta \quad (4)$$

for the cylinder, where $b/a$ can now be considered as a shock detachment parameter. Using Eqs. (3) and (4), the expressions for the pressure distributions over the surface, referred to the velocity $U(r = b, \theta = 0°)$, are

$$C_{p_{\text{sphere}}} = 1 - \left(\frac{q_{\theta_{\text{sphere}}}}{U}\right)^2 = 1 - \left[1 + \frac{2 + (b/a)^3}{2[(b/a)^3 - 1]}\right]^2 \sin^2\theta \quad (5)$$

$$C_{p_{\text{cyl}}} = 1 - \left[1 + \frac{(b/a)^2 + 1}{(b/a)^2 - 1}\right]^2 \sin^2\theta \quad (6)$$

Note that when $b \to \infty$, Eqs. (5) and (6) reduce to the well-known expressions for flow in a uniform stream at *true* infinity—namely,

$$C_{p_{\text{sphere}}}\big|_{b\to\infty} = 1 - (9/4)\sin^2\theta \quad (7)$$

$$C_{p_{\text{cyl}}}\big|_{b\to\infty} = 1 - 4\sin^2\theta \quad (8)$$

It is clear from Eqs. (5) and (6) that the pressure distributions are strong functions of the shock detachment parameter $b/a$.

The stagnation velocity gradients, $\beta_U$, referred to the velocity $U(r = b, \theta = 0°)$, are, from Eqs. (3) and (4), using $\theta = 2x/D = x/a$,

$$\left.\frac{dq_{\theta_{\text{sphere}}}}{dx}\right|_{x=0} = \beta_{U_{\text{sphere}}} = \frac{2U}{D}\left[1 + \frac{2 + (b/a)^3}{2[(b/a)^3 - 1]}\right] \quad (9)$$

$$\beta_{U_{\text{cyl}}} = \frac{2U}{D}\left[1 + \frac{(b/a)^2 + 1}{(b/a)^2 - 1}\right] \quad (10)$$

Again, when $b \to \infty$, the stagnation velocity gradients reduce to the well-known values for flow in a uniform stream at *true* infinity—namely, $3U/D$ for spheres and $4U/D$ for cylinders. On the other hand, Eqs. (9) and (10) show the stagnation velocity gradients to be dependent on the shock detachment distance $b$ –

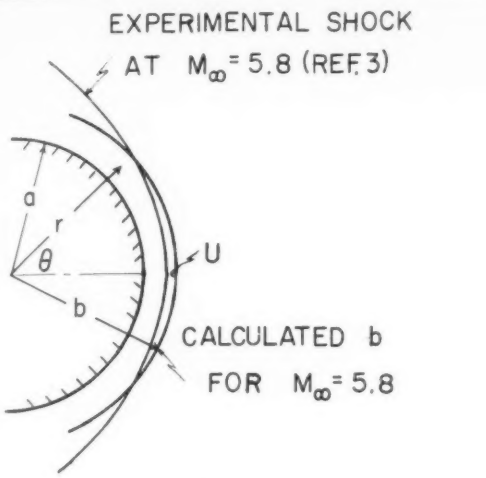


FIG. 1.

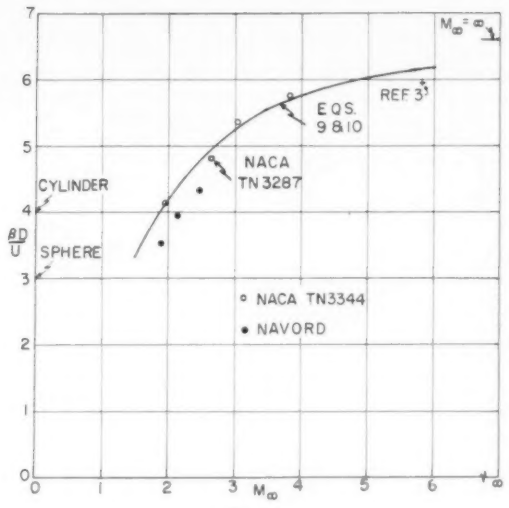


FIG. 2.

$a$—i.e., $\beta_U$ depends strongly on the free-stream Mach Number.

If it is assumed that, for hypersonic speeds, the pressure distribution in the low-speed stagnation region is adequately described by Eqs. (5) and (6), it is easy to show that the pressure distribution $C_{p_s}$, referred to the supersonic free stream, is given by

$$C_{p_s} = (2/\gamma M_\infty^2) \left\{ [(\gamma/2) M_1^2 (C_p) + 1] \times [(1 + \gamma M_\infty^2)/(1 + \gamma M_1^2)] - 1 \right\} \quad (11)$$

In Eq. (11), $C_p$ is the low-speed pressure distribution [Eq. (5) or (6)], $M_\infty$ is the free-stream Mach Number at infinity; and $M_1$ is the low subsonic Mach Number just downstream of the normal portion of the shock ($r = b, \theta = 0°$). The Mach Numbers $M_\infty$ and $M_1$ are related by the normal-shock expression

$$M_1 = \sqrt{\frac{1 + [(\gamma - 1)/2] M_\infty^2}{\gamma M_\infty^2 - [(\gamma - 1)/2]}} \quad (12)$$

### Newtonian Boundary Condition

Experimental pressure distributions for hypersonic flow over cylindrical and hemispherical noses follow the modified Newtonian type.[3] Thus, values of $b/a$ for the sphere and cylinder can be found from Eq. (11) by imposing, as a boundary condition, a single value of the modified Newtonian pressure distribution in the low-speed stagnation region—i.e., where $\theta$ is small. For example, assume the modified Newtonian pressure relation at $\theta = 15°$:

$$C_{p_s}/C_{p_{stag}} = \cos^2 \theta = 0.933 \quad (13)$$

Using this single value for $\theta = 15°$ in Eq. (11), values of $b/a$ for the sphere and cylinder can be calculated for a series of hypersonic Mach Numbers. Once the values of $b/a$ have thus been determined, it is a simple matter to calculate the stagnation velocity gradients [Eqs. (9) and (10)] and the velocity and pressure distributions [Eqs. (3), (4), and (11)] for any hypersonic Mach Number.

### Results

The shock detachment parameter $b/a$ has been calculated by the present method for a sphere and cylinder at $M_\infty = 5.8$; the results for the sphere are shown compared with experiment in Fig. 1. It is seen that the calculated value of $b$ agrees with the "average" radius of the experimental shock; similar results were found for the cylinder. It is important to note that a comparison of the theoretical ratio $(b/a)_{sphere}/(b/a)_{cyl}$, for $M_\infty = 5.8$, shows excellent agreement with the experimental ratio measured at the nose.

The calculated values of the dimensionless stagnation velocity gradient $\beta D/U$ are plotted versus $M_\infty$ in Fig. 2; the experimental values are for a hemispherical nose. Although the values of $b/a$ for a cylinder and sphere are different for the same Mach Number, the values of $\beta D/U$ are the same in the hypersonic range.

Pressure distributions have been calculated for a sphere at $M_\infty = 1.97$ and 3.8 and compared with experimental values of NACA TN 3344. Although the present analysis is valid only in the stagnation region, the calculated pressure distributions agree with experiment over practically the entire hemisphere.

### References

[1] Van Driest, E. R., *The Problem of Aerodynamic Heating*, Aeronautical Engineering Review, Vol. 15, No. 10, pp. 26–41, October, 1956.

[2] Stokes, G. G., *Mathematical and Physical Papers*, Vol. 1, pp. 38–41; Cambridge University Press, London, 1880.

[3] Oliver, Robert Earl, *An Experimental Investigation of Flow About Simple Blunt Bodies at a Nominal Mach Number of 5.8*, Journal of the Aeronautical Sciences, Vol. 23, No. 2, pp. 177–179, February, 1956.

## On the Flutter of Infinitely Long Panels on Many Supports

Robert W. Leonard and John M. Hedgepeth
*Langley Aeronautical Laboratory, NACA, Langley Field, Va.*
October 22, 1956

IN A RECENT PAPER,[1] John W. Miles severely criticizes the two-dimensional panel flutter analysis of an infinite panel on many supports presented in reference 2. In particular, he doubts the validity of the assumption of spatial periodicity over two bays on which the analysis of reference 2 is based. The following analysis, which was initiated as a result of Miles' criticism, not only clarifies this situation but yields some additional information about panel flutter.

We again consider an infinitely long panel of thickness $h$ continuous over many supports equally spaced at intervals of length $l$; the upper surface of the panel is exposed to a supersonic airflow of Mach Number $M$ in the direction of the positive $x$ coordinate. Following reference 3, we replace the unsteady linearized compressible flow theory of reference 2 by the simple "static" air force approximation of Hayes.[4] We seek the conditions under which the panel can execute simple harmonic motion of frequency $\omega$; this requires satisfaction of the equation[3]

$$\bar{w}_n^{IV} + R\bar{w}_n'' + \lambda\bar{w}_n' - k^2\bar{w}_n = 0, \qquad n = 0, \pm 1, \pm 2, \ldots \quad (1)$$

in the $n$th bay defined by $nl \leq x \leq (n + 1)l$. In Eq. (1), the

primes denote partial differentiation with respect to a coordinate $x_1 = (x/l) - n$, $\bar{w}_n(x_1)$ is the amplitude of the simple harmonic motion in the $n$th bay, and the real parameters $k$, $\lambda$, and $R$ are defined as follows:

$$k = \omega/\sqrt{D/ml^4}, \quad \lambda = 2ql^3/\beta D, \quad R = Pl^2/D = \pi^2(P/P_{Eu})$$

where $D$ is the plate modulus $Eh^3/12(1-\mu^2)$, $m$ is the panel mass per unit area, $q$ is the dynamic pressure, $\beta = \sqrt{M^2-1}$, and $P$ is an applied compressive load per unit width in the panel ($P_{Eu}$ being the Euler load).

The problem differs from that of reference 3 only in the specification of the following boundary conditions:

$$\left.\begin{aligned} &\left.\begin{aligned} \bar{w}_n(0) &= \bar{w}_n(1) = 0 \\ \bar{w}_n'(1) &= \bar{w}_{n+1}'(0) \\ \bar{w}_n''(1) &= \bar{w}_{n+1}''(0) \end{aligned}\right\} n = 0, \pm 1, \pm 2, \ldots \\ &\bar{w}_\infty, \ \bar{w}_{-\infty} \text{ finite} \end{aligned}\right\} \quad (2)$$

These include, in addition to the conditions of zero deflection at the supports, the conditions of continuous slope and moment across the supports and of finiteness of the deflections at both $x = \infty$ and $x = -\infty$

The exact solution of Eq. (1), satisfying the boundary conditions of zero deflection at the supports, may be written[3]

$$\bar{w}_n(x_1) = A_n[e^{\gamma(1-x_1)}\sin\delta\sinh\epsilon x_1 - e^{-\gamma(1-x_1)}\sinh\epsilon\sin\delta x_1] + B_n[e^{-\gamma x_1}\sin\delta\sinh\epsilon(1-x_1) - e^{\gamma x_1}\sinh\epsilon\sin\delta(1-x_1)] \quad (3)$$

where $\gamma$, $\delta$, and $\epsilon$ are real quantities related to $k$, $\lambda$, and $R$ by

$$\left.\begin{aligned} \delta &= \sqrt{(\lambda/4\gamma) + \gamma^2 + (R/2)} \\ \epsilon &= \sqrt{(\lambda/4\gamma) - \gamma^2 - (R/2)} \\ k &= \sqrt{(\lambda^2/16\gamma^2) - 4|\gamma^2 + (R/4)|^2} \end{aligned}\right\} \quad (4)$$

Substitution of Eq. (3) into the boundary conditions of continuous slope and moment yields the recurrence relation

$$\begin{vmatrix} A_{n+1} \\ B_{n+1} \end{vmatrix} = [K]\begin{vmatrix} A_n \\ B_n \end{vmatrix}, \qquad n = 0, \pm 1, \pm 2, \ldots \quad (5)$$

where

$$[K] = \frac{1}{ad - bc}\begin{bmatrix} -(bd' + b'd) & -(a'd - bc') \\ b'c + ad' & a'c + ac' \end{bmatrix}$$

$$a = \epsilon e^{\gamma}\sin\delta - \delta e^{-\gamma}\sinh\epsilon$$

$$b = -2\gamma\sin\delta\sinh\epsilon - \epsilon\sin\delta\cosh\epsilon + \delta\sinh\epsilon\cos\delta$$

$$c = -2\gamma(\epsilon e^{\gamma}\sin\delta + \delta e^{-\gamma}\sinh\epsilon)$$

$$d = (\epsilon^2 + \delta^2)\sin\delta\sinh\epsilon + 2\gamma(\epsilon\sin\delta\cosh\epsilon + \delta\sinh\epsilon\cos\delta)$$

and $a'$, $b'$, $c'$, and $d'$ are obtained from $a$, $b$, $c$, and $d$, respectively, by changing the sign of $\gamma$. The remaining boundary conditions of finiteness of deflections at $x = \pm\infty$ are equivalent to requiring finite $A_n$ and $B_n$ for $n = \pm\infty$. We may impose these conditions in the following manner:

Let the eigencolumns and associated eigenvalues of the matrix $K$ be $\xi_1$, $\xi_2$ and $\Lambda_1$, $\Lambda_2$, respectively—that is, $\xi_i$ and $\Lambda_i$ are the solutions of

$$[K]|\xi_i| = \Lambda_i|\xi_i| \quad (6)$$

which leads to the secular equation

$$(ad - bc)\Lambda^2 - (a'c + ac' - bd' - b'd)\Lambda + (a'd' - b'c') = 0 \quad (7)$$

for the eigenvalues $\Lambda_1$ and $\Lambda_2$. We may write

$$\begin{vmatrix} A_0 \\ B_0 \end{vmatrix} = C_1|\xi_1| + C_2|\xi_2|$$

where $C_1$ and $C_2$ are constants. It follows that

$$\begin{vmatrix} A_n \\ B_n \end{vmatrix} = C_1\Lambda_1^n|\xi_1| + C_2\Lambda_2^n|\xi_2| \quad (8)$$

for all $n$ (positive and negative). We can immediately deduce that only eigenvalues having unit absolute value can be permitted in this equation; for, if $|\Lambda_i| \neq 1$, the corresponding $C_i$ must be equal to zero so that $A_n$ and $B_n$ are finite at $n = \pm\infty$. Now it can be shown that, for $\lambda \neq 0$, the eigenvalues cannot both have unit absolute value. This follows from the fact (verified by direct computation) that

$$\Lambda_1\Lambda_2 = (a'd' - b'c')/(ad - bc)$$

is never unity for $\lambda \neq 0$. Thus, only one of the $\Lambda$'s can have unit absolute value, the coefficient $C$ associated with the other eigenvalue must be zero, and Eq. (8) becomes

$$\begin{vmatrix} A_{n+1} \\ B_{n+1} \end{vmatrix} = C\Lambda^{n+1}|\xi| = \Lambda\begin{vmatrix} A_n \\ B_n \end{vmatrix}, \qquad |\Lambda| = 1 \quad (9)$$

In the above case, clearly $|\Lambda_1| \neq |\Lambda_2|$; hence, because the coefficients of Eq. (7) are real (for real $k$), both $\Lambda$'s are real and, consequently, the only values of $\Lambda$ occurring in Eq. (9) are $\Lambda = \pm 1$. This leads immediately to the equality

$$\begin{vmatrix} A_{n+2} \\ B_{n+2} \end{vmatrix} = \begin{vmatrix} A_n \\ B_n \end{vmatrix} \quad (10)$$

Thus, by Eq. (3), the deflections in the $(n+2)$th bay must be the same as those in the $n$th bay.*

The above result establishes that the presence of air forces ($\lambda \neq 0$) restricts the allowable mode shapes to those which are periodic over two bays. Since the use of the more exact unsteady compressible flow theory is unlikely to change the character of this result, it follows that the basic assumption of reference 2 with regard to allowable deflection shapes is indeed justified. This refutes Miles' principal criticism of the analysis of reference 2.

The substitution of $\Lambda = \pm 1$ into Eq. (7) yields two closed-form frequency equations from which critical conditions corresponding to flutter could be determined. However, it is more expedient from a computational standpoint to rederive the frequency equations by the series method of reference 2. The two resulting equations are

$$-\frac{1}{2k^2} + \sum_{n=2,4,\ldots}^{\infty} \frac{n^4\pi^4 - n^2\pi^2R - k^2}{(n^4\pi^4 - n^2\pi^2R - k^2)^2 + n^2\pi^2\lambda^2} = 0 \quad (11)$$

* It is of interest to note that the result $\Lambda_1\Lambda_2 \neq 1$ is decisive in the above argument. If $\Lambda_1\Lambda_2 = 1$, the $\Lambda$'s could be complex conjugates having unit absolute values, and an infinite variety of mode shapes would be possible. Indeed, Miles' discrete bands of frequencies of natural vibration arise from the fact that $\Lambda_1\Lambda_2 = 1$ when there are no air forces present.

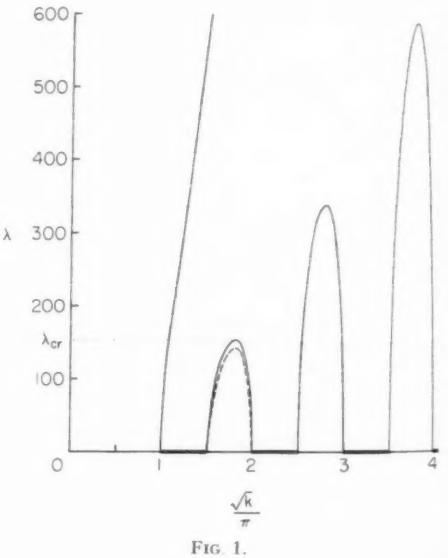


FIG. 1.

$$\sum_{n=1,3\ldots}^{\infty} \frac{n^4\pi^4 - n^2\pi^2 R - k^2}{(n^4\pi^4 - n^2\pi^2 R - k^2)^2 + n^2\pi^2\lambda^2} = 0 \qquad (12)$$

The combinations of real $k$ and $\lambda$ which satisfy Eqs. (11) and (12) for an unstressed panel ($R = 0$) are shown in Fig. 1. The dark portions of the abscissa are the frequency bands corresponding to natural (*in vacuo*) vibration of the panel as determined by Miles. The curves define all the frequencies of panel vibration at any given $\lambda$ ($>0$). Those curves that have an intersection with the abscissa at $\sqrt{k}/\pi = 1, 3, 5, \ldots$ were obtained from Eq. (12) while those with an intersection at $\sqrt{k}/\pi = 2, 4, \ldots$ were obtained from Eq. (11). In obtaining the solid curves, the series of Eqs. (11) and (12) were carried to convergence; the rapid convergence of the series (which was questioned by Miles) is demonstrated by the dashed curve which was obtained from Eq. (11) with only three terms retained corresponding to the two expansion shapes $\sin(2\pi x/l)$ and $1 - \cos(2\pi x/l)$ (the same shapes utilized in the computations of reference 2).

As the aerodynamic pressure parameter $\lambda$ is increased, the panel frequencies change smoothly until a critical value of $\lambda$ ($\lambda_{cr} = 154.8$) is reached where two frequencies coalesce and disappear—that is, the frequencies become complex.[3] Since one of these complex frequencies must have a negative (unstable) imaginary part, all values of $\lambda$ greater than $\lambda_{cr}$ correspond to unstable motion of the panel. Note that, contrary to intuition, the critical value of $\lambda$ is yielded by the even solution which does not contain the "dominant mode of the freely vibrating panel" $\sin(\pi x/l)$. This emphasizes the danger of relying too heavily on intuition in the investigation of flutter phenomena.

It is interesting to note that the critical value of $\lambda$ ($\lambda_{cr} \approx 143.1$) given by the three-term solution (dashed curve) yields, for Mach Numbers greater than about 2, thickness ratios of aluminum panels at sea level that are practically equal to those given by the lower boundary in Fig. 8 of reference 2. This suggests that the anomalous boundaries and regions of instability at higher thickness ratios can only be due to the differences in the air forces used in the two analyses. Chief among these is the existence of "sonic-type" infinities in the air forces of reference 2. Indeed, it has been found that empirical modification of the unsteady air forces to eliminate these infinities erases the upper regions of instability but leaves the lower boundary unaffected for $M > 1.7$. This boundary then is the only meaningful one for the higher Mach Numbers. Since the use of the simpler "static" air forces yields nearly identical thickness ratios, the $\lambda_{cr}(= 154.8)$ obtained by including all terms in Eq. (11) apparently gives the correct flutter boundary for the unstressed panel at the higher Mach Numbers. It should be mentioned that, at present, the location of the flutter boundary for the lower supersonic speeds is still uncertain. The flutter in this region is evidently not a "low-frequency" phenomenon; hence, the "static" air forces are unlikely to yield an accurate boundary.

Finally, it should be emphasized that the approximate stability boundary obtained for the supersonic Mach Number range by Miles (Fig. 7 of reference 1) is based on an analysis which does not satisfy the boundary conditions of the problem. This boundary requires thickness ratios many times those associated with the value $\lambda_{cr} = 154.8$. Indeed Miles' criterion does not "furnish an approximation of the right order of magnitude" for high Mach Numbers; it is *prohibitively* conservative and cannot be considered as a practical basis for design.

## References


[1] Miles, J. W., *On the Aerodynamic Instability of Thin Panels*, Journal of the Aeronautical Sciences, Vol. 23, No. 8, pp. 771–780, August, 1956.

[2] Hedgepeth, J. M., Budiansky, B., and Leonard, R. W., *Analysis of Flutter in Compressible Flow of a Panel on Many Supports*, Journal of the Aeronautical Sciences, Vol. 21, No. 7, pp. 475–486, July, 1954.

[3] Hedgepeth, J. M., *On the Flutter of Panels at High Mach Numbers*, Readers' Forum, Journal of the Aeronautical Sciences, Vol. 23, No. 6, pp. 609, 610, June, 1956.

[4] Hayes, W. D., *A Buckled Plate in a Supersonic Stream*, North American Aviation Report AL-1029, 1950.


# A Note on Steady-State Aeroelasticity


Alan H. Wickens
*Dynamics Engineer, Canadair Limited, Montreal, Canada*

December 17, 1956

THE PURPOSE of this note is to present a unified method of analysis of the effects of steady-state aeroelasticity. The small displacement at a point $P(x, y, z)$ of an aircraft structure may be expressed as

$$u_j(x, y, z) = g_{j\alpha}(x, y, z)q_\alpha \qquad (1)$$

where $u_j(x, y, z)$ is the displacement in direction $j$ and $g_{j\alpha}(x, y, z)$ is a matrix of modal shape functions which define the shape of the structure when given generalized displacements $q_\alpha$. The double suffix summation convention is used throughout; $i, j$ refer to Cartesian coordinates $x, y, z$ and therefore run from 1 to 3. Assuming linearity, the aerodynamic loading may be written

$$p(x, y, z) = q_\alpha p_\alpha(x, y, z) \qquad (2)$$

and an application of the principle of virtual work yields the equations of equilibrium

$$Q_\alpha = (C_{\alpha\beta} + \theta E_{\alpha\beta})q_\beta \qquad (3)$$

where $Q_\alpha$ is the generalized force in the $\alpha$th mode,

$$C_{\alpha\beta} = \int dS_i(x, y, z)g_{j\alpha}(x, y, z)p_\beta(x, y, z) \qquad (4)$$

$$E_{\alpha\beta} = \partial^2 U/\partial q_\alpha \partial q_\beta \qquad (5)$$

where $U$ is the elastic strain energy and $\theta$ is inversely proportional to the dynamic pressure $\rho V^2$.

Now the total number of degrees of freedom is made up of (a) a set of rigid body freedoms allocated the generalized coordinates $q_n$ so that, the most general case, $n = 1, \ldots 6$; (b) a set of distortional degrees of freedom which describe the distortion of the structure and are denoted by $q_s$; and (c) a set of control surface displacements $\beta_k$. In the following development, the displacements are referred to axes fixed in the aircraft with origin at the center of mass, and the distortional modes are chosen on the basis of fixity at the center of mass. It then follows that Eq. (3) may be written in the partitioned matrix form

$$\begin{bmatrix} Q_m \\ 0 \end{bmatrix} = \left[\begin{array}{c|c|c} C_{mn} & C_{ms} & C_{mk} \\ \hline C_{rn} & C_{rs} + \theta E_{rs} & C_{rk} \end{array}\right] \begin{bmatrix} q_n \\ \hline q_s \\ \hline \beta_k \end{bmatrix} \qquad (6)$$

if the $q_n$ are interpreted as the steady-state perturbation velocities and any inertial or gravitational forces which are present are assumed to act at the center of mass (and are therefore contained in the $Q_m$). It will also be noted that the control surface displacements are regarded as inputs—i.e., mechanically, irreversibility is assumed.

Given the control surface displacements and rigid body motion, the rigid body forces follow immediately from Eq. (6) as

$$Q_m = [C_{mn} - C_{ms}(C_{rs} + \theta E_{rs})^{-1} C_{rn}]q_n + [C_{mk} - C_{ms}(C_{rs} + \theta E_{rs})^{-1}C_{rk}]\beta_k \qquad (7)$$

or

$$Q_m = \bar{C}_{mn}q_n + \bar{C}_{mk}\beta_k \qquad (8)$$

The effects of flexibility on the dynamic and static stability and control of an aircraft can be investigated using the stability derivatives $\bar{C}_{mn}$ and $\bar{C}_{mk}$ in place of $C_{mn}$ and $C_{mk}$; this is accurate provided the distortions occur slowly compared with the natural periods of the aircraft structure so that inertia forces can be neglected in these modes.

The distortional coordinates are obtained directly from Eq. (6) as

$$q_s = -(C_{rs} + \theta E_{rs})^{-1} C_{rn}q_n - (C_{rs} + \theta E_{rs})^{-1} C_{rk}\beta_k \qquad (9)$$

and hence deflections and loadings can be obtained using Eqs. (1) and (2).

As a measure of control effectiveness, the steady motion resulting from a unit control surface displacement is required. Then, in Eq. (7) the $Q_m$ are zero and

$$q_n = -\bar{C}_{mn}^{-1}\bar{C}_{mk}\beta_k \tag{10}$$

Usually only one rigid body freedom is involved, and then Eq. (10) reduces to

$$q_n/\beta_k = -(\bar{C}_{mk}/\bar{C}_{mn}) \tag{11}$$

The control reversal condition is indicated by the vanishing of the numerator in Eq. (11).

According to the above relations, aeroelastic calculations can proceed as follows: The variation of deflections and loading are evaluated for a range of values of $\theta$ (and Mach Number if appropriate) using Eq. (9). From this the speed at which the deflections or loading reach some design limit can be obtained—this corresponds to divergence for practical purposes. Then the stability derivatives $\bar{C}_{mk}$ and $\bar{C}_{mn}$ are obtained from Eq. (7) making use of the results of the evaluation of Eq. (9). The control effectiveness and reversal conditions then follow from Eq. (11).

In practice, the matrix inversion involved in Eq. (9) is the only serious handicap of the method. However, this is no problem as long as digital computing facilities are available, and, provided a reasonable choice of distortional modes is made, the accuracy of the method is very satisfactory.

## The Buckling of Triangular or Skew Plates

Victor I. Weingarten
*Structures Research Engineer, Northrop Aircraft, Inc., Hawthorne, Calif.*
December 27, 1956

THE PROBLEM of determining the critical elastic buckling load of a triangular plate has attracted some notice.[1,4] The writer wishes to call attention to a simple solution of this problem through use of Richardson's $h^2$-extrapolation formula[2] in conjunction with the finite difference technique.[2]

The critical buckling load of an isosceles triangular plate, which has either clamped or simply supported edges and which is loaded by uniform axial compression normal to all edges of the plate or by compression normal to the base edge and shear along the other two edges, has been determined at Northrop Aircraft, Inc., by a method that appears to be simpler, more accurate, and more versatile than the one presented by Cox and Klein.[1] Richardson's extrapolation of the finite difference solution of the critical buckling load can be used on any triangular or skew plate with any distribution of load. The problem of thermal buckling of an arbitrarily shaped plate with any imposed temperature distribution is being investigated by this technique at the present time.

In order to illustrate the method, the critical buckling load of a simply supported equilateral triangular plate loaded by uniform axial compression on all edges will be determined. The differential equation which describes this problem is

$$D\nabla^4 W + N\nabla^2 W = 0 \tag{1}$$

where

$D$ = plate stiffness
$W$ = deflection of plate
$N$ = load per unit length acting perpendicular to the boundary

The boundary conditions to this problem are $\partial^2 w/\partial m^2 = 0$, where $m$ is the direction normal to the boundary. An equilateral triangular grid mesh[2] is used in the solution. Eq. (1) expressed in equilateral triangular coordinates is

$$\nabla^4 W + K\nabla^2 W = 0 \tag{2}$$

where

$K = 2h^2N/D$
$h$ = length of segments into which altitude of triangle is divided by grid $= a/n$
$a$ = altitude of triangle
$n$ = number of segments

Eq. (2) is first solved for one interior point in the equilateral triangle. Here, $n = 3$, hence $h = a/3$. The finite difference equations are

$$(42W_0 - 6W_0) + K(-6W_0) = 0$$
$$(36 - 6K)W_0 = 0, \quad K = 6.0$$

For three interior points ($n = 4$),

$$(42W_2 - 20W_2 - 6W_2) + K(-4W_2) = 0, \quad K = 4$$

For six interior points ($n = 5$),

$$(42W_3 - 10W_4 - 10W_4 + 2W_4 - 2W_3 - 2W_3 + W_3 - W_4 - W_4 + W_3) + K(-6W_3 + W_4 + W_4) =$$
$$(40 - 6K)W_3 + (-20 + 2K)W_4 = 0 \tag{3}$$
$$(42W_4 - 20W_4 - 20W_3 + 2W_3 - 2W_4 - W_3 - W_3) + (-6W_4 - 2W_3 + 2W_4)K =$$
$$(-20 + 2K)W_3 + (20 - 4K)W_4 = 0 \tag{4}$$

Setting the determinant of Eqs. (3) and (4) equal to zero yields

$$K = 2.7639$$

Therefore, for

| | | |
|---|---|---|
| $n = 3$ | $K = 6$ | $N_{cr} = 27(D/a^2)$ |
| $n = 4$ | $K = 4$ | $N_{cr} = 32(D/a^2)$ |
| $n = 5$ | $K = 2.7639$ | $N_{cr} = 34.549(D/a^2)$ |

Using Richardson's $h^2$-extrapolation formula, for

| | |
|---|---|
| $n_2/n_1 = 4/3$ | $N_{cr} = 38.428(D/a^2)$ |
| $n_3/n_2/n_1 = 5/4/3$ | $N_{cr} = 39.446(D/a^2)$ |

The correct answer[3] is $N_{cr} = 39.478\ (D/a^2)$. For comparison, $N_{cr} = 35.6\ (D/a^2)$.

As illustrated in this problem, the critical buckling solution for one interior point combined with three interior points of an isosceles triangle supported and loaded as described above gives an answer within 2.7 per cent of the correct value. In all cases checked at Northrop, the use of a one- and three-point solution has given a value which is in error by less than 10 per cent. It is further noted that in the above example, the relatively simple addition of a six-point solution to the extrapolation process reduced the error to 0.081 per cent.

### References

[1] Cox, H. L., and Klein, B., *The Buckling of Isosceles Triangular Plate*, Journal of the Aeronautical Sciences, Vol. 22, No. 5, pp. 321–325, May, 1955.
[2] Salvadori, M. G., and Baron, M. L., *Numerical Methods in Engineering*, pp. 77, 232; Prentice-Hall Publishing Co., New York, 1952.
[3] Timoshenko, S., *Theory of Elastic Stability*, 1st Ed., p. 371; McGraw-Hill Book Company, Inc., New York, 1936.
[4] Wittrick, W. H., *Buckling of a Simply Supported Triangular Plate in Combined Compression and Shear*, ARL Report No. SM 197, Melbourne, Australia, July, 1952.

## On Complex Roots of an *n*th Degree Equation

C. A. M. van der Linden
*Mathematician, Scientific Department, Werkspoor N. V., Amsterdam, Netherlands*
January 3, 1957

A SWIFT DETERMINATION of the complex roots of an $n$th degree equation can be established by application of the Hurwitz-Routh criteria in combination with Horner's algorithm.

Consider, after elimination of the real roots,

$$a_0 z^{2n} + a_1 z^{2n-1} + \ldots\ldots + a_{2n} = 0$$

to be the equation, the roots of which are

$$\xi_k \pm i\eta_k$$

The indices are to be arranged in such a way that

$$\xi_k < \xi_{k+1}$$

Assuming $p$ to be an arbitrary real number, it can be stated that if and only if $p > \xi_n$, all the roots of the equation in $z - p$ possess negative real parts and the equation satisfies the stability criteria.

Taking advantage of this property, approximation of $\xi_n$ is possible. The corresponding $\eta_n$ can immediately be derived from the values of the Hurwitz determinants. This will become evident with an example. Let the equation be

$$z^6 - 4z^5 + 2z^4 - 14z^3 + 70z^2 - 44z + 25 = 0$$

According to this method we obtain for the equation in $z - 3$: Horner's algorithm:

| | | | | | | |
|---|---|---|---|---|---|---|
| 1 | −4 | 2 | −14 | 70 | −44 | 25 |
| 1 | −1 | −1 | −17 | 19 | 13 | 64 |
| 1 | 2 | 5 | −2 | 13 | 52 | |
| 1 | 5 | 20 | 58 | 187 | | |
| 1 | 8 | 44 | 190 | | | |
| 1 | 11 | 77 | | | | |
| 1 | 14 | | | | | |
| 1 | | | | | | |

Hurwitz-Routh criteria:

| | | | | |
|---|---|---|---|---|
| 1 | 14 | 63.43 | 149.55 | 167.23 | −19.36 |
| 77 | 190 | 183.29 | 37.87 | 64 | |
| 187 | 52 | 64 | | |
| 64 | | | | |

thus proving the equation to be nonsteady. The value of the last determinant being $f(p)$, one may write in this case $f(3) = -19.36$. This number will be used for further approximation. Approximations of $\eta^2$ are

$$37.87/149.55 = 0.2532$$

and

$$64/167.23 = 0.3827$$

By way of this method we find for $f(3.1) = 22.22$ apparently steady. Approximations of $\eta^2$ are 0.4697 and 0.3397, respectively.

For the next approximation we take 3.05. We now find $f(3.05) = 0.4960$ together with $\eta^2 = 0.360367$ and $\eta^2 = 0.357267$. Interpolation between the values found using second-order differences yields $p = 3.04881$ and $\eta^2 = 0.35778$.

We thus find for the root $z = 3.04881 + 0.59815i$. This root appears to be accurate to half a unit of the fifth decimal.

## On the Prediction of Gust and Buffet Response of Wings and Airfoils

Albert S. Richardson, Jr.*
*Executive Officer, Aeroelastic and Structures Research Laboratory, Massachusetts Institute of Technology*
January 7, 1957

A RECENT PAPER by Ribner[1] reviews some of the advances in the prediction of gust and buffet response while delineating the various analytical schemes pertaining to lifting surfaces, lifting lines, and lifting points. While the *formulation* of any given problem in terms of any of these three alternatives follows a straightforward and perhaps even routine procedure, the actual solution of the problem becomes increasingly difficult (if not, in fact, ponderous) as one passes from the concept of (a) the lifting point to (b) the lifting line and finally to (c) the lifting surface. The complexities introduced by successive refinements of the aerodynamic theory are obvious, but the encumbrance due to the statistics is still another matter. Furthermore, a significant increase in the analytical and computational effort is required even in the simplest of the above cases—i.e., the lifting point simply by admitting another dimension to the random upwash field.

Consider, for example, a uniform straight wing of arbitrary aspect ratio at zero mean angle of attack in incompressible flow. The wing is assumed constrained against all motion and subject only to the influence of a random two-dimensional† upwash field. The first problem is to determine the root mean square total lift. We also compare these calculations with some measurements made by R. J. Hakkinen and the author[2] at M.I.T. in the summer of 1954. The second problem is to determine net r.m.s. mid-span twisting moment, mid-span shear (r.m.s.), and mid-span bending moment (r.m.s.).

The lift at any point on the wing is assumed to be zero when the point is not located on the quarter-chord line—i.e., the lift is assumed concentrated at the quarter chord. Furthermore, at each point on this line, the lift at that point is assumed to be independent of the lift at any neighboring point and the upwash at all neighboring points except those points lying on a line passing through the lifting point in the streamwise direction. The reader may easily verify that we are here concerned not with a lifting-line theory (in the usual sense of the Prandtl theory) but with a strip theory, which is merely an extension of the lifting-point idea to an infinitely dense array of points (along a line). Following the development of reference 2, the lift on the strip $dy$ is

$$dL(y) = dy \iint h_0(x - \zeta)\delta(y - \eta)\, w(\zeta, \eta)\, (C_{l_\alpha} qC/U) d\zeta d\eta$$

where $h_0(x - \zeta)$ is the (dimensionless) influence function for lift produced at the quarter-chord point by a unit upwash $w$ impulse at $\zeta$. The total lift as a function of $x$ is found by integration of $dL(y)$:

$$L(x) = (C_{l_\alpha} qC/U) \int_{-b/2}^{b/2} dy \int h_0(x - \zeta) w(y, \zeta) d\zeta$$

The mean square lift intensity is found by squaring $L(x)$ and forming the ensemble average

$$\overline{L^2(x)}/L_0^2 = \iint_{-b/2}^{b/2} dy dy^1 \times \iint h_0(x - \zeta) h_0(x - \zeta^1) \phi[(y - y^1), (\zeta - \zeta^1)] d\zeta d\zeta^1$$

where $L_0$ is the quasi-steady lift based on r.m.s. upwash intensity and $\phi(\alpha, \beta)$ is the (dimensionless) two-dimensional autocorrelation coefficient for homogeneous upwash. It is more convenient to put this in the spectral form

$$\overline{L^2(x)}/L_0^2 = \int_{-\infty}^{\infty} dk |S(k)|^2 \int_{-\infty}^{\infty} dk_2 \{[\sin^2 (bk_2/2)]/[(bk_2)^2/4]\}\ \tilde{\phi}\ (k, k_2)$$

where

$S(k)$ = Sears' sinusoidal gust function
$k$ = reduced frequency $\omega c/2U$
$k_2$ = spanwise wave variable $\omega_2/U$
$\tilde{\phi}\ (k, k_2)$ = "two-dimensional" upwash spectral density

If we compare this with the mean square lift of a lifting point (e.g., references 3 and 4), one notices that the function

$$[\sin^2 (bk_2/2)]/[(bk_2)^2/4]$$

modifies the spectral density $\tilde{\phi}(k, k_2)$ in the present instance, whereas the function is replaced by unity in the true lifting-point case. In fact, if one imagines that the wing span is shrunk to an arbitrarily small value ($b \to 0$), it is only in this case that the true lifting-point result is obtained. As an example of the influence of this spanwise modifying function, one may define a span-correction factor for lift which relates the spectral density for lift on a finite span wing to the spectral density for lift at a lifting point as follows:

* Also, President and Technical Director, Research Consulting Associates, Lexington, Mass.

† By two-dimensional we mean that the upwash normal to the plane of the wing is uncorrelated along any arbitrary line in the plane.

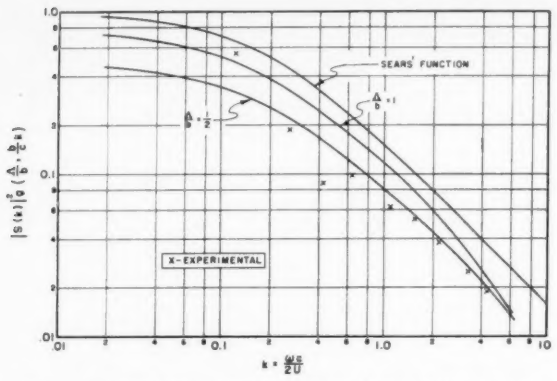


FIG. 1. Comparison of experimental results and theoretical estimate. (Obtained at M.I.T. under contract NAW-6304, NACA, 1954.)

$$g(b, k) = [\int \psi(bk_2)\tilde{\phi}(k, k_2)dk_2]/[\int \phi(k, k_2)dk_2]$$

where

$$\psi(bk_2) = [\sin^2 (bk_2/2)]/(bk_2/2)^2$$

One obtains the spectral density for lift on a finite span wing by multiplication of $g(b, k)$ into the spectral density for lift at a lifting point. One may also think of an effective transfer function for a finite span wing by multiplying $g(b, k)$ into the square magnitude of Sears' sinusoidal gust function (transfer function for a lifting point). Such a result is shown in Fig. 1. Experimental points are also shown on the graph. In arriving at these results the approximate Heisenberg spectrum for homogeneous turbulence was used in the analysis.[4] A free parameter $\Lambda$ occurs in the Heisenberg spectrum which is the integral turbulence scale. The conditions surrounding the experiment were such that a value of $\Lambda/b = 1/2$ seems reasonable. The principal conclusion to be drawn from the graph is that, for a wing of given aspect ratio, the effective transfer function for lift (and therefore the spectral density and mean square) differs from the values associated with a lifting point in a manner which depends quite strongly upon the integral turbulence scale compared to the wing span. However, interpretation of the result solely in terms of the ratio $\Lambda/b$ can be misleading. Intuitively, one might expect that large values of this ratio would produce behavior akin to that of a lifting point. However, from the analysis, one can show that when $\Lambda/b$ is large, such behavior is obtained only in the case of very small aspect ratio—i.e., for a narrow strip. The following quotation is from reference 2:

"In summary, if the wing span is increased from zero while keeping all other conditions unchanged, at very small spans, the mean square lift first increases proportionally to the wing area. For large values of the span, the low frequency part of the lift spectrum approaches asymptotically a constant non-zero value, while the high frequency part becomes asymptotically proportional to the span. Correspondingly, the asymptotic expression for the total mean square lift has a constant term and a term proportional to the span."

This behavior seems to be connected with the particular span-modifying function which, in turn, is connected with the total lift (mean square). Analyses which parallel the above may also be carried out for other quantities of interest, such as wing root shear, twisting moment, and bending moment. For these cases, span-modifying functions have been computed and are summarized for a uniform straight wing in Table 1.

Another order of magnitude of complexity is added to the analysis if one introduces motion effects in addition to spanwise correlation effects. The more degrees of freedom that are admitted, the more complex the analysis becomes not only because the motion influences the aerodynamics but also because the various modes of motion interact in such a way as to produce cross-correlation as well as autocorrelation effects.[5]

TABLE 1

| | Span-Modifying Function |
|---|---|
| Mean square total lift | $4 \sin^2 \beta^*/\beta^2$ |
| Mean square root twisting moment | $4 \sin^2 \beta/\beta^2$ |
| Mean square root shear | $2/\beta^2(1 - \cos \beta)$ |
| Mean square root bending moment | $2/\beta^4(-1 + \cos \beta) + 1/\beta^2[1 + (2 \sin \beta)/\beta]$ |

*$\beta = bk_2$.

REFERENCES

[1] Ribner, H. S., *Spectral Theory of Buffeting and Gust Response: Unification and Extension*, Journal of the Aeronautical Sciences, Vol. 23, No. 12, pp. 1075–1078, 1118, December, 1956.

[2] Hakkinen, R. J., and Richardson, A. S., Jr., *A Theoretical and Experimental Investigation of Random Gust Loads—Part I—Theoretical Analysis and Experimental Results of Aerodynamic Transfer Function of a Simple Wing Configuration in Incompressible Flow*, Technical Report 53-2, M.I.T. ASRL (NACA contract NAW-6304), July 1, 1955.

[3] Liepmann, H. W., *On the Application of Statistical Concepts to the Buffeting Problem*, Journal of the Aeronautical Sciences, Vol. 19, No. 12, pp. 793–800, 822, December, 1952.

[4] Liepmann, H. W., *Extension of the Statistical Approach to Buffeting and Gust Response of Wings of Finite Span*, Journal of the Aeronautical Sciences, Vol. 22, No. 3, pp. 197–200, March, 1955.

[5] Richardson, A. S., Jr., *A Theoretical and Experimental Investigation of Random Gust Loads—Part II—Formulation of the Problem and Some Results for Simplified Cases*, Technical Report 53-3, M.I.T., ASRL (NACA Contract NAW-6309), July 1, 1955.

## Experiment on the Variation of Airfoil Properties With Reynolds Number

A. F. Charwat

*Assistant Professor of Engineering, University of California at Los Angeles*

January 15, 1957

THE BEHAVIOR of airfoils at low Reynolds Numbers is apt to exhibit irregularities. Conceptually, these may be traced to boundary-layer phenomena. Thickening of the boundary layers can cause an apparent change in the airfoil thickness distribution or camber, thereby changing the lift at a fixed angle of attack. This effect can be particularly pronounced if there exist "bubbles" due to local separation followed by reattachment of the flow to the surface. The drag of the airfoil increases also with the thickness of the boundary layer; however, the influence of the three parameters—angle of attack, effective airfoil thickness distribution, and boundary-layer momentum loss—is complex and interdependent.

The bubble separation may occur in ranges of flow parameters which have application in turbomachines. Several investigations of the phenomenon (see the bibliography in reference 3), the effect of Reynolds Number on the performance of cascades[1] and on rotating machines[2, 3] have been conducted. Much more is needed, however, to define design criteria and gain insight into the details of the flow. The results of tests on compressors, particularly, show little more than that the efficiency of a given blade cascade drops abruptly below a "critical" Reynolds Number, which is between $70 \times 10^3$ and $100 \times 10^3$.

The data presented here are preliminary investigations of low Reynolds Number effects. This first phase consisted of tests on an isolated two-dimensional airfoil; further tests in two- and three-dimensional cascades are in progress. It was desired to observe in detail the variations of the lift and drag of a cambered airfoil through the "critical" range. The profile was chosen to give a sharp peak in negative pressure near the leading edge, based on the following argument: at very low Reynolds Numbers it is impossible to prevent separation of a laminar boundary layer even at moderate lift coefficients, and good performance can be maintained only if the separated layer transists and reattaches

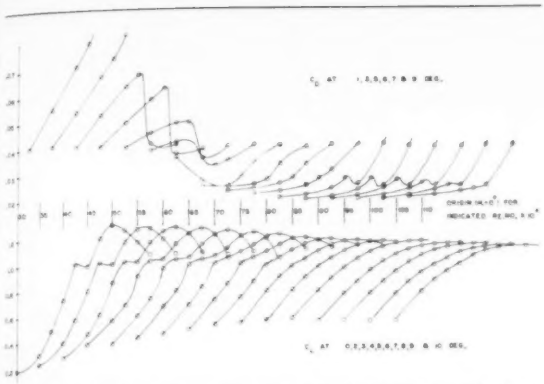

FIG. 1. Variation of lift and drag coefficients with angle of attack over a range of Reynolds Numbers. (Origin of curves displaced for each $Re$. The sequence of angles of attack is as indicated for all tests.)

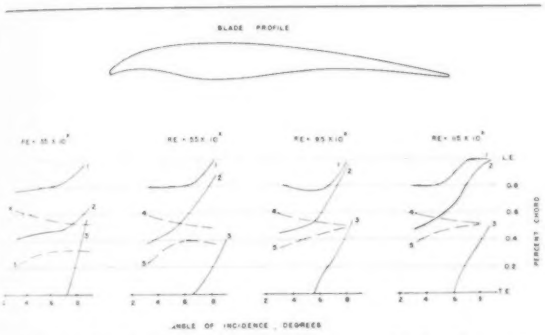


FIG. 2. Results of flow visualization tests. (1) Laminar separation; (2) turbulent reattachment; (3) turbulent separation on upper surface; (4) to (5) laminar-turbulent transition region and/or separation-reattachment on lower surface.

transition and reattachment is known to occur more readily when the negative pressure peak is sharp. This is possibly explained by the small thickness of the separating layer in the region of high acceleration.

The profile of the airfoil was suggested by Seredensky (not published).* The thin leading edge (approximately 2 per cent) is obtained by carving out the upstream lower surface of a relatively thick airfoil (maximum thickness 10 per cent at 35 per cent of chord). This scheme permits one to maintain a good structural rigidity for application to rotating machines. The profile is shown on Fig. 2. Tests were conducted in a $1^1/_2$ in. by 3 in. suction tunnel at wind speeds between 100 and 300 ft. per sec. Lift was measured by integrating the pressure induced by the airfoil over the tunnel sidewalls; drag was measured by integrating wake total-pressure traverses. Corrections as outlined in reference 4 were used; the data is believed to be accurate within 1 per cent.

Fig. 1 shows the results in the form of lift and drag coefficients. The experimental points are drawn in to show the consistency of the data. As expected, distinct irregularities in both the lift and the drag force are noticeable. To clarify their relation to the variations in the zones of separated flow several flow-visualization tests were made. For that purpose the airfoil was coated with a suspension of lampblack in kerosene, which, upon evaporation, permits an approximate interpretation of the laminar separation, turbulent reattachment and turbulent separation regions. Fig. 2 shows the results of these tests.

* The information was obtained by W. Pfenninger of Northrop Aircraft, Inc. Part of this work was done at Northrop and permission to publish it is gratefully acknowledged.

The correlation between the lift and drag data and the rudimentary observations of the extent of the separated region is not too obvious; this is not surprising inasmuch as the forces depend on the exact geometry of the bubble. Nonetheless, a few interesting remarks can be made. At the lowest Reynolds Numbers there exists a large bubble covering approximately 40 per cent of the chord and fairly constant in size. The drag rise with incidence is uniform. Note that the final turbulent separation starts at higher angles of attack but moves rapidly upstream. This is consistent with the abrupt stalling characteristic. The slope of the lift-curve is higher than the theoretical slope ($2\pi$) indicating that as the angle of attack increases the "effective" camber—i.e., the height of the "bubble" is growing. A different behavior of the "bubble" is evident in the regions where the drag shows a sharp drop at about 6° angle of attack. At just about that angle the extent of the separated region decreases rapidly and the bubble moves towards the leading edge. At still higher Reynolds Numbers the separated zone establishes itself at the leading edge at moderate angles of attack (although it never disappeared entirely within the range of the tests) and remains small. The lift and drag curves become smooth.

Some of the pertinent performance criteria are replotted on Fig. 3. For this purpose the step in the lift curve at low Reynolds Number (30 to 60 × $10^3$) and the irregularity in the drag curve in the intermediate range (70 to 90 × $10^3$) were smoothed out. The parameters plotted are the lift to drag ratios, the maximum lift coefficient and the angles of incidents at which they occur. The best lift-to-drag ratio decreases with Reynolds Number, as expected. However, a severe drop in airfoil maximum efficiency occurs only at the relatively low Reynolds Number of 35,000; conversely, if the angle of incidence is low, the efficiency of the airfoil begins to decrease substantially at Reynolds Number almost twice as high. This is shown by the curve of $L/D$ ratio for a 5° incidence.

Another interesting fact is that the maximum lift coefficient does not decrease but, on the contrary, increases at low Reynolds Numbers. The angle of attack for maximum lift decreases some-

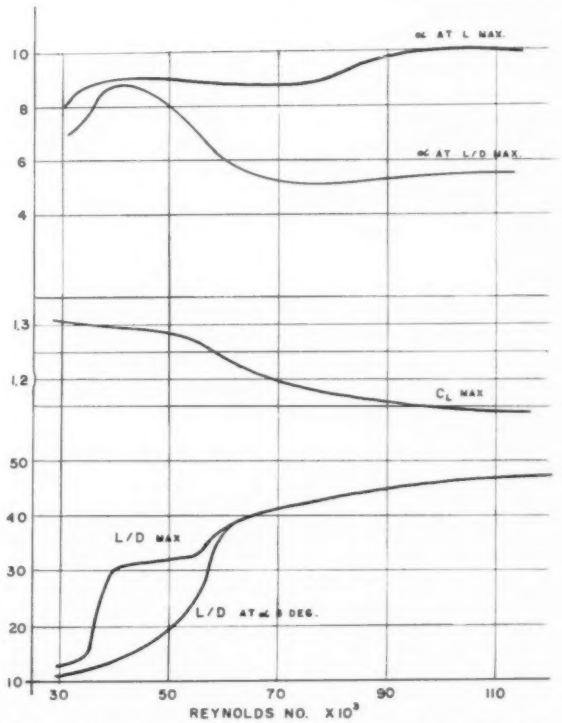


FIG. 3. Variation of the performance characteristics of the airfoil with Reynolds Number.

what. The maximum lift and the maximum efficiency incidences converge as the Reynolds Number decreases; for this airfoil they are almost equal in the range $Re$ 40 to 60 × $10^3$.

It would not be appropriate to interpret these tests on an isolated airfoil directly in terms of compressor performance. Besides the difference (pressure distribution over an isolated and a cascaded airfoil) the higher degree of turbulence which exists in a rotating machine would influence the transition and reattachment of the separated flow. Moreover, in an exhaustive series of tests Rannie and Neustein[5] showed the predominant effect of three-dimensional boundary-layer movements on the low Reynolds Number problem. However, the overall trends of this data suggests that the optimum performance of a compressor at low Reynolds Numbers may also occur at higher blade incidence angles than those normally used and that, if properly designed, the compressor "critical" Reynolds Number may be brought down below 70,000.

### References


[1] Sawyer, W. T., *Experimental Investigation of a Stationary Cascade of Aerodynamic Profiles*, Mitteilungen aus dem Institut für Aerodynamik, No. 17, Verlag Leeman, Zurich, 1949.

[2] Eckert, B., Pfluger, F., Weinig, F., and Fickert, D., *The Influence of Physical Dimensions and Flow Conditions on Compressor Characteristics*, Bureau of Ships Report 338, U. S. Navy Dept., Vol. 3, May, 1946.

[3] Sohn, R. L., *An Analysis of the Performance of an Axial-Flow Compressor at Low Reynolds Number*, Journal of the Aeronautical Sciences, Vol. 23, No. 8, pp. 741–746, 791, August, 1956.

[4] Abbott, I. H., Van Doenhoff, A. E., and Stevens, L. S., Jr., *Summary of Airfoil Data*, NACA Report 824, 1945.

[5] Neustein, J., *Experiments at Low Reynolds Number; Part II: Rotating Machines*, Ph.D. Thesis, California Institute of Technology, 1956.


## Comments on the Lagrangian Multiplier in Drag Minimization


Robert T. Stancil

*Aerodynamics Engineer, Convair, Fort Worth, A Division of General Dynamics Corporation*


January 18, 1957

A SIMPLE RELATION for the drag coefficient in terms of the boundary conditions and the Lagrangian multipliers used in the optimization of an aerodynamic body has been found to be useful. After the standard minimization procedure mentioned below has been carried through, the drag of the resulting body (or wing) can be calculated by

$$C_D = (1/2) \sum_{l=1}^{m} \lambda_l R_l \tag{1}$$

where the drag coefficient and the necessary boundary conditions were originally expressed as series of the form

$$\left.\begin{aligned} C_D &= \sum_{i=1}^{n}\sum_{j=1}^{n} a_i a_j d_{ij} \\ R_l &= \sum_{i=1}^{n} a_i r_{li} \end{aligned}\right\} \tag{2}$$

where the $d_{ij}$ and $r_{li}$ terms are constants for a given configuration and Mach Number. The boundary condition $R_l$ may be the lift coefficient of a wing, volume of a body, area at a number of points on a body, or any linear function of the coefficients of the assumed series.

The drag will be minimized if

$$\sum_{k=1}^{n} (\partial/\partial a_k)\left\{C_D - \sum_{l=1}^{m} \lambda_l R_l\right\} = 0 \tag{3}$$

where the $\lambda_l$'s are Lagrangian multipliers, and $m$ is the number of constraints. Noting that

$$\left.\begin{aligned} (\partial C_D/\partial a_k) &= \sum_{i=1}^{n} a_i d_{ik} + \sum_{j=1}^{n} a_j d_{kj} \\ &= \sum_{i=1}^{n} a_i (d_{ik} + d_{ki}) \end{aligned}\right\} \tag{4}$$

Thus

$$(\partial/\partial a_k)\left\{C_D - \sum_{l=1}^{m} \lambda_l R_l\right\} = 0 = \sum_{i=1}^{n} a_i (d_{ik} + d_{ki}) - \sum_{l=1}^{m} \lambda_l r_{lk} \tag{5}$$

Multiplying by $a_k$ and summing over $k$, we obtain

$$2 \sum_{i=1}^{n}\sum_{k=1}^{n} a_i a_k d_{ik} - \sum_{k=1}^{n}\sum_{l=1}^{m} \lambda_l r_{lk} a_k = 0 \tag{6}$$

Using Eq. (2), this can be written as

$$2C_D - \sum_{l=1}^{m} \lambda_l R_l = 0 \tag{7}$$

Thus

$$C_D = (1/2) \sum_{l=1}^{m} \lambda_l R_l \tag{8}$$

The coefficients $a_i$ and the Lagrangian multipliers $\lambda_l$ can be determined from the matrix formed by the $n$ equations of the form of Eq. (5) and the $m$ boundary conditions.

It is apparent that the calculation of the drag coefficient of the body (or wing) by means of Eq. (8) is much simpler than the same calculation using Eq. (2). It is also obvious from the matrix of linear equations that the coefficients and the Lagrangian multipliers are linear functions of the boundary conditions. Thus

$$\lambda_l = \sum_{t=1}^{m} b_{lt} R_t \tag{9}$$

and the drag is seen to be a parabolic function of the boundary conditions. For example, if the lift coefficient of a wing is the only boundary condition considered, then,

$$C_{D_{design}} = (1/2) b_{11} \, C_{L_{design}}{}^2 \tag{10}$$

An interesting sidelight is the fact that, for a wing whose camber shape has been determined, the theoretical drag polar is a displaced parabola which has the same shape factor as the plane wing of the same plan form. This can be shown by letting $a_0 = \alpha - \alpha_{design}$ and writing

$$\left.\begin{aligned} C_D &= \sum_{i=0}^{n}\sum_{j=0}^{n} a_i a_j d_{ij} \\ &= a_0{}^2 d_{00} + a_0 \sum_{i=1}^{n} a_i (d_{0i} + d_{i0}) + \sum_{i=1}^{n}\sum_{j=1}^{n} a_i a_j d_{ij} \\ &= \left[(C_L - C_{L_{design}})/C_{L_\alpha}\right]^2 d_{00} + \left[(C_L - C_{L_{design}})/C_{L_\alpha}\right] c_1 + c_2 \end{aligned}\right\} \tag{11}$$

where

$$a_0 = \alpha - \alpha_{design} = (C_L - C_{L_{design}})/C_{L_\alpha}$$

$$c_1 = \text{constant} = \sum_{i=1}^{n} a_i (d_{0i} + d_{i0})$$

$$c_2 = \text{constant} = \sum_{i=1}^{n}\sum_{j=1}^{n} a_i a_j d_{ij}$$

Now Eq. (11) can be written in the form

$$C_D = (d_{00}/C_{L_\alpha}{}^2)(C_L - \Delta C_L)^2 + \Delta C_{D_{min}} \tag{12}$$

where

$$\Delta C_L = C_{L_{design}} - (c_1 C_{L_\alpha}/2d_{00})$$

$$\Delta C_{D_{min}} = c_2 - (c_1{}^2/4d_{00})$$

Thus the statement is proved, because for the plane wing

$$C_D = \alpha^2 d_{00} = (d_{00}/C_{L_\alpha}{}^2) C_L{}^2 \tag{13}$$

These results are applicable to solutions which employ linearized planar-wing theory or slender-body theory but not to solutions obtained by higher order theory in which the boundary conditions are not linear functions of the assumed series or the drag is not a parabolic function of the series coefficients.

## Thermal Buckling of Clamped Cylindrical Shells

William Zuk*
*Associate Professor of Civil Engineering, University of Virginia, Charlottesville, Va.*
January 23, 1957

THE PROBLEM of thermal buckling of shells arises in connection with air-frame bodies subject to aerodynamic heating at supersonic speeds. The case of the shell with clamped edges is presented, as this case typifies all structures with a tubular shell stiffened at intervals with stiffening rings. The shell is assumed to be unrestrained longitudinally and fully restrained laterally at the edges.

The method of analysis is based upon Galerkin's method in conjunction with Donnell's shell equation. Donnell's equation is as follows:

$$D\nabla^8 w + (Et/r^2)(\partial^4 w/\partial x^4) + t\nabla^4 [\sigma x (\partial^2 w/\partial x^2) + 2\tau (\partial^2 w/\partial x \partial y) + \sigma y (\partial^2 w/\partial y^2) - (\sigma y/r)] + \nabla^4 p = 0 \tag{1}$$

where $w$ is the radial deflection, $x$ is the axial coordinate, $y$ is the transverse coordinate, $t$ is the shell thickness, $r$ is the shell radius, $D$ is the flexural rigidity of a plate, $E$ is the modulus of elasticity, $\nabla^4$ is an operator equal to $[(\partial^2/\partial x^2) + (\partial^2/\partial y^2)]^2$, and $\nabla^8$ is an operator equal to $[(\partial^2/\partial x^2) + (\partial^2/\partial y^2)]^4$.

For thermal buckling, the following values of loads and stresses are taken:

$$p = \sigma x = \tau = 0$$

It is assumed that the circumferential stress $\sigma y$ may be approximated by the function

$$\sigma y = (E\alpha T/2)[1 + \cos(2\pi x/L)]$$

where $\alpha$ is the coefficient of expansion, $L$ is the length of the shell, and $T$ is the shell temperature assumed constant.

A Fourier series solution satisfying the boundary conditions of zero slope and deflection is assumed as

$$w = \sin(\pi y/\lambda) \sum_{m=1,3,5}^{\infty} a_m \sin(\pi x/L) \sin(m\pi x/L) = \sum_{m=1,3,5}^{\infty} a_m \phi_m \tag{2}$$

where $a_m$ is an undetermined coefficient, and $\lambda$ is the half wavelength of buckling in the $y$ direction.

The Galerkin method prescribes substituting Eq. (2) into Eq. (1). In general, the left-hand side of Eq. (1) will not be zero after this operation. This resulting function on the left-hand side is the error function $Q$. For a first-order solution, only the first term of Eq. (2) will be used.

To reconcile this error, the Galerkin method prescribes this operation:

$$\int_0^\lambda \int_0^L Q\,\phi_1\,dx\,dy = 0 \tag{3}$$

After carrying out the operation of Eq. (3) and simplifying, the following characteristic equation of buckling is obtained:

$$3A - B - 2C = 0 \tag{4}$$

where

$$A = D\pi^8[(128/L^8) + (128/\lambda^2 L^6) + (48/\lambda^4 L^4) + (8/\lambda^6 L^2) + (1/\lambda^8)] + (8Et\pi^4/r^2 L^4) - (E\alpha T\pi^6/\lambda^2)[(4/L^4) + (2/\lambda^2 L^2) + (1/2\lambda^4)]$$

$$B = D\pi^8[(128/L^8) + (128/\lambda^2 L^6) + (48/\lambda^4 L^4) + (8/\lambda^6 L^2)] + (8Et\pi^4/r^2 L^4) - (2E\alpha t T\pi^6/\lambda^2 L^2)[(2/L^2) + (1/\lambda^2)]$$

$$C = (E\alpha t T\pi^6/\lambda^2)[(1/\lambda^4) - (6/\lambda^2 L^2) - (36/L^4)]$$

Simplifying Eq. (4) further, the critical buckling temperature $T_{cr}$ is obtained.

$$T_{cr} = [\pi^4 r^2 t^2 (6L^8 + 32L^6\lambda^2 + 384L^4\lambda^8] \div [12(1 - \mu^2)\pi^2 \alpha r^2 L^4 \lambda^2 (7L^4 - 16L^2\lambda^2)] \tag{5}$$

where $\mu$ is Poisson's ratio.

This equation must next be minimized with respect to $\lambda$. It has been found that the most convenient manner of minimizing this equation is numerically, using the constants involved in one's specific problem. It is simply necessary to plot a curve of $T_{cr}$ against assumed values of $\lambda$. The low point on the curve is then the minimum critical buckling temperature.

* The writer wishes to thank The Glenn L. Martin Company, under whose auspices this investigation was performed, for permission to publish this work.

## A Simple Relation Between the Shock and Expansion Pressure Coefficients for Two-Dimensional Hypersonic Flow

J. L. Raymond and E. P. Williams
*Aeronautics Department, The RAND Corporation, Santa Monica, Calif.*
January 25, 1957

ACCORDING to the hypersonic small-disturbance theory,[1, 2] the two-dimensional wedge pressure coefficients for shock and expansion are given by

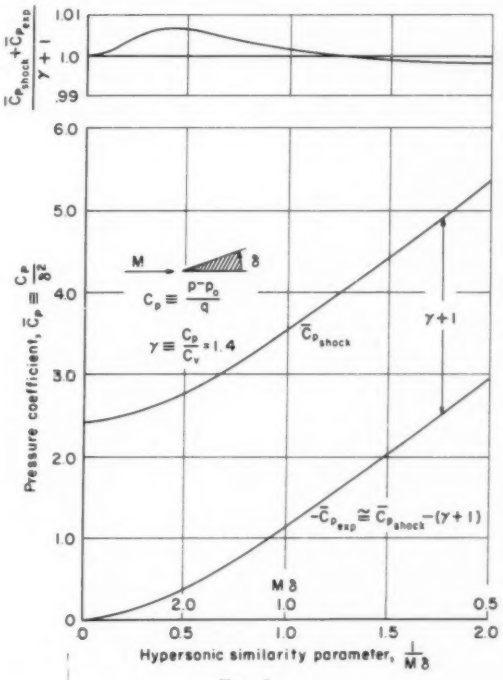


FIG. 1.

$$\bar{C}_{p\text{shock}} = C_p/\delta^2 = [(\gamma + 1)/2] + \sqrt{[(\gamma + 1)^2/4] + (4/M^2\delta^2)}$$

$$\bar{C}_{p\text{expansion}} = C_p/\delta^2 = (2/\gamma M^2\delta^2)\{[1 - [(\gamma - 1)/2]M\delta]^{2\gamma/(\gamma-1)} - 1\}$$

which for $M\delta > 2/(\gamma - 1)$ reduces to

$$\bar{C}_{p\text{expansion}} = -(2/\gamma M^2\delta^2)$$

The conventional symbols are defined in Fig. 1.

It is the purpose of this note to point out that

$$\bar{C}_{p\text{shock}} + \bar{C}_{p\text{expansion}} \leqq \gamma + 1$$

As can be seen from Fig. 1, this relation between the shock and expansion coefficients applies throughout the entire hypersonic regime. Considerable additional simplification of calculations in two-dimensional hypersonic flow results from this approximate relation.

A detailed discussion and analysis of this relation is contained in reference 3.

### References


[1] Van Dyke, Milton D., *A Study of Hypersonic Small-Disturbance Theory*, NACA Report 1194, 1954.

[2] Cole, J. D., Gazley, C., Jr., and Williams, E. P., Class Notes for a Hypersonic Aerodynamics Course, UCLA Extension, Spring Terms, 1956 and 1957.

[3] Raymond, J. L., *A Simple Relationship Between the Shock and Expansion Pressure Coefficients As a Basis for Studying Two-Dimensional Hypersonic Flow*, The RAND Corporation, Paper P-1011, January 15, 1957.


## A Note on Cone Base Pressures in Hypersonic Flow


Richard D. Linnell*

*Functional Engineer, General Electric Company, Schenectady, N. Y.*


January 28, 1957

THE BASE PRESSURE on a cone in a flow at hypersonic speeds may be greater than the free-stream pressure. This is of interest because it is contrary to the indications of extrapolated linear supersonic theory as well as to the known overexpansion effect at the corner of a cone-cylinder at supersonic speeds.

Calculated values of the base-pressure ratio are shown in Fig. 1, for arbitrary values of the wake convergence angle, on a similarity rule basis. Flow conditions just ahead of the base of the cone were taken from the M.I.T. cone tables.[1] A Prandtl-Meyer expansion to the initial wake convergence angle $\beta$ was assumed to give the base pressure as a function of $\beta$. The pressure just behind the corner of a cone-cylinder is obtained by taking $\beta = 0$. The calculated values of the ratio of the base pressure $p_B$ to the free-stream pressure $p_\infty$ are presented as a function of the cone similarity parameter $K_c = \sqrt{M^2 - 1}\sin\theta_c$, where $M$ is the free-stream Mach Number and $\theta_c$ is the half angle of the cone. The wake convergence similarity parameter $K_\beta = \sqrt{M^2 - 1}\sin\beta$ is constant on each of the curves shown.

The expansion on a cone-cylinder to pressures below free-stream pressure is represented by the dip in the $K_\beta = 0$ curve. When $K_c$ is greater than about 3.4, this overexpansion disappears. For larger values of $K_c$, there is a pressure greater than free stream just behind the corner. If the wake angle were zero on a cone, there would be a base thrust when $K_c$ is greater than 3.4. The increased pressure may also lead to increased heat-transfer rates on the base.

The curves for $K_\beta$ greater than zero show that pressures greater than free stream can still occur at hypersonic speeds even if the wake converges. But since $\beta$ was assumed in these calculations, conditions on the base are not completely determined. The trends shown by Fig. 1 indicate that theoretical and experimental data for $\beta$ are desirable, or other data to determine the actual conditions on the base.

Similar calculations have been made by Ferri and Pallone[2] for several cases of flow about wedges and the cone-cylinder. The similarity rule correlation used here generalizes the results for the cone-cylinder.

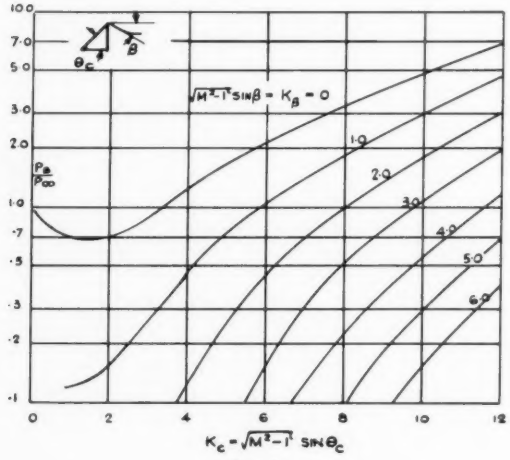


FIG. 1.

### References


[1] Kopal, Z., *Tables of Supersonic Flow Around Cones*, Report No. 1, Computing Section, Center of Analysis, Department of Electric Engineering, Massachusetts Institute of Technology, 1949.

[2] Ferri, A., and Pallone, A., *Note on the Flow Field on the Rear Part of Blunt Bodies in Hypersonic Flow*, WADC TN 56-294, July, 1956.


## An Extension of Donnell's Equation for a Circular Cylindrical Shell


Tsu-Tao Loo

*Associate Professor of Mechanics, Rensselaer Polytechnic Institute, Troy, N.Y.*


January 28, 1957

IN 1933, Donnell succeeded in simplifying the equations of equilibrium for a circular cylindrical shell to[1]

$$\left.\begin{aligned} \nabla^4 u &= (1/r)\,[\mu(\partial^3 w/\partial x^3) - (\partial^3 w/\partial x\partial y^2)] \\ \nabla^4 V &= (1/r)\,[(2 + \mu)\,(\partial^3 w/\partial x^2\partial y) + (\partial^3 w/\partial y^3)] \\ D\nabla^4 w - (1/r)\,[Et/(1 - \mu^2)]\,[\mu(\partial u/\partial x) + & \\ (\partial v/\partial y) - (w/r)] &= p + \sigma_x t(\partial^2 w/\partial x^2) + \\ & 2\,\tau_{xy} t(\partial^2 w/\partial x\partial y) + \sigma_y t(\partial^2 w/\partial y^2) \end{aligned}\right\} \quad (1)$$

or

$$D\nabla^8 w + (Et/r^2)\,(\partial^4 w/\partial x^4) = \nabla^4[p + \sigma_x t(\partial^2 w/\partial x^2) + 2\tau_{xy} t(\partial^2 w/\partial x\partial y) + \sigma_y t(\partial^2 w/\partial y^2)] \quad (2)$$

where $u$, $v$, $w$ are the longitudinal, circumferential, and radial displacements, respectively; $r$, $t$, $D$ are the radius, thickness, and flexual rigidity of the shell; $\sigma_x$, $\sigma_y$, $\tau_{xy}$ are the average uniform longitudinal, circumferential, and shearing membrane stresses due to the external loading; $p$ is the normal lateral load per unit area; and $E$ and $\mu$ are Young's modulus and Poisson's ratio of the material. With the above equations, he obtained simple relations between the critical buckling shearing stress and the physical properties of a thin circular cylinder under pure torsion.[1] His approach reduces the tedious computations involved in the classical solutions and is still in good agreement with them. Furthermore, it is easy to show that the well-known classical solution for critical compressive stress of the cylinder under axial compression can readily be obtained from Donnell's equation.[2]

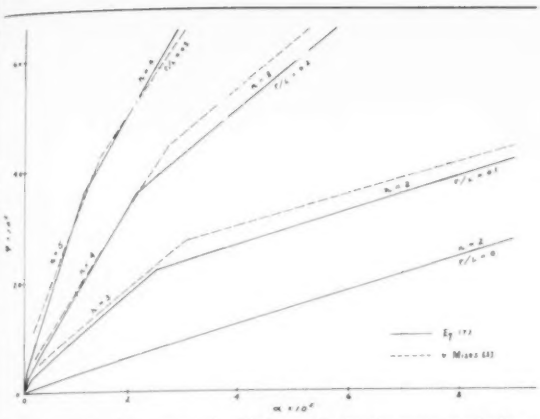

FIG. 1. Critical pressure of cylinder with simply supported edges.

However, when Donnell's equation, Eq. (2), is used to solve the case of the cylinder under a uniform external lateral pressure, the predicted critical pressure $p_{cr}$ deviates considerably from the analytical results obtained earlier by others[3-5] especially for the limiting case of infinitely long cylinders ($r/L \to 0$). In such a case, all classical solutions converge, as they should, to the same value as that for a circular ring under uniform external pressure—i.e.,

$$p_{cr} = [E/4(1 - \mu^2)]\,(t/r)^3 \tag{3}$$

whereas, from Eq. (2), the critical value is found to be 33 per cent higher. It is the purpose of the present note to suggest an extension of Donnell's equation which will remedy this discrepancy. In establishing his equation, Donnell neglected the transverse shearing forces while considering equilibrium in the circumferential direction. If these shearing forces are not neglected, then Eq. (2) becomes

$$D\nabla^8 w + (D/r^2)\,[(2 + \mu)\,(\partial^4/\partial x^2 \partial y^2)\,(\nabla^2 w) + (\partial^4/\partial y^4)\,(\nabla^2 w)] + (Et/r^2)\,(\partial^4 w/\partial x^4) = \nabla^4[p + \sigma_x t(\partial^2 w/\partial x^2) + 2\tau_{xy} t(\partial^2 w/\partial x \partial y) + \sigma_y t(\partial^2 w/\partial y^2)] \tag{4}$$

where the terms inside the bracket in the left-hand side of Eq. (4) are the correction terms.

In the case of a uniform external lateral pressure,

$$\left.\begin{aligned} \sigma_x &= \tau_{xy} = 0 \\ p &= p_{cr} = \text{constant} \\ \sigma_y &= -p_{cr}(r/t) \end{aligned}\right\} \tag{5}$$

Assume $$w = w_{mn} \sin (m\pi x/L) \sin (ny/r) \tag{6}$$

thereby satisfying the simply supported boundary conditions. Then, by putting Eqs. (5) and (6) in Eq. (4) and taking $m = 1$,

$$\left.\begin{aligned} \varphi &= [(1 - \mu^2)/n^2(1 + \beta^2)^2] + \alpha\{n^2[(1 + \beta^2)^2/\beta^4] - \\ &\qquad 1 - [(1 + \mu)/(1 + \beta^2)]\} \end{aligned}\right\} \tag{7}$$

where

$$\varphi = [(1 - \mu^2)p_{cr} r/ET], \quad \alpha = (1/12)\,(t/r)^2, \quad \beta = nL/\pi r$$

Eq. (7) indicates a linear relationship between $\varphi$ and $\alpha$ for given values of $r/L$ and $n$. In Fig. 1, several such relationships are drawn for various radius-length ratios, $r/L$. The dotted curves are the results obtained by von Mises[3] and appear to be in good agreement with the results of this note. Further, in the two limiting cases: (a) the infinitely long cylinder ($r/L \to 0$)—Eq. (7) reduces to Eq. (3); and (b) the finitely long cylinder of infinite radius (i.e., $L/r \to 0$, $t/r \to 0$)—Eq. (7) approaches the critical value for a flat plate. This is an improvement of von Mises' solution which is found to be 50 per cent too low for case (b).* Consequently, it seems that the present solution is applicable to the entire range of physical proportions of any cylinder.

It is further noted that the correction terms in the extended Donnell's equations, Eq. (4), have the effect of the order of magnitude of $1/n^2$. Thus, in the cases of axial compression and pure torsion, the effect of these terms diminishes due to the larger number of circumferential waves present during buckling.

* This author has recalculated von Mises' solution for this particular case and has found the above value, which disagrees with what was in Fig. 2 of reference 2.

### REFERENCES


1. Donnell, L. H., *Stability of Thin-Walled Tubes Under Torsion*, NACA Rept. 479, 1933.
2. Batdorf, S. B., *A Simplified Method of Elastic-Stability Analysis for Thin Cylindrical Shells*, NACA Rep. 874, 1947.
3. von Mises, R., *Der Kritische Aussendruck Zylindrischer Rohre*, z. VDI, Vol. 58, No. 19, 1914; also Timoshenko, S., *Theory of Elastic Stability*; McGraw-Hill Book Company, Inc., New York, 1936.
4. Southwell, R. V., *On the Collapse of Tubes by External Pressure*, Phil. Mag., Vol. 25, 1913.
5. Flügge, W., *Statik und Dynamik der Schalen*, Springer-Verlag, 1934.


## Real Part of the Square Root of a Complex Number


E. V. Laitone
*Professor of Mechanical Engineering, University of California, Berkeley, Calif.*

February 4, 1957

IN MANY PROBLEMS dealing with the dynamic stability of a system, especially for a rolling missile, it is convenient to evaluate the stability requirements by calculating the real part of the square root of a complex number (see references 1 and 2).

As is well known, the exact evaluation is given by

$$R\sqrt{\xi + i\eta} = \sqrt{(\xi + \sqrt{\xi^2 + \eta^2})/2} = (\xi^2 + \eta^2)^{1/4} \cos [(1/2) \tan^{-1} (\eta/\xi)] \tag{1}$$

when $\xi$ and $\eta$ are both real numbers. However, the exact value usually can only be obtained numerically and, in general, is not useful for developing any explicit criteria to be satisfied by the system parameters for stability. In order to accomplish this, the following expansions of Eq. (1) will prove useful:

$$R\sqrt{\xi + i\eta} = R\xi^{1/2}[1 + (i\eta/\xi)]^{1/2} = R(i\eta)^{1/2}[1 - (i\xi/\eta)]^{1/2}$$

etc., resulting in the exact, alternating power series developments

$$\sqrt{\xi}\,[1 + (1/8)(\eta/\xi)^2 - (5/128)(\eta/\xi)^4 + \ldots] \qquad |\eta/\xi| < 1, \quad \xi > 0 \tag{2}$$

$$\sqrt{-\xi}\,[(1/2)(\eta/-\xi) - (1/16)(\eta/-\xi)^3 + (7/256)(\eta/-\xi)^5 - \ldots] \qquad |\eta/\xi| < 1, \quad \xi < 0 \tag{3}$$

$$\sqrt{|\eta|/2}\,[1 + (1/2)(\xi/|\eta|) + (1/8)(\xi/|\eta|)^2 - (1/16)(\xi/|\eta|)^3 - (5/128)(\xi/|\eta|)^4 + (7/256)(\xi/|\eta|)^5 + \ldots], \quad 0 \leq |\xi| < |\eta| \tag{4}$$

Since these are alternating power series, Eq. (4) being the sum of two alternating series of the type represented by Eqs. (2) and (3), a rigorous upper bound is provided for all cases by

$$|R\sqrt{\xi + i\eta}| < \begin{cases} |\eta|/2\sqrt{-\xi}, & \xi < 0, \quad |\eta/\xi| < 1 \\ \sqrt{\xi}\,[1 + (1/8)|\eta/\xi|^2], & \xi > 0, \quad |\eta/\xi| < 1 \\ \sqrt{|\eta|/2}, & \xi \leq 0, \quad |\xi/\eta| < 1 \\ \sqrt{|\eta|/2}\,[1 + (1/2)|\xi/\eta| + (1/8)|\xi/\eta|^2], & \xi \geq 0, \quad |\xi/\eta| < 1 \end{cases} \tag{5}$$

Generally adequate design criteria for dynamic stability can be developed from these simple but rigorous upper bounds. This is particularly true for a statically stable missile having a moderately large negative $Cm_\alpha$ since in this case $\xi < 0$ for all rates of roll.

These bounds also provide a simple, useful comparison for the range of validity of other approximate evaluations. For example, it can be shown that conclusion (C) on page 400 of reference 1 is erroneous because of the breakdown, at slow rates of roll, of the approximate method used in reference 1 for extracting the square root of a complex number. The corresponding stability conditions in reference 2 would also be in error for this case, for the same reason.

### References


[1] Bolz, R. E., *Dynamic Stability of a Missile in Rolling Flight*, Journal of the Aeronautical Sciences, Vol. 19, No. 6, pp. 395–403, June, 1952.

[2] Bryson, A. E., *Note on the Dynamic Stability of a Missile in Rolling Flight*, Readers' Forum, Journal of the Aeronautical Sciences, Vol. 20, No. 1, pp. 69–71, January, 1953.

[3] Bolz, R. E., *Further Note on the Dynamic Stability of a Missile in Rolling Flight*, Readers' Forum, Journal of the Aeronautical Sciences, Vol. 20, No. 5, pp. 356, 357, May, 1953.


## Note on the Change From Multi-Cell to Single-Cell Rotating Stalls


F. Cheers

*Gas Dynamics Department, Division of Mechanical Engineering, National Research Council, Ottawa, Canada*


February 18, 1957

In most tests on single-stage compressor rigs the same general pattern appears. As the blades in the row stall, a small number of rotating stall cells of fairly small amplitude is detected; as the mean blade incidence is increased, the number of cells increases until the pattern of small cells breaks down to a single large cell of greater amplitude. A possible reason for this change in pattern is suggested.

In his theory of propagating stalls, Wood[1] assumes that the flow upstream of an infinite two-dimensional blade row consists of a small-amplitude unsteady potential flow superimposed on the mean steady flow. The potential of the perturbation flow is

$$\phi = \sum_{n=1}^{\infty} a_n \exp(2n\pi x/l) \cos[2n\pi(y - \lambda t)/l]$$

the $y$ axis lying in the front face of the cascade and the $x$ axis normal to it, $x$ and $y$ increasing in the direction of the incident flow; $l$ is the wavelength of the stall cells along the $y$ axis, and $\lambda$ their velocity in the direction $y$ increasing.

If we calculate the velocity variation upstream of the blades due to this potential flow, taking only the first term of the series, we find that it agrees fairly well with the measurements of Costilow and Huppert[2] for multi-cell stalls on a single blade row, and it is assumed, therefore, that this theory gives a reasonably accurate picture of the flow ahead of small-amplitude stalls. If this is so, air approaching a rotating row will travel very nearly in an axial direction with velocity

$$V = V_Z\{1 + (1/2)(\Delta V_Z/V_Z) \exp(2\pi x/l) \times \cos[2\pi(h/N)(U/V_Z)(x/l) + X]\}$$

where

$V_Z$ = mean axial air velocity
$U$ = rotor blade speed
$N$ = compressor rotative speed
$h$ = absolute rotative speed of the stall cells
$\Delta V_Z$ = amplitude of velocity variation due to stall cells immediately upstream of blade row
$X$ = a phase angle determined by the position of the air relative to the stall cell pattern

Using this theory and the measurements of Costilow and Huppert, assuming that transition occurs on the walls at the beginning of the parallel ducting upstream of the blades and that the flow is effectively two-dimensional, an estimate of the growth of the turbulent boundary layer on the walls of the duct has been made by the method of von Doenhoff and Tetervin.[3] Calculations were made for patterns with three stall cells and with four cells, which were observed occasionally to replace the single cell at higher incidences. As no measurements of the four cells were reported, it was assumed that they behaved, in general, like the three cells.

From this it appears that the boundary layer on the wall of the duct will separate upstream of the blade if $\Delta V_Z/V_Z$ exceeds 0.95 with four cells or 0.98 with three cells. This seems to be in reasonable agreement with the measurements reported, which show $\Delta\rho V/\overline{\rho V} = 0.62$ at the mean radius, or 0.87 near the outer wall for three cells (flow coefficient$\sim$0.68), apparently increasing as the incidence increases, with the single cell appearing at a flow coefficient of about 0.63.

The boundary layer ahead of a stall will spread laterally and so reduce the thickness compared with two-dimensional flow; at the same time, the effect of the thicker boundary layer on the blades should increase the adverse pressure gradient at the walls. If the boundary layer on the wall ahead of one of the cells did separate, it is most unlikely that the flow would reattach in the region of the stall. Rather, the separated region is likely to break down the flow through the blades and spread and so suppress the other stall cells and form a single cell. In view of the transient nature of the flow it would be difficult to make direct measurements; however, a small modification of the ducting to produce a favorable mean velocity gradient up to the face of the cascade should permit multi-cell patterns at higher blade incidences.

### References


[1] Wood, M. D., Cambridge Univ. Engineering Lab., Ph.D. Thesis, 1955.

[2] Costilow, E. L., and Huppert, M. C., *Rotating-Stall Characteristics of a Rotor With High Hub-Tip Radius Ratio*, NACA TN 3518, August, 1955.

[3] von Doenhoff, A. E., and Tetervin, N., *Determination of General Relations for the Behavior of Turbulent Boundary Layers*, NACA Rep. 772, April, 1943


## Correlation of Cone-Cylinder Normal Force . . . (*Continued from page 377*)


[2] Linnell, R. D., *Two-Dimensional Airfoils in Hypersonic Flows*, Journal of the Aeronautical Sciences, Vol. 16, No. 1, pp. 22–30, January, 1949.

[3] Dorrance, W. H., *Two-Dimensional Airfoils at Moderate Hypersonic Velocities*, Journal of the Aeronautical Sciences, Vol. 19, No. 9, pp. 593–600, September, 1952.

[4] Hayes, W. D., *On Hypersonic Similitude*, Quarterly of Applied Mathematics, Vol. 5, No. 1, pp. 105, 106, April, 1947.

[5] Hamaker, F. M., Neice, S. E., and Eggers, A. J., *The Similarity Law for Hypersonic Flow About Slender Three-Dimensional Shapes*, NACA TN 2443, August, 1951.

[6] Dorrance, W. H., *Three-Dimensional Hypersonic Flow Similarity Parameters*, Convair, A Division of General Dynamics, Report ZA-7-001, September 3, 1951.

[7] Dorrance, W. H., *Correlation of Supersonic Body of Revolution Data for Design Charts*, Convair, A Division of General Dynamics, Report ZA-7-032 TN, March 21, 1952.

[8] Van Dyke, M. D., *The Combined Supersonic-Hypersonic Similarity Rule*, Readers' Forum, Journal of the Aeronautical Sciences, Vol. 18, No. 7, pp. 499, 500, July, 1951.

[9] Chaplin, H., and DeMeritte, F. J., *Static Stability Measurements on Cone Cylinders*, Navord 2882, May 26, 1953.

[10] Schantz, I., *Cone Static Stability Investigation at Mach Numbers 1.56 Through 4.24*, Navord 3584, December 7, 1953.